Journal of Chemistry

Emerging Materials and Technologies for Water and Wastewater Treatment

Lead Guest Editor: Ibrahim H. Alsohaimi
Guest Editors: Hassan M. Hassan, Mohammad Saad Algamdi, Abdullah Mohammed Aldawsari, and Qiao Chen

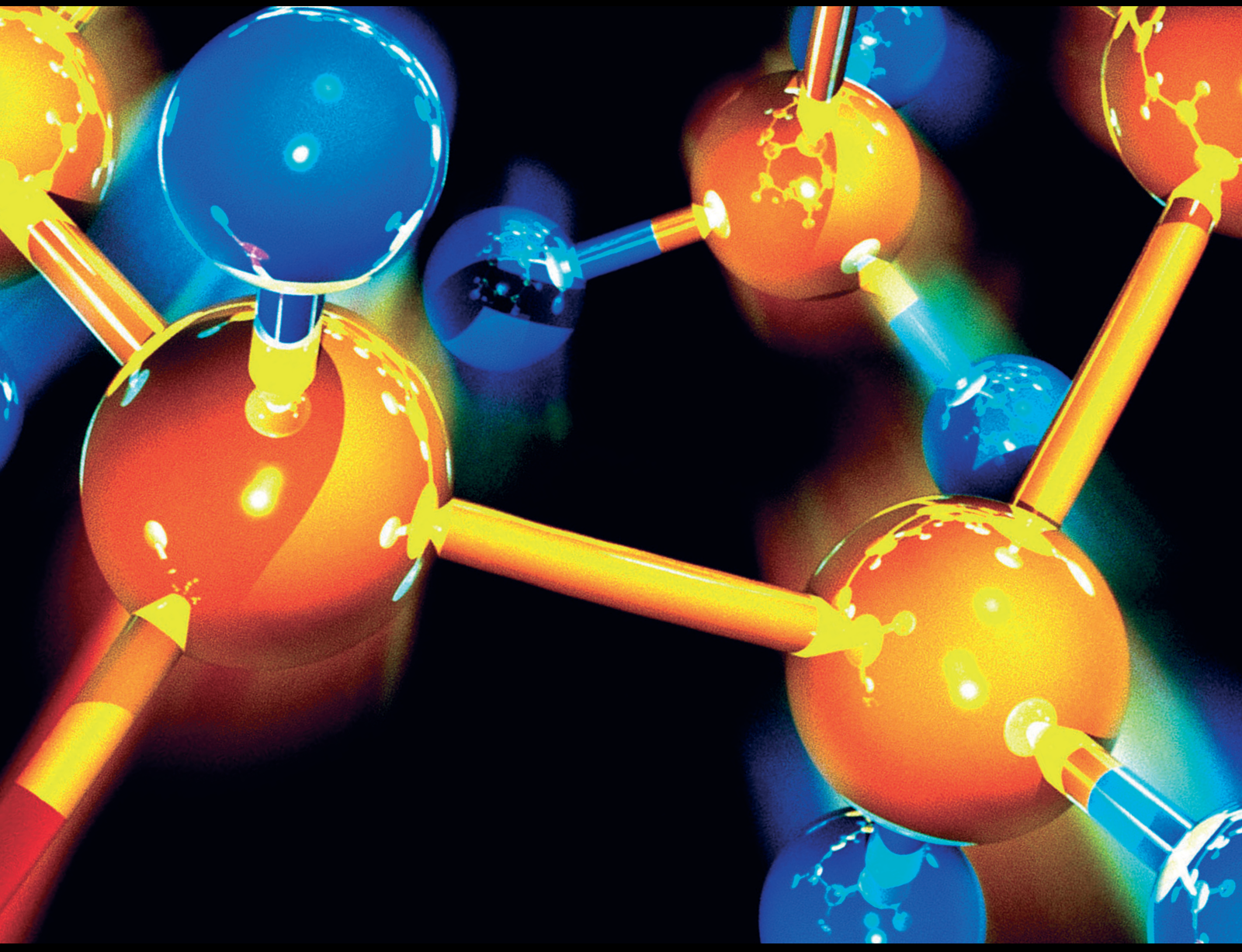

Emerging Materials and Technologies for Water and Wastewater Treatment

Journal of Chemistry

Emerging Materials and Technologies for Water and Wastewater Treatment

Lead Guest Editor: Ibrahim H. Alsohaimi
Guest Editors: Hassan M. Hassan, Mohammad Saad Algamdi, Abdullah Mohammed Aldawsari, and Qiao Chen

Contents

Treatment of Cutting Oil-in-Water Emulsion by Combining Flocculation and Fenton Oxidation
Chu Thi Hai Nam, Nguyen Thi Thu Hien, Nguyen Thi Thu Huyen, Hoang Huu Hiep, and Nghiem Thi Thuong
Research Article (9 pages), Article ID 7248402, Volume 2021 (2021)

Removal of Antibiotics from Real Hospital Wastewater by Cold Plasma Technique
Phuong Thi Thanh Nguyen, Hieu Trung Nguyen, Uyen Nhat Phuoc Tran, and Ha Manh Bui
Research Article (13 pages), Article ID 9981738, Volume 2021 (2021)

Hindawi
Journal of Chemistry
Volume 2022, Article ID 6918063, 12 pages
https://doi.org/10.1155/2022/6918063

Research Article

Removal of Tricyclazole and Total Organic Carbon in Real Pesticide Wastewater by Electro-Fenton

Ha Manh Bui [1] **and Loan Ngoc Huynh** [2]

[1] *Department of Environmental Sciences, Saigon University, 273 An Duong Vuong Street, District 5, Ho Chi Minh City 70000, Vietnam*
[2] *Institute for Environment and Resources, Vietnam National University of Ho Chi Minh City, Thu Duc City, Ho Chi Minh City 70000, Vietnam*

Correspondence should be addressed to Ha Manh Bui; manhhakg@yahoo.com.vn

Received 4 June 2021; Accepted 18 August 2021; Published 19 January 2022

Academic Editor: Ibrahim H. Alsohaimi

In this study, electro-Fenton (EF) was employed for the removal of tricyclazole (TC) and total organic carbon (TOC) in real pesticide wastewater (RPW). The central composite design (CCD) with three parameters, that is, current density, Fe^{2+} concentration, and electrolysis time, has been conducted to predict the TOC and TC removal efficiency. The high correlation of the quadratic models of 0.9842 and 0.9781 for TC and TOC removal, respectively, indicates the significance of the models. The obtained results revealed that the high-efficiency removal of both TC and TOC in RPW. Approximately 99.6% of TC was decomposed under the optimum conditions of a current density of 2.2 mA/cm^2 and an Fe^{2+} concentration of 0.2 mM during 188 min with an operating cost of 121.392 \$/kg TC or ~2.692 \$/m^3, while 84.2% TOC was eliminated at a current density of 2.2 mA/cm^2 and an Fe^{2+} concentration of 0.2 mM during 217 min with an operating cost of 3.019 \$/kg TOC or 3.916 \$/m^3. Acute toxicity tests at optimal condition revealed moderate exhibition toxicity of treated wastewater against *Daphnia magna* with LC_{50} values of 3.12%, 2.05%, 1.84%, and 1.36% at 24 h, 48 h, 72 h, and 96 h, respectively. The removal of TC and TOC followed pseudo-first-order kinetic with an R^2 of ~0.993 and 0.923, respectively.

1. Introduction

Agriculture is critical to the economies of Vietnam, in which export-oriented agricultural production is a significant source of foreign exchange earnings. The agricultural sector provides approximately 14.85% of the gross national product with over 18.8 million Vietnamese in 2019 [1]. However, the vast number of pesticides produced to prevent pests or diseases on crops resulting in threats to the environment and human health [2]. Extensive studies have reported that pesticides originating from agriculture factories are characterized by a high chemical oxygen demand (COD), total suspended solids (TSS), and toxicity. In particular, pesticide application to rice paddies has been detected in surface water, groundwater, and soil [3]. These kinds of pesticides also stand out in high production and worldwide distribution; tricyclazole (TC) is a unique fungicide among the most widely used pesticides for control of *Pyricularia oryzae* in rice fields [4, 5]. Duy et al. [6] stated that TC was moderately toxic to tropical freshwater *Daphnia* species (48 h LC_{50}, 32.68 mg/L). Werner et al. [7] also stated that TC could display human mutagenic and carcinogenic [8]. Therefore, it is necessary to use appropriate techniques to remove these pollutants to preserve the environment from contaminated water. Biological processes are quite economical for the treatment of wastewaters. Wu et al. [8] had isolated *Sphingomonas* sp. NJUST37 from activated sludge and successfully applied to degrade over 90% tricyclazole in pilot-scale powdered activated carbon treatment tank after 81 days. However, the COD is still high around 160 mg/L, and further treatment time has insignificant effect on the removal efficiency. Moreover, biological methods have

proven ineffective in removing refractory or nonbiodegradable compounds [9]. For instance, biological treatment processes have not successfully removed pesticide wastewater [10]. Alternatively, physicochemical techniques, that is, coagulation, adsorption, nanofiltration, and so on, are also used to treat wastewater; Azarkan et al. [11] had collected four clays with different characteristics from various locations in northern Morocco to adsorb 5 mg/L TC from solution; the TC mitigation obeyed pseudo-second-order kinetic model with R^2 values ≥ 0.95. However, the TC removal efficiency only reached from 0.27 to 28.59% for the clays. While Kiso et al. [12] indicated that 79.8% of TC were removed using nanomembrane; the authors also stated that three other nanomembranes were negligible on the rejection of TC. Even though these methods have some applications in TC removal, these techniques transfer only the pollution from one phase to another, requiring further treatment [9, 13]. Therefore, it is essential to develop more effective treatment methods to eradicate the contaminants.

For instance, advanced oxidation processes (AOPs) are proven to be the most effective techniques for the degradation of a wide range of pollutants in aqueous solutions such as pharmaceutical [14, 15], pesticide [6], dyeing, and textile [16, 17]. The process is characterized by their ability to generate hydroxyl radical ($^{\bullet}OH$) and other reactive oxygen species. One of the most important chemical reactions in the advanced oxidation process is Fenton (Fe^{2+}/H_2O_2) and Fenton-like systems. The Fenton reaction was the first described by H. J. H. Fenton in 1894 [18] with chemical mechanism according to the following equation:

$$Fe^{+2} + H_2O_2 \longrightarrow Fe^{3+} + \cdot OH + OH^{-}. \quad (1)$$

The Fenton reaction consists of reducing H_2O_2 until hydroxyl radicals and hydroxide caused by oxidation of Fe^{2+} to Fe^{3+}.

However, this method has drawbacks related to the wastage of oxidants (iron ions or H_2O_2) and the formation of excess sludge [19]. The new Fenton process based on electrolysis systems has been developed and called electro-Fenton (EF) to overcome the disadvantages of homogeneous Fenton. In the EF process, H_2O_2 can be generated at the cathode when bubbling oxygen gas through the acidic solution, followed by reducing H_2O_2. The electrochemical generation of Fe^{2+} ions occurs through the reaction of anodic material dissolution or cathodic reduction of Fe^{3+} ions [18]. In this process, pollutants are destroyed by Fenton's action reagent together with the combination of anode oxidation on the anode surface. The Fenton process and electrochemical are combined with the increasing degradability of organic compounds present in high-intensity wastes. Even several researchers have applied EF to eliminate pollutants from wastewater of dyeing and textile [20, 21], pharmaceuticals [14], coke [22], pesticides [23–25], or mixed industrial wastewater [26]. Very few studies focus on the mineralization and biodegradability of tricyclazole and pollutants from real pesticide production by EF process [27].

In the present work, the degradation of TC and total organic carbon (TOC) in real pesticide production wastewater are investigated using the EF process in a batch chemical reactor. This study aims to analyze how the degradation process of TC and TOC can be affected by current density, Fe^{2+} dosage, and electrolysis time using a central composite design (CCD). Additionally, the degradation mechanism is investigated based on kinetics studies, the toxicity of the wastewater on *Daphnia magna*, and operating costs.

2. Experimental

2.1. Chemical and Real Pesticide Wastewater (RPW). Ferrous sulfate ($FeSO_4$), sodium hydroxide (NaOH), sodium sulfate (Na_2SO_4), hydrogen chloride (HCl), and sulfuric acid (H_2SO_4) were purchased from Xilong Scientific Corporation Ltd., China. All the chemicals were of analytical grade, and solutions were prepared with deionized water of resistivity not less than 18.2 MΩ/cm. The pesticide effluent was obtained from an agriculture production company located in Longan province, Vietnam. It was collected in an equalization tank after a sieve system. Wastewater was collected in a glass container and preserved at 4°C for treatment by EF. The effluent characteristics are as follows: initial pH of 6.6–7.2, total organic carbon (TOC) of 1,236–1,358 mg/L, tricyclazole (TC) of 23.7–25.1 mg/L, and total nitrogen (TN) of 240–272 mg/L.

2.2. Acute Toxicity Assay. After treatment, the pesticide wastewater with the optimal condition for TOC was selected to test the toxicity to *D. magna*.

The effluent was characterized as pH of 6.8, total organic carbon (TOC) of 204.4 mg/L, tricyclazole (TC) of 0.185 mg/L, and total nitrogen (TN) of 72.6 mg/L. *D. magna* obtained from MicroBioTest Inc., Belgium, was used for the test. The acute test was performed according to the OECD guideline 202 [28]. *D. magna* live stocks were cultured in glass containers at a density of 1 individual/10 mL of ISO medium [29]. The test organisms were daily fed a mixture of *Scenedesmus* sp. and *Chlorella* sp. The culture medium was renewed every three days and maintained at 25 ± 1°C under a 12:12 h light-dark cycle. For each test samples, a serial dilution (0.1%, 0.25%, 0.5%, 1.0%, 2%, and 5%) of PWAT plus the blank control was used. All test concentrations were prepared in triplicate and spiked with 40 mL of ISO medium in 50 mL glass beakers. Ten neonates (<24 h old) were added to each beaker. The test was run for 96 h at a stable pH and temperature 7.5 and 25 ± 1°C, respectively. The mortality of tested neonates was checked at 24 h, 48 h, 72 h, and 96 h. The median lethal concentrations (LC_{50}) at 24 h, 48 h, 72 h, and 96 h were calculated using Probit analysis.

2.3. Experimental Procedures. The reactor used for the treatment was made of glass with the dimensions of 160 × 160 × 250 mm totalizing a volume of 3 L of effluent per treatment (Figure 1). The experiments were performed in a bipolar batch reactor, with two iron electrodes anode (Fe:

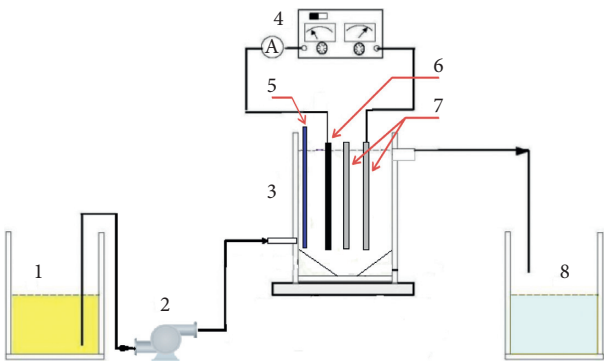

Figure 1: Schematic diagram of electro-Fenton experimental system: (1) feed tank, (2) pump, (3) EF reactor, (4) DC power supply, (5) feed air, (6) carbon-plated iron, (7) iron-plated tank, and (8) product tank.

99.25% – CT_2) and carbon plated iron cathode, dimensions of 146 × 150 × 4 mm connected in parallel. Only the outer electrodes were connected to the digital DC power supply (QJ3003XE, 30V–3A). While the air flow rate was fixed at 3 L/min [30], the electric current applied in the treatments was ranged from 1.11 to 3.33 mA/cm^2. For better electron conductivity in the effluent, 990 mg/L of Na_2SO_4 was added to each treatment. Furthermore, to avoid electrode passivation, at the end of each run, the electrodes were washed thoroughly with water and dipped in 0.5 M H_2SO_4 solution for at least 15 min to dissolve any oxide from the electrode surface All trials were performed at room temperature of 20 to 25°C (±1.0°C) and adjusted initial pH from 2.8 to 3.2 using H_2SO_4 (0.2 M) before conducting the experiments.

2.4. Experimental Design. Screening experiments with fixed current density of 2.22 mA/cm^2 and 0.2 mM of Fe^{2+} dosage for 180 min were conducted to determine kinetic reaction and also investigate the effect of these factors on TC and TOC removal efficiency. Then the central composite design (CCD) was then carried out to determine the optimal condition for TOC and TC removal during the EF process. Three independent variables were applied: current density (X_1), Fe^{2+} dosage (X_2), and electrolysis time (X_3). The level of each code ranged from low (−1) to high (1), as shown in Table 1 based on our previous screening experiments.

Twenty experimental sets were designed, including eight sets from 2 k of a factorial point, six sets from 2 k of the axial point, and six sets from the central point (Table 2), where k is the number of independent variables factors [31]. The TC and TOC removal efficiencies, calculated by the following equation, were defined as the dependent variable's response.

$$\text{Removal efficiency}\,(\%) = \frac{(C_0 - C_i)}{C_0} x100, \qquad (2)$$

where C_0 is the concentration of TC or TOC at the initial time and C_i is the concentration of TC or TOC at any time t of electrolysis.

The mathematics model was evaluated using Minitab version 18.1 software and expressed in a quadratic model

Table 1: Factors and their levels used for experiments by the CCD.

Parameters	Symbol	Level				
		Low		Center	High	
		$-\alpha$	-1	0	1	$+\alpha$
Current density (mA/cm^2)	X_1	0.35	1.11	2.22	3.33	4.09
Fe^{2+} dosage (mM)	X_2	0.03	0.1	0.2	0.3	0.37
Electrolysis time (min)	X_3	129	150	180	210	230

equation as follows. The least-square regression calculated the coefficient. The β_0, β_i, β_{ii}, β_{ij}, and e are the constant coefficient, linear coefficient, quadratic coefficient, interaction coefficient, and statistical error, respectively. The adequacy and significance of the model were justified by the analysis of variance (ANOVA).

$$Y = \beta_0 + \sum_{i=1}^{k} \beta_i X_i + \sum_{i=1}^{k} \beta_{ii} X_i^2 + \sum_{i=1}^{k-1} \sum_{j=2}^{k} \beta_{ij} X_i X_j + e. \qquad (3)$$

To verify the model accuracy, three confirmed experiments were also conducted at optimal condition (current density of 2.2 mA/cm^2, the Fe^{2+} dosage of 0.25 mM, and electrolysis time of 217 min).

2.5. Analysis Method and Energy Consumption. All assays were performed at room temperature (20 to 25°C), and the treated samples were collected, filtered, and analyzed for total nitrogen (TN) and total organic carbon (TOC), using TOC VCPH/CPN instrument (SHIMADZU, Japan). TC was analyzed by LC-tandem MS equipped with a turbo spray electrospray (ESI) interface (Agilent Technologies, Palo Alto, CA and MS/MS, 4000 QTRAP, Applied Biosystems, USA) according to our previous study [6]. Other parameters such as pH, conductivity, and chemical oxygen demand were evaluated according to the Standard Methods for the Examination of Water and Wastewater [32]. In addition to these parameters, sludge production was also analyzed using the gravimetric method. The statistical analysis was performed using the software Minitab 18.1 version (Minitab Inc., USA).

Energy consumed per contaminated pollutant (E) during the EF process could be determined by the following equation [33]:

$$\text{E}\,(\text{kWh/kg pollutant}) = \frac{\text{U} \times \text{I} \times \text{t} \times 1000}{(C_0 - C_i)60V}. \qquad (4)$$

The concentration of iron generated in the solution or anode consumption was expressed by the following equation:

$$\text{m}\left(\text{g}_{\text{Fe}}/\text{m}^3\right) = \frac{\text{I} \times \text{t} \times \text{M}}{\text{Z} \times \text{F} \times \text{V}} \times 60. \qquad (5)$$

where pollutant is TC or TOC, F is Faraday's constant (96485 Columb/mol), M is the molecular weight of iron (56 g/mol), Z is the number of electron transfer (assumed here $Z_{Fe} = 2$), I is the electric current (A), U is the voltage (V), t is the electrolysis time (min), and V is the treated volume (L).

Table 2: The matrix of the CCD experiment and the corresponding experimental data.

Run	Current density (mA/cm^2)	Fe^{2+} dosage (mM)	Electrolysis time (min)	TC removal (%)		TOC removal (%)	
				Actual	Predicted	Actual	Predicted
1	2.22	0.20	180.0	98.9	98.74	77.10	77.22
2	3.33	0.10	210.0	79.6	80.10	63.60	65.52
3	3.33	0.30	150.0	76.3	77.21	40.40	42.67
4	1.11	0.30	150.0	86.2	86.59	59.80	59.32
5	3.33	0.10	150.0	74.2	72.27	39.34	36.38
6	1.11	0.10	150.0	70.64	69.22	40.26	38.64
7	1.11	0.10	210.0	68.4	68.37	58.70	57.88
8	1.11	0.30	210.0	99.1	101.91	79.10	83.51
9	4.09	0.20	180.0	84.7	84.06	61.40	59.54
10	2.22	0.20	180.0	98.7	98.74	76.10	77.22
11	3.33	0.30	210.0	98.9	101.21	73.70	76.77
12	0.35	0.20	180.0	82.7	82.09	67.30	67.11
13	2.22	0.20	180.0	99.2	98.74	76.40	77.22
14	2.22	0.20	180.0	97.6	98.74	79.10	77.22
15	2.22	0.20	129.5	75.1	76.74	36.80	39.15
16	2.22	0.03	180.0	61.31	63.45	35.04	37.81
17	2.22	0.37	180.0	99.2	95.81	69.47	64.65
18	2.22	0.20	180.0	98.5	98.74	76.00	77.22
19	2.22	0.20	230.5	99.1	96.21	88.40	84.00
20	2.22	0.20	180.0	99.3	98.74	78.26	77.22

3. Results and Discussion

3.1. Effect of Electrolysis Time and Kinetic Reaction Model on TOC and TC Removal. Figure 2 shows the variation in the electrolysis time on the TC and TOC removal efficiencies. With the increase in the reaction time from 30 to 150 min, the removal efficiency sharply increases, and with the further increase in the electrolysis time, the removal efficiency reaches a plateau. The increase in the rapid and slow removal of TC and TOC with the rise in the electrolysis time can be explained by the reaction between •OH and TC or TOC in wastewater. At a constant TC or TOC concentration, the increased electrolysis time can accelerate •OH formation, leading to a rapid reaction with the TC or TOC contaminant. However, under saturated Fe^{2+} conditions (0.2 mM), fixed •OH formation inadequate react with the pollutants; therefore, the TC and TOC removal efficiency slowly increase. This trend also can be confirmed in some previous studies [20, 34]. The kinetics of the TOC and TC removal under fixed conditions (2.22 mA/cm^2 of current density and 0.2 mM of Fe^{2+} dosage) give a better understanding of the relationship between TOC or TC concentrations and electrolysis times. TOC and TC removal is performed under pseudo-first-order kinetics with R^2 around 0.923 and 0.993, respectively, as illustrated in Figure 2. These results are the following ones reported by Teymori et al. [20] that show that the pseudo-first-order reaction is suitable for degradation of Malachite green using the EF process or Covinich et al. [26], who indicated the TOC removal of mixed industrial wastewater using Fenton process followed by pseudo-first-order kinetics. The high removal efficiency at about 150 min and the fixed condition of Fe^{2+} and current density release level of each parameter on CCD design eliminate TC and TOC from RPW.

3.2. Model Fitting and Analysis. The ANOVA results of applying the EF process to the RPW are presented in Table 3, showing significant TC and TOC removal factors according to the CCD design.

Table 3 summarizes the individual and interactive effects and the statistical significance of the test variables on TC and TOC removal. The low P values (<0.05) indicate the significant impact of almost all factors on TC and TOC reduction. These should be included in the final model. These statements are also confirmed through the Pareto chart with 95% confidence (Figure S1).

Therefore, the model for predicting the removal of TC and TOC using EF is reconstructed to filter out the non-significant factors and predicted models, as expressed by the following equations:

$$Y_{TC} = 180.6X_2 + 1.513X_3 - 4.494X_1^2 - 675.5X_2^2 - 0.0048X_3^2 - 28X_1X_2 + 0.651X_1X_3 + 1.348X_2X_3 - 99.5, \quad (6)$$

$$Y_{TOC} = 8.76X_1 + 445.1X_2 + 2.409X_3 - 3.987X_1^2 - 918.8X_2^2 - 0.0061X_3^2 - 32.4X_1X_2 - 239.6. \quad (7)$$

The model F-values of 69.43 and 49.69 for the TC and TOC removal, respectively, indicated that the model is sufficiently significant for the regression analysis between response and variable effects. The fit of the model was verified by determining the regression coefficient (R^2). The R^2_{TC} and R^2_{TOC} values of 0.9842 and 0.9781, respectively,

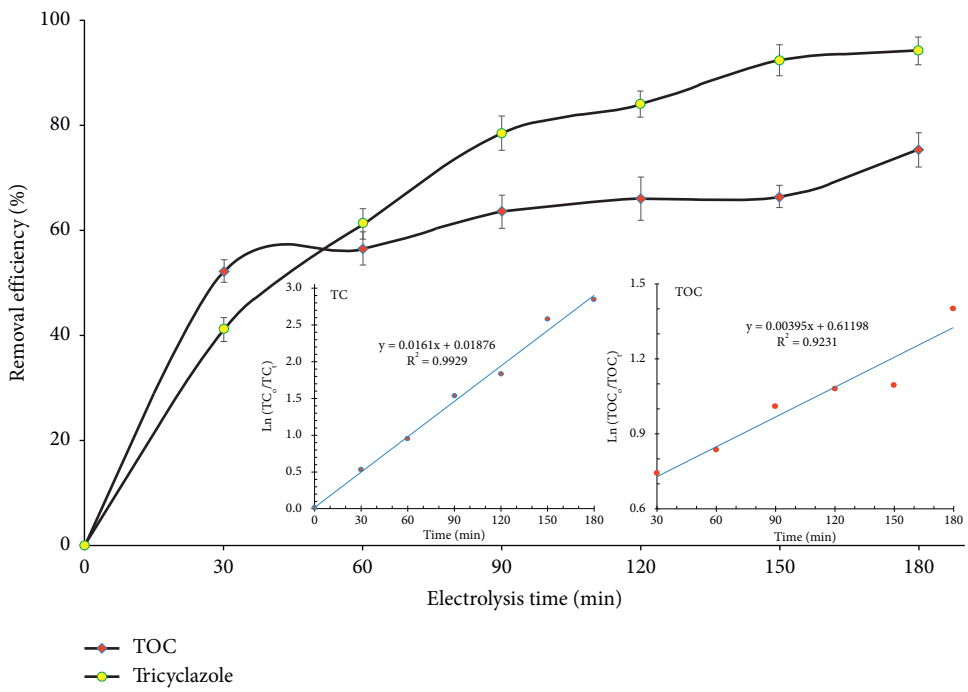

Figure 2: Effect of different electrolysis time points and reaction kinetic orders on TC and TOC removal with a current density of 2.22 mA/cm^2 and 0.2 mM Fe^{2+} dosage.

Table 3: ANOVA results for the TC and TOC removal from RPW using EF process.

Source	DF	Adj SS	Adj MS	*F*-value	*P* value
TC removal					
Model	9	3,126.26	347.36	69.43	≤0.001
X_1	1	4.71	4.71	0.94	0.355
X_2	1	1,263.95	1,263.95	252.65	≤0.001
X_3	1	457.25	457.25	91.40	≤0.001
X_1^2	1	441.80	441.80	88.31	≤0.001
X_2^2	1	657.55	657.55	131.44	≤0.001
X_3^2	1	270.79	270.79	54.13	≤0.001
X_1X_2	1	77.25	77.25	15.44	0.003
X_1X_3	1	37.58	37.58	751	0.021
X_2X_3	1	130.73	130.73	26.13	≤0.001
Residual error	10	50.03	5.00		
Pure error	5	1.90	0.38		
Total	19	3,176.29			
TOC reduction					
Model	9	5,247.22	583.02	49.69	≤0.001
X_1	1	69.20	69.20	5.90	0.036
X_2	1	870.03	870.03	74.15	≤0.001
X_3	1	2,427.60	2,427.60	206.91	≤0.001
X_1^2	1	347.73	347.73	29.64	≤0.001
X_2^2	1	1,216.69	1,216.69	103.60	≤0.001
X_3^2	1	440.85	440.85	37.57	≤0.001
X_1X_2	1	103.54	103.54	8.82	0.014
X_1X_3	1	49.10	49.10	4.19	*0.068*
X_2X_3	1	12.25	12.25	1.04	*0.331*
Residual error	10	117.33	11.73		
Pure error	5	8.02	1.60		
Total	19	5,364.55			

$R^2_{TC} = 0.9842$, $R^2_{TC\_adj} = 0.9701$, $R^2_{TOC} = 0.9781$, and $R^2_{TOC\_adj} = 0.9584$.

indicated that the models cannot explain only the 1.58–2.19% variation of the mean or that the models exhibit satisfactory adjustment of the quadratic models to the experimental data [35]. Moreover, some investigations revealed that an R^2 of greater than 0.70 is considered to be suitable for model fitting [36].

Figure 3 illustrates that the TOC removal increased with electrolysis time and varied with current density or Fe^{2+} dosage. As seen in Figure 3, the TOC removal could be greater than 80% occurred for conditions current density of 1.11 to 3.50 mA/cm^2, Fe^{2+} concentration of ≥0.18 mM, and electrolysis time of ≥190 min.

Figure 4 describes the interactive effect of current density, electrolysis time, and Fe^{2+} dosage on TC removal efficiency. The best condition for TC removal by EF was electrolysis time of higher 190 min, current density ranged from 2.0 to 3.0 mA/cm^2, and higher Fe^{2+} dosage of 0.2 mM. The increase in TOC removal efficiency as the Fe^{2+} concentration ≥ 0.2 mM or increase in electrolysis time could be attributed to the generation of an increased number of •OH through equation (1). The variation of removal efficiencies of TC and TOC in a range of current density is mainly due to the suitable range of current density of the experiment. As the current density increase, the amount of generated H_2O_2 and iron ion also increase, thus increasing •OH formation. However, further increase in the current density could accelerate the production of weak oxidative substances (such as $HO_2^{\bullet}$ or O_2) according to the following equations [6]:

$$H_2O_2 + {}^{\cdot}OH \longrightarrow HO_2^{\cdot} + H_2O, \quad (8)$$

$$HO_2^{\cdot} + OH \longrightarrow H_2O + O_2. \quad (9)$$

These increase and variations of trends in electrolysis time and current density are consistent with the previous study of Zhang et al. [37]; they stated that the decomposition of 5,000 mg/L of COD from landfill leachate to around 2,500 mg/L only within 30 min and obtained 1,000 mg/L around 75 min.

From the model, the optimization of the EF treatment was reached with the highest removal efficiency of both TC and TOC; the optimization indicated that at 2.2 mA/cm^2 of current density, 0.25 mM of Fe^{2+} concentration, and 217 min of electrolysis time, the TOC and TC removal reached 87.76% and 104.8% with the desirability function value of 0.901 (Figure 5). Two additional experiments were then performed to verify the optimum results. The average TOC and TC removal value obtained through the experiment was 84.24% and 99.23%, respectively, which agreed well with the predicted response value.

In the case of individual optimization for TC and TOC, the best conditions should be 2.2 mA/cm^2 of current density, 0.2 mM of Fe^{2+} concentration and 188 min of electrolysis time or 2.2 mA/cm^2 of current density, 0.25 mM of Fe^{2+} concentration, and 217 min of electrolysis time for elimination of 100% TC and 87.8% TOC as depicted in Figure 6. Two confirmation trials in optimization of TC reach 99.6%, which is better the optimization value of both TC and TOC and closer than the predicted value. The value was chosen for the cost evaluation.

3.3. Toxicity Evaluation. The toxicity of treated real pesticides at optimum condition for both TC and TOC was investigated using *D. magna*; the survival of *D. magna* in the controls without pesticide wastewater was 100%. According to OECD guidelines, this high control survival meets the requirement for the toxicity test [28]. The lethal concentration (LC) values of the treated pesticide wastewater (TPW) by EB against the microcrustacean *D. magna* at different time intervals are listed in Table 4. The results demonstrated that the TPW generated moderate toxic effects on *D. magna*, with LC_{50} values of 3.12%, 2.05%, 1.81%, and 1.36% at 24 h, 48 h, 72 h, and 96 h, respectively. These toxicity results are lower than our previous pesticide wastewater on *D. magna* [6]. However, the pesticide wastewater treatment with this condition still generates toxic effects on *D. magna*. Probably, the treated pesticide wastewater contained unknown or other toxic compounds that contributed to toxic effects on *D. magna*. Further study on the chemical composition and toxic effects of this treated wastewater on other aquatic organisms is recommended. The method could require more treatment steps to reach the standard for release to the environment.

3.4. Economic Aspect. One of the most contributions to EF cost is energy consumption, which significantly increases by current density or electrolysis time [18]. The energy consumption for EF treatment was described in equation (4). Given the Vietnamese market in May 2021, the electrical energy price is 0.06 \$/kWh, and chemical prices are H_2SO_4 0.25 \$/kg, $FeSO_4$ 0.17 \$/kg, Na_2SO_4 0.35 \$/kg, and electrode anode 0.33 \$/kg (iron). The optimal cost associated with treatment conditions is summarized in Table S1. As shown in Table S1, the operating costs to treat 99.6% TC and 84.2% TOC in RPW using EF were 3.019 \$/kg TOC and 121.392 \$/kg TC, corresponding to 3.916 \$/m^3 and 2.962 \$/m^3 containing 1,297 mg/L TOC and 24.4 mg/L TC, respectively. The high energy consumption in TC removal was mainly due to the low concentration of TC in RPW, which required many chemicals or energy costs for treatment. While the energy consumption to remove 1 kg of TOC in real wastewater is far below the energy consumption of EF reported from previous studies [38–42]. Flox et al. [39] indicated an energy consumption cost of around 2.872 \$/kg TOC to eliminate 97% TOC of Mecoprop solution using boron-doped diamond (BDD)/stainless steel electrodes. Guinea et al. [42] applied BDD anode to degrade over 97% TOC of enrofloxacin solution with very high energy consumption (14.76 \$/kg TOC). A summary list of different contaminant sources degradation by EF along with their treatment efficiency is presented in Table 5. The results indicated that the EF process was suitable for wastewater treatment in a future large-scale application.

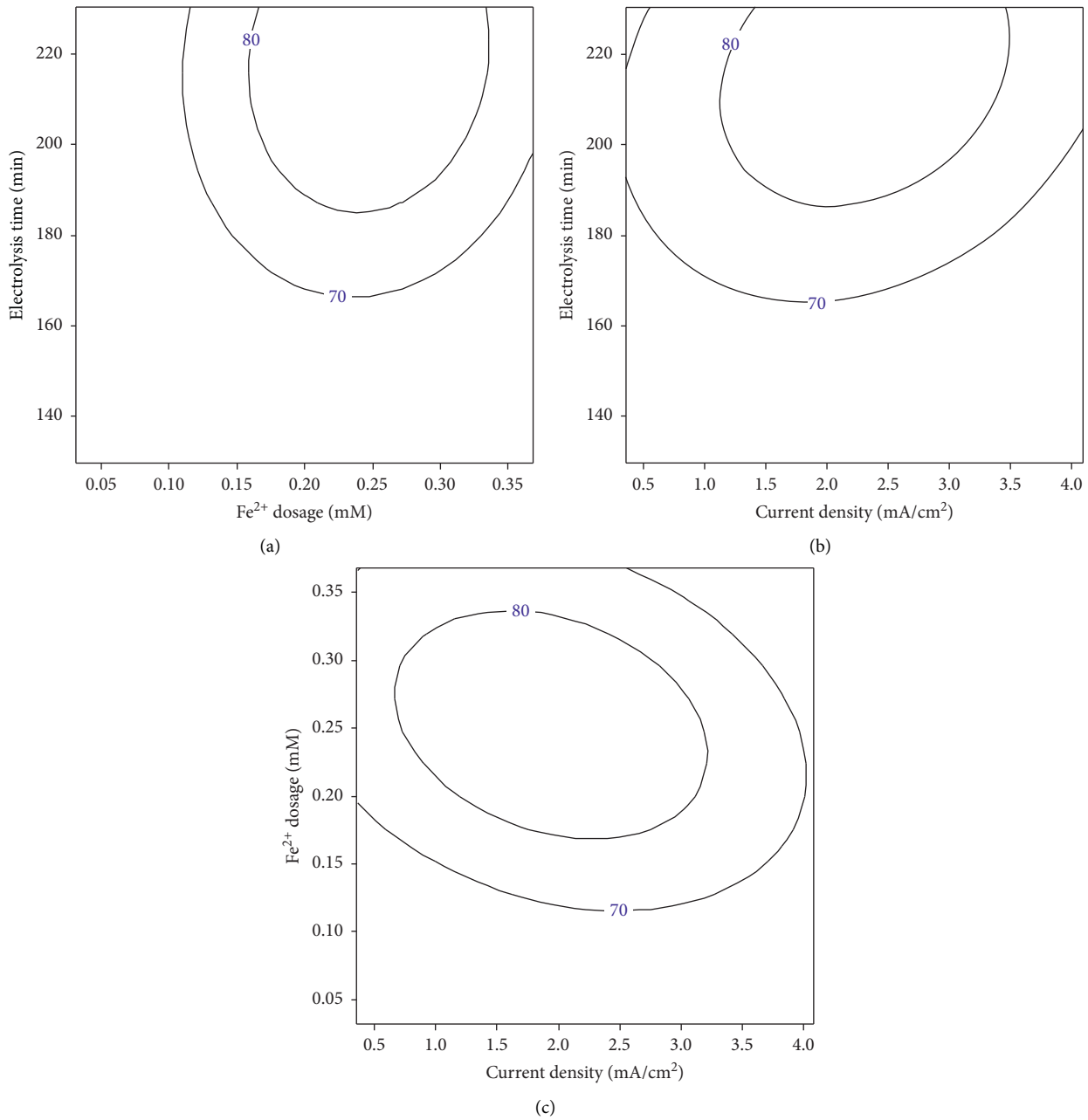

Figure 3: Respond contour plot of TOC removal at fixed condition: (a) current density of 2.5 mA/cm^2, (b) Fe^{2+} dosage of 0.2 mM, and (c) electrolysis time of 200 min.

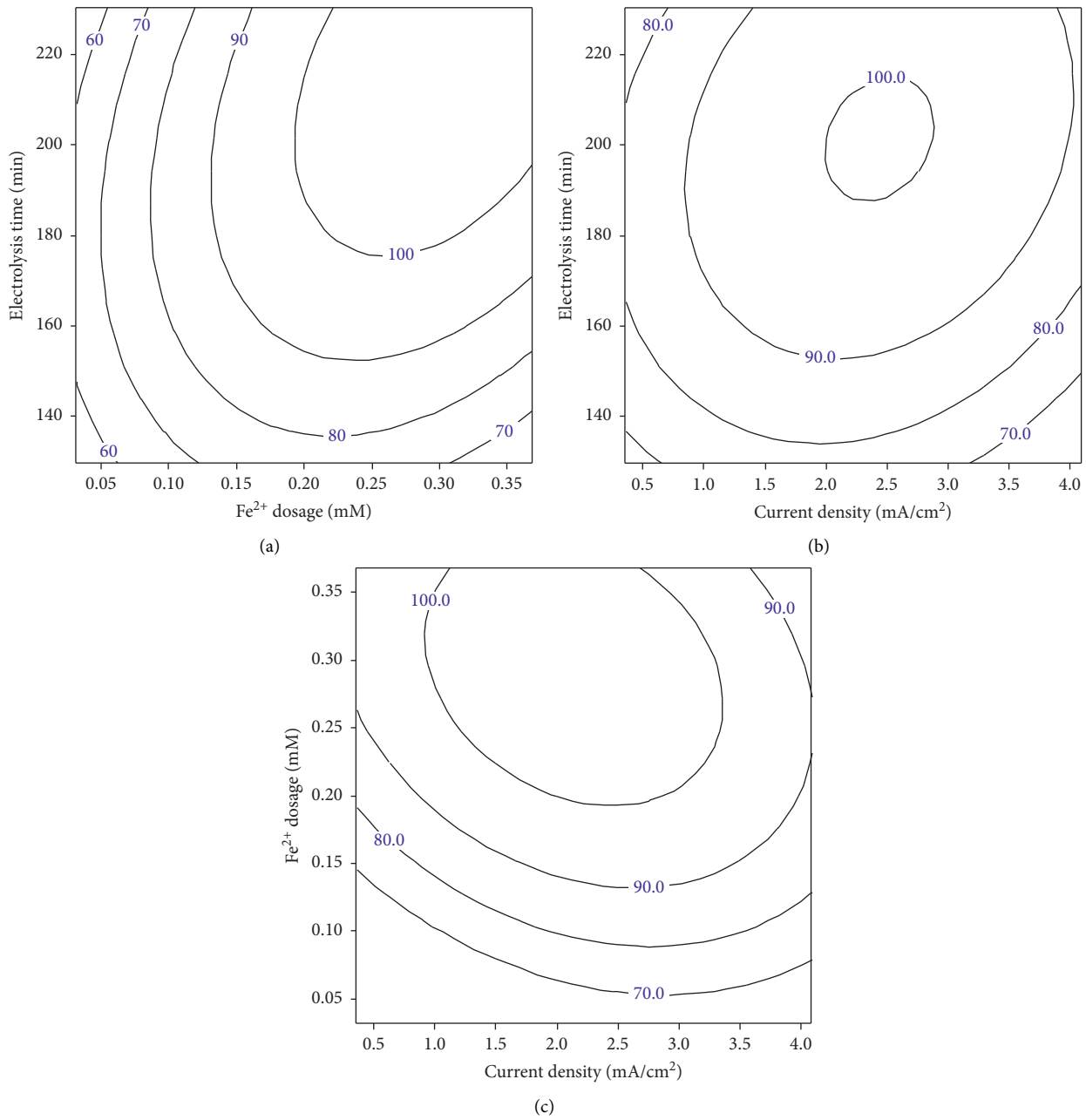

Figure 4: Respond contour plot of TC removal at fixed condition: (a) current density of 2.5 mA/cm^2, (b) Fe^{2+} dosage of 0.2 mM, and (c) electrolysis time of 200 min.

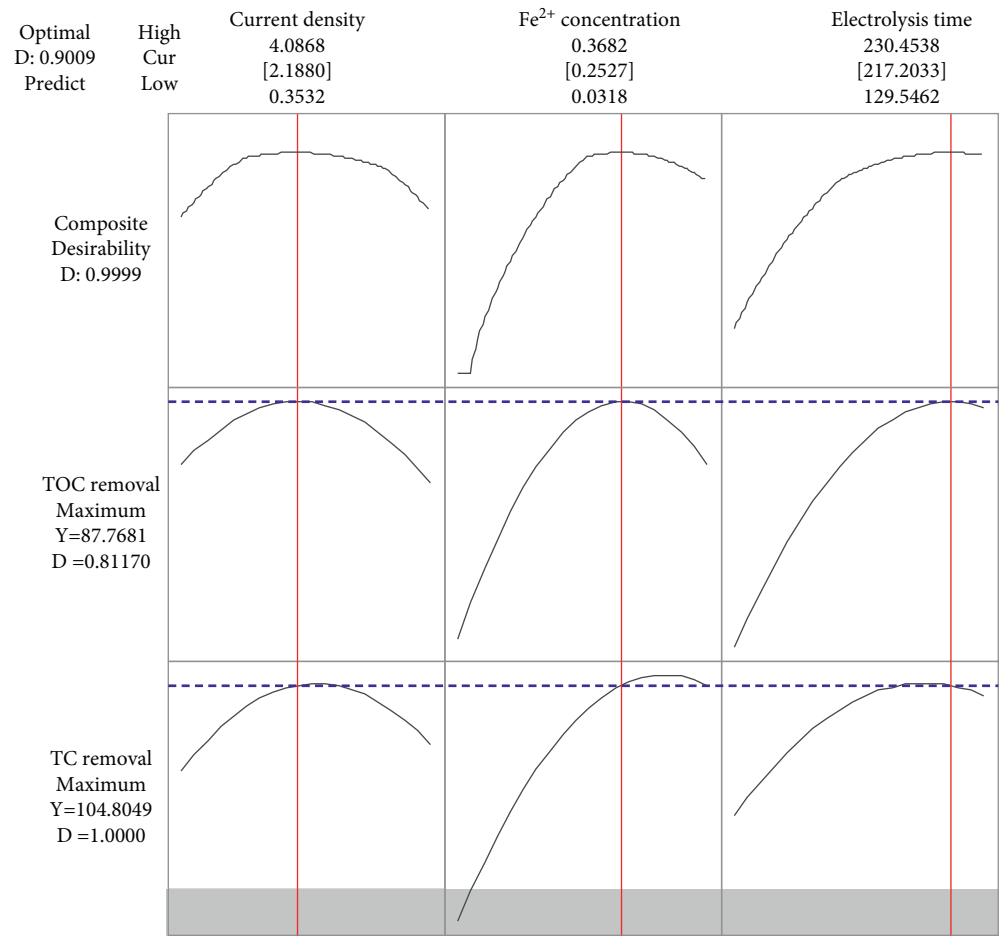

Figure 5: Response optimization plot of maximum both TOC and TC removal efficiency.

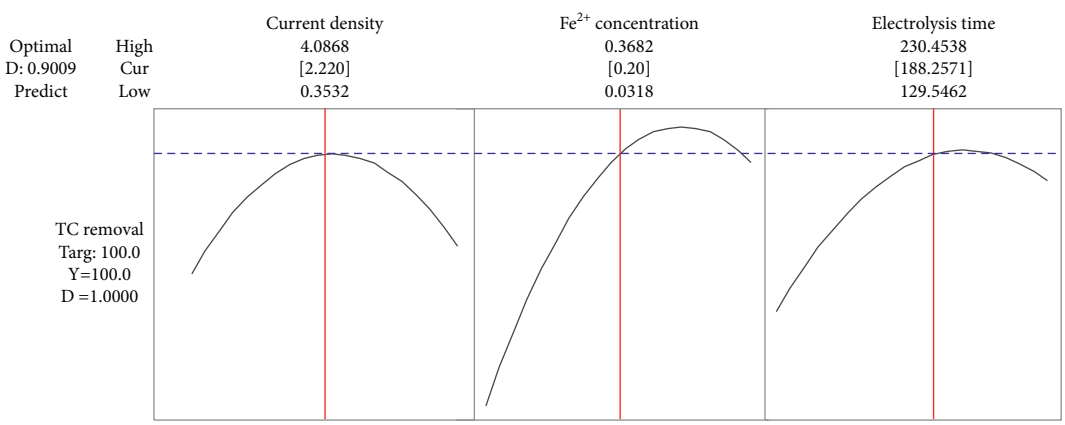

(a)

Figure 6: Continued.

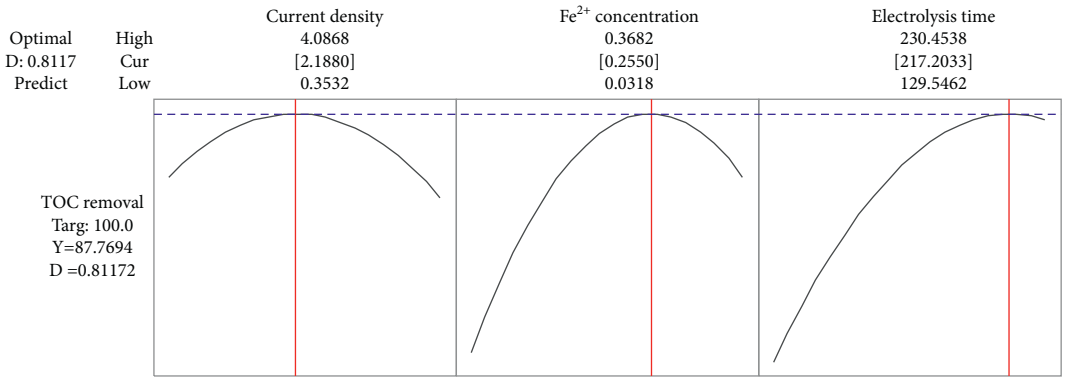

(b)

Figure 6: Response optimization plot of individual: (a) TC and (b) TOC removal efficiency in RWP using EF.

Table 4: Lethal dose LC_{50} of the TPW samples on *D. magna*.

Chemical	Time (h)	24 h	48 h	72 h	96 h
TPW (%)	LC_{10}	1.34	0.98	0.69	0.49
	LC_{50}	3.12	2.05	1.81	1.36
	LC_{90}	3.54	2.24	1.92	1.54

Table 5: Energy consumption per unit TOC mass for the degradation of several organic pollutant solutions by the EF process.

Compounds	Cell	Conditions	Removal efficiency (%)	*E* (kWh/kg)	Ref.
Mecoprop	BDD/stainless steel	643 mg/L pesticide in 0.5 M Na_2SO_4, pH 3.0, 0.5 mM Fe^{2+}, 50 mA/cm^2, and 40°C for 540 min	97 (TOC)	47.87	[39]
Cresol	BDD/gas diffusion electrode (GDE)	128 mg/L substrate in 0.05 M Na_2SO_4, pH 3.0, 1 mM Fe^{2+}, 1°A, and 35°C for 180 min	98 (TOC)	155	[40]
Diuron, glyphosate	Dimensionally stable electrode (DSA)/carbon felt	Diuron (0.1 mM) and glyphosate (0.13 mM) dissolved in 1L of 0.05 M Na_2SO_4, pH 3.0, and 1°A for 180 min	33.78 (TOC)	850	[38]
Acid yellow 36	BDD/GDE	108 mg/L dye in 0.05 M Na_2SO_4, pH 3.0, 0,5 mM Fe^{2+}, 50 mA/cm^2, and 40°C for 540 min	95 (TOC)	130	[41]
Enrofloxacin	Pt/BDD	158 mg/L drug in 0.05 M Na_2SO_4, 0.2 mM Fe^{2+}, pH 3, 1°A, and 35°C for 300 min	97 (TOC)	246	[42]
Tricyclazole	Carbon plate/stainless steel	1297 mg/L pesticide in 990 mg/L Na_2SO_4, pH 3.0, 0.25 mM Fe^{2+}, 2.22 mA/cm^2, and 25°C for 217 min	99.6 (TC) 84.2 (TOC)	121.4 3.02	This study

4. Conclusions

This study employed the electro-Fenton process with stainless steel and carbon fiber as electrodes to treat tricyclazole (TC) and TOC in real pesticide production wastewater (RPW). The removal of TC and TOC was obeyed pseudo-first-order kinetic with R^2 of 0.993 and 0.923, respectively. The central composite design (CCD) with three factors was successfully applied to develop a mathematical model predicting TC and TOC removal. The $R^2_{TC} = 0.9842$ and $R^2_{TOC} = 0.9781$ for the obtained quadratic model indicate a high correlation between observed and predicted values by the mathematical model. At optimum values of variables (current density of 2.2 mA/cm^2, Fe^{2+} dosage of 0.2 mM, and electrolysis time of 217 min), most of the TC (99.6%) and TOC (84.2%) was eliminated. The acute toxicity of this contaminant at optimization conditions still generated toxic effects on *D. magna*. Besides, the operation cost per mass unit of EF at individual optimization was around 3.019 $/kg TOC and 121.392 $/kg TC also represented the practical technique in wastewater treatment.

Data Availability

All data are included within the article.

Conflicts of Interest

The authors declare that they have no conflicts of interest.

Acknowledgments

This research was funded by Vietnam National University Ho Chi Minh City (VNU-HCM) under grant number C2019-24-01.

Supplementary Materials

Table S1. Operation cost for the mineralization of wastewater containing pesticide compounds for EF treatments. *Figure S1.* Pareto chart for the analysis of the experimental data obtained to remove: (a) TC and (b) TOC from the RPW by EF technique with 95% confidence. (*Supplementary Materials*)

References

[1] Statista, "Agriculture in Vietnam—statistics & facts," *Statista Research Department*, vol. 2021, 2021.

[2] J.-Y. Liao, C. Fan, Y.-Z. Huang, and K. J.-C. Pei, "Distribution of residual agricultural pesticides and their impact assessment on the survival of an endangered species," *Journal of Hazardous Materials*, vol. 389, Article ID 121871, 2020.

[3] S. Cui, R. Hough, K. Yates et al., "Effects of season and sediment-water exchange processes on the partitioning of pesticides in the catchment environment: implications for pesticides monitoring," *The Science of the Total Environment*, vol. 698, Article ID 134228, 2020.

[4] T. Wang, M. Zhong, M. Lu et al., "Occurrence, spatiotemporal distribution, and risk assessment of current-use pesticides in surface water: a case study near Taihu Lake, China," *The Science of the Total Environment*, vol. 782, Article ID 146826, 2021.

[5] H. Hamsan, Y. B. Ho, S. Z. Zaidon, Z. Hashim, N. Saari, and A. Karami, "Occurrence of commonly used pesticides in personal air samples and their associated health risk among paddy farmers," *The Science of the Total Environment*, vol. 603-604, pp. 381–389, 2017.

[6] N. N. Duy, T. N. Hieu, T. P. Luu et al., "Degradation of tricyclazole from aqueous solution and real wastewater by electron-beam irradiation," *Environmental Technology & Innovation*, vol. 21, Article ID 101315, 2021.

[7] I. Werner, L. A. Deanovic, D. E. Hinton et al., "Toxicity of stormwater runoff after dormant spray application of diazinon and esfenvalerate (asana) in a French prune orchard, glenn county, California, USA," *Bulletin of Environmental Contamination and Toxicology*, vol. 68, no. 1, pp. 29–36, 2002.

[8] H. Wu, J. Shen, X. Jiang et al., "Bioaugmentation potential of a newly isolated strain *Sphingomonas* sp. NJUST37 for the treatment of wastewater containing highly toxic and recalcitrant tricyclazole," *Bioresource Technology*, vol. 264, pp. 98–105, 2018.

[9] L. Feng, E. D. van Hullebusch, M. A. Rodrigo, G. Esposito, and M. A. Oturan, "Removal of residual anti-inflammatory and analgesic pharmaceuticals from aqueous systems by electrochemical advanced oxidation processes. A review," *Chemical Engineering Journal*, vol. 228, pp. 944–964, 2013.

[10] G. Briceño, M. S. Fuentes, J. M. Saez, M. C. Diez, and C. S. Benimeli, "*Streptomyces* genus as biotechnological tool for pesticide degradation in polluted systems," *Critical Reviews in Environmental Science and Technology*, vol. 48, no. 10-12, pp. 773–805, 2018.

[11] S. Azarkan, A. Peña, K. Draoui, and C. I. Sainz-Díaz, "Adsorption of two fungicides on natural clays of Morocco," *Applied Clay Science*, vol. 123, pp. 37–46, 2016.

[12] Y. Kiso, Y. Sugiura, T. Kitao, and K. Nishimura, "Effects of hydrophobicity and molecular size on rejection of aromatic pesticides with nanofiltration membranes," *Journal of Membrane Science*, vol. 192, no. 1-2, pp. 1–10, 2001.

[13] I. Oller, S. Malato, and J. A. Sánchez-Pérez, "Combination of advanced oxidation processes and biological treatments for wastewater decontamination-a review," *The Science of the Total Environment*, vol. 409, no. 20, pp. 4141–4166, 2011.

[14] O. Ganzenko, C. Trellu, N. Oturan et al., "Electro-Fenton treatment of a complex pharmaceutical mixture: mineralization efficiency and biodegradability enhancement," *Chemosphere*, vol. 253, Article ID 126659, 2020.

[15] P. T. T. Nguyen, H. T. Nguyen, U. N. P. Tran, and H. Manh Bui, "Removal of antibiotics from real hospital wastewater by cold plasma technique," *Journal of Chemistry*, vol. 2021, Article ID 9981738, 13 pages, 2021.

[16] N. N. Duy, T. N. Hieu, T. P. Luu et al., "Removal of leucomalachite green in an aqueous solution by the electron beam process," *Journal of Water Process Engineering*, vol. 40, Article ID 101781, 2021.

[17] E. Brillas and C. A. Martínez-Huitle, "Decontamination of wastewaters containing synthetic organic dyes by electrochemical methods. An updated review," *Applied Catalysis B: Environmental*, vol. 166-167, pp. 603–643, 2015.

[18] M. B. Ha and X. B. Thanh, *Degradation of Complex Organic Pollutants in Wastewater by Homogeneous Electro-Fenton in: Water and Wastewater Treatment Technologies*, pp. 145–166, Springer, Berlin, Germany, 2019.

[19] C. T. Benatti, A. C. S. da Costa, and C. R. G. Tavares, "Characterization of solids originating from the Fenton's process," *Journal of Hazardous Materials*, vol. 163, no. 2-3, pp. 1246–1253, 2009.

[20] M. Teymori, H. Khorsandi, A. A. Aghapour, S. J. Jafari, and R. Maleki, "Electro-Fenton method for the removal of malachite green: effect of operational parameters," *Applied Water Science*, vol. 10, pp. 1–14, 2020.

[21] Ö. Gökkuş, N. Yıldız, A. S. Koparal, and Y. Yıldız, "Evaluation of the effect of oxygen on electro-Fenton treatment performance for real textile wastewater using the Taguchi approach," *International journal of Environmental Science and Technology*, vol. 15, no. 2, pp. 449–460, 2018.

[22] X. Zhou, Z. Hou, L. Lv, J. Song, and Z. Yin, "Electro-Fenton with peroxi-coagulation as a feasible pre-treatment for high-strength refractory coke plant wastewater: parameters optimization, removal behavior and kinetics analysis," *Chemosphere*, vol. 238, Article ID 124649, 2020.

[23] C. M. Dominguez, N. Oturan, A. Romero, A. Santos, and M. A. Oturan, "Optimization of electro-Fenton process for effective degradation of organochlorine pesticide lindane," *Catalysis Today*, vol. 313, pp. 196–202, 2018.

[24] N. T. Hoang and R. Holze, "Degradation of pesticide Cartap in Padan 95SP by combined advanced oxidation and electro-fenton process," *Journal of Solid State Electrochemistry*, vol. 25, no. 1, pp. 73–84, 2021.

[25] A. Da Pozzo, C. Merli, I. Sirés, J. A. Garrido, R. M. Rodríguez, and E. Brillas, "Removal of the herbicide amitrole from water by anodic oxidation and electro-Fenton," *Environmental Chemistry Letters*, vol. 3, no. 1, pp. 7–11, 2005.

[26] L. Covinich, F. Felissia, P. Massa, R. Fenoglio, and M. C. Area, "Kinetic modeling of a heterogeneous Fenton-type oxidative treatment of complex industrial effluent," *International Journal of Integrated Care*, vol. 9, no. 3, pp. 215–229, 2018.

[27] S. O. Ganiyu, C. A. Martínez-Huitle, and M. A. Oturan, "Electrochemical advanced oxidation processes for wastewater treatment: advances in formation and detection of reactive species and mechanisms," *Current Opinion in Electrochemistry*, vol. 27, Article ID 100678, 2021.

[28] OECD, *Daphnia sp. Acute Immobilization Test: OECD Guideline for Testing of Chemicals*, Organization for the Economical Cooperation and Development, Paris, France, 2004.

[29] I. Römer, A. J. Gavin, T. A. White et al., "The critical importance of defined media conditions in *Daphnia magna* nanotoxicity studies," *Toxicology Letters*, vol. 223, no. 1, pp. 103–108, 2013.

[30] L. Zhou, Z. Hu, C. Zhang, Z. Bi, T. Jin, and M. Zhou, "Electrogeneration of hydrogen peroxide for electro-Fenton system by oxygen reduction using chemically modified graphite felt cathode," *Separation and Purification Technology*, vol. 111, pp. 131–136, 2013.

[31] M. B. Ha, "Optimization of electrocoagulation of instant coffee production wastewater using the response surface methodology," *Polish Journal of Chemical Technology*, vol. 19, pp. 67–71, 2017.

[32] APHA, *Standard Methods for the Examination of Water and Wastewater*, American Public Health Association (APHA), Washington, DC, USA, 2005.

[33] L. Tirado, Ö. Gökkuş, E. Brillas, and I. Sirés, "Treatment of cheese whey wastewater by combined electrochemical processes," *Journal of Applied Electrochemistry*, vol. 48, no. 12, pp. 1307–1319, 2018.

[34] M. Malakootian and A. Moridi, "Efficiency of electro-Fenton process in removing Acid Red 18 dye from aqueous solutions," *Process Safety and Environmental Protection*, vol. 111, pp. 138–147, 2017.

[35] D. C. Montgomery, *Design and Analysis of Experiments*, John Wiley & Sons, Inc., Hoboken, NJ, USA, 2013.

[36] D. Granato and M. L. Masson, "Instrumental color and sensory acceptance of soy-based emulsions: a response surface approach," *Ciência e Tecnologia de Alimentos*, vol. 30, no. 4, pp. 1090–1096, 2010.

[37] H. Zhang, D. Zhang, and J. Zhou, "Removal of COD from landfill leachate by electro-Fenton method," *Journal of Hazardous Materials*, vol. 135, no. 1-3, pp. 106–111, 2006.

[38] M. P. Rosa Barbosa, N. S. Lima, D. B. de Matos et al., "Degradation of pesticide mixture by electro-Fenton in filter-press reactor," *Journal of Water Process Engineering*, vol. 25, pp. 222–235, 2018.

[39] C. Flox, P. L. Cabot, F. Centellas et al., "Electrochemical combustion of herbicide mecoprop in aqueous medium using a flow reactor with a boron-doped diamond anode," *Chemosphere*, vol. 64, no. 6, pp. 892–902, 2006.

[40] C. Flox, P. Cabot, F. Centellas et al., "Solar photoelectro-Fenton degradation of cresols using a flow reactor with a boron-doped diamond anode," *Applied Catalysis B: Environmental*, vol. 75, no. 1-2, pp. 17–28, 2007.

[41] E. J. Ruiz, C. Arias, E. Brillas, A. Hernández-Ramírez, and J. M. Peralta-Hernández, "Mineralization of Acid Yellow 36azo dye by electro-Fenton and solar photoelectro-Fenton processes with a boron-doped diamond anode," *Chemosphere*, vol. 82, no. 4, pp. 495–501, 2011.

[42] E. Guinea, J. A. Garrido, R. M. Rodríguez et al., "Degradation of the fluoroquinolone enrofloxacin by electrochemical advanced oxidation processes based on hydrogen peroxide electrogeneration," *Electrochimica Acta*, vol. 55, no. 6, pp. 2101–2115, 2010.

Hindawi
Journal of Chemistry
Volume 2021, Article ID 7107058, 7 pages
https://doi.org/10.1155/2021/7107058

Research Article

Evaluation of the Safety of High-Salt Wastewater Treatment in Coal Chemical Industry Based on the AHP Fuzzy Method

Shijun Guo,[1,2] Shubham Sharma,[3] Alibek Issakhov,[4] and Nima Khalilpoor[5]

[1]*Shanghai University of Finance and Economics, Shanghai 200433, China*
[2]*Space Culture Research Center, Guilin University of Aerospace Technology, Guilin 541004, China*
[3]*Deptt. of Mechanical Engg., IK Gujral Punjab Technical University, Main Campus, Kapurthala 144603, India*
[4]*Faculty of Mechanics and Mathematics, Department of Mathematical and Computer Modelling, Al-Farabi Kazakh National University, Almaty, Kazakhstan*
[5]*Department of Energy Engineering, Graduate School of the Environment and Energy, Science and Research Branch, Islamic Azad University, Tehran, Iran*

Correspondence should be addressed to Nima Khalilpoor; nimakhalilpoor@gmail.com

Received 22 April 2021; Revised 23 June 2021; Accepted 29 September 2021; Published 7 December 2021

Academic Editor: Ibrahim H. Alsohaimi

Aim. Epichlorohydrin (ECH) is a widely used chemical product. The production of glycerol has its irreplaceable advantages. With the development of biodiesel industry, it will become the main trend of ECH production in the future. *Methods.* A vacuum evaporation device is built to investigate the effect of evaporation on the treatment of this kind of high-salt wastewater, and the feasibility of the thermodynamic equation of the simulation process is verified. *Process.* An AHR fuzzy mathematics evaluation algorithm is used to compare experimental values with simulated numerical values in brine. *Results and Conclusions.* In the multieffect evaporation process simulation with glycerin-containing brine, the amount of salt precipitated by unit steam energy is arranged in order from more to less than that of seven-effect parallel flow evaporation, is greater than five-effect parallel flow evaporation, and is larger than three-effect parallel flow evaporation, which shows that the increase of validity number is beneficial to the utilization of heat.

1. Introduction

As a chemical product, epichlorohydrin (ECH) is very useful. It is the main raw material for the production of glass fiber-reinforced plastics, electrical insulation products, chlorine alcohol rubber, nitroglycerin explosives, and epoxy resins. It can also be used as plasticizer, surfactant, stabilizer, medicine, and solvent, and cellulose ether of cellulose ester resin and cellulose ether, and so on [1]. Due to its wide range of applications, large market demand, and long-term supply of tension, the production of epichlorohydrin has a good momentum of development. The total production capacity of epichlorohydrin in the world in 2008 reached approximately 1.81 million t/a, and it is estimated that by 2012, it will exceed 2.3 million t/a [2]. It can be seen that the glycerol production of cyclic chlorine has its irreplaceable advantages. This process, along with the development of the biodiesel industry, is bound to become the main trend for the production of chlorine in the future. There have been a number of patents and plans put into practice [3]. Dow's patent for glycerol-based ECH (GTC) requires only half of the chlorine and reduces environmental pollution. Compared with traditional processes, it has great cost and environmental friendliness [4]. Solvay's new plant Epicero process uses a new series of catalysts and contains several patent applications. The Czech chemical metallurgy joint company reported a continuous cycle reaction process of glycerol to ECH [5]. Japan's process plant has begun to operate one after another. Jiangsu Yangnong Chemical Co., Ltd. has built a 60,000 t/a plant in 2006. Formosa Plastics Group, Dow Chemical Fine Chemicals (Shanghai) Co., Ltd., and Guangxi Tiandong Petrochemical Industrial Park all

directly produce glycerin as raw materials. ECH has a related production plan [6].

Many chemical and pharmaceutical companies produce wastewater containing large amounts of salt and containing many chemicals during the production process. Due to the complex chemical composition, high organic concentration, and high-salt content, these wastewater chemistries are difficult to directly process using more economical biochemical processes, and it is difficult to achieve satisfactory results using traditional wastewater treatment technologies [7]. However, this type of wastewater is treated by evaporation to achieve the purpose of recovering condensed water and inorganic salts of organic matter. There are many examples of evaporative treatment of high-salt wastewater [8]. The wastewater of chemical additives production is difficult to biodegrade, and the concentration, alkalinity, and salt content are high. The pretreatment process is critical, and vacuum evaporation will be used. The volatile components can be distilled off by the evaporation operation, so that a large amount of salt and organic substances are reduced in the distillate. In Hebei Province, a chemical additives Co., Ltd., a self-modified evaporator can effectively achieve this goal. First of all, the wastewater discharged from the production process is separately adjusted, so that the pH is adjusted to about 8 before evaporation, and then, 0.6–0.8 MPa of saturated steam is added to the self-aligned evaporator as raw steam, followed by vacuum evaporation and concentration. During the evaporation process, the precipitated salt and the evaporated residue at the bottom of the evaporation vessel are periodically discharged to the outside of the vessel. The specific treatment effect is that the amount of wastewater entering the evaporator is 42 m^3/d, and the COD is about 28300 mg/L. The evaporated distillate is condensed and then collected in a collection tank. The amount of water is 30–35 m3/ d, and the COD is 1800–2000 mg/L.

An experimental device is designed and constructed for measuring the bubble point of a saturated sodium chloride solution containing glycerol, examining the feasibility of the device to detect the boiling point of a salt solution under a certain pressure and concentration. Based on an externally heated evaporator, a multieffect evaporation of the brine system and glycerin-containing brine is simulated by the chemical process using PRO II software. The model three-effect cocurrent evaporation process, five-effect cocurrent evaporation process, and seven-effect cocurrent evaporation process were used. The effects of different multieffect evaporation processes on steam economy of multieffect evaporation are investigated. The following conclusions are drawn. Based on PRO II simulations, it is found that in the brine system or in the glycerin brine system, the amount of salt precipitated by unit steam energy is arranged in order from much to less: the seven-effect parallel flow evaporation is greater than the five-effect parallel flow evaporation which is greater than the three-effect parallel flow evaporation. From the point of view of heat utilization, the increase of validity is beneficial to the utilization of steam and the precipitation of salt. The purpose of reducing energy consumption is to study the economy of steam and select the appropriate flow.

2. Methodology

2.1. Fuzzy Mathematics Evaluation Algorithm. ECH production wastewater is a common industrial saponification wastewater, with high salt, high COD content, and other difficult characteristics [9]. In the former Soviet Union in 1981, a method for treating the wastewater was reported. The method includes first aggregating calcification in a sedimentation tank and then filtering out a clear liquid containing $CaCl_2$ at a concentration of from 5 to 10 to 250 to 360 g/L. The clear solution was concentrated by evaporation while crystallizing the organic chloride. Esch also invented a treatment method for ECH production wastewater, which includes the recovery of salt compounds, including pretreatment, evaporation and condensation, coarse crystallization, and fine crystallization [10]. In the preconcentration stage, the falling film evaporator is used, and evaporation is also used to achieve the purpose of concentrating the wastewater to precipitate salts (Figure 1). Some scholars have used other processes and low-temperature multiple-effect evaporation (LT-MED) combination process to treat heavy-salt and high-hardness heavy-oil wastewater. The results show that it is feasible to use LT-MED as the core technology to treat heavy oil wastewater and can be used for thermal recovery boilers.

A thing either belongs to the set A or does not belong to the set A, and no other belongs to the relation. In modern science and engineering applications, the concept of fuzzy sets often occurs, that is, a certain thing a belongs to set A to a certain degree. This idea is the basis of fuzzy set. The concept of fuzzy sets was proposed by the cybernetics expert Professor Lotfi A Zadeh in 1965. At present, fuzzy logic has been widely used in various fields such as science, engineering, agriculture, and medicine. The description of things in the real world is not always as accurate as possible. Professor Zadeh pointed out that "When the complexity of the problem increases, the precise description will lose meanings, and meaningful description will lose accuracy."

Fuzzy data are obfuscated by the membership function. The commonly used membership functions include triangle membership function, bell membership function, Gaussian membership function, and Sigmund-type membership function. Gauss membership function is used to fuzzily the indicator data because the function is continuous, symmetrical, and has good resolution. The mathematical expression of the Gauss membership function is

$$f(x) = e^{(x-c)^2/2\sigma^2}. \tag{1}$$

The shape of the Gauss membership function with different c and σ parameters is consistent with the shape of the probability density function of the normal distribution [11].

$$f(x) = \frac{(x-c)^2}{2\sigma^2}. \tag{2}$$

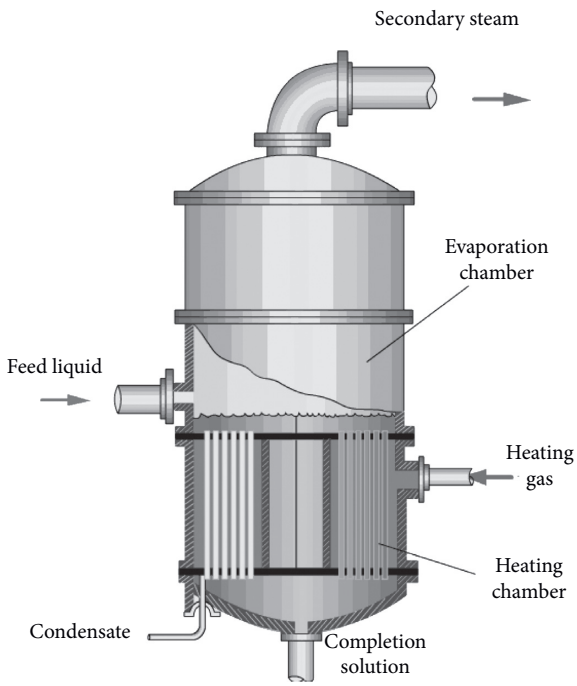

Figure 1: Design of the vacuum evaporator.

From its analytical formula, it can be deduced that when c changes, the membership function curve becomes wider and the shape does not change, but only shifts left and right, and when σ changes, the curve becomes wider or narrower, and the horizontal position remains unchanged [12].

$$f(x) = 2(x - c)\sigma^2. \tag{3}$$

So, when the index data are blurred, the σ and c parameters can be changed according to actual conditions or requirements, so that when the data is blurred, the degree of membership of different fuzzy sets (intervals) changes accordingly [13].

$$f(x) = 2x\sigma^e. \tag{4}$$

Pattern recognition mainly includes stratification of index systems and hierarchical classification of indicators. The stratification refers to the hierarchical division of the index system. The index system is divided into four levels: A, B, C, and D. The index division is to divide the actual data of the indicator into N segments according to the range of values. Each segment is represented by a membership function [3]. An accurate actual experiment or survey data can be fuzzified by such a set of membership functions and become fuzzy data. If the actual data range is divided into three segments, it means that it belongs to three fuzzy sets and can be represented by three membership functions. Generally, the corresponding physical meanings are "very small," "medium," and "larger". In this study, the actual data are divided into four fuzzy sets and expressed by four membership functions. The corresponding physical meanings are "better," "good," "general," and "poor." The classification of indicators is given in tables [14–17].

The fuzzy inference system (FIS) can be constructed using the newfis() function and providing in the MatLab fuzzy logic toolbox to obtain the data structure of the fuzzy inference system of the problem. Its contents include fuzzy and or operations and resolution algorithms. These attributes can be defined directly by the newfls() function or after the definition [18]. There are two types of HS—Mamdani and Sugeno. The main difference between the two methods is that the FIS output membership function of the Sugeno class can only be linear or the oriented FIS can be arbitrary. The Mamdani method is intuitive, it is now widely accepted, and it is very similar to people's thinking habits, so the Mamdani type of FIS is used. After defining the fuzzy inference system (FIS), it is possible to add system input and output variables and their range of values. In this study, the input variables are each evaluation index and the output is the evaluation value [19].

There are four levels of the regional developmental ecosystem suitability index system set up in this study, which are denoted by A, B, C, and D, respectively. Adopt a bottom-up, layer-by-layer recursive method to evaluate the entire region's ecological system suitability. First, use the D-layer index as input and obtain the C-level evaluation output. Then, use the C-layer index as input and obtain the B-level. The evaluation output finally obtains the evaluation output of layer A.

2.2. Wastewater Treatment Process Simulation Basic Algorithm. So far, the commonly used chemical process simulation methods are the following: first is the sequential module method. The sequential module method is the most commonly used process simulation algorithm in engineering applications. The main steps include the following: calculate the unit modules through which the feed streams are passed in order, until the final material flow, and then, you can get all the material parameters in the system. Since the flow direction of the logistics is certain, the output logistics parameters can only be calculated based on the input logistics parameters. The existence of the recycling logistics requires more complex iterative calculations. The specific content is to cut off the recycling logistics and then determine the fracture logistics and operation sequence until the entire process converges. The advantages are that a variety of specialized algorithms can be used to solve the model equations of a certain unit module, which has the characteristics of high efficiency; both the accelerating lamination and the direct iteration can achieve the purpose of stable convergence; the simulation in the physical process of logistics and modules information flow can correspond to each other, easy to understand; and the process of diagnosing errors is relatively simple.

The second is the simultaneous equations method. The description of the chemical process system will involve the establishment of mathematical models. This process requires the establishment of a large number of equations. The simultaneous set up of these equations is called simultaneous equations. This chemical process simulation method is essentially the establishment and solution of equations.

Compared to the sequential module method, the simultaneous equation method does not require iterative calculations. The advantages are that faster solution of the equation, flexible and convenient, high efficiency, and easy to implement with dynamic simulation. Disadvantages are strict requirements on initial values, and the process of diagnosing errors is complex and difficult to achieve.

The third is the simultaneous module method. The simultaneous module method is also called the double-layer method. The first layer refers to the process level and the second layer refers to the module level. From the abstract classification of the model, it is divided into the "simplified model" and "strict model." The advantage of the simplified model is that it can easily solve some input data, share these input data with the rigorous model, and then obtain the output data through the rigorous model and recalculate into the mathematical model of the simplified model. This method inherits the advantages of the sequential module method and the simultaneous equation method, that is, it can use the existing unit operation module, and it can avoid loop iterations and achieve universalization. PRO/II is calculated using a sequential module approach. When a chemical process is simulated, the first task is to determine the process simulation software. The basis for the determination usually includes physical parameters involving materials, thermodynamic methods, and unit modules. The accuracy and flexibility of the required results are also not negligible. The accuracy of the results of different process simulation software is not only related to the system itself but also has a lot to do with the method of use. Different software provides various optional thermodynamic methods and unit modules. If the method is used improperly, it will result in larger errors. Under normal circumstances, the results of running different process simulation software are not much different. The difference in the accuracy of results often lies in the selection of the unit module and the determination of the thermodynamic method.

Process simulation system software is used for process simulation. The following steps are often used: first, analyze the target simulation problem, combine the actual situation of the target simulation problem, convert it into a mathematical model, analyze the known and solved problems, and select the appropriate process simulation software. There are differences in the use of each software, and the determination of the software will help us in the next step; Second, establish a simulation process, use the method provided by the process simulation software to establish the simulation process, that is, establish the connection sequence of the relevant unit modules and logistics. Third, participate in the process of components. In conjunction with the substances involved in the actual problem, enter the corresponding components in the simulation system and determine the thermodynamic model; inappropriate thermodynamic methods will lead to the inaccurate simulation process and data, according to the actual situation. Choosing the most suitable thermodynamic method is the prerequisite for successful simulation. Finally, input known parameters. This includes the original logistics and unit module parameters, which can be input to the chemical process simulation.

3. Results and Discussion

Pure water was added and the pressure was increased from 20 kPa to normal pressure. Through the above experimental apparatus and experimental procedures, the boiling point corresponding to a certain pressure was measured, and the influence of the increase in pressure on the boiling point was examined.

As can be seen from Figure 2, the pure water measured in the experiment is basically consistent with the literature data. The results show that the experimental device process is feasible to detect the bubble point of the solution under a certain pressure and concentration. From the viewpoint of simplifying the calculation, it can be considered that in this concentration range, the bubble point of the saturated aqueous sodium chloride solution is equal to the bubble point of the saturated sodium chloride solution. The bubble point of saturated sodium chloride solution containing glycerin was measured by adjusting the pressure of different systems. The boiling point of the water measured by this device is basically consistent with the literature data obtained. The results show that the device is capable of detecting the bubble point of the solution under a certain pressure. Use the above experimental procedure to measure the bubble point of saturated sodium chloride solution with different glycerol concentrations. When pressure is constant, the increase of glycerol concentration will increase the bubble point slowly, but the increase is not obvious. When the glycerol concentration is constant, the increase in pressure will increase the bubble point. Compared with the bubble point of the saturated sodium chloride solution without glycerol, the absolute pressure is in the range of 20 kPa to atmospheric pressure, and the addition of glycerol concentration of 11–500 g/L will increase the bubble point of the solution by 0–5°C. To simplify the calculation, it is considered that when the glycerol concentration is less than 100 g/L, the bubble point of the saturated sodium chloride solution is equal to the bubble point of the saturated sodium chloride solution. Determination of COD in distillate and conversion to glycerol is given in Table 1.

From the above table, it can be seen that the COD content in the distillate is almost zero, and it can be regarded that the distillate after the vacuum evaporation treatment does not substantially contain glycerin organics. Using PRO/II to simulate the bubble point of saturated sodium chloride brine, the result is compared with the bubble point obtained by the gas-liquid equilibrium experiment, as shown in Figure 3 [17–19].

The simulated data and the experimental data were basically in agreement and proved that the application of the thermodynamic equation to the brine system is feasible. The main economic indicators of evaporating operation are measured by evaporating salt content/raw steam, and the comparison of three-effect parallel flow, five-effect parallel flow, and seven-effect parallel flow is given in Table 2.

From the table, we can see that in the saltwater system, the unit of raw steam can precipitate the salt in order of decreasing from seven to more than five and more than three. This shows that, considering the use of heat, the

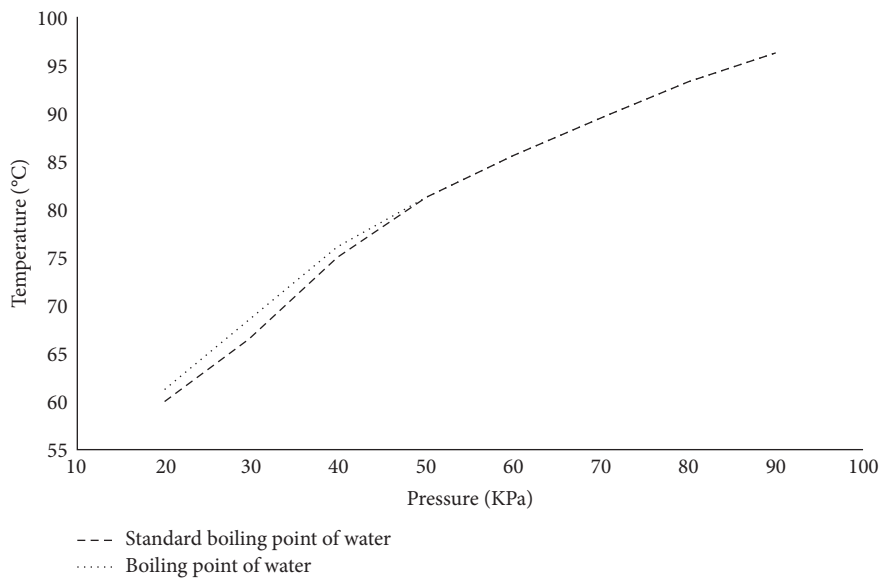

Figure 2: Pressure–boiling point diagram of water.

Table 1: The concentration of COD and glycerol in the distillate.

Mass of distillate (gm)	COD (mg/L)	Glycerol (mg/L)
6	6	0.003

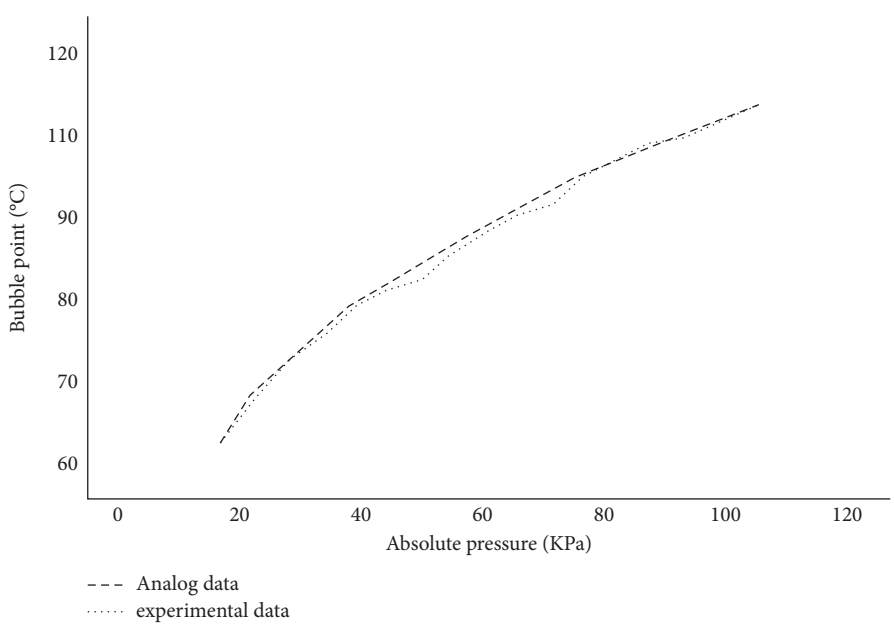

Figure 3: Brine system bubble simulated data compared with the experimental data.

Table 2: Comparison of steam generation and discharge of different efficiency in the brine system.

Technological process	Discharge flow (kmol/h)				Steam generating (kmol/h)	Precipitated salt (kmol/h)	Salt/steam
	Water	Sodium chloride	Hydrogen chloride	Sodium hydroxide			
Three-effect flow	0.3596	0.015	0.0299	0.0299	5	0.29	0.058
Five-effect flow	0.4512	0.0188	0.0375	0.0375	3.7	0.25	0.0675676
Seven-effect flow	0.0862	0.0036	0.0072	0.0072	3	0.29	0.09666667

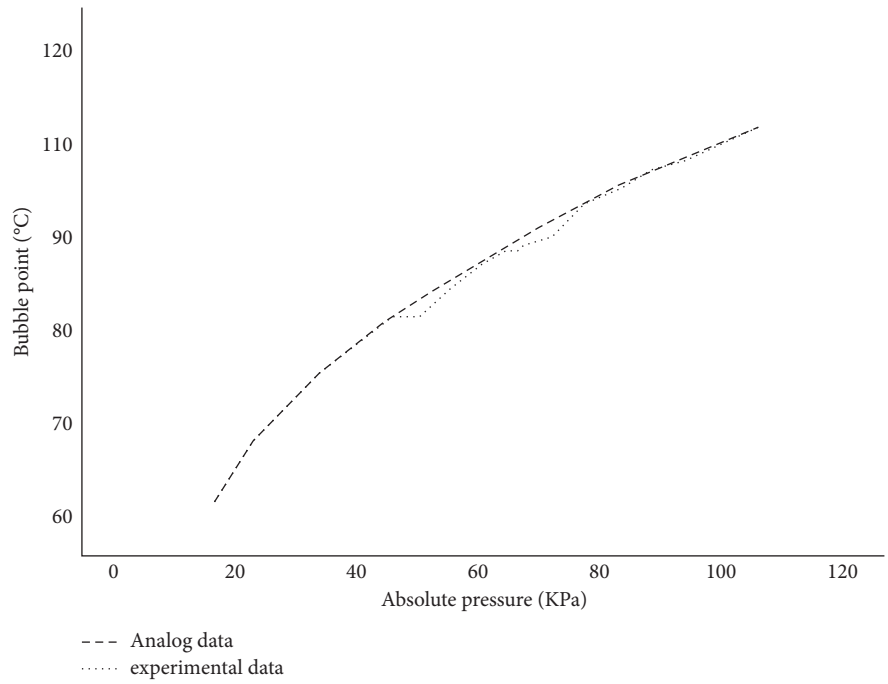

Figure 4: Glycerol saline system bubble simulation data and experimental data.

Table 3: Comparison of different steam generation and discharging conditions of the glycerin brine system.

Technological process	Discharge flow (kmol/h)				Steam generating (kmol/h)	Precipitated salt (kmol/h)	Salt/steam
	Water	Sodium chloride	Hydrogen chloride	Sodium hydroxide			
Three-effect flow	0.182	0.007	0.003	0.016	5.000	0.300	0.060
Five-effect flow	0.346	0.014	0.003	0.030	3.700	0.250	0.067
Seven-effect flow	0.538	0.022	0.003	0.046	3.000	0.270	0.090

increase in the number of efficiencies favors the use of steam and the precipitation of salt. Using PRO/II to simulate the bubble point of saturated sodium chloride solution containing 11 g/L of glycerol, the results are compared with the bubble point obtained from the gas-liquid equilibrium experiment, as shown in Figure 4.

The glycerol-containing sodium chloride water systems can be modeled by using this thermodynamic equation. If the main economic indicators of evaporating operation are measured by evaporating salt content/raw steam, the comparison of three-effect parallel flow, five-effect parallel flow, and seven-effect parallel flow is given in Table 3.

From this table, it can be seen that in the system containing glycerol, the unit steam energy precipitates the salt in order from more to less in order of seven-effect, five-effect, and three-effect.

4. Conclusions

An experimental device is designed and constructed for measuring the bubble point of a saturated sodium chloride solution containing glycerol, examining the feasibility of the device to detect the boiling point of a salt solution under a certain pressure and concentration. Based on an externally heated evaporator, a multieffect evaporation of the brine system and glycerin-containing brine is simulated by the chemical process using PRO II software. The model three-effect cocurrent evaporation process, five-effect cocurrent evaporation process, and seven-effect cocurrent evaporation process were used. The effects of different multieffect evaporation processes on steam economy of multieffect evaporation are investigated. Based on PRO II simulations, it is found that in the brine system or the glycerin brine system, the amount of salt precipitated by unit steam energy is arranged in order from much to less: the seven-effect parallel flow evaporation is greater than the five-effect parallel flow evaporation which is greater than the three-effect parallel flow evaporation. From the point of view of heat utilization, the increase of validity is beneficial to the utilization of steam and the precipitation of salt. The purpose of reducing energy consumption is to study the economy of steam and select the appropriate flow.

Data Availability

No data were used to support this study.

Conflicts of Interest

The authors declare that they have no conflicts of interest.

References

[1] H. Wei, G. Liu, and T. Yong, "Wastewater treatment evaluation for enterprises based on fuzzy-AHP comprehensive evaluation: a case study in industrial park in Taihu Basin, China," *SpringerPlus*, vol. 5, no. 1, p. 907, 2016.

[2] W. Liang, C. Ying, L. Min, and Y. Zhai, "Comprehensive performance evaluation of municipal wastewater treatment plants," *Chinese Journal of Environmental Engineering*, vol. 10, no. 1, pp. 490–494, 2016.

[3] M. A. Dursun, "Fuzzy approach for the assessment of wastewater treatment alternatives," *Engineering Letters*, vol. 24, no. 2, pp. 231–236, 2016.

[4] J. Fernandez de Canete, P. Del Saz-Orozco, R. Baratti, M. Mulas, A. Ruano, and A. Garcia-Cerezo, "Soft-sensing estimation of plant effluent concentrations in a biological wastewater treatment plant using an optimal neural network," *Expert Systems with Applications*, vol. 63, no. C, pp. 8–19, 2016.

[5] K. Liu, Y. Hu, and J. Lei, "The chemical product mode transition of the air DBD driven by AC power: a plausible evaluation parameter and the chemical behaviors," *Physics of Plasmas*, vol. 24, no. 10, p. 103513, 2017.

[6] S. Ditommaso, M. Giacomuzzi, E. Ricciardi, R. Garbuio, and C. M. Zotti, "The role of chemical products at low doses in preventing the proliferation of bacteria in dental unit waterlines: the ICX experience," *Journal of Water and Health*, vol. 16, no. 1, pp. 150–158, 2018.

[7] S. Cignitti, S. S. Mansouri, J. M. Woodley, and J. Abildskov, "Systematic optimization-based integrated chemical product-process Design framework," *Industrial & Engineering Chemistry Research*, vol. 57, no. 2, pp. 677–688, 2018.

[8] J.-B. Xu, J.-P. Chen, S.-L. Wu, Y.-H. Pan, W. Wang, and Q.-Q. Luo, "Prediction of large deformation behavior in tunnels based on AHP-FUZZY method and numerical simulation method," *Geotechnical & Geological Engineering*, vol. 36, no. 1, pp. 151–163, 2018.

[9] A. A. Aghapour, G. Moussavi, and K. Yaghmaeian, "Degradation and COD removal of catechol in wastewater using the catalytic ozonation process combined with the cyclic rotating-bed biological reactor," *Journal of Environmental Management*, vol. 157, pp. 262–266, 2015.

[10] P. M. Vallejo LLamas and P. Vega, "Analytical fuzzy predictive control applied to wastewater treatment biological processes," *Complexity*, vol. 2019, Article ID 5720185, 29 pages, 2019.

[11] M. Hammer and M. Hammer, *Water and Wastewater Technology*, Prentice-Hall, New York, NY, USA, 2005.

[12] M. Yao, Z. Li, X. Zhang, and L. Lei, "Polychlorinated biphenyls in the centralized wastewater treatment plant in a chemical industry zone: source, distribution, and removal," *Journal of Chemistry*, vol. 2014, Article ID 352675, 10 pages, 2014.

[13] J. Shi, C. Xu, Y. Han, and H. Han, "Case study on wastewater treatment technology of coal chemical industry in China," *Critical Reviews in Environmental Science and Technology*, vol. 51, no. 10, pp. 1003–1044, 2020.

[14] A. E. Anqi and A. Mohammed, "Evaluating critical influencing factors of desalination by membrane distillation process-using multi-criteria decision-making," *Membranes*, vol. 11, p. 164, 2021.

[15] R. R. Tan, K. B. Aviso, A. P. Huelgas, and M. A. B. Promentilla, "Fuzzy AHP approach to selection problems in process engineering involving quantitative and qualitative aspects," *Process Safety and Environmental Protection*, vol. 92, no. 5, pp. 467–475, 2014.

[16] European Commission, *Integrated Pollution Prevention and Control, Reference Document on Best Available Techniques in the Chlor-Alkali Manufacturing Industry*, European Commission, Brussels, Belgium, 2001.

[17] S. D. Pohekar and M. Ramachandran, "Application of multi-criteria decision making to sustainable energy planning-A review," *Renewable and Sustainable Energy Reviews*, vol. 8, no. 4, pp. 365–381, 2004.

[18] H. An, Z. Liu, X. Cao et al., "Mesoporous lignitecoke as an effective adsorbent for coal gasification wastewater treatment," *Environmental Sciences: Water Research & Technology*, vol. 3, no. 1, pp. 169–174, 2016.

[19] G. Boczkaj and A. Fernandes, "Wastewater treatment by means of advanced oxidation processes at basic pH conditions: a review," *Chemical Engineering Journal*, vol. 320, pp. 608–633, 2017.

Hindawi
Journal of Chemistry
Volume 2021, Article ID 4558271, 10 pages
https://doi.org/10.1155/2021/4558271

Research Article

Nickel Removal from Aqueous Solution Using Chemically Treated Mahogany Sawdust as Biosorbent

Rajesh Chanda, Amir Hamza Mithun, Md. Abu Hasan, and Biplob Kumar Biswas

Department of Chemical Engineering, Jashore University of Science and Technology, Jashore 7408, Bangladesh

Correspondence should be addressed to Biplob Kumar Biswas; bk.biswas@just.edu.bd

Received 30 June 2021; Revised 4 September 2021; Accepted 6 September 2021; Published 21 September 2021

Academic Editor: Abdullah Aldawsari

Sawdust is a waste material, which is generally produced during making furniture and other necessary wood products. With a view to utilizing this waste material, a biosorbent was prepared from mahogany (*Swietenia macrophylla*) sawdust through simple chemical treatment and was used to remove nickel ion (Ni^{2+}) from an aqueous solution. The adsorbent material was characterized by Fourier transform infrared (FTIR) spectroscopy, scanning electron microscopy (SEM), and energy dispersive X-ray (EDX) analysis. The effects of biosorbent dosage (2~18 g/L), pH of the tested solution (4~10.5), contact time (up to 360 min), and temperature (298~318 K) were studied in batchwise experiments. The maximum adsorption capacity of the treated sawdust was determined to be 13.42 mg/g at an optimum condition (sorbent dose of 15 g/L, pH of 9, and temperature of 298 K). The experimental data extrapolation revealed that the adsorption process fitted the Langmuir isotherm model and the kinetics was a pseudo-second-order kinetic model. The obtained thermodynamic parameters indicated that the adsorption reaction was spontaneous, endothermic, and random in nature. The study revealed that sawdust biosorbent has potential adsorption efficiency for nickel ion removal from an aqueous solution.

1. Introduction

Environmental pollution by the presence of heavy metals has aroused enormous attention of researchers because of their toxicity, harmfulness, and nondegradability in the ecosystem [1–3]. Metal-containing effluents from different activities (e.g., domestic, industrial, and agriculture) pollute the aqueous environment (both surface and underground water) continuously. Heavy metals are considered to be significantly dangerous to mankind because of their hazardous nature [4]. Mining, jewelry, Cd-Ni battery, alloy, metallurgical, and metal plating industries are stated to be the major source of metal-containing waste pollution [5, 6]. Nickel concentrations in air are typically 0.00001–0.003 $\mu g/m^3$ in remote places, 0.003–0.03 $\mu g/m^3$ in municipal and metropolitan places, and 0.07–0.77 $\mu g/m^3$ in nickel processing industries as well as in similar manufacturing plants [7]. According to the World Health Organization (WHO, the year 2020), the nickel concentration in drinking water is 2–13 $\mu g/L$ in European countries.

Nickel (Ni) is found in several minerals formed in nature. For example, in the earth's crust, nickel is the 24th most abundant natural element that covers about 3% of the earth's composition [7]. In the periodic table, nickel stands in group VIII B along with other transition metal elements such as iron, cobalt, palladium, and platinum. Being a toxic metal, nickel poses serious concern due to its carcinogenic potency to human beings. Nickel causes various diseases such as cardiac arrest, respiratory problems, kidney damage, and gastrointestinal distress [8]. Therefore, along with other metals such as Cd, Zn, and Pd, it is necessary to remove Ni ions from wastewater of industrial establishments before their discharge to the water reservoirs as well as to the environment [9]. However, still, an efficient and cost-effective method of Ni ions removal from industrial wastewater remains a challenge.

Since nickel contamination is a global environmental problem, several research works have been conducted to develop improved as well as effective treatment technologies for the removal of nickel along with harmful metal ions from

wastewater. Technologies to remove metal ions are solvent extraction, electrochemical precipitation, membrane filtration, ion-exchange process, reverse osmosis method, photocatalytic reduction, adsorption [10–13], etc. Despite such varieties of nickel removal technologies, none of them alone is cheap, easy to operate, and environmentally friendly. For example, the precipitation-coagulation method is simple in operation; however, it produces a large amount of sludge that must be treated afterward and leads to high disposal costs. Anion-exchange processes have a quite low selectivity in the dynamic presence of other competing metal ions [14, 15]. Reverse osmosis and ion exchange, although efficient, are expensive due to high operational and maintenance costs throughout their working life.

Adsorptive removal is a simple process, which can be cheap and environmentally benign depending on the nature of adsorbents. Therefore, in recent years, a trend toward using low-cost and readily available waste materials as biosorbents for the removal of heavy metals from wastewater is observed. A number of waste materials-based biosorbents such as coconut husk, wheat and barley straw [16], blood banana [13], orange waste [14], waste paper [17], nutshells [18], and sawdust [2, 19, 20] have been exploited for the removal of metal ions from aquatic media. Among the low-cost biosorbents, sawdust is a promising one, which can be effectively used for dye removal after treatment with formaldehyde [21, 22]. Even though various types of sawdust have been used as biosorbents, to the best of our knowledge, studies on the use of locally obtained mahogany (*Swietenia macrophylla*) sawdust as well as other types of sawdust for nickel removal from aqueous solutions are not available. Mahogany is a common tree in Bangladesh and is widely used in furniture making. In this investigation, mahogany sawdust was chemically treated and used as a biosorbent for the removal of nickel ions (Ni^{2+}) from an aqueous solution. The effects of various parameters such as solution pH, adsorbent dosage, contact time, metal concentration, and temperature on the removal of Ni (II) were studied through different sets of batch experiments. The adsorption isotherm, kinetics, mechanism, and various thermodynamic parameters have also been presented.

2. Materials and Methods

2.1. Chemicals. Nickel chloride ($NiCl_2$) was dissolved in distilled water to prepare a synthetic stock solution of nickel (1000 mg/L), which was diluted as necessary to prepare a working solution while conducting batch adsorption experiments. As-received formaldehyde (H-CHO) was used to prepare 2% of its solution. However, to adjust the pH of the working solutions, hydrochloric acid (0.1 M HCl) and sodium hydroxide (0.1 M NaOH) solutions were used throughout the investigation. All the reagents and chemicals (Merck, Germany) used in this work were of analytical reagent grade and purchased from the local supplier.

2.2. Preparation of Chemically Treated Mahogany Sawdust as Biosorbent. Mahogany (*Swietenia macrophylla*) sawdust was collected from a sawmill located in the suburban area of Jashore, Bangladesh. The sawdust was first washed with distilled water to eliminate dust and other unwanted particles. It was then dried in a convection dryer at 70°C until all the moisture from the sawdust was completely evaporated. The sawdust was ground to make a fine powder using a mortar and pestle [3]. The powdered material obtained after grinding was sieved to obtain a particle size range of 100–150 μm. For chemical treatment of the sawdust powder, 2% formaldehyde was mixed with powdered sawdust at a ratio of 4 : 1 (formaldehyde : sawdust, v/w) to immobilize the water-soluble substances and color at room temperature by shaking for three hours. After that treatment, the sawdust was filtered and washed with distilled water to remove free formaldehyde (not bonded with the surface), and it was dried in a convection dryer (HDG-9030, Korea) at 70°C for 24 hours. The obtained material was kept in an air-tight container for further use.

2.3. Characterizations. Fourier transform infrared spectroscopy (IRTracer-100, Shimadzu, Japan) was analyzed to comprehend the major contributing functional groups of the biosorbent that might take part in metal adsorption. FTIR spectra of the biosorbent before and after nickel ions adsorption were performed so that the involvement of functional groups becomes clear. The surface morphology of the biosorbent in both cases (before and after nickel ions adsorption) was studied with a field emission scanning electron microscope (FESEM, JSM 7600F, JEOL Inc., Japan) at a working voltage of 5 kV with different magnifications.

2.4. Batch Adsorption Experiments. Batch adsorption tests were carried out by taking 1000 mg of the treated sawdust in an Erlenmeyer flask in which 100 ml of adsorbate (nickel) solution was taken at the required concentration. The entire suspension was then shaken at 200 rpm in a magnetic stirrer (MS300HS, Korea). After a certain time, the suspension was filtered using filter paper. The liquid fraction was then used to analyze the amount of nickel ion using atomic absorption spectrophotometer (AA-7000, Shimadzu, Japan). It is important to note that either 0.1 M HCl or 0.1 M NaOH solution was added to the solution to keep a constant pH of the solution to avoid nickel precipitation. The pH of the solution was measured by a portable pH meter (EZODO 6011, Taiwan). In general, batch adsorption tests were carried out to study the impact of pH of the initial nickel solution at pH ranging from 4 to 10.5, amount of adsorbent dosage of 200–1800 mg, contact time of 0–360 min, initial nickel ion concentrations of 10–500 mg/L in the mother solution, and sorption temperature of 298–318 K. All the experiments were performed at room temperature unless otherwise stated. To avoid experimental errors, all the investigations were replicated three times. The average value of these three was taken for further data interpretation and graph plotting.

The total nickel ion adsorption percentage was calculated using the following equation:

$$\%\,\text{adsorption} = \left\{ \frac{\left(C_{in} - C_{eq}\right)}{C_{in}} \right\} \times 100, \quad (1)$$

where C_{in} and C_{eq} are the initial and equilibrium nickel ion concentration (mg/L) in the solution, respectively.

In addition, the adsorption capacity (q) for any single experiment was calculated using the following equation:

$$q = \frac{\left\{\left(C_{in} - C_{eq}\right) \times V\right\}}{M}, \quad (2)$$

where q is the amount of nickel adsorbed (mg/g), V is the volume of the liquid solution (L), and M is the amount of the powdered sawdust biosorbent (g).

3. Results and Discussion

3.1. Characterization of the Biosorbent. The structure of the adsorbent is important to know the morphology of the biosorbent and to understand the adsorption process. The cell walls of sawdust mainly consist of cellulose, hemicellulose, lignin, tannins, etc., which contain a considerable amount of hydroxyl groups [23]. All these components are active ion-exchange compounds since they contain different functional groups. Being a polymeric material, the lignin molecule is made up of the phenylpropane nucleus, an aromatic ring having three-carbon side chains, which are readily available to interact with cationic metal ions [2, 23].

3.1.1. Fourier Transform Infrared (FTIR) Spectroscopy. Sawdust contains cellulose, hemicellulose, lignin, pectin, and other extractives such as waxes. Metal ions are supposed to be adsorbed to carboxylic (present in hemicellulose, pectin, and lignin), phenolic (present in lignin), hydroxyl (present in cellulose, hemicellulose, lignin, and pectin), and carbonyl groups (lignin and pectin). The FTIR spectrum of sawdust biosorbent exhibited numerous absorption peaks (Supplementary Figure S1), which indicated the complex nature and heterogeneity of this material [23]. The assignment of each peak at a specific wavenumber for sawdust (before and after adsorption) is listed in Table 1. The peaks, which correspond to different functional groups, are the possible adsorption sites. The functional groups present in the sawdust biosorbent may donate protons, and thus deprotonated groups are created at the surface of the biosorbent. These deprotonated groups may be involved in coordination with nickel ions resulting in adsorption of the metal ions [23].

As seen from Table 1, many wavenumbers are found to slightly deviate (both position and intensity) after nickel ion adsorption, which may be attributed to the shift of some functional group's band during the process of adsorption. These shifts may occur because of changes in counterions associated with carboxylate and hydroxylate anions. The deviation of wavenumbers demonstrates that a metal-binding process took place at the biosorbent surface [24]. The similarity of spectra between the biosorbent without metal adsorption and after metal adsorption indicates that the adsorption of nickel ions on the surface of the biosorbent was accomplished either through complexation or through physical processes that include both weak electrostatic interaction and Van der Waals force [2].

Table 1: The FTIR spectral characteristics of sawdust before and after adsorption of nickel ions.

Wavenumber (cm^{-1})			Assignments
Before adsorption	After adsorption	Differences	
3437	3410	−27	O-H stretching
2924	2916	−8	C-H stretching
1737	1737	0	C-H bending
1635	1631	−4	C=C stretching
1510	1504	−6	N-O stretching
1462	1462	0	C-H bending
1423	1425	+2	O-H bending
1373	1375	+2	O-H bending
1321	1330	+9	S=O stretching
1247	1247	0	C-O stretching
1161	1161	0	C-O stretching
1120	Nil	Absent	C-O stretching
1056	1056	0	S=O stretching
900	898	−2	C-H bending

3.1.2. Scanning Electron Microscopy (SEM) Analysis and Energy Dispersive X-Ray (EDX) Spectroscopy. The morphological properties (surface texture and porosity) of treated mahogany sawdust before and after nickel adsorption were investigated using SEM, which is depicted in Figure 1. In the case of fresh treated sawdust (before adsorption), the figure shows the interior microstructure of the biosorbent, which confirms a well-defined porous structure. Moreover, the sawdust (before metal adsorption) contains a rough surface with many tunnel-like structures, and the porous structure slightly decreased after the adsorption of nickel ions. The EDX spectroscopy clearly shows that after the adsorption process nickel is adsorbed onto the treated sawdust. From EDX analysis, the nickel content was found to increase by 0.98%, which indicated successful adsorption of nickel on treated sawdust. A lesser nickel content (0.09%) was reported to be adsorbed using dried biomass (named *Ulva lactuca*) from an aqueous solution [25].

3.2. Effect of Solution pH. The pH of the working solution is one of the important parameters that influence metal ion adsorption. The pH of the solution influences the dissociation of functional groups as well as solution chemistry, and thus it has a significant effect on biosorption capacity [26]. Moreover, the pH affects the metal ion chemistry (such as degree of ionization and state) in the solution as well as the stability of different metal ion species in the solution [3, 27]. In the present study, the effect of change in solution pH on the removal of Ni (II) was studied by varying the pH of the solution from 4 to 10.5 at a fixed Ni (II) initial concentration of 25 mg/L. As depicted in Figure 2, the adsorptive removal of nickel significantly depends on pH. Nickel removal percentage increases with the increase in solution pH, and

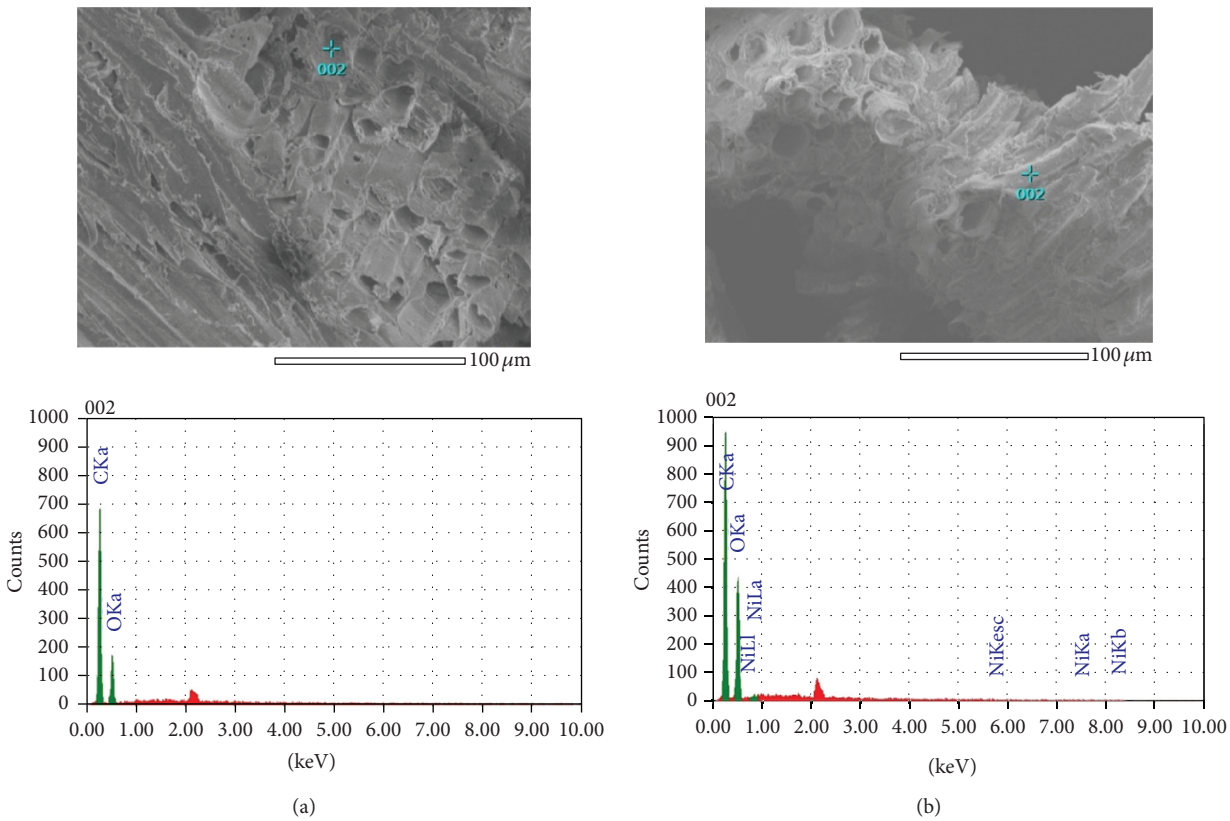

Figure 1: SEM-EDX images and spectra of treated sawdust (a) before and (b) after adsorption of nickel ions.

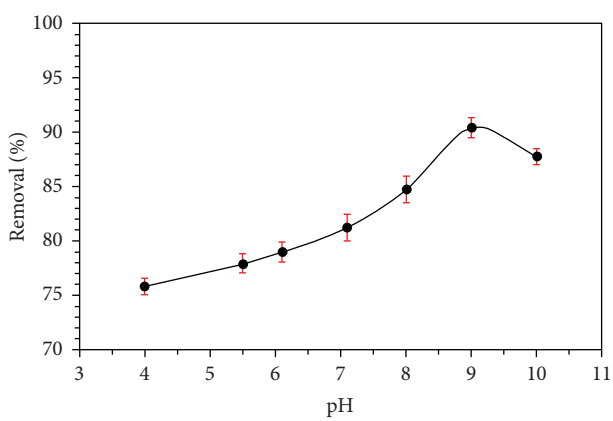

Figure 2: Effect of pH on the removal of Ni (II) using sawdust. Condition: $T = 298$ K, $t = 6$ h, and dose = 15 mg/ml.

maximum adsorption was found to occur at pH 9 (at the stated conditions). The point of zero charge (pH_{pzc}) of the adsorbent was determined too, and the extent of pH_{pzc} was found to be 6.8 (as shown in Supplementary Figure S2). Cation adsorption used to improve at pH higher than pH_{pzc}. The experimental results (Figure 2) show a similar trend as the nickel removal increases significantly after pH 6.8. Depending on the pH of the solution, nickel exists mainly as four different species with different coordination numbers such as Ni^{2+}, $Ni(OH)^{+}$, $Ni(OH)_2$, and $Ni(OH)_3^{-}$. From the speciation diagram, as reported by Gonsalvesh et al., it is obvious that up to pH 9 the predominant nickel species is Ni^{2+} [27]. Therefore, it is comprehended that cation exchange, as well as direct surface complexation, might play a vital role in removing (through adsorption) metal ions in this case [28].

One thing to note here is that as the pH of the stock solution was increased above pH 9, the percentage removal of nickel decreased. This phenomenon can be elucidated with the fact that soluble hydroxyl complexes formed at higher pH and, thus, the sorption mechanism changes. A similar explanation has been reported for various metal ions adsorption by biosorbents [2, 25].

3.3. Effect of Biosorbent Dosage. To find out a perfect biosorbent dose, batchwise adsorption studies of Ni (II) ions onto the treated mahogany (*Swietenia macrophylla*) sawdust were carried out at 30°C where the dose was varied from 2 g/L to 18 g/L keeping the solution pH constant. The percentage of nickel adsorption on sawdust concerning the adsorbent dosage is shown in Figure 3. The figure shows that as the adsorbent dosage increases (from 2 g/L to 15 g/L), the total adsorption percentage increases gradually (from 41% to 85%). However, the adsorption percentage remains almost constant despite a further increase in adsorbent dosage (i.e., higher than 15 g/L). The observed tendency can be explained by the fact that the total surface area of the adsorbent and the number of active sorption sites increase with the increase of adsorbent quantity. A similar phenomenon has been

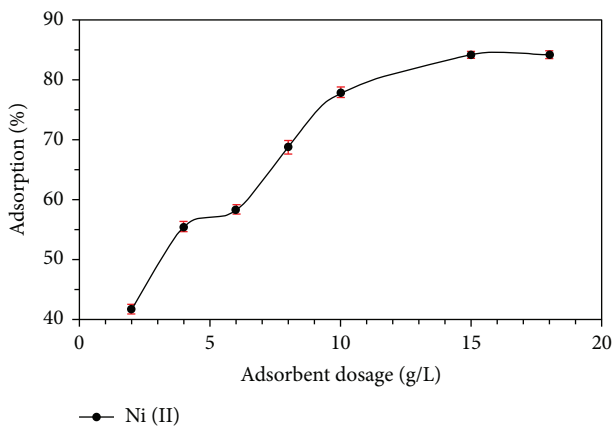

Figure 3: Effect of amount of adsorbent on the removal of nickel using treated sawdust. Condition: $T = 303$ K and $t = 6$ h.

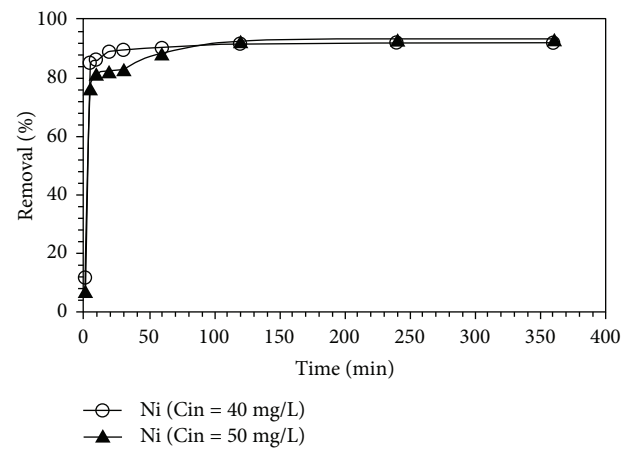

Figure 4: Percent removal of nickel with respect to time at different initial nickel concentrations.

reported in the literature for nickel adsorption onto sawdust and/or sawdust-derived biosorbents [1, 3]. Taking these results into consideration, an adsorbent dosage of 15 g/L was chosen for further adsorption studies.

3.4. Effect of Contact Time. To select the required time for the equilibrium to be attained, preliminary experiments were conducted at initial Ni (II) concentrations of 40 mg/L and 50 mg/L in the solution, and the result is presented in Figure 4. As seen from this figure, the amount of adsorbed Ni^{2+} ions increased with increasing time. It is obvious that a significant separation of Ni (II) ions occurred within 120 min under 200 rpm stirring, and in the later stage, the adsorption capacity became invariable. A similar result has been reported for the removal of Cu (II), Pb (II), and Cd (II) ions from an aqueous solution by inexpensive biopolymeric sorbent [29]. However, to ensure complete adsorption, all other experiments were allowed to run for 6 h at the given conditions. The initial high rate of percentage uptake of Ni^{2+} ions is perhaps due to the availability of a larger surface area of the biosorbent which gives free adsorption sites of treated mahogany sawdust. Nickel ions are transported firstly from the bulk solution to the outer biosorbent surface and then from the outer surface to the inner surface of the pores. Thus, with time the surface adsorption sites (outer as well as inner) become gradually occupied. However, the rate of adsorption is thought to be controlled by the transport rate of metal ions from the exterior to the interior sites (through pores) of the biosorbent.

3.5. Kinetic Studies of Nickel Ions Adsorption. The rate of adsorptive interaction onto the sawdust was estimated using the linearized integral form of Lagergren's pseudo-first-order and pseudo-second-order kinetic models [30]. The respective model equations are given as follows:

$$\log(q_e - q_t) = \log q_e - \frac{k_1 t}{2.303}, \quad (3)$$

$$\frac{t}{q_t} = \frac{1}{k_2 q_e^2} + \frac{t}{q_e}, \quad (4)$$

where q_e (mg/g) and q_t (mg/g) are the amount of nickel adsorbed onto the sawdust biosorbent at equilibrium and the amount of nickel adsorbed at time t (min), respectively; k_1 (1/min) is the first-order adsorption rate constant; and k_2 (g/(mg·min)) is the second-order adsorption rate constant.

To determine the adsorption kinetics, both pseudo-first-order and pseudo-second-order models were tested and are shown in Figure 5. The conformity between the experimental data and the predicted values from the model was expressed by correlation coefficient (R^2). The pseudo-second-order model is the best-suited because its R^2 values (0.9998 and 0.9982 for 40 mg/L and 50 mg/L, respectively) were near to conformity compared to the R^2 values (0.8119 and 0.9582 for 40 mg/L and 50 mg/L, respectively) of the pseudo-first-order kinetic model. Moreover, calculated values (from (4)) of amounts adsorbed exhibited excellent agreement with the values obtained from experiments ($q_{\exp}$). Similar results have been reported for the adsorption of metal ions with other types of dried biomass [25, 31]. Both experimental and calculated values of rate constants, correlation coefficients, and amounts adsorbed are tabulated in Table 2.

In general, for well-stirred batch-mode adsorption experiments, transport of absorbate from the bulk solution to the adsorbent pores may be considered as the rate-controlling step [32]. Such postulation can be generally studied by applying Webber–Morris intraparticle diffusion model [33]. Thus, for comprehending the adsorption mechanism of nickel on mahogany sawdust, the kinetic data were further analyzed using the Webber–Morris intraparticle diffusion model, and the related equation is expressed as follows:

$$q_t = k_{i\,d} t^{1/2} + C, \quad (5)$$

where q_t (mg/g) is the adsorption capacity at time t, while k_{id} (g/(mg.min$^{-0.5}$)) and C are intraparticle diffusion rate constant and boundary layer thickness, respectively. By plotting q_t vs $t^{1/2}$, the parameters (i.e., k_{id} and C) were then calculated from the slope and intercept of the linear plot, respectively (shown in Figure 6). It is evident from Figure 6 that there are two separate regions in each of the plotted

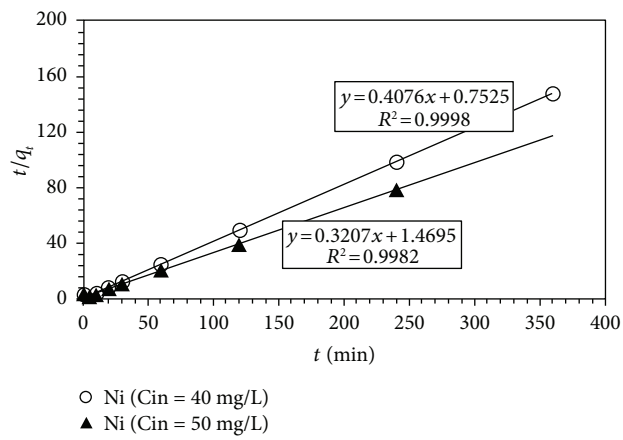

Figure 5: Pseudo-second-order kinetic plot for the adsorption of nickel at 303 K.

Table 2: Pseudo-first-order and pseudo-second-order kinetic models for the adsorption of Ni(II) on mahogany sawdust.

Metal (mg/L)	q_{exp} (mg/g)	Pseudo-first-order			Pseudo-second-order		
		q_e (mg/g)	k_1 (1/min)	R^2	q_e (mg/g)	k_2 (g/(mg·min))	R^2
40	2.44	0.20	0.0073	0.8119	2.45	0.2208	0.9998
50	3.05	0.89	0.0132	0.9582	3.11	0.067	0.9982

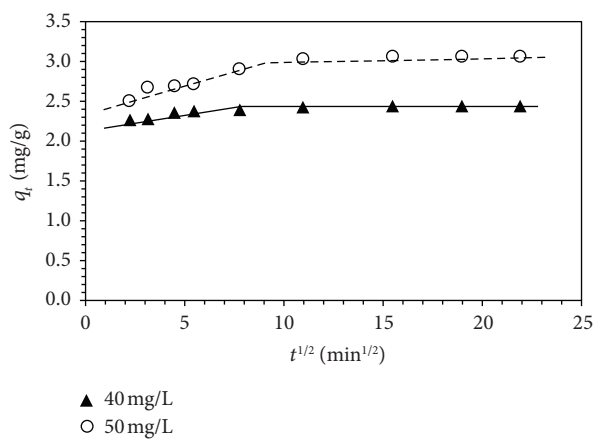

Figure 6: Weber–Morris plot for nickel ion adsorption.

lines, which is an indication of multistage adsorption of nickel on mahogany sawdust. The first linear region was the instantaneous adsorption or external surface adsorption stage, while the second linear region represented the intraparticle diffusion or pore diffusion stage. The intraparticle diffusion rates (k_{id}) for the first and second linear stages were calculated to be 0.0263 g/(mg.min$^{-0.5}$) and 0.0008 g/(mg.min$^{-0.5}$), respectively (for the initial nickel concentration of 40 mg/L). Similarly, k_{id} in case of the initial nickel concentration of 50 mg/L was determined as 0.0626 g/(mg.min$^{-0.5}$) and 0.0019 g/(mg.min$^{-0.5}$) for the first linear portion and second linear portion, respectively.

3.6. Adsorption Isotherm Studies. The relationship between the concentration of the adsorbate and its extent of adsorption onto the adsorbent surface at a fixed temperature can be well described by adsorption isotherms. In the present investigation, Langmuir, Freundlich, and Dubinin–Radushkevich (D-R) isotherm models were used to quantify the adsorption capacity of mahogany sawdust for the removal of Ni (II) from aqueous solution. The adsorption isotherm studies were conducted using an initial nickel concentration range of 10–500 mg/L and at an operating sorption temperature range of 298–318 K.

3.6.1. Langmuir Model. The Langmuir isotherm model is developed on the assumption that the adsorption takes place on specific homogeneous sites by monolayer adsorption process, which signifies that once an adsorbate occupies a vacant adsorption site, then no further adsorption takes place on that site. However, the Langmuir isotherm model can be defined by the following equation [25, 33]:

$$\frac{C_e}{q_e} = \frac{C_e}{q_{\max}} + \frac{1}{bq_{\max}}, \tag{6}$$

where C_e (mg/L) is the equilibrium concentration of nickel, q_e (mg/g) is the amount of nickel adsorbed at equilibrium, $q_{\max}$ (mg/g) is the maximum adsorption capacity, and b (L/mg) is the equilibrium constant. Hence, a straight line is obtained by plotting C_e/q_e vs C_e for three different temperatures. Values of $q_{\max}$ and b can be obtained, respectively, from the slope and intercept of the straight lines of the figure. However, the calculated values are presented in Table 3.

3.6.2. Freundlich Model. Another isotherm model tested in this study was the Freundlich isotherm model, which is supposed to deal with the multilayer adsorption of adsorbate (nickel ions) on the biosorbent (sawdust). The model can be applied for a nonideal sorption process where heterogeneous

Table 3: Isotherm constants and correlation coefficients for the adsorption of nickel on sawdust.

Isotherms	Parameters	T (K)		
		298	308	318
Langmuir	$q_{\max}$ (mg/g)	13.42	14.03	14.43
	b (L/mg)	0.031	0.029	0.024
	R^2	0.9856	0.9904	0.9835
Freundlich	$1/n$	0.568	0.554	0.558
	K_f	0.696	0.720	0.704
	R^2	0.9740	0.9256	0.9596
Dubinin–Radushkevich	K_{ad} (mol^2/kJ^2)	0.1732	0.2006	0.165
	q_s (mg/g)	22.43	27.36	19.70
	E (kJ/mol)	1.699	1.579	1.741
	R^2	0.9016	0.9031	0.7948

sites are in effect. The isotherm is commonly expressed as follows [24]:

$$\log q_e = \log K_f + \frac{1}{n}\log C_e, \tag{7}$$

where q_e (mg/g) and C_e (mg/L) are symbolized as adsorption capacity and adsorbate concentration at equilibrium, respectively; K_f is the Freundlich constant that indicates a relationship between the adsorption capacity and bonding energy; and $1/n$ is designated as the Freundlich coefficient that represents the factor of heterogeneity as follows [24]. The values of K_f and $1/n$ for different temperatures (for example, 298 K, 308 K, and 318 K in this study) can be obtained from the intercepts and the slopes of linear plots of $\log q_e$ vs $\log C_e$. The related parameters of the Freundlich isotherm model were calculated and the values are presented in Table 3.

3.6.3. Dubinin–Radushkevich (D-R) Model. The D-R isotherm model is an empirical adsorption model based on the consideration of multilayer character involving Van der Waals force, which is related to the physical adsorption process on heterogeneous surfaces. The model also presumes the adsorption on the microporous adsorbent and is applied for distinguishing between chemical and physical sorption processes. The model is expressed as follows:

$$\ln q_e = \ln q_s - K_{a\,d}\varepsilon^2, \tag{8}$$

where q_e (mg/g) is the amount of adsorbate in the adsorbent at equilibrium, q_s (mg/g) is the theoretical isotherm saturation capacity, K_{ad} (mol^2/kJ^2) is the activity coefficient related to the mean free energy or often called D-R constant, and ε is the Polanyi potential. The term Polanyi potential (ε) is expressed as follows [34]:

$$\varepsilon = RT\left(1 + 1/C_e\right), \tag{9}$$

where R (J/(mol·K)), T (K), and C_e (mg/L) signify gas constant, absolute temperature, and adsorbate concentration at equilibrium, respectively. From the resulting linear plot of $\ln q_e$ vs ε^2, the values of q_s and K_{ad} are determined from the intercept and slope, respectively (values are given in Table 3). However, the mean adsorption energy (E, kJ/mol) is a characteristic parameter, which defines the chemical or physical nature of the adsorption reaction. The value of E is calculated from the following equation:

$$E = \frac{1}{\sqrt{2K_{ad}}}. \tag{10}$$

The necessary parameters (E and K_{ad}) derived from the D-R isotherm model are tabulated in Table 3 along with the parameters obtained from Langmuir as well as Freundlich isotherm models. Results showed that the Langmuir isotherm model had a higher coefficient of determination (R^2) for all tested temperatures. This leads to the conclusion that the Langmuir model described the entire adsorption method better than the Dubinin–Radushkevich and Freundlich models. It is also evident that an elevated temperature was more favorable for the adsorption of nickel at the stated conditions. This indicates that the adsorption process is endothermic. The calculated E values from the D-R model are in the range of 1.5–1.8 kJ/mol, so it is physical adsorption [35].

Moreover, the adsorption capacity for the removal of nickel ions of the present biosorbent has been compared with that of several other biosorbents published in the literature, and the values of adsorption capacities are presented in Table 4. The extent of the sorption capacity of the present investigation is considerably high and very much comparable with the reported values.

Further analysis of the Langmuir isotherm was carried out to determine a dimensionless constant, which is known as the equilibrium parameter or separation factor (R_L) [41]. It indicates the favorability of the isotherm, and the separation factor is expressed as follows:

$$R_L = \frac{1}{1 + bC_i}, \tag{11}$$

where b (L/mg) and C_i (mg/L) are the equilibrium constant and the initial concentration of the adsorbate. Here, if the value of R_L stands between 0 and 1, this means the adsorption is favorable, and if R_L is greater than 1 ($R_L > 1$), this means the adsorption is unfavorable. In addition, $R_L = 1$ signifies a linear adsorption while $R_L = 0$ denotes an irreversible adsorption process [42]. Figure 7 shows a plot of R_L vs C_i, from which it is obvious that the R_L values remained between 0.061 and 0.823. Therefore, the adsorption of nickel by sawdust was termed as favorable at the studied conditions.

Safe disposal of biosorbent after adsorption of the metal ion is an issue to be considered very carefully. Although the cost estimation is not performed in the present study, it is envisaged that the disposal cost might be offset from the overall cost of the biosorption process because the spent biosorbent might be applied in other fields such as the production of building materials (e.g., cement), particle boards, and biogas [43].

3.7. Effect of Sorption Temperature and Subsequent Thermodynamic Study. The adsorption capacity of mahogany sawdust for nickel ions adsorption increases with the

Table 4: Comparison of adsorption capacities of different water material-based adsorbents for nickel ion adsorption.

Adsorbent material	Adsorption capacity (mg/g)	References
Treated mahogany sawdust	13.42	This investigation
Raw mahogany sawdust	5.35	This investigation
Banana peel	6.88	[36]
Orange peel	6.01	[36]
Pine sawdust	0.065	[37]
Rice husk	0.21–7.63	[38]
Aluminum impregnated fly ash	12.67	[39]
Coconut coir pith	24.39	[40]
Activated carbon/chitosan bead	108.7	[39]

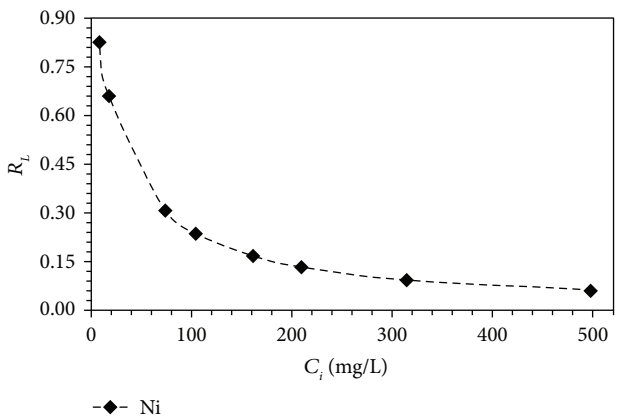

Figure 7: Separation factor of nickel adsorption by sawdust.

increase of sorption temperature. This trend might be explained by a chemical interaction between adsorbate and adsorbent through the movement of the adsorbing nickel ion species and/or enlargement of the pore size. These phenomena eventually enhance the rate of intraparticle diffusion of Ni (II) into the biosorbent pores [20].

Moreover, to assess the effect of temperature on the adsorption of Ni (II) onto mahogany sawdust, important thermodynamic parameters, which include standard Gibb's free energy (ΔG°), standard enthalpy change (ΔH°), and standard entropy change (ΔS°), were calculated using the following two thermodynamic equations [3, 25]:

$$\Delta G^0 = -RT \ln b, \tag{12}$$

$$\ln b = \frac{\Delta S^0}{R} + \frac{\Delta H^0}{RT}, \tag{13}$$

where R (J/(mol·K)) represents the ideal gas constant and T (K) and b (L/mg) represent the absolute temperature and equilibrium constant, respectively. The values of ΔH° and ΔS° were obtained from van't Hoff's plot (equation (10)) of $\ln b$ versus $1/T$ and are tabulated in Table 5. Gibb's free energy (ΔG°) of the adsorption process at all temperatures was found to be negative, which indicates that the sorption of Ni(II) was spontaneous [25]. This further signifies the feasibility of the adsorption reaction. The positive value of enthalpy change (ΔH°) indicates the endothermic nature of the adsorption process, which is substantiated by the increase in the sorption capacity with the temperature rise. The value of entropy change (ΔS°) was positive too, which indicates high randomness at the adsorbent-adsorbate interface during the adsorption of nickel ions on sawdust.

Table 5: Thermodynamic parameters for the adsorption of Ni (II) onto sawdust.

T (K)	ΔG° (kJ/mol)	ΔH° (kJ/mol)	ΔS° (kJ/(mol·K))
298	−6.434		
308	−6.763	2.865	0.0312
318	−7.057		

4. Conclusions

In this study, the mahogany sawdust, a locally available and cheap material, is applied as a biosorbent (after simple chemical treatment) for the removal of nickel ions (Ni (II)) from an aqueous solution. The kinetic studies specified that the equilibrium state in the adsorption of nickel ions on sawdust was reached in 120 min of contact between the adsorbate and adsorbent at a stirring speed of 200 rpm. In addition, based on the correlation coefficient value (R^2), it was found that adsorption kinetics fitted better in the pseudo-second-order model compared to the pseudo-first-order model. Multistage adsorption (external surface adsorption and intraparticle diffusion) was supposed to occur. Based on the sorption isotherm fitting analysis, the adsorption of Ni (II) on treated mahogany sawdust follows the Langmuir model, which indicates monolayer adsorption. The maximum sorption capacity was calculated to be 13.42 mg/g. Thermodynamic studies showed that higher sorption temperature was more favorable. The calculated values of thermodynamic parameters implied that the adsorption process was spontaneous and endothermic. In the end, considering the abundance, availability, and low cost of sawdust, along with the presented results, it can be concluded that the investigated biosorbent (mahogany sawdust) is suitable for and effective in removing nickel ions from aqueous solution.

Data Availability

All data generated through experiments and/or analyzed during this study are included in this article as well as in the Supplementary Materials.

Disclosure

This research was performed as part of the employment at Jashore University of Science and Technology.

Conflicts of Interest

The authors declare that they have no known competing financial interests or personal relationships that could have appeared to influence the work reported in this article.

Supplementary Materials

Figure S1: FTIR spectra of (i) raw sawdust, (ii) treated sawdust, and (iii) spent sawdust. Nickel removal from aqueous solution by chemically treated mahogany sawdust adsorbent is linked with functional groups present in the adsorbent. Figure S1 describes the absorbance spectra of raw sawdust, treated sawdust, and spent sawdust within the wavenumber range of 4000–400 cm^{-1}. The spectra were used to evaluate the rearrangement of chemical bonds as well as the change in structures of sawdust. It is observed from this figure that some wavenumbers slightly deviate after the adsorption process. This is the indication of nickel adsorption by the adsorbent through a metal-binding process. Figure S2: point of zero charge of chemically treated mahogany sawdust. The point of zero charge (pH_{pzc}) provides important information about the adsorbent surface charge, which might be helpful for understanding the adsorption mechanism. The pH_{pzc} can be defined as the pH at which the net charge of an adsorbent surface is zero. Figure S2 demonstrates the point of zero charge of the adsorbent (chemically treated mahogany sawdust). The pH_{pzc} was determined to be 6.8. It signifies that the adsorbent surface has positive charge at a solution pH less than pH_{pzc} and the surface is supposed to adsorb negatively charged anions. On the contrary, the adsorbent surface has negative charge at a solution pH higher than pH_{pzc}, and the adsorbent adsorbs positively charged cations. It is evident from experiments that nickel removal significantly increases at pH higher than the pH_{pzc}. . (*Supplementary Materials*)

References

[1] O. A. Oyewo, B. Mutesse, T. Y. Leswifi, and M. S. Onyango, "Highly efficient removal of nickel and cadmium from water using sawdust-derived cellulose nanocrystals," *Journal of Environmental Chemical Engineering*, vol. 7, no. 4, Article ID 103251, 2019.

[2] M. Rafatullah, O. Sulaiman, R. Hashim, and A. Ahmad, "Adsorption of copper (II), chromium (III), nickel (II) and lead (II) ions from aqueous solutions by meranti sawdust," *Journal of Hazardous Materials*, vol. 170, no. 2-3, pp. 969–977, 2009.

[3] Y. Wu, H. Luo, H. Wang, L. Zhang, P. Liu, and L. Feng, "Fast adsorption of nickel ions by porous graphene oxide/sawdust composite and reuse for phenol degradation from aqueous solutions," *Journal of Colloid and Interface Science*, vol. 436, pp. 90–98, 2014.

[4] M. A. Khan, A. A. Alqadami, M. Otero et al., "Heteroatom-doped magnetic hydrochar to remove post-transition and transition metals from water: synthesis, characterization, and adsorption studies," *Chemosphere*, vol. 218, pp. 1089–1099, 2019.

[5] A. Öztürk, T. Artan, and A. Ayar, "Biosorption of nickel (II) and copper (II) ions from aqueous solution by Streptomyces coelicolor A3(2)," *Colloids and Surfaces B: Biointerfaces*, vol. 34, no. 2, pp. 105–111, 2004.

[6] N. Sharma, K. Kaur, and S. Kaur, "Kinetic and equilibrium studies on the removal of Cd2+ ions from water using polyacrylamide grafted rice (Oryza sativa) husk and (Tectona grandis) saw dust," *Journal of Hazardous Materials*, vol. 163, no. 2-3, pp. 1338–1344, 2009.

[7] S. A. Maddodi, H. A. Alalwan, A. H. Alminshid, and M. N. Abbas, "Isotherm and computational fluid dynamics analysis of nickel ion adsorption from aqueous solution using activated carbon," *South African Journal of Chemical Engineering*, vol. 32, pp. 5–12, 2020.

[8] D. Bulgariu and L. Bulgariu, "Equilibrium and kinetics studies of heavy metal ions biosorption on green algae waste biomass," *Bioresource Technology*, vol. 103, no. 1, pp. 489–493, 2012.

[9] A. A. Alqadami, M. A. Khan, M. R. Siddiqui, and Z. A. Alothman, "Development of citric anhydride anchored mesoporous MOF through post synthesis modification to sequester potentially toxic lead (II) from water," *Microporous and Mesoporous Materials*, vol. 261, pp. 198–206, 2018.

[10] S. Rengaraj, C. K. Joo, Y. Kim, and J. Yi, "Kinetics of removal of chromium from water and electronic process wastewater by ion exchange resins: 1200H, 1500H and IRN97H," *Journal of Hazardous Materials*, vol. 102, no. 2–3, pp. 257–275, 2003.

[11] V. Hasija, P. Raizada, P. Singh et al., "Progress on the photocatalytic reduction of hexavalent Cr (VI) using engineered graphitic carbon nitride," *Process Safety and Environmental Protection*, vol. 152, pp. 663–678, 2021.

[12] Y. C. Sharma, B. Singh, A. Agrawal, and C. H. Weng, "Removal of chromium by riverbed sand from water and wastewater: effect of important parameters," *Journal of Hazardous Materials*, vol. 151, no. 2-3, pp. 789–793, 2008.

[13] A. Hariharan, V. Harini, S. Sandhya, and S. Rangabhashiyam, "Waste Musa acuminata residue as a potential biosorbent for the removal of hexavalent chromium from synthetic wastewater," *Biomass Conversion and Biorefinery*, 2020.

[14] B. K. Biswas, K. Inoue, K. N. Ghimire, H. Kawakita, K. Ohto, and H. Harada, "Effective removal of arsenic with lanthanum (III)- and cerium (III)-loaded orange waste gels," *Separation Science and Technology*, vol. 43, no. 8, pp. 2144–2165, 2008.

[15] M. Tsuji, ""SeO32−selective properties of inorganic materials synthesized by the soft chemical process," *Solid State Ionics*, vol. 151, no. 1–4, pp. 385–392, 2002.

[16] R. Chand, T. Watari, K. Inoue, T. Torikai, and M. Yada, "Evaluation of wheat straw and barley straw carbon for Cr (VI) adsorption," *Separation and Purification Technology*, vol. 65, no. 3, pp. 331–336, 2009.

[17] C. Raj Adhikari, D. Parajuli, H. Kawakita, K. Inoue, K. Ohto, and D. Fujiwara, "Adsorption behavior of iminodiacetic acid type of chelating gel prepared from waste paper," *Separation Science and Technology*, vol. 42, no. 3, pp. 579–590, 2007.

[18] A. Das, N. Bar, and S. K. Das, "Pb (II) adsorption from aqueous solution by nutshells, green adsorbent: adsorption studies, regeneration studies, scale-up design, its effect on biological indicator and MLR modeling," *Journal of Colloid and Interface Science*, vol. 580, pp. 245–255, 2020.

[19] A. Witek-Krowiak, "Application of beech sawdust for removal of heavy metals from water: biosorption and desorption

studies," *European Journal of Wood and Wood Products*, vol. 71, no. 2, pp. 227–236, 2013.

[20] M. H. Kalavathy and L. R. Miranda, "Comparison of copper adsorption from aqueous solution using modified and unmodified Hevea brasiliensis saw dust," *Desalination*, vol. 255, no. 1-3, pp. 165–174, 2010.

[21] V. K. Garg, R. Gupta, A. Bala Yadav, and R. Kumar, "Dye removal from aqueous solution by adsorption on treated sawdust," *Bioresource Technology*, vol. 89, no. 2, pp. 121–124, 2003.

[22] S. R. Khan, A. Inayat, and A. Rana, "Sorption of reactive and acid dyes from aqueous solutions onto sawdust," *Bangladesh Journal of Scientific & Industrial Research*, vol. 45, no. 1, pp. 35–38, 2010.

[23] A. Shukla, Y. H. Zhang, P. Dubey, J. L. Margrave, and S. S. Shukla, "The role of sawdust in the removal of unwanted materials from water," *Journal of Hazardous Materials*, vol. 95, no. 1–2, pp. 137–152, 2002.

[24] T. K. Naiya, P. Chowdhury, A. K. Bhattacharya, and S. K. Das, "Saw dust and neem bark as low-cost natural biosorbent for adsorptive removal of Zn(II) and Cd(II) ions from aqueous solutions," *Chemical Engineering Journal*, vol. 148, no. 1, pp. 68–79, 2009.

[25] J. Long, X. Huang, X. Fan, Y. Peng, and J. Xia, "Effective adsorption of nickel (II) with Ulva lactuca dried biomass: isotherms, kinetics and mechanisms," *Water Science and Technology*, vol. 78, no. 1, pp. 156–164, 2018.

[26] Z. A. Alothman, A. H. Bahkali, M. A. Khiyami et al., "Low cost biosorbents from fungi for heavy metals removal from wastewater," *Separation Science and Technology*, vol. 55, no. 10, pp. 1766–1775, 2020.

[27] L. Gonsalvesh, S. P. Marinov, G. Gryglewicz, R. Carleer, and J. Yperman, "Preparation, characterization and application of polystyrene based activated carbons for Ni(II) removal from aqueous solution," *Fuel Processing Technology*, vol. 149, pp. 75–85, 2016.

[28] K. Anoop Krishnan, K. G. Sreejalekshmi, and R. S. Baiju, "Nickel(II) adsorption onto biomass based activated carbon obtained from sugarcane bagasse pith," *Bioresource Technology*, vol. 102, no. 22, pp. 10239–10247, 2011.

[29] N. Ünlü and M. Ersoz, "Adsorption characteristics of heavy metal ions onto a low cost biopolymeric sorbent from aqueous solutions," *Journal of Hazardous Materials*, vol. 136, no. 2, pp. 272–280, 2006.

[30] Y. S. Ho and G. McKay, "Sorption of dye from aqueous solution by peat," *Chemical Engineering Journal*, vol. 70, no. 2, pp. 115–124, 1998.

[31] C. Pang, Y.-H. Liu, X.-H. Cao et al., "Biosorption of uranium(VI) from aqueous solution by dead fungal biomass of Penicillium citrinum," *Chemical Engineering Journal*, vol. 170, no. 1, pp. 1–6, 2011.

[32] S. Gupta, S. K. Sharma, and A. Kumar, "Biosorption of Ni(II) ions from aqueous solution using modified Aloe barbadensis Miller leaf powder," *Water Science and Engineering*, vol. 12, no. 1, pp. 27–36, 2019.

[33] S. Parvin, B. K. Biswas, M. A. Rahman, M. H. Rahman, M. S. Anik, and M. R. Uddin, "Study on adsorption of Congo red onto chemically modified egg shell membrane," *Chemosphere*, vol. 236, Article ID 124326, 2019.

[34] D. A.O, A. P. Olalekan, A. M. Olatunya, and O. Dada, "Langmuir, Freundlich, temkin and dubinin-radushkevich isotherms studies of equilibrium sorption of Zn 2+ unto phosphoric acid modified rice husk," *IOSR Journal of Applied Chemistry*, vol. 3, no. 1, pp. 38–45, 2012.

[35] E. Çalışkan and S. Göktürk, "Adsorption characteristics of sulfamethoxazole and metronidazole on activated carbon," *Separation Science and Technology*, vol. 45, no. 2, pp. 244–255, 2010.

[36] G. Annadurai, R. S. Juang, and D. J. Lee, "Adsorption of heavy metals from water using banana and orange peels," *Water Science and Technology*, vol. 47, no. 1, pp. 185–190, 2003.

[37] K. Moodley, R. Singh, E. Musapatika, M. Onyango, and A. Ochieng, "Removal of nickel from wastewater using an agricultural adsorbent," *WaterSA*, vol. 37, no. 1, 2011.

[38] M. Bansal, D. Singh, V. K. Garg, and P. Rose, "Use of agricultural waste for the removal of nickel ions from aqueous solutions: equilibrium and kinetics studies," *International Journal of Civil and Environmental Engineering*, vol. 3, no. 3, 2009.

[39] N. Chaudhary and C. Balomajumder, "Optimization study of adsorption parameters for removal of phenol on aluminum impregnated fly ash using response surface methodology," *Journal of the Taiwan Institute of Chemical Engineers*, vol. 45, no. 3, pp. 852–859, 2014.

[40] S. Ratan, I. Singh, J. Sarkar, and N. RM, "The removal of nickel from waste water by modified coconut coir pith," *Chemical Sciences Journal*, vol. 7, no. 3, 2016.

[41] T. W. Weber and R. K. Chakravorti, "Pore and solid diffusion models for fixed-bed adsorbers," *AIChE Journal*, vol. 20, no. 2, pp. 228–238, 1974.

[42] M. Arami, N. Yousefi Limaee, and N. M. Mahmoodi, "Investigation on the adsorption capability of egg shell membrane towards model textile dyes," *Chemosphere*, vol. 65, no. 11, pp. 1999–2008, 2006.

[43] A. Adewuyi, "Chemically modified biosorbents and their role in the removal of emerging pharmaceutical waste in the water system," *Water*, vol. 12, no. 6, pp. 1551–1631, 2020.

Hindawi
Journal of Chemistry
Volume 2021, Article ID 2451836, 12 pages
https://doi.org/10.1155/2021/2451836

Research Article

Polyaniline Supported Ag-Doped ZnO Nanocomposite: Synthesis, Characterization, and Kinetics Study for Photocatalytic Degradation of Malachite Green

Fikradis Habtamu,[1] Sintayehu Berhanu ,[2] and Teshome Mender[2]

[1]*Department of Chemistry, Wollega University, Nekemte P.O. Box: 395, Nekemte, Ethiopia*
[2]*Department of Chemistry, Bonga University, P.O. Box 334, Bonga, Ethiopia*

Correspondence should be addressed to Sintayehu Berhanu; sintayehuberhanu38@gmail.com

Received 15 June 2021; Accepted 20 August 2021; Published 8 September 2021

Academic Editor: Ibrahim H. Alsohaimi

Ag-ZnO/PANI nanocomposite was prepared via the sol-gel technique following in situ oxidative polymerization of polyaniline (PANI). XRD, UV-Vis, and FT-IR spectroscopy were employed to study the crystal size, bandgap energy, and bond structure of as-synthesized nanocomposites. The mean crystallite size of the nanocomposite determined from XRD was 35.68 nm. Photocatalytic degradation of malachite green (MG) dye using as-synthesized photocatalysts was studied under visible light irradiation. The highest degradation efficiency was recorded for Ag-ZnO/PANI nanocomposites (98.58%) than Ag-ZnO nanoparticles (88.23%) in 120 min. The kinetics of photocatalytic degradation of MG follows pseudo-first-order reaction with rate order of 1.16 10^{-2} min^{-1}. Moreover, the photocatalytic activity of Ag-ZnO/PANI nanocomposites was evaluated and compared with Ce-Cd oxide, electrospun P(3HB)-TiO2, and with other catalysts in the literature. The optimal conditions for photocatalytic degradation are as follows: the concentration of malachite green (0.2 g/l), pH (8), and the concentration of catalyst load (0.2 g/l) under visible light with an irradiation time of 120 min.

1. Introduction

Malachite green (MG) is an organic compound that has arisen as a dubious agent in hydroponics in aquaculture, and it is utilized as a dyestuff for coloring materials such as cotton silk, paper, wool, and leather [1]. It is strongly dissolvable in water and ethanol to form blue-green solutions. Dye-contaminated wastewaters mostly enter the environment as discharges, and their release into the environment in processing wastewater poses a serious risk to both human health and the ecosystem [2–8]. MG has strong effects on the immune and reproductive systems and exhibits potential carcinogenic and genotoxic effects [9]. There are a range of methodologies, such as physical (adsorption), biodegradation, chemical, and electrochemical techniques, that have been developed to eliminate these pollutants from wastewater. However, they are nondestructive, since they just transfer organic compounds from water to another phase, thus causing secondary pollution.

Heterogeneous semiconductor photocatalysis is the most extensively read technique for the degradation and decolorization of numerous wastes in the watery medium under UV-Visible light [10, 11]. It takes out defilements as opposed to just moving them to another stage without the usage of possibly hazardous oxidants [12]. Photocatalysis is started by photons from UV light, which cause the electrons on the superficial of the photocatalyst to become excited in the valance band; these cause the electrons to go up into the conduction band and then leave positive openings [13]. The produced electron/hole pair incites a complex arrangement of reactions that can bring about the total degradation of

organic contaminants, for example, a dye adsorbed on the semiconductor surface [14, 15].

In such a manner, the use of photocatalysis gives off an impression of being a really engaging methodology for the decomposition of poisonous mixtures (toxic compounds) to nonhazardous products [2–8, 16–18].

ZnO is a significant semiconductor material with a wide bandgap (3.37 eV) and enormous excitation binding energy (60 eV), effective nonlinear resistance, and better thermal conductivity [19, 20]. ZnO has a few limitations including the quick recombination rate of photogenerated electron-hole pairs, low quantum yield in the photocatalytic reaction in aqueous solution, and photocorrosion which impede the commercialization of the photocatalytic degradation process.

Even if various modification techniques are reported in the literature, neither metal nor nonmetal doping alone can solve the above problems; there is still a dearth of knowledge on metal-nonmetal codoping. Reports related to Cr-N codoped ZnO, Cr-doped ZnO, or N-doped ZnO are well documented [21, 22].

Conducting polymers (CPs) are appreciably used as adsorbents for the removal of heavy metal ions or dyes from waste water and have attracted great attention due to facile synthesis, electrical conductivity, porosity and low fabrication cost, and environmental stability. Among the conductive polymers (CPs), polyaniline (PANI) was picked as one of the promising conductive polymers to tune composites' optical, electrical, and photocatalyst properties [23]. However, it possessed poor life span owing to the fragile backbone chain. There for synthesizing PANI/ZnO composite photocatalysts has benefits of the capacity to prevent corrosion dissolution of ZnO during photocatalysis as well as the capacity to empower photocatalysis under solar irradiation due to a decreased bandgap [24].

There are earlier reports on the improvement of the electronic properties and catalytic potential of ZnO by introducing noble metals such as silver, gold, platinum, and palladium [25, 26]. Among these, silver merits exceptional consideration due to its stability, conductivity, nontoxic nature, and comparatively less expensive. The incorporation of Ag-doped ZnO nanoparticles in the polymer matrix upgrades the mechanical properties and conductivity of polymer composite [27, 28]. Doping factor is another parameter to amplify the conducting properties of the inorganic filler. Subsequently, in the present study, Ag-ZnO/PANI composites have synthesized via the chemical oxidative in situ polymerization process of metal nanoparticles with the monomer unit.

To the best of our knowledge, there is no study in the literature that investigates the reaction kinetics of photocatalytic degradation of malachite green using polyaniline/Ag-ZnO nanocomposite to improve optical and photocatalytic performance. Thus, this research was deliberated to synthesize the photocatalysts by incorporating Ag and PANI comodified ZnO nanoparticles and discovering the optical properties and kinetics of the photocatalytic activity under visible light irradiation for the degradation and decolorization of MG dye.

2. Experimental

2.1. Materials. All chemicals were analytical grade (Sigma-Aldrich) and used as received without further purification: Zn(II) acetate dehydrate ($ZnC_4H_6O_4$, MW: 183.48 g/mol), silver nitrate ($AgNO_3$, MW: 169.87 g/mol), oxalic acid ($C_2H_2O_4$, MW: 90.03 g/mol), sulphuric acid (H_2SO_4, MW: 98 g/mol), sodium hydroxide (NaOH, MW: 40 g/mol), aniline ($C_6H_5NH_2$, MW: 93.13 g/mol), HCl (MW 36.46 g/mol), ethanol (C_2H_5OH MW 46.07 g/mol), ammonium per sulfate $(NH_4)_2S_2O_8$ MW 228.18 g/mol), and malachite green ($C_{23}H_{25}N_2$, MW: 364.911 g/mol). The structural formula for MG is given in Figure 1).

2.2. Synthesis of Photocatalyst

2.2.1. Synthesis of Ag-Doped ZnO Nanoparticle. Silver-doped zinc oxide (Ag-doped ZnO) nanoparticles were prepared by a sol-gel method [29]. About 50 mmol of Zn(II) acetate dehydrate was dissolved in ethanol (100 ml), and the solution was stirred for 30 min.

Oxalic acid dehydrate (2.51 g) was dissolved in ethanol (40 ml), and the solution was added slowly with constant stirring to the above Zn(II) acetate dehydrate solution. After the addition of oxalic acid, a white sol was formed, and the stirring was continued for three hours. To this, 2 wt% of silver nitrate ($AgNO_3$) was added and stirred for a further three hours. Sol was dried on a waterbath to form xerogel.

The xerogel was then calcined at 500°C in a muffle furnace at a heating rate of 5°C/min and held at this temperature for 120 min. Then, it was grinded by using the mortar and pestle. The powder was kept in the desiccator at room temperature.

2.2.2. Synthesis of Ag-ZnO/PANI Nanocomposite. 1 g of Ag-doped ZnO nanoparticles was added into 100 ml of 1 M H_2SO_4. 1 ml of aniline was added drop wise to the solution and stirred for 30 min until a silvery white color was formed. A solution of 2 g of ammonium per sulfate (APS) oxidant in 100 ml H_2SO_4 solution was added in drop wise under a refrigerator and stirred for 30 min. The solution was changed into dark green color confirming the formation of Ag-ZnO/PANI hybrid. It was kept at room temperature for 24 hrs. On the next day, the solution was filtered and washed with distilled water until the filtrate becomes colorless. The precipitated material was filtered and dried in a vacuum oven at 80°c for 6 hours [30].

2.2.3. Characterization of As-Synthesized Photocatalysts. X-ray diffraction patterns were obtained using a BRUKER D8 (West Germany and equipped with Cu Kα radiation ($\lambda = 1.5405$ Å) at room temperature in the scan range 2θ between 10 and 90°. Accelerating voltage and the applied current were 40 kV and 30 mA, respectively. The absorbance of the photocatalysts was recorded by the Sanyo UV-Vis spectrophotometer model (SP65, UK). 0.2 g of the photocatalyst was dissolved in 100 ml of deionized water. The absorbance was measured using a quartz tube with a scanning range of 400–800 nm. Fourier transform infrared (FT-IR) spectroscopy was used in the region between 4000 and 400 cm^{-1} to

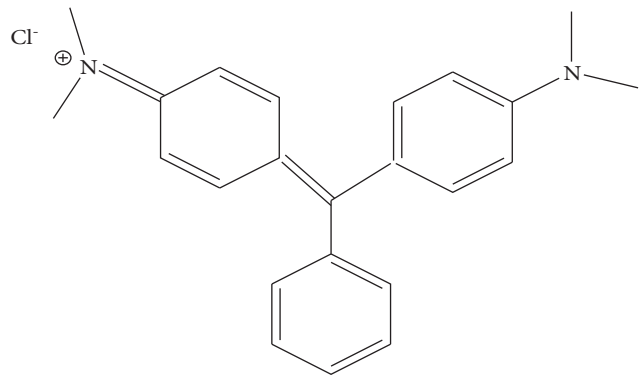

Figure 1: Structural formula of MG ($C_{23}H_{25}N_2Cl$).

determine the functional groups and surface structure of the samples using a model of Shimadzu 8400S (German). About 5–10 mg of photocatalyst powder was mixed with a drop of paraffin and sandwiched between two KBr plates to measure the wave number.

2.2.4. Photocatalytic Activity. Catalytic activities of the synthesized photocatalysts were studied for the degradation of malachite green (MG) under dark and visible light. 0.02 g of MG was dissolved in 500 ml (at pH = 8 and $T = 25^{\circ}$c) of deionized water and MG solution was prepared. 0.2 g of Ag-doped ZnO nanoparticles and Ag-ZnO/PANI nanocomposite samples were dispersed in 100 ml of MG solution separately and stirred for 30 min in the dark to establish the adsorption-desorption equilibrium of dye with the catalyst. NaOH was used to adjust the pH value of the solution. Then, the reaction was carried out for 120 min because no further degradation was observed after that. The photocatalytic degradation was assessed by recording the absorbance values at definite time intervals. Percentage degradation of MG dye was calculated using the following formula:

$$\%\text{ of degradation} = \frac{C_o - C_t}{C_o} \times 100, \quad (1)$$

where C_t is the concentration of dye at time t and C_o is the concentration of dye at initial stage.

2.3. Effect of Operational Parameters on the Activities of Photocatalyst

2.3.1. Initial Concentration of Malachite Green and pH. Effect of initial concentration of MG on its degradation was observed by taking the difference dye initial concentrations 0.1–0.5 g/L and fixing other parameters constant. And the effect of pH was also investigated by taking the pH range from 6 to 10 keeping other parameters constant (photocatalyst load = 0.2 g, pH = 8).

2.3.2. Catalyst Load. The effect of catalyst load was observed by taking the difference amount of Ag-ZnO and PANI-Ag-ZnO nanocomposites (0.1–0.4 g) at constant dye concentration (0.2 g/L) and constant pH 8. The relation between the percent degradation of MG with irradiation time was studied over the reaction time 20–120 min, using a fixed concentration of dye (50 mg/L), catalyst load (0.2 g/L), and pH 8.

2.3.3. Kinetic Studies of Photocatalytic Degradation of MG. The kinetics of the photocatalytic degradation of MG solutions was investigated using optimized photocatalyst load, dye initial concentration, and pH at ultraviolet and visible irradiations.

3. Results and Discussion

3.1. X-Ray Diffraction Analysis. The average crystallite size (d) was calculated from the XRD pattern according to the Scherrer equation [31]:

$$d = \frac{k\lambda}{\beta cos\theta}, \quad (2)$$

where k is a constant (about 0.9), λ is the wavelength (0.15405 nm), β is the full width at half maximum (FWHM) of the diffraction line, and θ is the diffraction angle. The XRD patterns of Ag-doped ZnO nanoparticles showed the crystalline peaks at diffraction angles $2\theta = 31.79$, 34.44, 36.27, 47.55, 62.87, 67.97, and 69.11° for the diffraction plane from (100), (002), (101), (102), (110), (103), (112), and (201), respectively, and XRD result shows the typical peak patterns of Ag-ZnO nanoparticles were wurtzite structure (Figure 2(a)). The peaks at $2\theta = 38.12$, 38.53, 64.45, and 77.40° which correspond to the reflection planes of (111), (200), (120), and (311), respectively, show the characteristics of metallic silver [25, 32].

The average crystal grain size of Ag-doped ZnO nanoparticles was at the reflecting peaks of $2\theta = 36.27$, 38.12, and 31.79°. Thus, the average size of the nanoparticle becomes 35.68 nm. From the XRD pattern of Ag-ZnO/PANI composites, it can be seen that the crystalline peaks of the nanoparticles at $2\theta = 38.06$, 44.23, 64.36, and 77.4° correspond to the reflection of (111), (200), (220), and (311), respectively (Figure 2(b)). It was observed that PANI has a broad amorphous nature, and the diffraction peak is located at $2\theta = 25.42^{\circ}$. The average crystal grain size of the composite materials calculated at $2\theta = 38.06$, 44.23, and 64.36° is chosen to determine the average diameter; the average size of the nanoparticle is 31.52 nm. The change in the intensity or broadness of the nanocomposite is due to the strong interfacial interaction between nanoparticles and the polymer matrix.

3.2. UV-Vis Absorption Spectra. UV/Vis absorption spectra of the as-synthesized photocatalysts Ag-ZnO, PANI, and Ag-ZnO/PANI are shown in Figure 3. The bandgap of the catalyst directly influenced the photocatalytic activity in this way that the direct absorption of bandgap photons would lead to the generation of electron-hole pairs within the catalysts; subsequently; the charge carriers started to difuse to the surface of the catalysts.

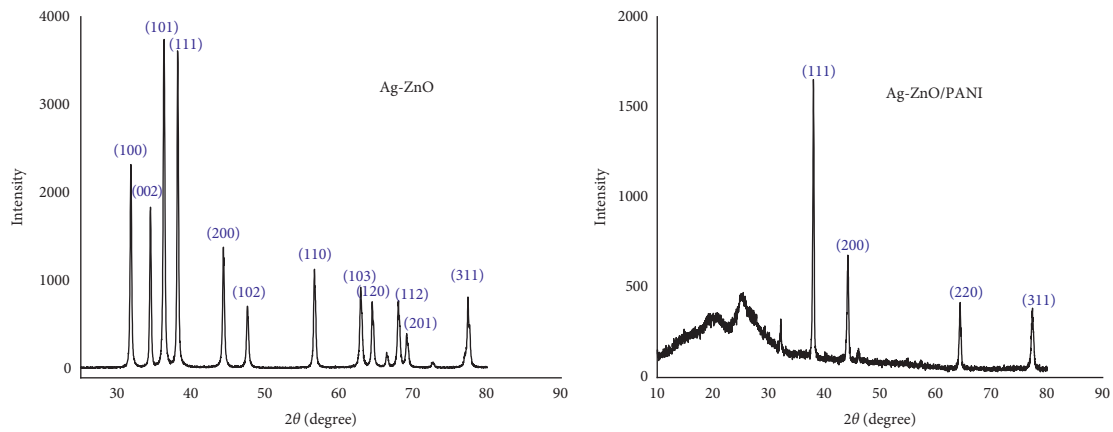

Figure 2: XRD pattern of Ag-ZnO nanoparticle (a) and Ag-ZnO/PANI nanocomposite (b).

This could be due to the bandgap narrowing resulting from the creation of dopant energy levels below the conduction band [33]. The wavelengths of the absorption edges in the UV-Vis spectra were determined by plotting a vertical line from the apex of the curve which is given in Table 1, and the energies are calculated using the following Debye–Scherer's equation

$$E_g\,(\mathrm{eV}) = \frac{1240}{\lambda_{\max}}. \tag{3}$$

The delocalized metal electron of Ag 3d state accounts for narrowing bandgap energy of Ag-ZnO nanoparticles from 3.2 eV to 2.87 eV. Ag-doped ZnO has also showed a red shift compared to the bare ZnO nanoparticles by transferring electrons from the conduction band of ZnO to the conduction band of metal 4d states. Addition codoping of PANI enhances further shift in wavelength to large wavelength of 474 nm and narrowing the bandgap to 2.61 eV of former Ag-ZnO/PANI photocatalysts.

However, some holes are also created in the VB of PANI due to electron transfer from VB of PANI to VB of Ag/ZnO, as the VB of PANI (3.25 eV) is at higher energy than the VB of Ag/ZnO (2.87 eV). The transferred electrons will neutralize some holes in the VB of Ag/ZnO. In this way, a certain fraction of the holes in the VB and electrons in the CB of PANI get separated, reducing the chance of recombination and thereby enhancing the chance of photocatalytic activity. This is the advantage of using a coupled system [33, 34]. Further reduction in the bandgap of the Ag-ZnO/PANI might be due to the synergetic effect of the two dopants Ag and PANI that control the crystal size and enhance the photo harvesting of nanocomposites.

3.3. FT-IR Analysis. Ag-doped ZnO shows a peak at the wavenumber from 3400 to 3452 cm^{-1}. The peak at 3442 cm^{-1} is attributable to the HO^- stretching vibration of water and an O-H group on the surface of the photocatalyst. The strong absorption peak centered at 508 cm^{-1} is the metallic stretch assigned to the Ag-doped ZnO.

The symmetric and asymmetric bending modes of C-O bonds were in 1636 cm^{-1}. There were some bands that originated from the presence of water moisture and carbon dioxide in the air in the process of making the pellet (Figure 4(a)). The FT-IR spectrum of Ag-ZnO/PANI shows a strong peak of Ag-doped ZnO at 609 cm^{-1}.

The absorption band of PANI has occurred at 1126 cm^{-1}. The peak associated with the N-H, C-H, and C-N stretching vibrations is located at 3442, 2932, and 1470 cm^{-1}, respectively. The spectrum at 1293 and 801 cm^{-1} corresponds to the C-N in plane deformation and = CH in plane vibration (Figure 4(b)) of PANI. Thus, from the FT-IR spectra, it is confirmed that the nanoparticles are well inserted into the macromolecular chain of PANI, and aniline monomers are successfully polymerized on the surface of Ag-doped ZnO nanoparticles.

3.4. Photodegradation of Malachite Green under Visible Irradiation. The photodegradation of malachite green dye was performed for a total of 2 hours under visible light irradiation as shown in Figure 5. The absorption band intensities of the dyes decrease, and this indicated that the dyes have been degraded completely by the photocatalysts. Ag-ZnO/PANI nanocomposite showed the highest photoactivity (98.58%) compared with Ag-ZnO (88.23%). The pronounced enhancement of the photocatalytic activity of the Ag-ZnO/PANI nanocomposites may be attributed to their having more than one path to form electron-hole pairs because of the existence of different interfaces, and the electron-hole recombination prevented to the maximum extent in such system.

The experiments were also realized in dark conditions to understand the effect of the light source when the catalyst material was added into the dyes. As a result, no significant changes were observed in the absorption spectrum of the dyes. Remarkable degradation was observed in visible light.

3.5. Effect of Operational Parameters on Activities of Photocatalyst

3.5.1. Initial Concentration of Malachite Green. The effect of the initial concentration of MG on its degradation was observed by taking different initial concentrations from

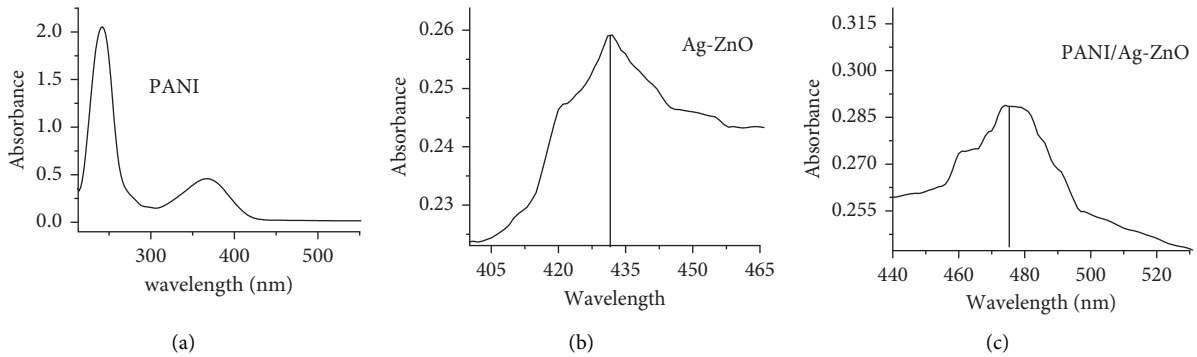

Figure 3: UV-Visible spectra of PANI (a), Ag/ZnO (b), and Ag-ZnO/PANI nanocomposites (c).

Table 1: Absorbance, maximum wavelength, and optical bandgap energy of Ag-ZnO and Ag-ZnO/PANI.

Sample photocatalysts	Absorbance	Maximum wavelength (nm)	Band gap energy (eV)
PANI	0.423	382	3.25
Ag-ZnO	0.2424	432	2.87
Ag-ZnO/PANI	0.2985	474	2.61

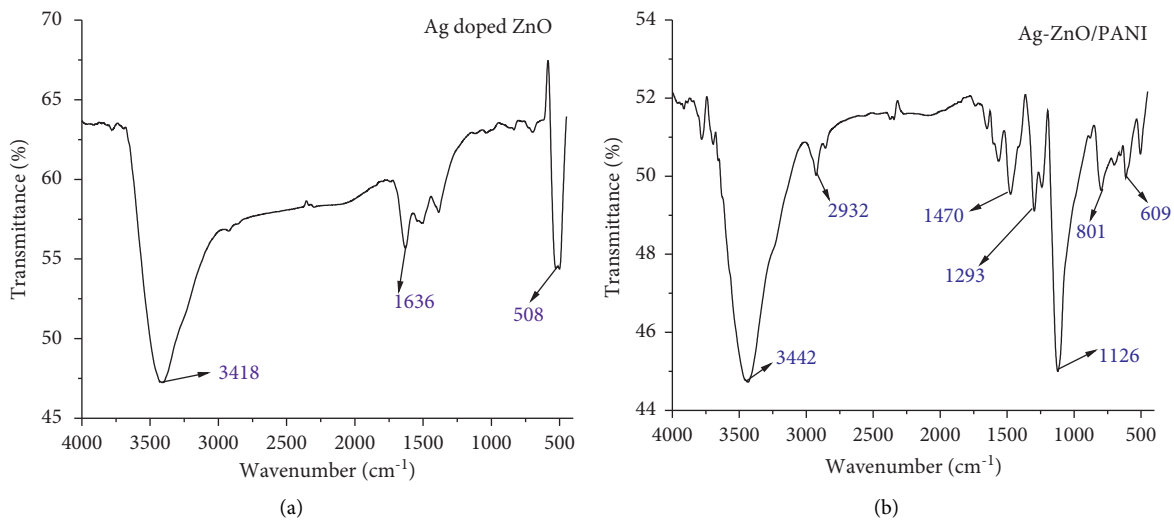

Figure 4: FT-IR spectra of (a) Ag-ZnO nanoparticle and (b) Ag-ZnO/PANI nanocomposite.

0.1 g/L to 0.5 g/L and fixing other parameters constant (photocatalyst load 1 mg/L, pH = 8) (Table 2). The degradation efficiency of MG was increased with an increase in dye concentration up to 0.2 g/L (Figure 6).

Increasing excess dye concentration leads to covering the active sites of the photocatalysts by the dye, and the path length of the photons entering the solution is decreased, resulting in only a few photons reaching the catalyst surface.

Hence, the productions of hydroxyl radicals are reduced. Therefore, the degradation efficiency is reduced [35]. It shows that more dye molecules are adsorbed on the active sites of the photocatalysts. The decrease in degradation above 0.2 g/L may be due to the competition of adsorption between dye molecules and dissolved O_2 on the catalyst surface.

3.5.2. Catalyst Load. The effect of the photocatalyst loading on the decolorization rate of the dyes was examined by varying the photocatalyst concentration from 0.1 g/L to 0.4 g/L of the dye solution as shown in Figure 7 at constant dye concentration and constant pH 8.

The degradation of MG initially increases with increase in photocatalyst load from 0.1 g/L to 0.2 g/L. However, further increase of the catalyst load from 0.2 g/L to 0.4 g/L results in decrease of the degradation of dye. The increase in percent degradation at 0.2 g/L is due to the increase in the number of active sites of the photocatalysts. The decrease can be explained by the excess photocatalyst particles that can create a light screening effect that reduces the surface area that is exposed to light illumination and the photocatalytic efficiency [36].

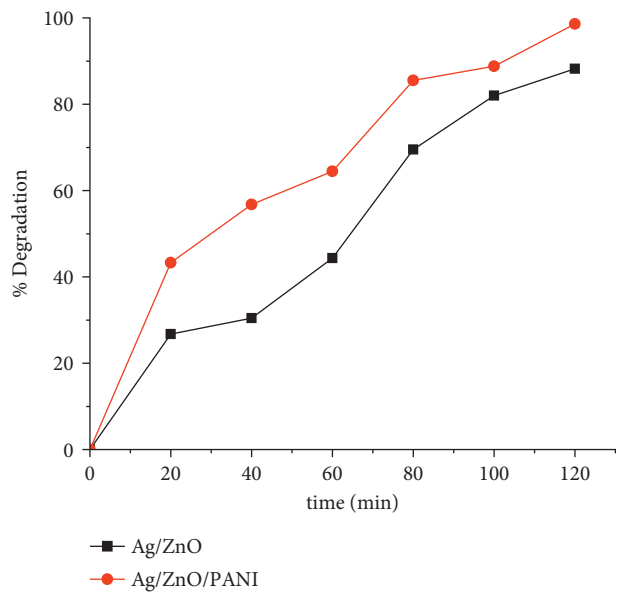

Figure 5: Photocatalytic degradation of MG at different irradiation time.

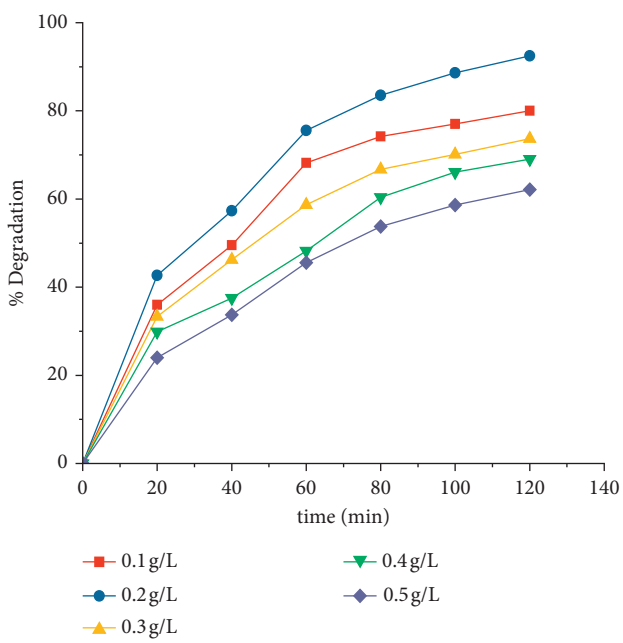

Figure 6: Effect of initial concentration on the degradation of MG.

3.6. pH. pH affects the surface charge properties, size of photocatalyst aggregates, and the position of conductance. The effect of pH on the photocatalytic degradation of MG was investigated by taking the pH range from 6 to 10, keeping other parameters constant.

The photocatalyst exhibited a maximum rate of degradation (98.58%) at pH = 8 in 120 min (Figure 8). Therefore, at alkaline pH, the number of hydroxyl groups of the photocatalyst was increased, which facilitates the adsorption of MG. The probable reason for the difference in pH can be the adsorption of MG onto the catalyst surface depending on its surface area [37].

3.7. Effect of Irradiation Time. The relation between the percent degradation of MG with irradiation time was studied over reaction time from 20 to 120 min, using a fixed concentration of dye (50 mg/L), catalyst load (1 mg/L), and pH of 8.

It was observed that at 120 min, the dye was completely degraded and becomes colorless. This is due to the fast adsorption rate before the equilibrium is reached; this may be explained by an increased availability in the number of active binding sites on the photocatalyst surface. At the equilibrium stage, the adsorption is likely an attachment-controlled process due to less available sorption sites (Figure 9).

Table 2: Percent degradation of malachite green under dark and solar irradiation with different initial concentrations of nanocomposite and the relation between time and ln (c/c_0).

	Initial concentration (g/l) of Ag-ZnO/PANI					ln (c/c_0)		% of degradation	
Time (min)	0.1	0.2	0.3	0.4	0.5	Ag-ZnO	Ag-ZnO/PANI	Ag-ZnO	Ag-ZnO/PANI
0	0	0	0	0	0	0	0	0	0
20	36.01	42.68	33.34	29.88	24.012	0.3465	0.2328	26.73	43.28
40	49.54	57.34	46.23	37.54	33.72	0.6318	0.4331	38.46	56.75
60	68.20	75.57	58.69	48.21	45.54	1.0181	0.7149	44.33	64.44
80	72.21	83.54	66.73	60.39	53.74	1.3417	0.9224	69.53	85.54
100	74.05	88.65	70.13	68.12	58.61	1.6111	1.1586	81.98	88.78
120	77.52	92.48	73.71	70.03	62.12	1.8782	1.3948	88.23	98.58

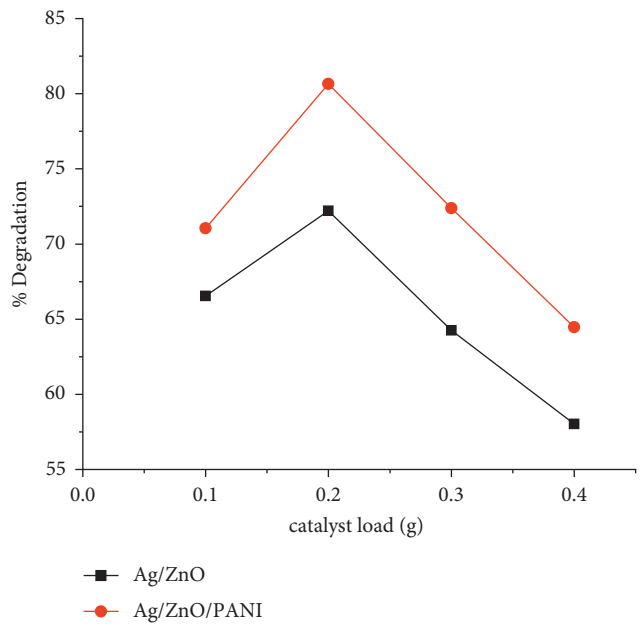

Figure 7: Effect of catalyst load on the degradation of MG dye.

3.8. Kinetics of Photocatalytic Degradation of Malachite Green. The kinetic study of the degradation of MG was determined by using different initial concentrations of MG from 0.1 to 0.5 g/L. The photocatalytic activity of the synthesized nanocomposites under visible light can be evaluated by comparing the apparent rate constants [17, 38] using the following Langmuir–Hinshelwood equation.

$$ln\left(\frac{c}{c_o}\right) = K_{\text{app}}.t, \tag{4}$$

where c_o and c are the initial and final absorbance of MG, and K_{app} is the apparent rate constant.

It can be seen that the photocatalytic activity of Ag-ZnO/PANI nanocomposites under visible light irradiation is higher than Ag-doped ZnO nanoparticles. Figure 10 shows the relationship between time and the degradation rate ($\ln(c_0/c)$) of MG for visible light illumination. The regression correlation coefficient (R^2) is found to be 0.9972 for Ag-doped ZnO nanoparticles and 0.9991 for Ag-ZnO/PANI nanocomposite. From the plot, the K_{app} value for Ag-ZnO nanoparticle and Ag/ZnO/PANI nanocomposite is $1.56 \times 10^{-2}\,\text{min}^{-1}$ and $1.16 \times 10^{-2}\,\text{min}^{-1}$, respectively. The kinetics curve was pseudo-first-order with respect to Ag-doped ZnO and Ag/ZnO/PANI nanocomposites.

The proposed mechanism is presented schematically in Figure 11 according to Pham et al., 2020, described in detail as follows [18]. The MG dye adsorbed onto the full photocatalyst. The possible photocatalytic mechanism involves the following steps:

$$\begin{aligned}
\text{PANI} &\xrightarrow{\text{hv}} (\text{h}^+_{\text{VB}} + \text{e}^-_{\text{CB}})\,\text{PANI},\\
\text{Ag/ZnO} &\xrightarrow{\text{hv}} (\text{h}^+_{\text{VB}} + \text{e}^-_{\text{CB}})\text{Ag} - \text{ZnO},\\
\text{Dye} &\xrightarrow{\text{hv}} \text{dye}^*,\\
\text{Dye}^* + (\text{h}^+_{\text{VB}})\text{PANI/Ag} - \text{ZnO} &\xrightarrow{\text{hv}} \text{dye}^+,\\
\text{O}^-_2 + \text{H}_2\text{O} + (\text{h}^+_{\text{VB}})\,\text{PANI/Ag} - \text{ZnO}\,\text{H}_2\text{O}_2 &\\
\text{H}_2\text{O}_2 &\longrightarrow 2\,\text{HO}^{\cdot}.
\end{aligned} \tag{5}$$

The holes present in the VB of Ag/ZnO react with H_2O to form H_2O_2 which leads to the formation of hydroxyl radicals (•OH). It is a powerful oxidant which decomposes effectively

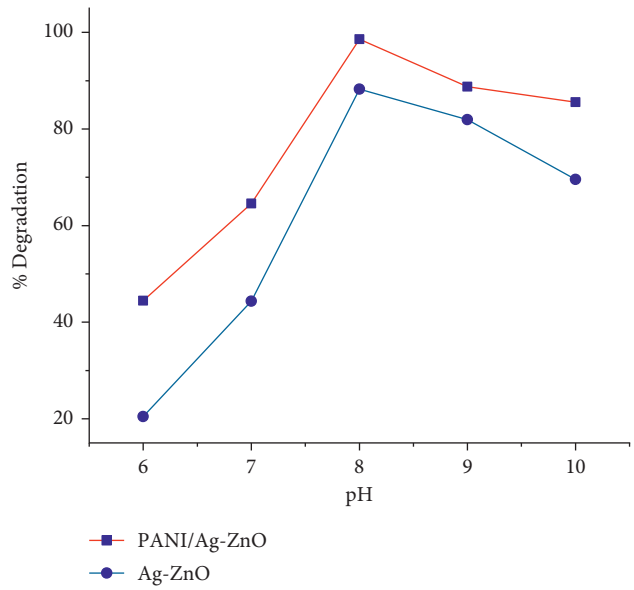

Figure 8: Effect of pH of the solution on the degradation of MG dye.

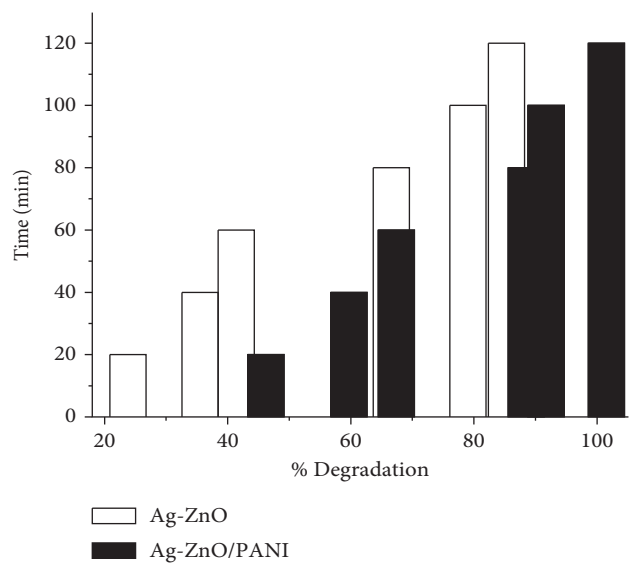

Figure 9: Effect of irradiation time on photocatalytic degradation of MG using Ag-ZnO and PANI/Ag-ZnO.

the malachite green into a nontoxic degraded product (such as water and carbon dioxide).

$$^{\cdot}OH + Dye^{+} \longrightarrow H_2O + CO_2 \text{ (colourless)}. \quad (6)$$

The role of PANI is clearly observed in movement and reduction of the carrier recombination due to the existence of linking doped ZnO particles and successive reduction of the surface resistivity of the entire photocatalyst to the photodegradation of MG.

Table 3 provides a short comparison of MG degradation efficiency by different authors using different catalysts through the photocatalytic activity. It could be observed that the degradation efficiency under simulated solar light irradiation by xenon lamp of the PANI/Ag-ZnO was much higher than those of Fe^{3+}/H_2O_2, electrospun P(3HB)-TiO_2, Ce-Cd oxide, TiO_2, and ZnO and CA/TiO_2 bio-nanocomposites, and the degradation rate of MG on PANI/Ag-ZnO nanocomposite was also faster.

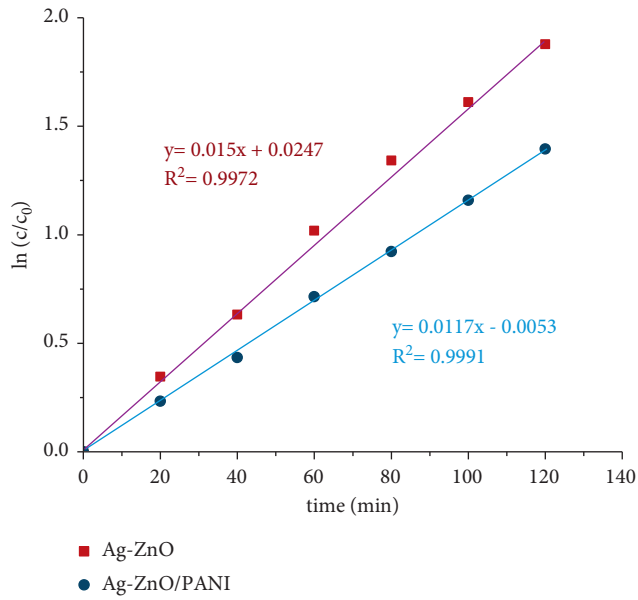

Figure 10: Pseudo-first-order kinetics of photocatalytic degradation of MG dye.

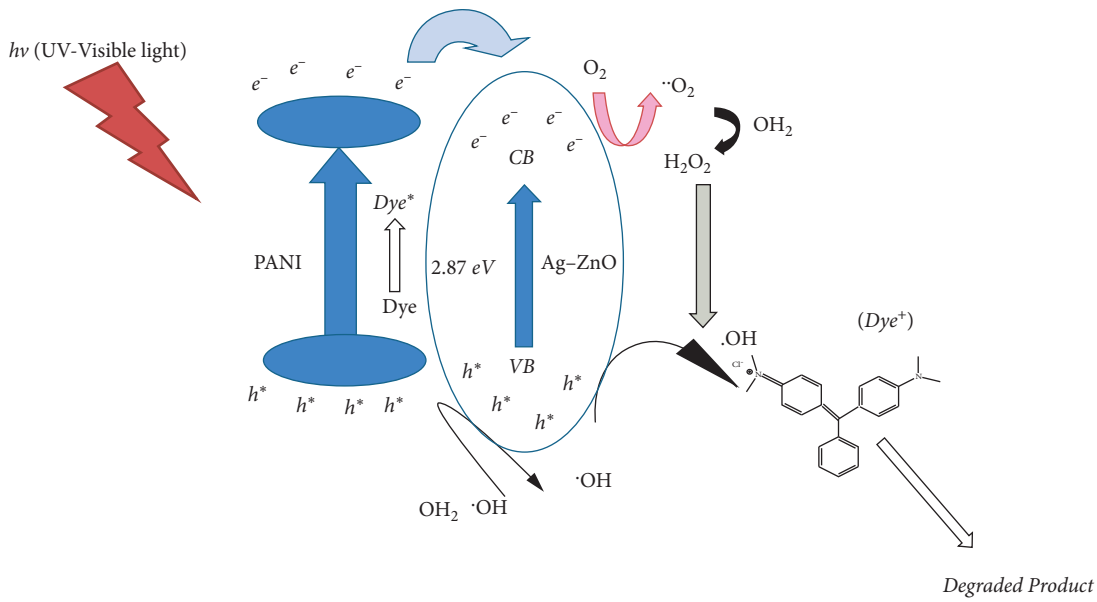

Figure 11: Diagrammatic illustration of the mechanism for MG dyes degradation using the optimized photocatalyst composite by attaching PANI to Ag-doped ZnO nanoparticles.

Table 3: Comparison of polyaniline/Ag-ZnO nanocomposite for degradation of MG by various catalysts.

Catalyst	Reaction condition	Degradation efficiency	Reference
Fe^{3+}/H_2O_2 (fenton-like oxidation)	$(MG) = 3 \times 10^{-5}$ M, $(Fe^{3+}) = 1.0 \times 10^{-3}$ M, $(H_2O_2) = 5 \times 10^{-2}$ M, pH = 3. Under visible light irradiation.	95% of MG in 120 min	[2]
Electrospun P (3HB)-TiO_2	4 g of TiO_2 in 100 mL of 4 w/v% P(3HB). Under UV light illumination	98% of MG with in less than 2h	[3]
Nanosized Ce-Cd oxide	$(MG) = 2.50 \times 10^{-5}$ M; pH = 8.0 with light intensity 600 Wm^{-2}; and catalyst loading 0.03 g/50 mL.	-	[4]
Bi_2WO_6	$(Bi_2WO_6) = 1.0$ g·L^{-1}; (MG)= 10 mg L^{-1}; pH = 2 under visible light illumination.	The degradation efficiency 98.9% in 30 min	[5]
Microbial consortium CM-4	pH = 7.5 at with UV light; no correlation between the percentage of decolorization and COD removal.	99% within 2 h	[6]
TiO_2 and ZnO nanoparticles	UV lamp (200–600 nm).	TiO_2 (49.35%) and ZnO (23.31%.)	[7]
CA/TiO_2 bio-nanocomposites	(MG) = 10 ppm, pH = 7 using visible light.	99.5% in 240 min	[8]
Polyaniline/Ag-ZnO nanocomposite	Catalyst load = 0.2 g, pH = 8 initial concentration of MG = 0.2 g/l, and irradiation time = 120 min using visible light with light intensity 120 Wm^{-2}.	98.58 with 120 min	This work

Therefore, the nanocomposite is likely a decent and environment friendly catalyst in the removal of MG from contaminated (polluted) water.

4. Conclusions

PANI/Ag-ZnO nanocomposite was successfully synthesized in situ chemical oxidative polymerization. The FT-IR result proved the strong interfacial interaction between the metal oxide nanoparticles and polar segments of the PANI chain. The XRD results showed that the amorphous nature of PANI got reduced with an increase in the content of metal oxide nanoparticles. The nanoparticle is 35.68 nm, whereas the nanocomposite is 31.52 nm. Ag-ZnO has a bandgap of 2.87 eV (432 nm) and the PANI/Ag-ZnO nanocomposite has 2.61 eV (474 nm). The photocatalytic activity of the MG was investigated, and a photocatalytic oxidation mechanism was proposed. Ag-ZnO and PANI/Ag/ZnO degrade the MG dye 88.23% and 98.58%, respectively. The highest photocatalytic activity of Ag-ZnO/PANI nanocomposites over ZnO photocatalysts was qualified due to dopants, low rate of recombination of the photogenerated electrons-holes, as well as its lower crystal size and bandgap energy.

Adding PANI to the Ag-doped ZnO leads to extra benefits in both surface textures with a high surface area and a simple electron transfer process. The optimal conditions for photocatalytic degradation of malachite green are as follows: the concentration of malachite green is 0.2 g/l, at pH of 8, and the concentration of catalyst load is 0.2 g/l under visible light illumination for 120 min. The kinetics of photocatalysis (PANI/Ag-ZnO) is a pseudo-first-order reaction with a positive slope and rate constant of 1.6×10^{-2} min^{-1}. Our PANI-supported Ag-ZnO is predictable to be a promising applicant for environmental claims. The prevalent performance for various dye photodegradations and recycling abilities with a similar presentation is profoundly anticipated.

Data Availability

No data were used to support this study.

Conflicts of Interest

The authors declare that there are no conflicts of interest.

Acknowledgments

The authors are grateful for the financial support provided by the Ministry of Science and Higher Education of Ethiopia.

References

[1] D. Robati, M. Rajabi, O. Moradi et al., "Kinetics and thermodynamics of malachite green dye adsorption from aqueous solutions on graphene oxide and reduced graphene oxide," *Journal of Molecular Liquids*, vol. 214, pp. 259–263, 2016.

[2] S. Hashemian, "Fenton-like oxidation of Malachite green solutions: kinetic and thermodynamic study," *Journal of Chemistry*, vol. 2013, Article ID 809318, 7 pages, 2013.

[3] N. Sridewi, Y. F. Lee, and K. Sudesh, "Simultaneous adsorption and photocatalytic degradation of malachite green using electrospun P (3HB)-TiO2 nanocomposite fibers and films," *International Journal of Photoenergy*, vol. 2011, Article ID 597854, 11 pages, 2011.

[4] K. L. Ameta, N. Papnai, and R. Ameta, "Synthesis, characterization, and use of novel bimetal oxide catalyst for photoassisted degradation of malachite green dye," *Journal of Materials*, vol. 2014, Article ID 480107, 5 pages, 2014.

[5] A. Karimi, M. Aghbolaghy, A. Khataee, and S. Shoa Bargh, "Use of enzymatic bio-Fenton as a new approach in decolorization of malachite green," *Science World Journal*, vol. 2012, Article ID 691569, 5 pages, 2012.

[6] J. Cheriaa, M. Khaireddine, M. Rouabhia, and A. Bakhrouf, "Removal of triphenylmethane dyes by bacterial consortium," *The Scientific World Journal*, vol. 2012, Article ID 512454, 9 pages, 2012.

[7] A. K. Singh and U. T. Nakate, "Photocatalytic properties of microwave-synthesized TiO2 and ZnO nanoparticles using malachite green dye," *Journal of Nanoparticles*, vol. 2013, Article ID 310809, 7 pages, 2013.

[8] M. Bahal, N. Kaur, N. Sharotri, and D. Sud, "Investigations on amphoteric chitosan/TiO2 bionanocomposites for application in visible light induced photocatalytic degradation," *Advances in Polymer Technology*, vol. 2019, Article ID 2345631, 9 pages, 2019.

[9] E. S. Baeissa, "Photocatalytic degradation of malachite green dye using Au/NaNbO3 nanoparticles," *Journal of Alloys and Compounds*, vol. 672, pp. 564–570, 2016.

[10] M. Chen, C. Bao, T. Cun, and Q. Huang, "One-pot synthesis of ZnO/oligoaniline nanocomposites with improved removal of organic dyes in water: effect of adsorption on photocatalytic degradation," *Materials Research Bulletin*, vol. 95, pp. 459–467, 2017.

[11] A. Pfitzner, S. Dankesreiter, A. Eisenhofer, and M. Cherevatskaya, "12 Heterogeneous semiconductor photocatalysis," in *Chemical Photocatalysis*, pp. 211–246, De Gruyter, Berlin, Germany, 2013.

[12] H. Zangeneh, A. A. L. Zinatizadeh, M. Habibi, M. Akia, and M. Hasnain Isa, "Photocatalytic oxidation of organic dyes and pollutants in wastewater using different modified titanium dioxides: a comparative review," *Journal of Industrial and Engineering Chemistry*, vol. 26, pp. 1–36, 2015.

[13] C. Byrne, G. Subramanian, and S. C. Pillai, "Recent advances in photocatalysis for environmental applications," *Journal of Environmental Chemical Engineering*, vol. 6, no. 3, pp. 3531–3555, 2018.

[14] T. Welderfael, M. Pattabi, R. M. Pattabi, and A. K. Thilipan, "Photocatalytic activity of Ag-N co-doped ZnO nanorods under visible and solar light irradiations for MB degradation," *Journal of Water Process Engineering*, vol. 14, pp. 117–123, 2016.

[15] K. Soutsas, V. Karayannis, I. Poulios et al., "Decolorization and degradation of reactive azo dyes via heterogeneous photocatalytic processes," *Desalination*, vol. 250, no. 1, pp. 345–350, 2010.

[16] D. Chatterjee and S. Dasgupta, "Visible light induced photocatalytic degradation of organic pollutants," *Journal of Photochemistry and Photobiology C: Photochemistry Reviews*, vol. 6, no. 2-3, pp. 186–205, 2005.

[17] G. Sharma, Z. A. ALOthman, A. Kumar, S. Sharma, S. K. Ponnusamy, and M. Naushad, "Fabrication and characterization of a nanocomposite hydrogel for combined photocatalytic degradation of a mixture of malachite green and fast green dye," *Nanotechnology for Environmental Engineering*, vol. 2, no. 1, p. 4, 2017.

[18] T. A. T. Pham, V. A. Tran, V. D. Le et al., "Facile preparation of ZnO nanoparticles and Ag/ZnO nanocomposite and their photocatalytic activities under visible light," *International Journal of Photoenergy*, vol. 2020, Article ID 8897667, 14 pages, 2020.

[19] M. T. Ramesan and K. Suhailath, "Role of nanoparticles on polymer composites," in *Micro and Nano Fibrillar Composites (MFCs and NFCs) from Polymer Blends*, pp. 301–326, Woodhead Publishing, Amsterdam, Netherlands, 2017.

[20] H. Sun, X. Feng, S. Wang, H. M. Ang, and M. O. Tadé, "Combination of adsorption, photochemical and photocatalytic degradation of phenol solution over supported zinc oxide: effects of support and sulphate oxidant," *Chemical Engineering Journal*, vol. 170, no. 1, pp. 270–277, 2011.

[21] S. Colis, H. Bieber, S. Begin-Colin, G. Schmerber, C. Leuvrey, and A. Dinia, "Magnetic properties of Co-doped ZnO diluted magnetic semiconductors prepared by low-temperature mechanosynthesis," *Chemical Physics Letters*, vol. 422, no. 4-6, pp. 529–533, 2006.

[22] B. M. Rajbongshi, A. Ramchiary, and S. Samdarshi, "Influence of N-doping on photocatalytic activity of ZnO nanoparticles under visible light irradiation," *Materials Letters*, vol. 134, pp. 111–114, 2014.

[23] K. Namsheer and C. S. Rout, "Conducting polymers: a comprehensive review on recent advances in synthesis, properties and applications," *RSC Advances*, vol. 11, no. 10, pp. 5659–5697, 2021.

[24] O.-G. Vanja, P. Violeta, P.-B. Marijana et al., "Physical properties and biocompatibility of nanostructural biomaterials based on active calcium silicate systems and hydroxyapatite," in *Dental Applications of Nanotechnology*, pp. 247–271, Springer, Cham, Switzerland, 2018.

[25] D. Li and H. Haneda, "Morphologies of zinc oxide particles and their effects on photocatalysis," *Chemosphere*, vol. 51, no. 2, pp. 129–137, 2003.

[26] T. K. Pathak, H. C. Swart, and R. E. Kroon, "Structural and plasmonic properties of noble metal doped ZnO nanomaterials," *Physica B: Condensed Matter*, vol. 535, pp. 114–118, 2018.

[27] B. Bethi, S. H. Sonawane, B. A. Bhanvase, and S. P. Gumfekar, "Nanomaterials-based advanced oxidation processes for wastewater treatment: a review," *Chemical Engineering and Processing - Process Intensification*, vol. 109, pp. 178–189, 2016.

[28] B. L. Martínez-Vargas, S. M. Durón-Torres, D. Bahena, J. L. Rodríguez-López, J. M. Peralta-Hernández, and A. Picos, "One-pot synthesis of ZnO-Ag and ZnO-Co nanohybrid materials for photocatalytic applications," *Journal of Physics and Chemistry of Solids*, vol. 135, Article ID 109120, 2019.

[29] T. Chitradevi, A. Jestin Lenus, and N. Victor Jaya, "Structure, morphology and luminescence properties of sol-gel method synthesized pure and Ag-doped ZnO nanoparticles," *Materials Research Express*, vol. 7, no. 1, Article ID 015011, 2019.

[30] M. F. Nsib, S. Saafi, A. Rayes, N. Moussa, and A. Houas, "Enhanced photocatalytic performance of Ni-ZnO/Polyaniline composite for the visible-light driven hydrogen generation," *Journal of the Energy Institute*, vol. 89, no. 4, pp. 694–703, 2016.

[31] A. Monshi, M. R. Foroughi, and M. R. Monshi, "Modified Scherrer equation to estimate more accurately nano-crystallite size using XRD," *World Journal of Nano Science and Engineering*, vol. 2, no. 3, pp. 154–160, 2012.

[32] K. Takahashi and T. Morizumi, "Growth of InAs whiskers in wurtzite structure," *Japanese Journal of Applied Physics*, vol. 5, no. 8, pp. 657–662, 1966.

[33] J. Luan and Z. Hu, "Synthesis, property characterization, and photocatalytic activity of novel visible light-responsive photocatalyst," *International Journal of Photoenergy*, vol. 2012, Article ID 301954, 11 pages, 2012.

[34] S. Kuriakose, V. Choudhary, B. Satpati, and S. Mohapatra, "Facile synthesis of Ag-ZnO hybrid nanospindles for highly efficient photocatalytic degradation of methyl orange," *Physical Chemistry Chemical Physics*, vol. 16, no. 33, pp. 17560–17568, 2014.

[35] A. Khataee, R. D. C. Soltani, A. Karimi, and S. W. Joo, "Sonocatalytic degradation of a textile dye over Gd-doped ZnO nanoparticles synthesized through sonochemical process," *Ultrasonics Sonochemistry*, vol. 23, pp. 219–230, 2015.

[36] B. Neppolian, H. C. Choi, S. Sakthivel, B. Arabindoo, and V. Murugesan, "Solar/UV-induced photocatalytic degradation of three commercial textile dyes," *Journal of Hazardous Materials*, vol. 89, no. 2-3, pp. 303–317, 2002.

[37] R. Saleh and N. F. Djaja, "Transition-metal-doped ZnO nanoparticles: synthesis, characterization and photocatalytic activity under UV light," *Spectrochimica Acta Part A: Molecular and Biomolecular Spectroscopy*, vol. 130, pp. 581–590, 2014.

[38] C. G. da Silva and J. L. Faria, "Photochemical and photocatalytic degradation of an azo dye in aqueous solution by UV irradiation," *Journal of Photochemistry and Photobiology A: Chemistry*, vol. 155, no. 1-3, pp. 133–143, 2003.

Hindawi
Journal of Chemistry
Volume 2021, Article ID 9535644, 11 pages
https://doi.org/10.1155/2021/9535644

Research Article

Removal of Congo Red by Silver Carp (*Hypophthalmichthys molitrix*) Fish Bone Powder: Kinetics, Equilibrium, and Thermodynamic Study

Shahanaz Parvin, Md. Manjur Hussain, Farhana Akter, and Biplob Kumar Biswas

Department of Chemical Engineering, Jashore University of Science and Technology, Jashore 7408, Bangladesh

Correspondence should be addressed to Biplob Kumar Biswas; bk.biswas@just.edu.bd

Received 1 July 2021; Accepted 30 August 2021; Published 7 September 2021

Academic Editor: Ibrahim H. Alsohaimi

Powdered form of bones of silver carp fish, an available species in Bangladesh, was investigated as a prominent bioadsorbent for the removal of Congo red from synthetic solution. Experiments were conducted in batch process, and a number of influencing parameters, such as solution pH, adsorbent dosage, contact time, and initial Congo red concentration, were thoroughly investigated for optimization. Kinetic and equilibrium data were well described by pseudo-second-order model and Langmuir isotherm, respectively. Suitability of pseudo-second-order model to best fit with the adsorption process was corroborated by squared sum of errors analysis. Mass transfer mechanism was confirmed by intraparticle pore diffusion and Bangham's diffusion models. Maximum sorption capacity of fish bone powder was found to be 666.67 $mg{\cdot}g^{-1}$. The optimum condition (adsorbent dose: 5 $g{\cdot}L^{-1}$; pH: 2.0; operating time: 4 h) for maximum sorption was determined as well. The increasing negative value of Gibbs free energy (ΔG) with temperature rise indicated spontaneous nature and feasibility of adsorption. The positive values of ΔH and ΔS suggested that the adsorption reaction is endothermic and random (at the solid/liquid interface) in nature. The activation energy (29.84 $kJ{\cdot}mol^{-1}$) indicated that the sorption process was of physisorption type. A considerably high adsorption capacity pointed towards utilization of this apparently useless biomaterial as an effective adsorbent.

1. Introduction

Industries, such as textile, leather, pulp and paper, cotton, paint, plastic, and cosmetics, use dyes to color their products and thus consume substantially a large volume of synthetic dye as well as process water for their production. As a result, they produce a considerable amount of colored wastewater. The textile industry consumes more than ten thousand tonnes of dye per annum out of which approximately one hundred tonnes of dye are discharged annually into the water stream [1]. Although dye-containing effluent contains aesthetic contaminants, it has negative impact on overall aquatic inhabitants through reduction in phytoplankton photosynthesis [2, 3]. Toxicity, contamination by color, nonbiodegradability, and complex structure of dye can cause enormous threat to human health and the aquatic environment as a whole [4]. Several classes of dyes are reported in the literature that include anionic dyes (e.g., all sort of direct dye, acid dye, and reactive dye), cationic dyes (all basic dyes), and nonionic dye (e.g., dispersed dyes) [5].

Congo red (CR) is known to be an anionic benzidine-based diazo synthetic dye, which is characterized by large molecular structure with two azo groups that are bound to aromatic rings having recalcitrant molecular structure [6]. The effluent from the above-mentioned industries, if not treated properly, can cause severe damage to aquatic habitants. Moreover, Congo red is responsible for causing cancer to mammals. However, it is a challenging task to biodegrade Congo red due to the stability of its structure [1]. Hence, effective removal of this dye form wastewaters has to be performed before discharging into the water bodies.

Removal of dyes from water and wastewater can be done by means of any of the methods, namely, biological, chemical, and physical methods. Several wastewater

treatment techniques have been reported to treat dyes from wastewaters, which include but not limited to, biological degradation [7], membrane separation [8], electrolysis [9], and oxidation [10]. These methods are having limitations such as high cost of plant, higher operational costs, interference by another constituents, and excessive sludge generation. Adsorption, on the other hand, is a much better process for contaminants removal from wastewater because of the availability of adsorbents, efficiency of the process, uncomplicated operation, and low-cost of the adsorbent. Some conventional adsorbents were used for treating the dye-containing wastewater that includes ash, nanomaterials, and activated carbon. Nowadays biomaterials and agricultural waste materials (such as pine bark, orange peel, peanut shell, sawdust, and sunflower) are getting more priority from the researchers throughout the world [11–13]. In this context, adsorption of CR by using waste biomaterials would have been a promising process in the field of wastewater treatment.

Numerous investigations have been conducted by using various bioadsorbents in the view to remove Congo red from industrial wastewater [14]. Parvin et al. reported considerably high adsorption capacity of chemically treated eggshell membrane (117.65 $mg{\cdot}g^{-1}$) for Congo red removal through adsorption [15]. Rejected tea and tea dust, on the other hand, were reported to be effective adsorbents in case of methylene blue (MB) dye removal with high adsorption capacity of 242.11 $mg{\cdot}g^{-1}$ and 175.4 $mg{\cdot}g^{-1}$, respectively [16,17]. Ghanizadeh and Asgari conducted an experiment for the quest of MB removal by using cattle and sheep bone charcoal as adsorbent where a maximum sorption capacity was found to be 5 $mg{\cdot}g^{-1}$ [18]. Furthermore, a different study was conducted for the removal of methylene blue dye from the wastewater using NaOH modified fish bone charcoal as adsorbent where the extent of sorption capacity was reported to be 605.82 ± 9.09 $mg{\cdot}g^{-1}$ [19]. Although different bioadsorbents were reported to be used in wastewater treatment, bone of silver carp fish, in particular, as an adsorbent in Congo red removal from simulated effluent has not been reported to the best of our knowledge. Silver carp is a very common and locally available fish in Bangladesh. Although different income groups of the country have different levels of fish consumptions, more than 50% of consumption of fish belongs to carp species that includes silver carp with few other species [20]. Huge consumption of silver carp fish generates a considerable number of bones as environmental waste. So, the conversion of this waste to potential adsorbent for dye removal from aqueous solution would be a promising technique to keep environment clean [21].

The aim of this research was to develop an adsorbent from bone of silver carp fish (*Hypophthalmichthys molitrix*) through some simple steps and to find out the potentiality of this adsorbent in removing Congo red from synthetic aqueous solution. In this regard, the influence of several essential operating parameters (e.g., solution pH, dosages of adsorbent, initial concentration of adsorbate, and contact time) on Congo red removal using fish bone powder (FBP) adsorbent was investigated. In addition, adsorption kinetics and equilibrium were analyzed by applying mathematical models to elucidate a plausible adsorption mechanism.

2. Materials and Methods

2.1. Adsorbent Preparation. The fish bone of silver carp (*Hypophthalmichthys molitrix)* was collected from a local fish market (Jashore, Bangladesh). The bones were separated from the fish meat, and the separated fish bones were washed with hot distilled water (343 K) for quite a few times. After that, the washed fish bones were dried under 423 K for 40 min using a drier (DGH-9030) and then cooled down to room temperature. The dried bones were pulverized by using a locally fabricated ball mill, and a particle size of 60 to 100 mesh was taken. The powdered form of fish bone was kept in an airtight container for conducting adsorption studies [19].

2.2. Adsorbate. Congo red (chemical formula: $C_{32}H_{22}N_6Na_2O_6S_2$; molar mass: 696.664 $g{\cdot}mol^{-1}$; $\lambda_{max} = 500$ nm), an anionic dye, was used in this study as an adsorbate. As-received analytical grade Congo red (Merck, Germany) was used in this study. A synthetic stock solution of 1000 $mg{\cdot}L^{-1}$ was prepared by dissolving a required amount of Congo red into a certain amount of distilled water. Varying concentration of Congo red dye solution was prepared by diluting synthetic stock solution of Congo red with distilled water.

2.3. Sample Characterization. Solution pH was measured over the range of 2–8 by a pH meter. Concentrations of dye were measured by a double beam ultraviolet-visible (UV-VIS) spectrophotometer (SHIMADZU UV-1800) at its characteristic wavelength. The functional group of FBP before and after adsorption experiment were determined from infrared (IR) spectra, which were recorded by Perkin Elmer (Spectrum 100) Fourier Transform Infrared (FTIR) spectrophotometer, with a wavelength range of 4,000 cm^{-1} to 400 cm^{-1}.

2.4. Batch Adsorption Study. Batchwise adsorption experiments were conducted to investigate the influence of different parameters, that is, pH (2 to 8), adsorbent dosage (100 mg to 700 mg), contact time (0 to 240 min), and initial dye concentration (50~300 $mg{\cdot}L^{-1}$) on the adsorptive removal of CR. At a certain concentration, measured amount of Congo red solution (100 mL) was taken with a specific amount of FBP in a 250 mL Erlenmeyer flask. The initial pH of each solution was properly adjusted by adding either 0.1 M hydrochloric acid (HCl) or 0.1 M sodium hydroxide (NaOH). Proper mixing of the solutions was done by using a continuous stirrer with a constant speed of 150 rpm and at 303 K for each experiment (unless otherwise stated). After a certain time of stirring, the samples were taken out of the shaker and then filtered. The filtrates were taken for their absorbance measurement. However, removal percentage (% R) of CR dye and the equilibrium amount of dye adsorption ($mg{\cdot}g^{-1}$) was determined by utilizing the following equations [21]:

$$\%R = \frac{C_0 - C_e}{C_0} \times 100, \quad (1)$$

$$q_e = \frac{C_0 - C_e}{w} \times v, \quad (2)$$

where the symbols C_0 and C_e are defined as the initial and final concentration of the Congo red solution (mg·L^{-1}), respectively, q_e is denoted as the amount of Congo red adsorbed (mg·g^{-1}), w is symbolized as the weight of FBP adsorbent, and v is termed as the solution quantity in liter (L).

2.5. Kinetics Study. To analyze the CR adsorption mechanism onto FBP, the adsorption kinetics were investigated by using both Lagergren's pseudo-first-order equation (equation (3)) and pseudo-second-order rate equation (equation (4)). The equations can be expressed as follows [21]:

$$\ln(q_e - q_t) = \ln q_e - k_1 t, \quad (3)$$

$$\frac{t}{q_t} = \frac{1}{k_2 q_e^2} + \frac{t}{q_e}, \quad (4)$$

where q_e and q_t are symbolized as the adsorption capacity (mg·g^{-1}) at equilibrium and that at time t (min), respectively, while k_1 (min^{-1}) and k_2 (g·mg^{-1}·min^{-1}) are termed as the reaction rate constant for Lagergren's pseudo-first-order model and pseudo-second-order model, respectively.

In order to examine the inherent mechanism of the Congo red adsorption onto FBP, the intraparticle diffusion model, as well as Bangham's equation, was also investigated. Intraparticle diffusion can be well explained according to Weber–Morris model, which is expressed as follows [22]:

$$q_t = k_{i\,d} t^{(1/2)} + I, \quad (5)$$

where q_t is denoted as the amount of CR dye adsorbed per an unit mass of FBP adsorbent (mg·g^{-1}) at time t and k_{id} is termed as the rate constant for intraparticle diffusion model (mg·g^{-1}·min$^{-1/2}$).

On the other hand, Bangham's pore diffusion model can be equated as follows [23,24]:

$$\log\left[\log\left(\frac{C_0}{C_0 - q_t \cdot m}\right)\right] = \log\left(\frac{k_0 \cdot m}{2.303 \cdot v}\right) + \sigma \cdot \log t, \quad (6)$$

where m (g·L^{-1}) is adsorbent concentration and k_0 and σ are constants (often called Bangham's parameters), while C_0, q_t, and v possess their usual meaning as stated earlier in this article.

2.6. Isotherm Study. To explain the equilibrium distribution of dye particles onto the surfaces of FBP, the three most common adsorption isotherm models were studied. In this study, the Langmuir isotherm, the Freundlich isotherm, and the Temkin isotherm models were analyzed, which were mentioned correspondingly in the following equations [25]:

$$\frac{C_e}{q_e} = \frac{1}{bq_m} + \frac{C_e}{q_m}, \quad (7)$$

$$\log q_e = \log k_F + \frac{1}{n} \log C_e, \quad (8)$$

$$q_e = B\ln K_T + B\ln C_e, \quad (9)$$

where C_e (mg·L^{-1}) signifies the equilibrium adsorbate (CR) concentration, while q_e (mg·g^{-1}) and q_m (mg·g^{-1}) indicate the equilibrium sorption capacity and the maximum capacity of sorption of the adsorbent, respectively, b (L·mg^{-1}) indicates the Langmuir adsorption constant related to free energy of adsorption, k_F (mg·g^{-1}) designates the adsorption capacity at unit concentration, $1/n$ denotes the adsorption intensity, K_T signifies the Temkin equilibrium binding constant (L·mg^{-1}) corresponding to the maximum binding energy, and B (kcal·mol^{-1}) is the heat of adsorption ($B = RT/b$).

2.7. Thermodynamic Study. Thermodynamic investigations for adsorption of CR on FBP were conducted by considering four dissimilar temperatures (298, 308, 318, and 328 K) where all other key parameters (e.g., solution pH, solution concentration, and adsorbent dose) were kept constant. The thermodynamic parameters, such as Gibbs energy (ΔG, kJ·mol^{-1}), enthalpy of adsorption (ΔH, kJ·mol^{-1}), and entropy of adsorption process (ΔS, kJ·mol^{-1}·K^{-1}), at different temperatures for the adsorption of CR onto FBP surface were calculated from the following equations [26]:

$$\Delta G = -RT \ln q, \quad (10)$$

$$\ln q = \frac{\Delta S}{R} - \frac{\Delta H}{RT}, \quad (11)$$

where R (kJ·mol^{-1}·K^{-1}), T (K), and q (mg·g^{-1}) indicate the ideal gas constant, temperature, and the uptake capacity related to Langmuir constant, respectively.

3. Results and Discussion

3.1. Characterization of the FBP Adsorbent

3.1.1. General Characterization. The bulk density of the fish bone powder was measured to be 0.67 g·cm^{-3}. The moisture content and the ash content of the adsorbent were found to be 3.1% and 36%, respectively. The pH of the adsorbent was determined by mixing fish bone powder with distilled water, and the value of pH was found as 7.8.

3.1.2. Determination of pH_{pzc}. The pH of the point of zero charge (pH_{pzc}) is an important parameter that gives idea to understanding the surface chemistry of an adsorbent. It is one of the essential physicochemical parameters that indicate the net charge of an adsorbent when it comes in contact with water [27]. It is defined as pH of the solution at which the surface charge of the adsorbent has zero value. The global surface charge of the adsorbent is negative at pH higher than

pH_{pzc} (i.e., $pH > pH_{pzc}$) and positive at pH lower than pH_{pzc} (i.e., $pH < pH_{pzc}$). Published reports revealed that adsorption of cationic dye occurred at $pH > pH_{pzc}$ due to the existence of some functional groups, such as COO^- and OH^-. On the other hand, the adsorption of anionic dye occurred at $pH < pH_{pzc}$ [28]. In this investigation, pH_{pzc} of the fish bone powder was determined to be 7 as shown in Figure 1. This signifies that at $pH < pH_{pzc}$, the adsorbent surface carries positive charge and at $pH > pH_{pzc}$, the negative charge exists on the adsorbent surface.

3.1.3. FTIR Analysis. Adsorbent surface properties play a vital role in the entire adsorption process [1]. Therefore, the Fourier transform infrared (FTIR) spectrum is very important to understand the functional groups available in an adsorbent. Fish bone powder is supposed to consist of different functional groups on its surface. These functional groups may have acidic or alkaline properties. The FTIR spectra of FBP in case of before Congo red adsorption and after Congo red adsorption are presented in Figure S1(Supplemental File 1). The spectrum of FBP before adsorption shows several peaks at different wavelengths, which indicates that various functional groups are present in the adsorbent. The FTIR spectroscopic study showed strong and broad peak at 3478.85 cm^{-1} and 3415.00 cm^{-1} for hydroxyl group (O-H) stretching of alcohol group for intermolecular bonding, while the peak at 3236.10 cm^{-1} is assigned by O-H stretching of carboxylic group [29]. The medium band at 1638.54 cm^{-1} and 1617.81 cm^{-1} commonly appeared due to N-H bending of amine [29]. The band at 1112 cm^{-1} is due to O-H vibration of methanol. The absorption bands at 613.85 cm^{-1} and 470.15 cm^{-1} signify the presence of PO_3^{-4} group on the adsorbent surface. It is obvious from Figure S1 that the absorption bands (after adsorption) at lower range slightly shifted due to adsorption of Congo red. This can be attributed to the fact that the functional groups present in the adsorbent might be involved in complexation with adsorbate.

3.2. Effect of Solution pH. There are several factors that affect adsorption of anionic dyes. Solution pH is one of them because of its impact on both the active sites of the adsorbent and the ionization process of the dye molecule in the solution. The effect of solution pH on the adsorption process of Congo red is shown in Figure 2. The experiments were conducted by pouring 100 mL Congo red (150 $mg{\cdot}L^{-1}$) into 100 mg of fish bone adsorbent. It was seen that pH of the adsorbate provides a noteworthy effect on the adsorption process of CR onto FBP surface. Maximum adsorption (96.3%) was found to occur at pH 2, while the adsorption decreased with further rise in pH. The Congo red removal decreased from 96.3% to 17% when the pH was changed from 2 to 8. This phenomenon can be explained by different interactions between adsorbate and adsorbent surface, such as electrostatic force, degree of ionization, hydrogen bonding, and speciation. The sulfonate moiety of Congo red contains negative sulfonic groups ($-SO_3^-$), which dissociates to polar groups ($R - SO_3^-$) at acidic medium [30]. Hence, the

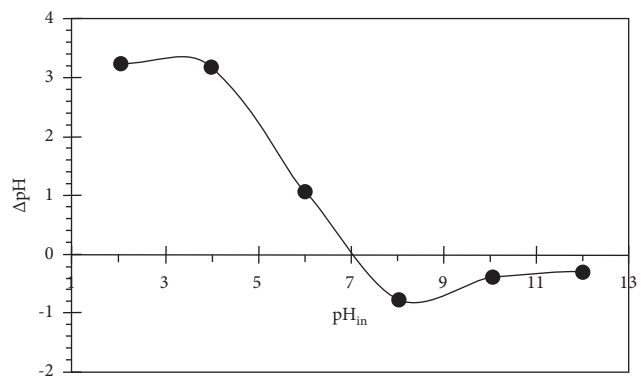

Figure 1: Plot of determination of point of zero charge of fish bone.

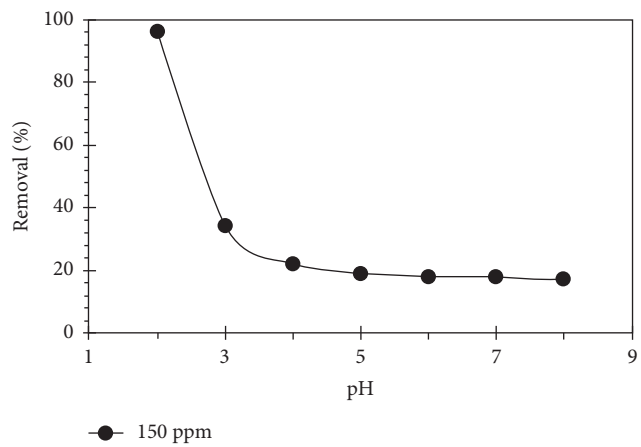

Figure 2: Effect of initial solution pH on Congo red adsorption by fish bone powder (FBP) (adsorbent: 100 mg; adsorbate volume: 100 mL; adsorbate concentration: 150 $mg{\cdot}L^{-1}$; contact time: 4.0 h).

acidic medium favors the adsorption of Congo red onto FBP surface. According to the point of zero charge ($pH_{pzc} = 7$) of fish bone powder shown in Figure 1, the predominant functional groups of the adsorbent surface are positive at $pH < pH_{pzc}$ and negative at $pH > pH_{pzc}$. In acidic condition, the hydrophilic adsorption (electrostatic forces as well as hydrogen bonding) become dominant in the adsorption mechanism. However, the decrease in Congo red removal at higher pH may be due to the competition between excess OH^- ions and dye anions for the adsorption sites. Similar results have been reported for Congo red adsorption on pine bark and activated carbon [11,30]. However, for carrying out further studies using different parameters, the pH value 2 was considered as an optimum value.

3.3. Effect of Adsorbent Dosage on CR Dye Adsorption. The optimum adsorbent dosage is a significant parameter that affects the amount of adsorbed CR by fish bone powder. Varying amounts of FBP (from 100 mg to 700 mg) were used in the present study keeping all other parameters constant. Percent removal of CR is depicted in Figure 3 from where it is obvious that, irrespective of the initial concentrations, removal of Congo red increased from about 91% to 97% with

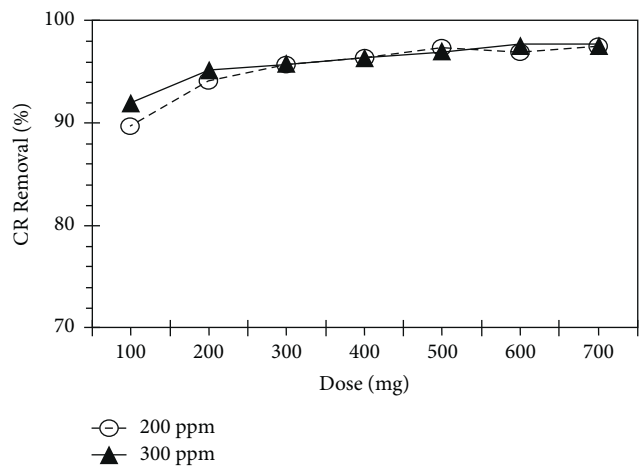

Figure 3: Effect of adsorbent dosages on adsorptive removal of Congo red by using fish bone powder (FBP) (adsorbate volume: 100 mL, pH: 2; adsorbate concentration: 200, 300 mg·L^{-1}; contact time: 4.0 h).

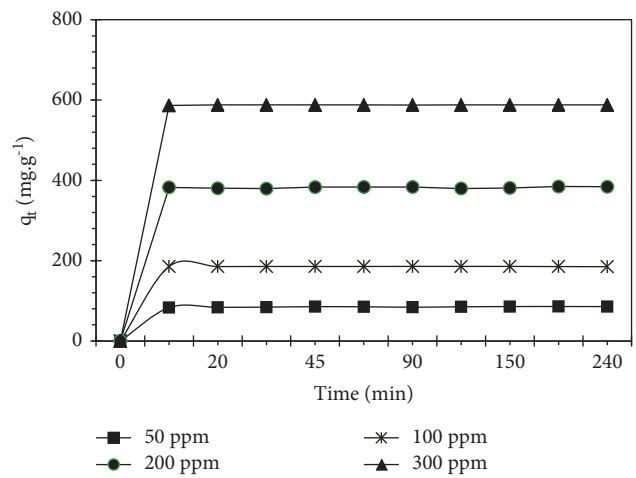

Figure 4: Influence of contact time at various initial concentration on CR removal by fish bone powder (FBP) (adsorbate: 100 mL; pH: 2; adsorbent dose: 500 mg; adsorbate concentration: 50–300 mg·L^{-1}).

increasing adsorbent dosages at the given condition. With the increase in the amount of adsorbent, the total number of active sites of the FBP increases. Therefore, significantly large amount of CR dye can be adsorbed by the FBP resulting in higher dye removal efficiency. Similar results were reported to occur for the Congo red removal by utilizing eggshell membrane [15].

3.4. Effect of Contact Time for Adsorption Reaction at Varying Dye Concentration. In adsorption process, contact time is supposed to be an important parameter to consider because it gives an idea about how long it will take to reach equilibrium. To demonstrate the effect of contact time on adsorption, a series of experiments were conducted by varying the initial concentration of Congo red (50–300 mg·L^{-1}) keeping all other parameters constant. The obtained results are depicted in Figure 4, which demonstrates that the dye uptake (mg·g^{-1}) was very fast at the initial stage (e.g., up to 45 min) after which it became slow and formed plateau. However, for the sake of ensuring a complete reaction, 60 min was selected for performing all other experiments. It is also obtained from Figure 4 that the adsorbed amount of dye increased with the increase in initial concentration. It signifies that the more adsorption sites of the adsorbent were occupied with the increased amount of Congo red. The result is consistent with the findings reported by other research groups [17, 31].

3.5. Adsorption Kinetics. For determining the adsorptive removal mechanism of CR onto FBP surface, two types of kinetic models were studied to analyze the experimental data. The models were (i) pseudo-first-order and (ii) pseudo-second-order kinetic models. Considering the extent of the correlation coefficient (R^2), it was obvious that the process of adsorption could not be well matched by the pseudo-first-order kinetic model. On the other hand, pseudo-second-order kinetic model ((t/q_t)versus t according to (4) was analyzed at different initial CR concentrations, which is shown in Figure 5. It was found that the experimental data fitted very well with pseudo-second-order kinetic model. However, the values of reaction rate constant (k_2), equilibrium uptake capacity (q_e), and correlation coefficient (R^2) were tabulated in Table 1 along with other parameters determined from different models. The values of correlation coefficient were between 0.9999 and 1, while the values of sorption capacities determined from this model ($q_{e,\text{cal}}$) were closer to that obtained experimentally ($q_{e,\text{exp}}$). These outcomes articulate that the pseudo-second-order model can describe the sorption kinetics very well. Similar results were reported for the adsorptive removal of Congo red on various adsorbents, such as pine cone [32], Bengal Gram Seed Husk [33], and eggshell membrane [15].

To reconfirm the best fit kinetic model, the data was further analyzed by squared sum of errors (SSE) method. It is presumed that the lower the value of SSE, the more fit the model. The SSE values for different concentrations were calculated by using the following equation [34]:

$$\text{SSE} = \sum \frac{\left(q_{e,\ \text{exp}} - q_{e,\text{cal}}\right)^2}{q_{e,\ \text{exp}}}, \tag{12}$$

where $q_{e,\text{exp}}$ (mg·L^{-1}) is the experimental sorption capacity at equilibrium and $q_{e,\text{cal}}$ (mg·L^{-1}) is the calculated sorption capacity obtained from corresponding kinetic model. The SSE values for different initial concentrations obtained were tabulated in Table 1. The lower SSE values for pseudo-second-order kinetic model indicated that the sorption kinetics of Congo red onto fish bone powder could be better described by pseudo-second-order model.

3.6. Mass Transfer Mechanism. There are several steps involved in the solid-liquid sorption process. The transmission of the adsorbate initially occurs from the bulk solution to the exterior of the adsorbent. Then, the adsorbate diffuses

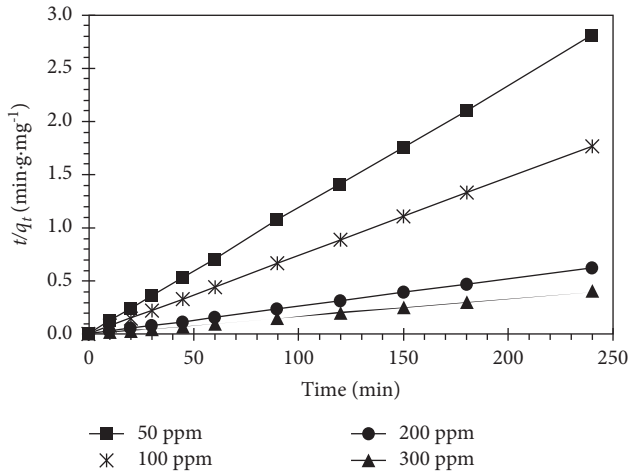

Figure 5: Pseudo-second-order kinetic study.

Table 1: Kinetic parameters for the adsorption of CR onto FBP surface.

C_{in} (mg·L^{-1})	Pseudo-second-order model					Intraparticle diffusion model		Bangham's model		
	$q_{e.cal}$ (mg·g^{-1})	$q_{e.exp}$ (mg·g^{-1})	k_2 (mg·g^{-1}·min^{-1})	R^2	SSE	k_{id2} (mg·g^{-1}·min$^{-1/2}$)	I	k_0	σ	R^2
50	85.47	82.43	0.0253	0.9999	0.1490	4.04	52.82	0.3994	0.0314	0.9644
100	185.13	181.02	0.0456	1	0.0091	8.41	118.10	0.4562	0.0411	0.8565
200	384.61	383.42	0.0112	1	0.2369	17.56	242.09	0.4895	0.0419	0.7802
300	588.23	583.71	0.3612	1	0.0061	26.76	373.75	0.5671	0.0116	0.7588

through the boundary layer and at the end it moves through the pores of the adsorbent. In the course of the transmission of adsorbate, it is adsorbed at the available active sites. Although the pseudo-second-order kinetic model was found to be the best fit model, it did not provide any information regarding mass transfer mechanism. In this study, the mass transfer mechanism was analyzed by using a well-known diffusion model, namely, Weber–Morris intraparticle diffusion model [35]. Diffusion control is supposed to be the most consistent explanation for almost all reported results in which the rate equation of pseudo-second order for adsorption has been found to fit the data well [36]. Intraparticle diffusion model was studied by plotting q_t versus $t^{0.5}$ according to equation (5) and is depicted in Figure 6 where two distinct linear regions are noticed. The first linear region signifies the rapid external surface loading or film diffusion, while the second linear region represents the pore diffusion. The rate constant of pore diffusion (k_{id2}) was determined from the slope of each line, while intercept of each line represented the boundary layer thickness during adsorption process. A schematic diagram of Congo red transport is presented in Figure 7. The calculated values of k_{id} and I are tabulated in Table 1. Similar outcomes were reported for activated carbon as well [37].

The kinetic data for Congo red adsorption on FBP was further interpreted by using Bangham's diffusion model (equation (6)) in order to examine whether or not the pore diffusion was the only rate controlling step in the sorption process. For determining Bangham's parameters, a plot of $\log[\log(C_0/(C_0 - q_t \cdot m))]$ versus $\log t$ for different initial concentration was drawn as shown in Figure S2 (Supplemental File 2). The plot was found to be linear for each initial concentration. Bangham's parameters (k_0 and σ) were calculated from the intercept and slope, respectively, and were tabulated in Table 1. The correlation coefficients for different initial concentrations were in a range from 0.9644 to 0.7588. According to the above-mentioned analysis, it could be concluded that both film diffusion and pore diffusion are involved in different stages of the sorption process [24].

3.7. Adsorption Isotherm Studies. Isotherms of adsorption are the indicative of adsorbate partitioning among the solid phase (adsorbent) as well as the liquid phase (adsorbate). The isotherms find the extent of adsorption of certain adsorbate onto a specific adsorbent at defined conditions. In this present study, two common isotherm models were used to discuss the adsorption isotherms for CR removal onto FBP at pH 2. The discussed models were Langmuir as well as Freundlich isotherm models by which the data were analyzed.

Langmuir isotherm model considers a monolayer adsorption process where the sorption occurs at homogeneous surfaces of the adsorbent. In this case, by using equation (7), $(1/q_e)$ versus $(1/C_e)$ is plotted, which is shown in Figure 8(a). The maximum sorption capacity q_m (mg·g^{-1}) and the Langmuir constant b (L·mg^{-1}) are determined from the slope and intercept of the straight line, respectively.

Freundlich isotherm model (equation (8)), on the other hand, is supposed to be applied for adsorption of adsorbent on heterogeneous surfaces. This model can deal with

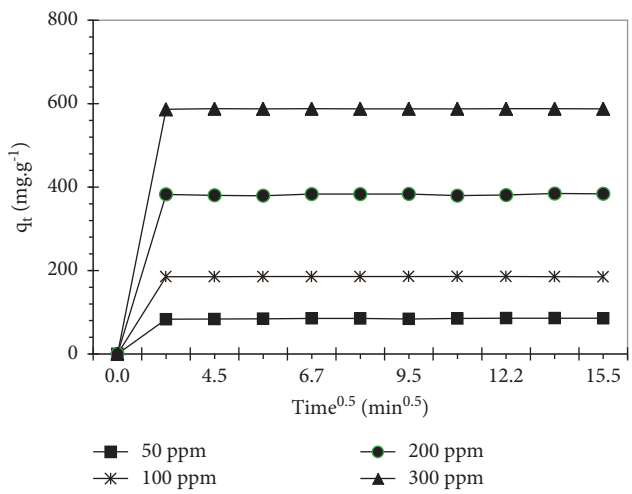

Figure 6: Intraparticle diffusion analysis.

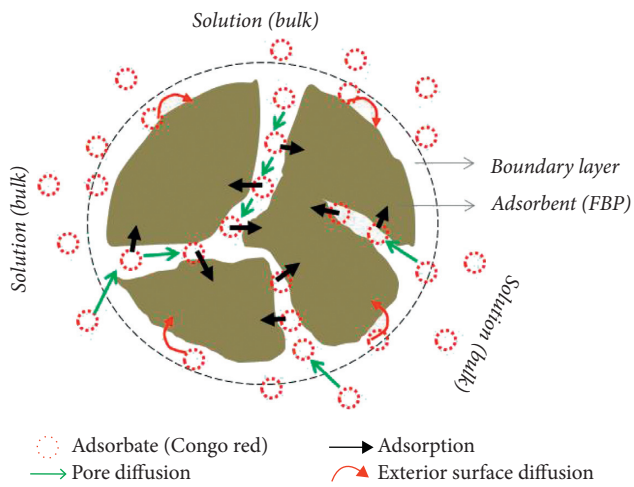

Figure 7: Schematic diagram of Congo red transport and sorption mechanism.

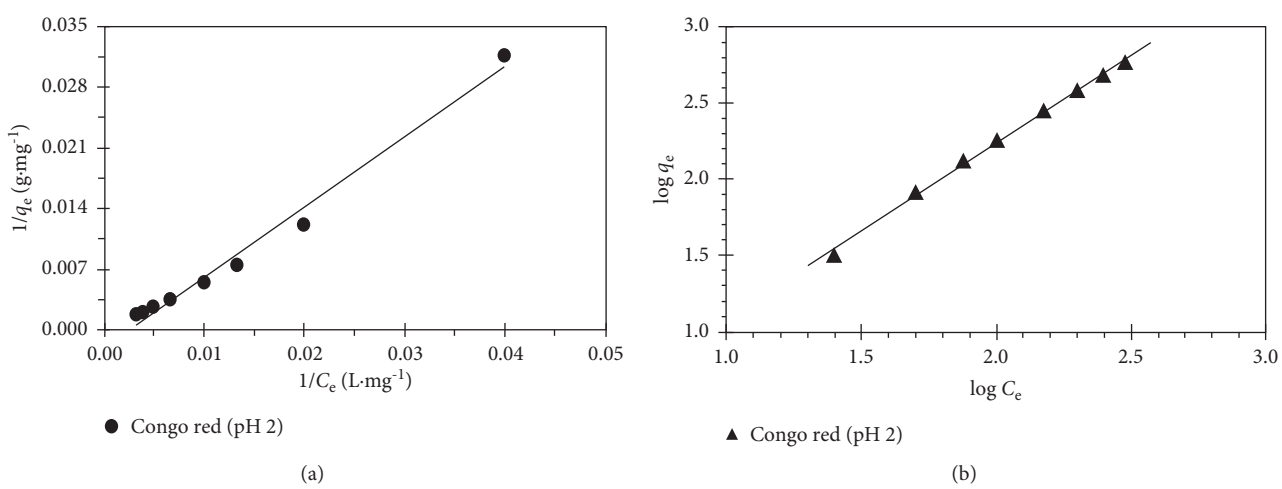

Figure 8: Isotherm analysis using (a) Langmuir and (b) Freundlich model.

multilayer adsorption process too. However, the related parameters such as K_F and n can be determined from the intercept and slope of the straight line of a plot log C_e versus log q_e, which is depicted in Figure 8(b). Temkin isotherm parameters such as Temkin isotherm constant (K_T) and heat of adsorption (B) are determined from the slope and intercept of the plot of a plot q_e versus ln C_e (for simplicity figure not shown) by using equation (9).

The extent of different isotherm parameters obtained from the above-mentioned analyses is tabulated in Table 2. On the basis of the extent of the correlation coefficients, it can be summarized that the adsorption process can be better explained by using the Langmuir isotherm model ($R^2 = 0.9929$) compared to the Freundlich and Temkin isotherm models. Thus, the result indicated that a monolayer adsorption occurred during the discussed adsorption process. Similar findings were reported by various researchers for different adsorbents [15, 33, 38]. It is noteworthy to mention that the adsorption capacity of the current adsorbent (FBP) is considerably high compared to other biomaterial-derived adsorbents as shown in Table 3.

Table 2: Linearized isotherm coefficients for Congo red adsorption onto FBP surface.

Isotherms	Parameters	Value
Langmuir isotherm	q_m (mg·g^{-1})	666.67
	b (L·mg^{-1})	0.0020
	R^2	0.9929
Freundlich isotherm	K_F (L·mg^{-1})	1.358
	N	0.848
	R^2	0.9895
Temkin isotherm	B (kcal·mol^{-1})	0.05
	K_T (L·mg^{-1})	0.031
	R^2	0.8971

Table 3: Comparison of sorption capacities of low-cost adsorbents for various dyes.

Materials	Dye	q_m (mg·g^{-1})	References
Fish bone powder (FBP)	CR	666.67	In this work
Fish bone	BB41, BY28	37.36	[4]
Eggshell membrane	CR	117.65	[15]
Modified fishbone charcoal	MB	605.82	[19]
Untreated fishbone charcoal	MB	70.42	[19]
Raw pine cone	CR	32.65	[32]
Acid-treated pine cone	CR	40.19	[32]
Bone char	AR.TF	73.91	[39]
Tuna fish bone	CR	329.0	[40]

3.8. Effect of Temperature and Thermodynamic Studies. The effect of temperature on Congo red adsorption from aqueous solution using fish bone powder was tested in this study. Batch experiments were carried out at varying temperatures keeping all other parameters constant. The results are depicted in Figure 9 where it is evident that the removal of Congo red increases from 141 mg·g^{-1} to 381 mg·g^{-1} with the increase in temperature from 298 K to 328 K. An increase in temperature leads to fast diffusion of Congo red molecules through the external boundary layer and the internal pores of the adsorbent due to less resistance offered by viscous forces in the aqueous phase [41]. Moreover, the increase in sorption capacity at elevated temperature may happen due to the pore size enlargement of the adsorbent [42].

Thermodynamic parameters are the essential parametric tools to understand whether the adsorption process is physical or chemical, spontaneous or nonspontaneous, and exothermic or endothermic. To determine these parameters, ln q versus $(1/T)$ was plotted using equation (11), which is shown in Figure 10. The values of change in enthalpy (ΔH) and entropy (ΔS) can be determined from the slope and intercept of the graphical plot, while the values of Gibbs energy (ΔG) are calculated by using equation (10). However, the thermodynamic parameters calculated from this study are presented in Table 4. From the table, it is obvious that the values of ΔG become successively more negative with the temperature rise. Such phenomenon signifies the process of CR adsorption onto FBP surface is spontaneous and feasible. The positive value of change in enthalpy indicates that the adsorption is endothermic in nature, which can be substantiated by the increase in adsorption capacity with increase in temperature. To know about the binding method between Congo red and fish bone powder, the activation energy (Ea) of the adsorption process was determined as well. Physical adsorption (physisorption) generally has low activation energy (<40 kJ·mol^{-1}), while chemical adsorption

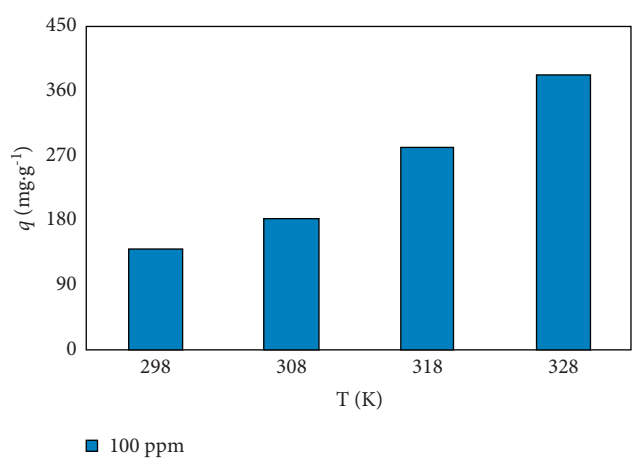

Figure 9: Effect of temperature on Congo red removal by fish bone powder.

(chemisorption) has considerably high activation energy (>40 kJ·mol^{-1}) [43]. The activation energy was determined to be 29.84 kJ·mol^{-1}, which indicated that the adsorption process was of physisorption type. On the other hand, the affinity and increased randomness or disorderliness at the adsorbent-adsorbate interface during the period of adsorption of Congo red by FBP were corroborated by the positive value of ΔS [15,44].

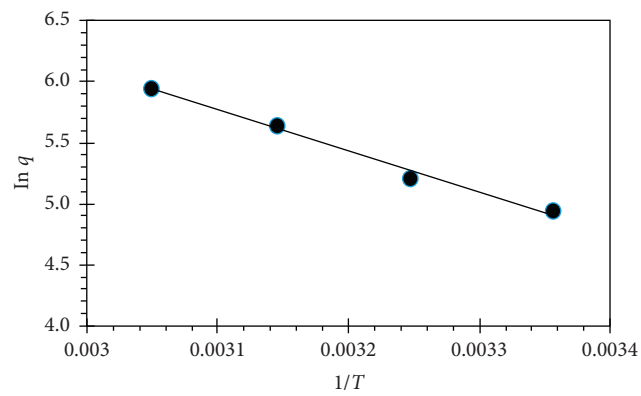

Figure 10: Thermodynamic study of adsorption of Congo red on fish bone powder.

Table 4: Thermodynamic parameters for the adsorption of Congo red on FBP.

T (K)	ΔG (kJ·mol^{-1})	ΔH (kJ·mol^{-1})	ΔS (kJ·mol^{-1}·K^{-1})
298	−12.26	27.70	0.13
308	−13.34		
318	−14.91		
328	−16.19		

4. Conclusion

This research investigated the applicability of fish bone as an adsorbent in the view to the anionic dye (Congo red) removal from synthetic wastewater solution. The isoelectric point (pH_{PZC}) indicated that the adsorbent surface is positive below the value of pH 7, which resulted in a favorable Congo red adsorption at low pH. From the analysis of kinetic data, it was obvious that the adsorption of Congo red followed a pseudo-second-order reaction model. Experimental data was analyzed with different models of isotherm, and it was perceived that the Langmuir isotherm model fitted very well with the experimentally obtained data compared with Freundlich and Temkim isotherm models. The maximum sorption capacity was evaluated to be 666.67 mg·g^{-1}. The extent of activation energy (29.84 kJ·mol^{-1}) confirmed that the binding between Congo red and fish bone powder occurred through a physisorption process. In addition to this, the adsorption process was observed to be endothermic and spontaneous in nature. The findings of this research proclaimed that fish bone powder derived from a locally available fish (silver carp) can be an effective adsorbent for Congo red removal from wastewater.

Data Availability

The data used to support the findings of this study are available from the corresponding author upon request.

Conflicts of Interest

The authors declare that they have no known conflicts of interest or personal relationships that could have appeared to influence the work reported in this paper.

Authors' Contributions

Shahanaz Parvin was responsible for conceptualization, methodology, validation, and supervision. Manjur Hussain and Farhana Akter were responsible for investigation, formal analysis, and writing of the original draft. Biplob Kumar Biswas was responsible for conceptualization, supervision, and review and editing of the manuscript.

Supplementary Materials

Figure S1: FTIR spectra of the fish bone powder (a) before and (b) after adsorption. Figure S2: Bangham's diffusion model for Congo red adsorption by fish bone powder adsorbent. (*Supplementary Materials*)

References

[1] R. Ahmad and R. Kumar, "Adsorptive removal of congo red dye from aqueous solution using bael shell carbon," *Applied Surface Science*, vol. 257, no. 5, pp. 1628–1633, 2010.

[2] N. Dizge, C. Aydiner, E. Demirbas, M. Kobya, and S. Kara, "Adsorption of reactive dyes from aqueous solutions by fly ash: kinetic and equilibrium studies," *Journal of Hazardous Materials*, vol. 150, no. 3, pp. 737–746, 2008.

[3] M. J. Iqbal and M. N. Ashiq, "Adsorption of dyes from aqueous solutions on activated charcoal," *Journal of Hazardous Materials*, vol. 139, no. 1, pp. 57–66, 2007.

[4] A. Ebrahimi, M. Arami, H. Bahrami, and E. Pajootan, "Fish bone as a low-cost adsorbent for dye removal from wastewater: response surface methodology and classical method," *Environmental Modeling & Assessment*, vol. 18, no. 6, pp. 661–670, 2013.

[5] M. T. Yagub, T. K. Sen, S. Afroze, and H. M. Ang, "Dye and its removal from aqueous solution by adsorption: a review," *Advances in Colloid and Interface Science*, vol. 209, pp. 172–184, 2014.

[6] M. A. H. Dhaif-Allah, S. N. Taqui, U. T. Syed, and A. A. Syed, "Kinetic and isotherm modeling for acid blue 113 dye adsorption onto low-cost nutraceutical industrial fenugreek seed spent," *Applied Water Science*, vol. 10, no. 2, 2020.

[7] R. K. Prasad, "Color removal from distillery spent wash through coagulation using *Moringa oleifera* seeds: use of optimum response surface methodology," *Journal of Hazardous Materials*, vol. 165, no. 1-3, pp. 804–811, 2009.

[8] N. P. Khumalo, G. D. Vilakati, S. D. Mhlanga et al., "Dual-functional ultrafiltration nano-enabled PSf/PVA membrane for the removal of Congo red dye," *Journal of Water Process Engineering*, vol. 31, Article ID 100878, 2019.

[9] M. Panizza, A. Barbucci, R. Ricotti, and G. Cerisola, "Electrochemical degradation of methylene blue," *Separation and Purification Technology*, vol. 54, no. 3, pp. 382–387, 2007.

[10] E. G. Solozhenko, N. M. Soboleva, and V. V. Goncharuk, "Decolourization of azodye solutions by Fenton's oxidation," *Water Research*, vol. 29, no. 9, pp. 2206–2210, 1995.

[11] K. Litefti, M. S. Freire, M. Stitou, and J. González-Álvarez, "Adsorption of an anionic dye (congo red) from aqueous solutions by pine bark," *Scientific Reports*, vol. 9, no. 1, p. 16530, 2019.

[12] F. Kallel, F. Chaari, F. Bouaziz, F. Bettaieb, R. Ghorbel, and S. E. Chaabouni, "Sorption and desorption characteristics for the removal of a toxic dye, methylene blue from aqueous

solution by a low cost agricultural by-product," *Journal of Molecular Liquids*, vol. 219, pp. 279–288, 2016.

[13] R. Slimani, A. Anouzla, Y. Abrouki et al., "Removal of a cationic dye-Methylene Blue-from aqueous media by the use of animal bone meal as a new low cost adsorbent," *Journal of Materials and Environmental Science*, vol. 2, no. 1, pp. 77–87, 2011.

[14] P. Bhatia and M. Nath, "Green synthesis of p-NiO/n-ZnO nanocomposites: excellent adsorbent for removal of Congo red and efficient catalyst for reduction of 4-nitrophenol present in wastewater," *Journal of Water Process Engineering*, vol. 33, Article ID 101017, 2020.

[15] S. Parvin, B. K. Biswas, M. A. Rahman, M. H. Rahman, M. S. Anik, and M. R. Uddin, "Study on adsorption of congo red onto chemically modified egg shell membrane," *Chemosphere*, vol. 236, Article ID 124326, 2019.

[16] N. Nasuha and B. H. Hameed, "Adsorption of methylene blue from aqueous solution onto NaOH-modified rejected tea," *Chemical engineering journal*, vol. 166, no. 2, pp. 783–786, 2011.

[17] M. M. R. Khan, M. W. Rahman, H. R. Ong, A. B. Ismail, and C. K. Cheng, "Tea dust as a potential low-cost adsorbent for the removal of crystal violet from aqueous solution," *Desalination and Water Treatment*, vol. 57, no. 31, pp. 14728–14738, 2016.

[18] G. Ghanizadeh and G. Asgari, "Adsorption kinetics and isotherm of methylene blue and its removal from aqueous solution using bone charcoal," *Reaction Kinetics, Mechanisms and Catalysis*, vol. 102, no. 1, pp. 127–142, 2011.

[19] W. Wang, Y.-Y. Liu, X.-F. Chen, and S.-X. Song, "Facile synthesis of NaOH-modified fishbone charcoal (FBC) with remarkable adsorption towards methylene blue," *Procedia engineering*, vol. 211, pp. 495–505, 2018.

[20] M. F. Alam, "Socioeconomic aspects of carp production and consumption in Bangladesh," in *Proceedings of a Workshop on Genetic Management and Improvement Strategies for Exotic Carps in Asia*, Dhaka, Bangladesh, February 2002.

[21] J. M. Jabar, Y. A. Odusote, K. A. Alabi, and I. B. Ahmed, "Kinetics and mechanisms of congo-red dye removal from aqueous solution using activated *Moringa oleifera* seed coat as adsorbent," *Applied Water Science*, vol. 10, no. 6, p. 136, 2020.

[22] W. J. Weber Jr and J. C. Morris, "Kinetics of adsorption on carbon from solution," *Journal of the Sanitary Engineering Division*, vol. 89, no. 2, pp. 31–59, 1963.

[23] A. Pholosi, E. B. Naidoo, and A. E. Ofomaja, "Intraparticle diffusion of Cr(VI) through biomass and magnetite coated biomass: a comparative kinetic and diffusion study," *South African Journal of Chemical Engineering*, vol. 32, no. 1, pp. 39–55, 2020.

[24] U. A. Edet and A. O. Ifelebuegu, "Kinetics, isotherms, and thermodynamic modeling of the adsorption of phosphates from model wastewater using recycled brick waste," *Processes*, vol. 8, no. 6, p. 665, 2020.

[25] S. Kumari, D. Mankotia, and G. S. Chauhan, "Crosslinked cellulose dialdehyde for Congo red removal from its aqueous solutions," *Journal of environmental chemical engineering*, vol. 4, no. 1, pp. 1126–1136, 2016.

[26] M. E. Argun, S. Dursun, C. Ozdemir, and M. Karatas, "Heavy metal adsorption by modified oak sawdust: thermodynamics and kinetics," *Journal of Hazardous Materials*, vol. 141, no. 1, pp. 77–85, 2007.

[27] V. Bernal, L. Giraldo, and J. Moreno-Piraján, "Physicochemical properties of activated carbon: their effect on the adsorption of pharmaceutical compounds and adsorbate-adsorbent interactions," *Chimia*, vol. 4, no. 4, p. 62, 2018.

[28] D. Savova, N. Petrov, M. F. Yardim et al., "The influence of the texture and surface properties of carbon adsorbents obtained from biomass products on the adsorption of manganese ions from aqueous solution," *Carbon*, vol. 41, no. 10, pp. 1897–1903, 2003.

[29] Website of Sigma-Aldrich, "IR spectrum table and chart," 2021, https://www.sigmaaldrich.com/technical-documents/articles/biology/ir-spectrum-table.html.

[30] R. Lafi, I. Montasser, and A. Hafiane, "Adsorption of congo red dye from aqueous solutions by prepared activated carbon with oxygen-containing functional groups and its regeneration," *Adsorption Science & Technology*, vol. 37, no. 1-2, pp. 160–181, 2019.

[31] M. Dehvari, M. H. Ehrampoush, M. T. Ghaneian, B. Jamshidi, and M. Tabatabaee, "Adsorption kinetics and equilibrium studies of reactive red 198 dye by cuttle powder," *Iranian Journal of Chemistry & Chemical Engineering-International English Edition*, vol. 36, no. 2, pp. 143–151, 2017.

[32] S. Dawood and T. K. Sen, "Removal of anionic dye congo red from aqueous solution by raw pine and acid-treated pine cone powder as adsorbent: equilibrium, thermodynamic, kinetics, mechanism and process design," *Water Research*, vol. 46, no. 6, pp. 1933–1946, 2012.

[33] M. C. Somasekhara Reddy, V. Nirmala, and C. Ashwini, "Bengal gram seed husk as an adsorbent for the removal of dye from aqueous solutions-batch studies," *Arabian Journal of Chemistry*, vol. 10, no. 2, pp. S2554–S2566, 2017.

[34] C. Chakrapani, C. S. Babu, K. N. K. Vani, and S. Rao, "Adsorption kinetics for the removal of fluoride from aquesou solution by activated carbeon adsorbents derived from the peels of selected citrus fruits," *E-Journal of Chemistry*, vol. 7, no. S1, pp. S419–S427, Article ID 582150, 2010.

[35] B. H. Hameed and M. I. El-Khaiary, "Removal of basic dye from aqueous medium using a novel agricultural waste material: pumpkin seed hull," *Journal of Hazardous Materials*, vol. 155, no. 3, pp. 601–609, 2008.

[36] M. Hubbe, S. Azizian, and S. Douven, "Implications of apparent pseudo-second-order adsorption kinetics onto cellulosic materials: a review," *BioResources*, vol. 14, no. 3, pp. 7582–7626, 2019.

[37] Z. Cheng, L. Zhang, X. Guo, X. Jiang, and T. Li, "Adsorption behavior of direct red 80 and Congo red onto activated carbon/surfactant: process optimization, kinetics and equilibrium," *Spectrochimica Acta Part A: Molecular and Biomolecular Spectroscopy*, vol. 137, pp. 1126–1143, 2015.

[38] A. H. Jawad, R. A. Rashid, R. M. A. Mahmuod, M. A. M. Ishak, N. N. Kasim, and K. Ismail, "Adsorption of methylene blue onto coconut (*Cocos nucifera*) leaf: optimization, isotherm and kinetic studies," *Desalination and Water Treatment*, vol. 57, no. 19, pp. 8839–8853, 2016.

[39] R. A. Moura, A. A. Seolatto, M. E. De Oliveira Ferreira, and F. F. Freitas, "The adsorption study of Royal Blue Tiafix and Black Tiassolan dyes using bone char as adsorbent," *Adsorption Science & Technology*, vol. 36, no. 3-4, pp. 1178–1198, 2018.

[40] Q. Peng, F. Yu, B. Huang, and Y. Huang, "Carbon-containing bone hydroxyapatite obtained from tuna fish bone with high adsorption performance for Congo red," *RSC Advances*, vol. 7, no. 43, pp. 26968–26973, 2017.

[41] S. Banerjee and M. C. Chattopadhyaya, "Adsorption characteristics for the removal of a toxic dye, tartrazine from aqueous solutions by a low cost agricultural by-product," *Arabian Journal of Chemistry*, vol. 10, no. 2, pp. S1629–S1638, 2017.

[42] E. Demirbas, M. Kobya, and M. T. Sulak, "Adsorption kinetics of a basic dye from aqueous solutions onto apricot stone activated carbon," *Bioresource Technology*, vol. 99, no. 13, pp. 5368–5373, 2008.

[43] V. J. Inglezakis and A. A. Zorpas, "Heat of adsorption, adsorption energy and activation energy in adsorption and ion exchange systems," *Desalination and Water Treatment*, vol. 39, pp. 149–157, 2012.

[44] Y. T. Gebreslassie, "Equilibrium, kinetics, and thermodynamic studies of malachite green adsorption onto Fig (*Ficus cartia*) leaves," *Journal of analytical methods in chemistry*, vol. 2020, Article ID 7384675, 11 pages, 2020.

Hindawi
Journal of Chemistry
Volume 2021, Article ID 5554353, 9 pages
https://doi.org/10.1155/2021/5554353

Research Article

Adsorption Phenomenon of *Arundinaria alpina* Stem-Based Activated Carbon for the Removal of Lead from Aqueous Solution

Yosef Asrat,[1] **Amare Tiruneh Adugna**,[1,2] **M. Kamaraj**,[2,3] **and Surafel Mustefa Beyan**[4]

[1]*Department of Environmental Engineering, College of Biological and Chemical Engineering, Addis Ababa Science and Technology University, P. O. Box 16417, Addis Ababa, Ethiopia*
[2]*Bioprocess and Biotechnology Center of Excellence, Addis Ababa Science and Technology University, Addis Ababa 16417, Ethiopia*
[3]*Department of Biotechnology, College of Biological and Chemical Engineering, Addis Ababa Science and Technology University, Addis Ababa 16417, Ethiopia*
[4]*School of Chemical Engineering, Jimma Institute of Technology, Jimma University, Jimma, P. O. Box 387, Ethiopia*

Correspondence should be addressed to Amare Tiruneh Adugna; amardugna@yahoo.com

Received 11 February 2021; Accepted 8 June 2021; Published 16 June 2021

Academic Editor: Ibrahim H. Alsohaimi

In this study, activated carbon was prepared from locally available bamboo (*Arundinaria alpina*) in Ethiopia to remove Pb (II) from wastewater. Various effects such as solution pH, initial Pb (II) ion concentration, and adsorbent dose were investigated and accordingly discussed, and the process was carried out on a batch adsorption base. Dried *Arundinaria alpina* stem was activated with potassium hydroxide (KOH) at a ratio of 1 : 1 (w/v) and carbonized in a furnace at three temperature ranges (500°C, 600°C, and 700°C) for 3 h. The physicochemical of *Arundinaria alpina* stem activated carbon (AASAC) was investigated and the resultant of 500°C treatment setup is found as ideal in terms of yield (40.6 g), ash (3.5%), porosity (0.704%), moisture (7.7%), and iodine number (814.69 mg/g). The further characterization of ideal AASAC was carried out by scanning electron microscopy (SEM), X-ray diffraction (XRD) spectroscopy, and Fourier transform infra-red (FTIR). The optimum Pb (II) removal efficiency of AASAC was 99.8% at pH 5 in a synthetic solution, but the efficiency declined to 60.42% on real industrial wastewater due to the presence of its mixed pollutant nature. Freundlich isotherm model is more favorable than Langmuir with a high correlation coefficient (R^2-0.9496) for Pb (II) adsorption. The study revealed that AASAC has a potential adsorption efficiency to remove the Pb (II) ion from the aqueous solution which is also recommended as an adsorbent for real industry wastewater treatment.

1. Introduction

Heavy metals pollution has been a major concern globally. Sources of heavy metal pollution come from discharges of various industries such as petroleum refining, pesticides, smelting, mining, electroplating, tanning, glass, herbicides, and ceramic manufacturing industries [1]. Pb (II) is considered to be an extremely toxic metal without known biological function and higher concentrations; it can endorse poisoning and has a hazardous nature because it cannot be degraded or destroyed and tend to bioaccumulate [2, 3]. It possesses risks not only to humans but also to animals and plants because of its severe toxic effects, and it has been the main reason behind the number of afflictions [2, 4]. Different techniques have been employed to remove the lead ions from effluent solutions, for instance, chitosan, the biomass of microbial, coagulation, ion exchange, flotation, sedimentation, composite material, solvent extraction, membrane filtration, evaporation, and reverse osmosis [2]. But still, they have many limitations; for instance, chitosan has poor chemical resistance as well as thermal and mechanical properties [5]. Although microbial adsorbents are environmentally friendly compared to the conventional method, they have high limitations such as incomplete metal ions removal, high energy consumption, a large requirement of nutrients, and generations of waste products mostly toxic

byproducts [6]. Among those methods, adsorption using agrobased activated carbon is widely used due to its high efficacy, being ecofriendly, simplicity, and cost-effectiveness [2, 7]. The characteristics features of the adsorbent layout are the major factor for the effective adsorption of metal ions from the solution. Thus, many researchers are looking at different agrowaste and agromaterials for the preparation of activated carbon that can be used as adsorbents for the removal of heavy metal from industrial effluents or/and other wastewater environments. Consequently, novel agrobased activated carbon for the absorption of metal ions with high removal efficiency and high rate of adsorption is of great concern. This study is an attempt to investigate the Ethiopian bamboo-based activated carbon as an alternative option for lead removal. In Ethiopia, the natural bamboo forest has been estimated at around 1 million hectares which is the largest in the African continent accounting for 67% within the continent and 7% of the world total [8, 9]. It produces an average annual stem increment of 8.5–10 tonnes (t) of oven-dry matter per ha and possible to harvest about 3 mills t yr-1 of oven-dry biomass on a sustainable basis from 1 mill. ha of bamboo in Ethiopia, assuming selective felling of culms 3 or more years of age. This could be used to supply part of the woodwork, pulp, furniture, construction, and energy requirements of the nation [8, 9]. The demand for activated carbon is increasing owing to the increased utility of the carbon material in pollution control. As the applications of activated carbon are immense, the gap between demand and supply is ever widening. Exploring effective and low-cost activated carbon may contribute to environmental sustainability and offer benefits for future commercial applications. As discussed in detail in this paragraph, the availability of bamboo represents the feedstock to the activated carbon plant; thus, the raw material is very cheap. Plant resources are presently getting consideration as raw materials for water pollution treatment due to their availability and low cost [7, 10].

Hence, the objective of the study mainly revolves around the production of activated carbon from *Arundinaria alpina* bamboo as a locally abundant material and assessing its adsorption performance in Pb (II) removal in different experimental conditions. Furthermore, the study was designed for the investigation of process parameters, namely, solution pH, initial Pb (II) concentration, and adsorbent dose. Moreover, experimental figures were subjected to kinetics and thermodynamical analysis for the investigation of removal rates of Pb (II) from the solution.

2. Materials and Methods

2.1. Collection and Preparation of Plant Biomass. The *Arundinaria alpina* bamboo used in this work was obtained from southwest Ethiopia (Tepi, District of Yeki), located in lat/long 7°3′N, 35°18′E with an altitude of 1700–2500 m and the total annual rainfall 1678 mm in a temperature of 30°C and a minimum of 15°C. The collected bamboo stems were cut into pieces and grained with 1.5–2 cm size for the production of powdered activated carbon. The chopped bamboo was washed by tap water followed by distilled water to remove dirt matter on the surface of the bamboo stem and, then, dried in the oven at 105°C/24 h for removing the moisture. Then, the dried samples were impregnated with potassium hydroxide pellets in a 1 : 1 ratio as an activating agent and the mixture was kept for 4 h and dried at 15°C/12 h [11].

2.2. Carbonization for the Development of Adsorbent. The impregnated dried sample is carbonized in a Muffle Furnace (MF 106, NUVE) at three different temperatures of 500°C, 600°C, and 700°C for 3 h [12]. The obtained carbon was cooled for 24 h in a dissector and repeatedly washed with 0.1 M HCl and distilled water until the washing was free from the base medium; it must be down to neutral media (pH H183141 Romania). The dried carbon samples were crushed using a mortar and pestle to obtain the desired particle size (sieve size 125 μm model IC-205/EV, Italy). The resultant materials are designated as AASAC1, AASAC2, and AASAC3, based on the temperature setup as 500°C, 600°C, and 700°C, respectively.

2.3. Characterization of AASAC. The physical analysis (moisture, ash content, volatile matter, specific gravity, and porosity of the AASAC) was conducted according to an American Standard Testing Method (ASTM) [13–16]. The ideal AASAC samples will be further characterized by analytical techniques such as SEM, XRD, and FTIR. SEM analysis was carried to capture the morphological structure of AASAC (HV/20.0 KV), model INSPECT F 50, FIY USA; FTIR (model IRAffinity-1S) was used to identify the functional group of bamboo activated carbon as follows: 2 mg of AASAC powder with 300 mg of anhydrous KBr (potassium bromide). The mixture was pressed under vacuum (hydraulic press Model-15) and the spectra were recorded between 4000 and 400 cm^{-1} for the evaluation of the surface composition of a material. The XRD (Miniflex 600 PxRD) was operated at Cu Ka 40 kV/40 mA and a current of 15 mA. The XRD patterns were collected with a scan rate of 4.2°C/min and the results were analyzed using standard software (Origin 2018 Version 9.55).

2.4. Batch Adsorption Experiments for Pb (II) Removal. A lead stock solution (1000mgL^{-1}) was prepared by dissolving 1.5985 g of lead nitrate, Pb $(NO_3)_2$ in 1000 ml of distilled water. Adsorption experiments were carried out at room temperature in batch mode with a volume of 250 ml. The adsorption experiment is performed at different operating conditions such as varied pH (3, 5, and 6), adsorbent dose (1 g, 1.5 g, and 2 g), and initial concentration (50 mgL^{-1}, 100 mgL^{-1}, and 150 mgL^{-1}). Microwave Plasma Atomic Emission Spectrometry (Agilent 4200 MP-AES) was used to measure the residual metal ion concentration. The percentage of Pb (II) removal was calculated in the following formula:

$$\%\text{removal} = \frac{C_0 - C_t}{C_0} * 100\%, \quad (1)$$

where C_0 = initial concentration of adsorbate and C_t = final concentration of the adsorbate after the time (t).

2.5. Isotherm Study for the Adsorption Experiment. The adsorption of Pb (II) by AASAC was assessed using Langmuir (Equation (2)) and Freundlich (Equation (3)) model as follows [17]:

$$\frac{C_e}{q_e} = \frac{1}{q_o K_L} + \frac{C_e}{q_o}, \quad (2)$$

where C_e is the equilibrium concentration of the adsorbate (mg L^{-1}), q_e is the mass of solute adsorbed per unit mass of adsorbent, q_o is a constant related to the adsorption capacity (mg g^{-1}), and K_L is the experimental constant.

$$\log(q_e) = \log K_L + \frac{1}{n}\log C_e, \quad (3)$$

where C_e is the equilibrium concentration of the adsorbate, q_e is the mass of solute adsorbed per unit mass of adsorbent, and k_L and n are Freundlich constants representing the adsorption capacity of adsorbents and the intensity of the adsorption, respectively.

2.6. Pb (II) Removal Efficiency of AASAC on Real Industrial Wastewater. The wastewater is collected from the paint factory (located in the subcity of Nefas Silk-Lafto, Addis Ababa) from the equalization tank three times in five-day intervals. The adsorption experiment was carried out with the operational condition as follows at its original pH, adsorbent dose 2 g, and contact time 120 mins. The physicochemical characteristics (pH, turbidity, BOD_5) of the effluent before and after adsorption were identified using ASTM [18, 19]. The Pb (II) metal ion concentrations are measured using Microwave Plasma Atomic Emission Spectrometry (Agilent 4200 MP-AES), and the adsorption efficiency (%) is calculated as per (1).

3. Results and Discussion

3.1. Physicochemical Characterization of AASACs. The physicochemical characteristics of resultant bamboo stem-based activated carbons are reported in Table 1. The moisture content (7.70% to 6.20%) of AASAC directly influences the carbonization time and temperature. The ash of AASAC1 is its inorganic constituent, which is a white substance after bamboo carbon has burned completely; the ash percentage increased from 3.51% to 5.53%. The low ash content would result in minimal effects of inorganic impurities on pore development during the activation process. Previous studies suggested that good quality carbon should be low in Ash but rich in carbon and volatile. Ash in activated carbon is undesirable and taken as an impurity. Ash could interfere with carbon adsorption through competitive adsorption and catalysis of adverse reactions [20]. At higher temperatures, organic substances became unstable as the heat provides energy to the molecules to break their bonding and linkages, and once these are broken.

The fact that decreasing tendency of porosity is observed due to carbonization temperature increase inversely correlated with that of percent porosity of AASAC's, and this can be ascribed as to the significant amount of volatile matter released during carbonization. Tar derived from the degradation of hemicellulose and lignin not only blocks the pore structure but also obstructs the formation and development of new pores resulting in low total pore volume and specific surface area [21]. The effect of iodine number adsorption of AASAC's results showed a reduction in the adsorptive capacity of carbon value. It is an indication of the beginning of structural deformation, and the activation temperature had a significant influence on the iodine number too. Increasing the temperature to 600°C and beyond will lead to the decrease of iodine number value [22]. Iodine number is a measure of activity level and the micropore content of the activated carbon; a higher number indicates a higher degree of activation [23].

3.2. Effects of Carbonization Temperature on Removal Efficiency. The temperature variance in the production of AASAC yielded the variation in removal efficiency from 97.9 to 77.5% for the solution containing initial metal ion concentration of 100 mg L^{-1}, AASAC dose of 2 g, and pH 5 (Table 1). The reduction in removal might be due to a decrease in porosity of AASAC from 0.704% to 0.6926% up on increment with temperature which is due to the thermal influence and the lack of active site on the adsorbent; longer activation can lead to a higher weight loss of carbon precursor or formation of ash [24]. The maximum porosity occurs during the optimal activation process. When the process is carried out at elevated temperature, it depends upon whether the agricultural product or the naturally existing amorphous carbon structure has been distracted. The situation leads to unfavorable adsorption conditions or weak performance of the products [21]. Based on the primary characterization of three samples, the AASAC1 is found to be a better adsorbent. Hence the further instrumental characterizations and Pb (II) adsorption studies at varied parameters have proceeded with only AASAC1.

3.3. SEM Analysis of AASAC1. The surface texture and porosity of AASAC1 in a secondary electron image mode showed the presence of an organized pore region in the fibrovascular bundle wall (Figure 1(a)). The activated carbon surface has abundant pores characterized by thick pore walls and circular pores. The pores on the surface could be macropores which lead to the branching micropores in the interiors of the activated carbon [25]. Figure 1(b) shows the changes in some parts of the surface particles with native biosorbent which depicts that Pb (II) ion has deposited as aggregates in the AASAC1. The surface nature of the AASAC1 is highly supportive of the physical adsorption, which provides an active site to the positive contaminant, and the ion can easily enter at the existing pores, but the interaction may not be strong enough to separate the contaminant from the solution.

Table 1: Physicochemical and Pb (II) removal characteristics of AASAC.

Parameters	Activated carbon samples		
	AASAC 1 (500°C)	AASAC 1 (600°C)	AASAC 1 (700°C)
Proximate analysis (%)			
Moisture	7.7	7.01	6.20
Ash	3.5	4.73	5.53
Yield	40.6	38.04	36.01
Volatile matter	23.4	22.27	21.07
Porosity (%)	0.704	0.6962	0.6926
Volatile matter (%)	23.4	22.27	21.07
Specific gravity (gm/cm3)	1.470	1.486	1.550
Pb (II) removal (%)	99.8	86.3	77.5

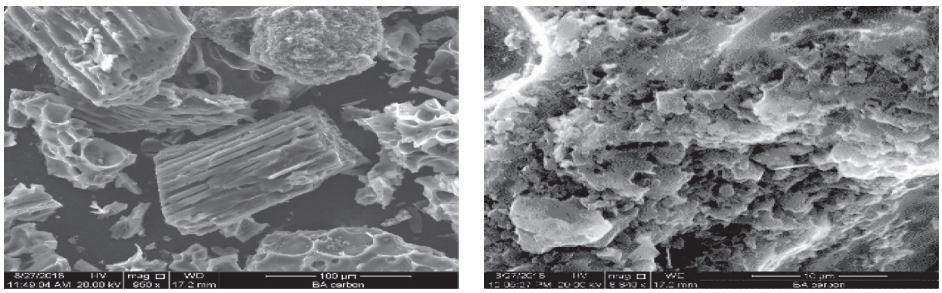

(a) (b)

Figure 1: SEM micrograph of BMSAC1 (before (a) and after (b) adsorption).

3.4. FTIR Analysis of AASAC1. FTIR spectrum results revealed the presence of different surface functional groups of AASAC1 in Figure 2. Functional groups in the adsorbent are contributed significantly to enhance the adsorption efficiency of the activated carbon by surface complexation [26]. The assignment of peaks at specific wavenumbers is listed in Table 2. The band observed at 1630 cm^{-1} is assigned to C=C bond (Alkane), and the bands 1315 and 1210 cm^{-1} are assigned to C–O stretch (alcohols, ethers, acids, and esters) [27]. These peaks which correspond to different functional groups are possible sites for the adsorption of this metal ion by the adsorbents. The peak intensities indicate that especially the OH groups, the C–O stretch of either alcohol, ethers, carboxylic acids or esters, the N–H stretch of the primary or secondary amines, N–H bend of the amine or amides, and the C=C stretch of the alkenes may play a major role in the adsorption of Pb (II) from aqueous solution. These functional groups contain either π-electron which is electron rich in or lone pairs on nitrogen or oxygen, with which they can coordinate with the metal ion leading to adsorption [28]. Many wavenumbers of AASAC1 are found to differ after adsorption (Figure 2(b)) when compared to before adsorption, which is attributed to a shift during the adsorption process.

3.5. XRD Analysis of AASAC1. The X-ray diffraction was used to investigate the surface structure of locally produced AASAC1, based on the diffraction pattern; the crystalline and graphite structures in the matrix were analyzed. Figure 3 shows seven broad intense peaks around 35, 45, 50, 52, 69, and 72. The peak that forms at $2\Theta = 35$ degrees shifts to a low angle in the case of KOH-activated AASAC1, which mean that their amorphous structures are strengthened. In other words, their graphitic microcrystalline is destroyed more severely, which may lead to the widening of pores because the walls are containing graphitic microcrystalline [29].

3.6. Effects of Solution pH on the Adsorption Process. The removal efficiency greatly increased from pH 3 (70.37%) to pH 5 (99.8) and then decreased slightly with pH 6 (90.8%) (Figure 4(a)). These phenomena attribute to the interaction of the positive ion with the AASAC1 surface metal ion. At higher than 7, the precipitation of Pb (II) ion takes place [30]. Such a trend can be explained based on a surface charge on the adsorbent and speciation of Pb (II) [17]. At low pH, the surface of the adsorbent was surrounded by H^+ ions which could compete with Pb (II) ion surface adsorption sites, thereby preventing the Pb (II) ion from approaching the binding sites on the adsorbent. With the increase of pH, some of the adsorption sites are deprotonated and Pb (II) ions are adsorbed along with H^+ ions, and when pH is higher than 5, competition between H^+ and Pb (II) ion for surface adsorption sites decreases. At the same time, the negative charge density on the carbon surface increases due to deprotonation of the H^+ ions containing sites, thereby improving the adsorption capacity towards Pb (II) ion [30]. Researchers also found an optimum pH obtained at 5.50 for removal of Pb (II) based on the sensitivity [31, 32]. pH value significantly influences the adsorption behavior; it leads to

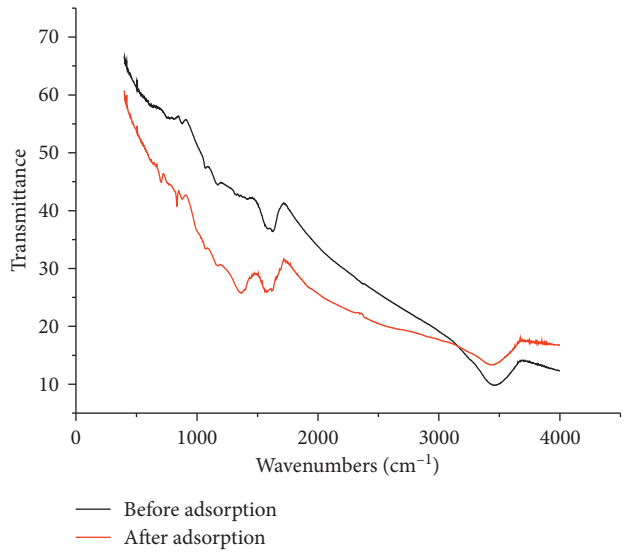

Figure 2: FTIR spectra for BMSAC1 (before (a) and after adsorption (b)).

Table 2: FTIR spectral characteristics of AASAC1 before and after adsorption.

Wavenumber (cm^{-1})		Assignment
Before	After	
3454	3384	O-H stretching in a hydrogen bond
1612	1630	C=C alkane, C=O
1315	1516	C-C=C asymmetric stretch, N=O stretch, N=O bend
1167	1210	C=O stretch, C-O alcoholic stretch, carboxylic acid, anhydrides
782	503	Aromatic (out-of-plane band)

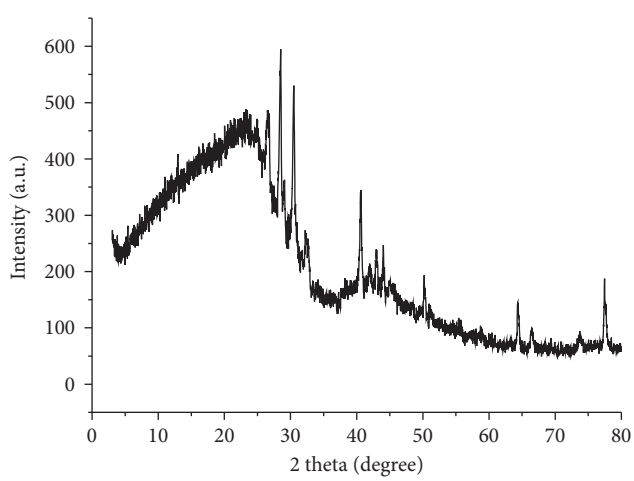

Figure 3: XRD analysis of BMSAC1.

precipitation of the metal which is very likely to occur in environments with high pH (above 7), in which there are also carbonates, sulfur, or phosphate with which it can react [33]. Also, above the pH neutral area, the Pb(II) adsorption is very low because of the precipitation matter [34].

3.7. Effects of Initial Metal Ion Concentration on Adsorption. The Pb (II) removal efficiency was observed optimum as 99.8% at 50 mg L^{-1} and found to be decreased as 98.2 (100 mg L^{-1}) and 94.2 (150 mg L^{-1}) with the increment of Pb (II) ion concentration which increases the number of available molecules per binding sites of the adsorbent (Figure 4(b)). An increase in initial metal ion concentration enhances the interaction between the metal molecules and the surface of the adsorbent [35]. Meaning, it provides a driving force to overcome mass transfer resistance between the biosorbent and biosorption medium. The effect of initial concentration is more efficient at low Pb (II) concentration. This is because at low Pb (II) concentration, the ratio of the adsorption site to the total mean ions in the solution is high, and hence all the Pb (II) may interact with the adsorbent and finally be removed from the solution [30]. Concentration increases with a greater number of ions and the same charge to be adsorbed and compete for the same adsorption sites. This may cause to leave many ions without being adsorbed and to decrease the efficiency of removal upon increase of the concentration of Pb (II) ion. At higher initial solution concentration, the total available adsorption sites are limited, thus resulting in a decrease in the percentage of removal of metal ion [36].

3.8. Effects of AASAC1 Dose on Removal Efficiency of Pb (II). Determination of a suitable adsorbent dose is considered one of the important parameters to ensure optimal adsorption without losing adsorbents. The effect of the

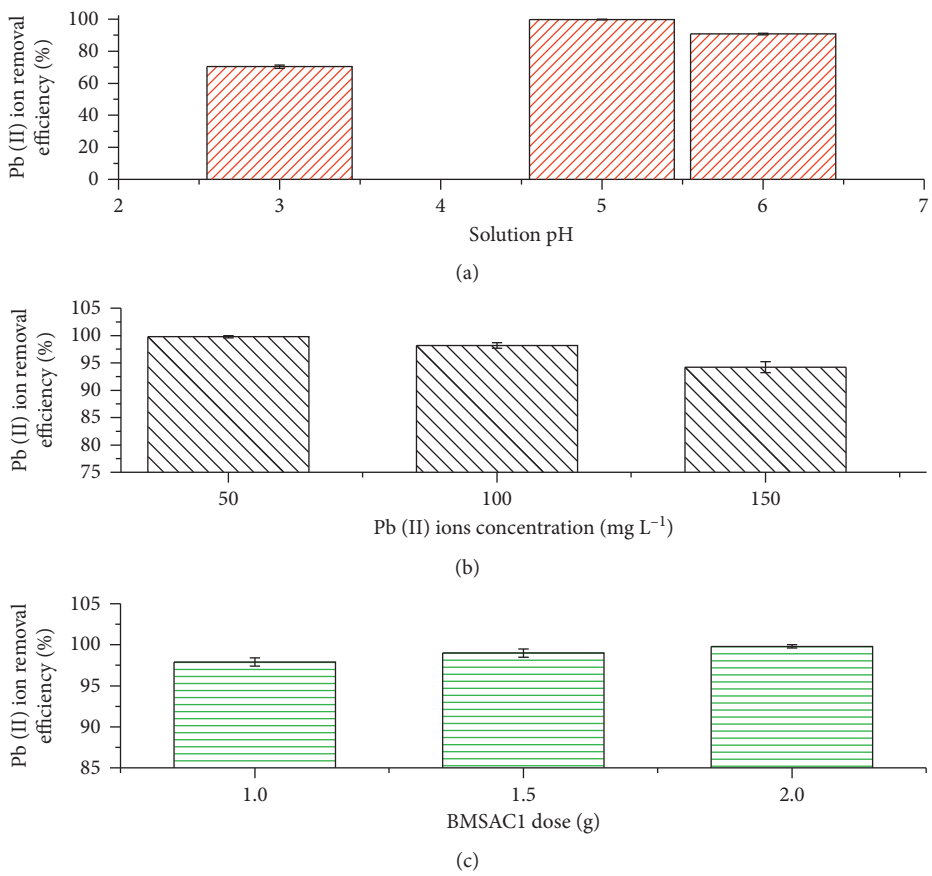

Figure 4: Effects of pH, Pb (II) ion concentration and adsorbent dose on Pb (II) removal efficiency of BMSAC1 in a synthetic solution.

adsorbent dose is shown in this study as 97.9% removal efficiency for 1 and it raised to 99% for 1.5 g adsorbent dose; however, a slight increase was observed for the 2 g adsorbent dose (Figure 4(c)). The percentage of metal sorbed increases with an increase in adsorbent dose for the heavy metals [37]. Since the quantity of metal ion is constant, an increase in the amount of adsorbent above a quantity that can completely adsorb the available metal ion had no apparent effect on a further increase of percent adsorption [25]. The percentage removals of metal increase rapidly with an increase in the dose of the adsorbents due to the greater availability of the exchangeable sites or surface area [38].

3.9. Effect of Pb (II) Concentration, Dose, and pH versus Removal Efficiency (%). The interaction of the three independent variables, initial Pb (II) ion concentration, and pH of the solution has indirect relationships, at each condition from 50 mg L^{-1} to 150 mg L^{-1}, while there is a constant adsorbent dose (2 g), at lower pH (3) percent removal efficiency, whereas at low initial Pb (II) ion concentration, removal efficiency increases, while above 50 mg L^{-1} of initial concentration, the removal efficiency starts to decline, in Figure 5(a). Varying the independent variables that are pH and adsorbent dose while initial Pb (II) ion concentration is constant, both variables pH from (3 to 5) and adsorbent dose from (1 g to 2 g), it increases the removal efficiency of AASAC1; however, in a certain pH >5, it starts to slow the removal efficiency of AASAC1 (Figure 5(b)), and the reason for this has been discussed in the above section.

3.10. Equilibrium Sorption Study. Sorption studies describe the interaction of adsorbates with adsorbents and establish the equilibrium between the adsorbed metal ion and the residual metal ion in solution during the surface sorption. The plot in Figure 6(a) has an R^2 value of 0.9232 with a slope and intercepts value of 0.2091, respectively. The Freundlich parameters (K_f and n) for adsorption of the Pb (II) ion into AASAC1 are determined from the slope and intercept values of the equilibrium data well fitted in this isotherm which means it had a greater R^2 value, indicating that sorption of Pb (II) metal ion studied adsorbents was favorable. The higher value of the coefficient of regression $R^2 = 0.9496$ was obtained (Figure 6(b)) for the adsorption of metal ion Pb (II) ion. It was clear that the adsorption of lead onto bamboo-activated carbons derived from these adsorbents obeys the Freundlich isotherm model.

3.11. The Efficiency of AASAC1 for Real Industrial Wastewater. In conclusion, the experiment was carried out on real waste samples to check the viability of the adsorbent in the real wastewater. The paint industry wastewater treated with AASAC1 has shown a significant improvement in its

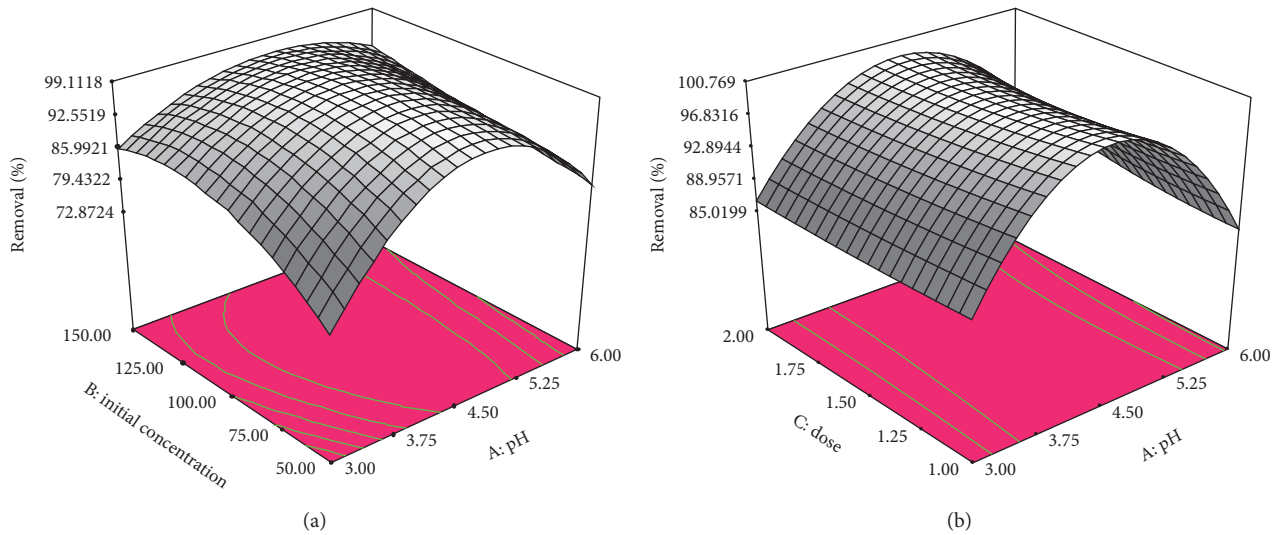

Figure 5: 3D plots for the effect of the combined factors on removal efficiency. Pb^{2+} concentration and pH on removal (a) and initial adsorbent dose and pH on removal (b).

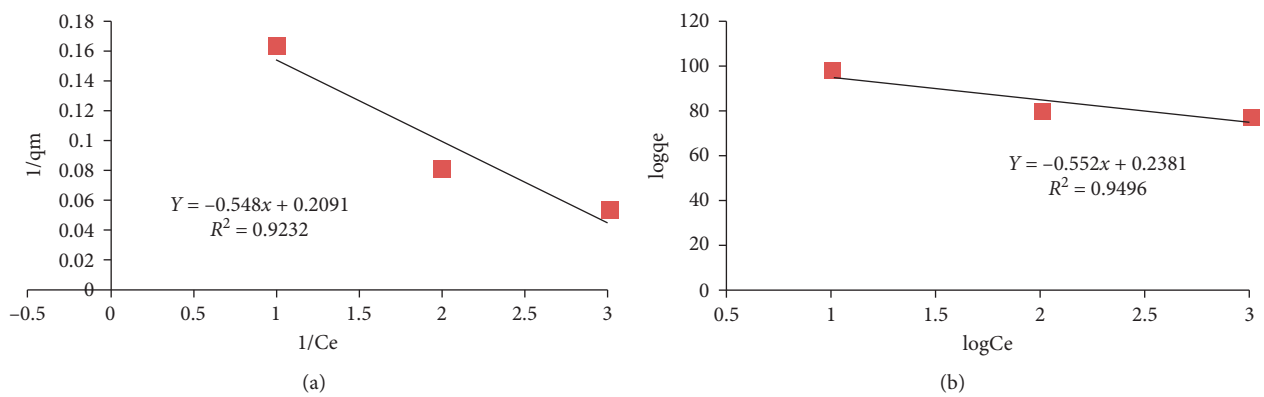

Figure 6: Langmuir (a) and Freundlich (b) adsorption isotherm for adsorption of Pb (II) on BMSAC (pH: 5, adsorbent dose: 2 g and contact time 120 mins).

Table 3: Real paint industry wastewater (untreated and treated) characteristics.

Parameters	Unit	Untreated wastewater	Treated wastewater
pH	pH unit	5.5	6.5
Turbidity	NUT	255	10
BOD_5	mg L^{-1}	171	25
COD	mg L^{-1}	2402	150
TSS	mg L^{-1}	619	138
Pb (II)	ppm	2.99	0.428

physicochemical characteristics (Table 3). The wastewater initially contained 2.99 ppm of Pb (II) metal ion which is reduced to 1.185 ppm, pH of the treated wastewater nearly 6.5 after adsorption with AASAC1. However, the removal efficiency of AASAC1 in synthetic aqueous solution (99.8%) is declined to 60.42% in real industrial wastewater. This is due to the nature of synthetic wastewater containing individual ion, where the real wastewater containing mixed pollutant in the solution affected the removal efficiency by competing for one another to the adsorbent site.

4. Conclusion

This study concentrated on Pb (II) ion removal from aqueous solution using Ethiopian bamboo activated carbon with an extended application on real paint industry wastewater. The characterization of AASAC1 indicated its excellent capacity of removing Pb (II) from aqueous solution and average capacity in paint industry wastewater. Among the tested operational parameters conditions, the better range is found as 2 g adsorbent dosage, 200 rpm agitation speed with the contact time of 120 min, and the pH 5. At lower temperature 500°C and more holding time (3 h), it was observed that greater iodine values were recorded, the residual volatile matter was completely released, and more microporous structures have developed. Greater R^2 value indicated the sorption of Pb (II) ion into AASAC1 favorable to Freundlich isotherms. The study suggests that the

AASAC1 mediated adsorption is effective in the removal of Pb (II) ions from synthetic aqueous solution. However, it is recommended for in-depth analysis and further studies to know its application behavior in real industrial wastewater.

Data Availability

Data are available from the corresponding author upon request.

Conflicts of Interest

The authors have no conflicts of interest.

Acknowledgments

The authors would like to thank Ethiopian Road Authority for financial support.

References

[1] H. M. Zwain, M. Vakili, and I. Dahlan, "Waste material adsorbents for zinc removal from wastewater: a comprehensive review," *International Journal of Chemical Engineering*, vol. 2014, Article ID 347912, 13 pages, 2014.

[2] M. R. Awual, "Assessing of lead(III) capturing from contaminated wastewater using ligand doped conjugate adsorbent," *Chemical Engineering Journal*, vol. 289, pp. 65–73, 2016.

[3] M. R. Awual, "An efficient composite material for selective lead(II) monitoring and removal from wastewater," *Journal of Environmental Chemical Engineering*, vol. 7, no. 3, Article ID 103087, 2019.

[4] M. R. Awual and M. M. Hasan, "Novel conjugate adsorbent for visual detection and removal of toxic lead(II) ions from water," *Microporous and Mesoporous Materials*, vol. 196, pp. 261–269, 2014.

[5] L. Jin and R. Bai, "Mechanisms of lead adsorption on chitosan/PVA hydrogel beads," *Langmuir*, vol. 18, no. 25, pp. 9765–9770, 2002.

[6] D. W. O'Connell, C. Birkinshaw, and T. F. O'Dwyer, "Heavy metal adsorbents prepared from the modification of cellulose: a review," *Bioresource Technology*, vol. 99, no. 15, pp. 6709–6724, 2008.

[7] S. M. Beyan, S. V. Prabhu, T. T. Sissay, and A. A. Getahun, "Sugarcane bagasse based activated carbon preparation and its adsorption efficacy on removal of BOD and COD from textile effluents: RSM based modeling, optimization and kinetic aspects," *Bioresource Technology Reports*, vol. 14, Article ID 100664, 2021.

[8] K. Embaye, "The indigenous bamboo forests of Ethiopia: an overview," *AMBIO: A Journal of the Human Environment*, vol. 29, no. 8, pp. 518–521, 2000.

[9] J. Lin, S. Gupta, T. Loos, and R. Birner, "Opportunities and challenges in the Ethiopian bamboo sector: a market analysis of the bamboo-based value web," *Sustainability*, vol. 11, no. 6, p. 1644, 2019.

[10] S. Tadesse and D. Ambo, "Removal of basic dye from aqueous medium using activated carbon from Erythrina brucei, Arundinaria alpina and manihot esculenta," *Food Science and Quality Management*, vol. 86, pp. 19–27, 2019.

[11] K. Ukanwa, K. Patchigolla, R. Sakrabani, E. Anthony, and S. Mandavgane, "A review of chemicals to produce activated carbon from agricultural waste biomass," *Sustainability*, vol. 11, no. 22, pp. 6204–6235, 2019.

[12] Y. Alhamed, "Activated carbon from dates' stone by ZnCl2 activation," *Journal of King Abdulaziz University-Engineering Sciences*, vol. 17, no. 2, pp. 75–98, 2006.

[13] ASTM D2866-11, *Standard Test Method for Total Ash Content of Activated Carbon*, ASTM International, West Conshohocken, PA, USA, 2018, http://www.astm.org.

[14] ASTM D5832-98, *Standard Test Method for Volatile Matter Content of Activated Carbon Samples*, ASTM International, West Conshohocken, PA, USA, 2014, http://www.astm.org.

[15] ASTM D2854-09, *Standard Test Method for Apparent Density of Activated Carbon*, ASTM International, West Conshohocken, PA, USA, 2019, http://www.astm.org.

[16] ASTM D2867-17, *Standard Test Methods for Moisture in Activated Carbon*, ASTM International, West Conshohocken, PA, USA, 2017, http://www.astm.org.

[17] M. R. Awual and M. M. Hasan, "A ligand based innovative composite material for selective lead(II) capturing from wastewater," *Journal of Molecular Liquids*, vol. 294, Article ID 111679, 2019.

[18] ASTM E70-19, *Standard Test Method for pH of Aqueous Solutions With the Glass Electrode*, ASTM International, West Conshohocken, PA, USA, 2019, http://www.astm.org.

[19] ASTM D888-18, *Standard Test Methods for Dissolved Oxygen in Water*, ASTM International, West Conshohocken, PA, USA, 2018, http://www.astm.org.

[20] M. Ahmedna, "Granular activated carbons from agricultural by-products: preparation, properties, and application in cane sugar refining," in *LSU Agricultural Experiment Station Reports*, LSU AG Center, Baton Rauge, LA, USA, 2000, http://digitalcommons.lsu.edu/agexp/456.

[21] P.-H. Huang, J.-W. Jhan, Y.-M. Cheng, and H.-H. Cheng, "Effects of carbonization parameters of moso-bamboo-based porous charcoal on capturing carbon dioxide," *The Scientific World Journal*, vol. 2014, Article ID 937867, 8 pages, 2014.

[22] B. Prakashkumar, K. Shivakamy, L. Miranda, and M. Velan, "Preparation of steam activated carbon from rubberwood sawdust (Hevea brasiliensis) and its adsorption kinetics," *Journal of Hazardous Materials*, vol. 136, no. 3, pp. 922–929, 2006.

[23] F. T. Ademiluyi and E. O. David-West, "Effect of chemical activation on the adsorption of heavy metals using activated carbons from waste materials," *ISRN Chemical Engineering*, vol. 2012, Article ID 674209, 5 pages, 2012.

[24] K. L. Wasewar, M. Atif, B. Prasad, and I. M. Mishra, "Adsorption of zinc using tea factory waste: kinetics, equilibrium and thermodynamics," *CLEAN-Soil, Air, Water*, vol. 36, no. 3, pp. 320–329, 2008.

[25] H. Xia, J. Wu, C. Srinivasakannan, J. Peng, and L. Zhang, "Effect of activating agent on the preparation of bamboo-based high surface area activated carbon by Microwave heating," *High Temperature Materials and Processes*, vol. 35, no. 6, pp. 535–541, 2016.

[26] T. Dula, K. Siraj, and S. A. Kitte, "Adsorption of hexavalent chromium from aqueous solution using chemically activated carbon prepared from locally available waste of bamboo (oxytenanthera abyssinica)," *ISRN Environmental Chemistry*, vol. 2014, Article ID 438245, 9 pages, 2014.

[27] W. Kidus Tekleab, S. M. Beyan, S. Balakrishnan, and H. Admassu, "Chicken feathers based Keratin extraction process data analysis using response surface-box-Behnken design method and characterization of keratin product," *Current Applied Science and Technology*, vol. 20, no. 2, pp. 163–177, 2020.

[28] S. Odoemelam, F. Onwu, S. Uchechukwu, and M. Chinedu, "Adsorption isotherm studies of Cd(ll) and Pb(ll) ions from aqueous solutions by bamboo-based activated charcoal and bamboo dust," *American Chemical Science Journal*, vol. 5, no. 3, pp. 253–269, 2015.

[29] Y. Gao, Q. Yue, B. Gao, and A. Li, "Insight into activated carbon from different kinds of chemical activating agents: a review," *Science of the Total Environment*, vol. 746, Article ID 141094, 2020.

[30] Y. Wang, X. Wang, X. Wang et al., "Adsorption of Pb(II) from aqueous solution to Ni-doped bamboo charcoal," *Journal of Industrial and Engineering Chemistry*, vol. 19, no. 1, pp. 353–359, 2013.

[31] M. R. Awual, "Novel conjugated hybrid material for efficient lead(II) capturing from contaminated wastewater," *Materials Science and Engineering: C*, vol. 101, pp. 686–695, 2019.

[32] M. R. Awual, A. Islam, M. M. Hasan et al., "Introducing an alternate conjugated material for enhanced lead(II) capturing from wastewater," *Journal of Cleaner Production*, vol. 224, pp. 920–929, 2019.

[33] V. Godoy, G. Blázquez, M. Calero, L. Quesada, and M. A. Martín-Lara, "The potential of microplastics as carriers of metals," *Environmental Pollution*, vol. 255, Article ID 113363, 2019.

[34] M. R. Awual, "Innovative composite material for efficient and highly selective Pb(II) ion capturing from wastewater," *Journal of Molecular Liquids*, vol. 284, pp. 502–510, 2019.

[35] W. Zhang, Y. An, S. Li et al., "Enhanced heavy metal removal from an aqueous environment using an eco-friendly and sustainable adsorbent," *Scientific Reports*, vol. 10, no. 1, Article ID 16453, 2020.

[36] F. Y. Wang, H. Wang, and J. W. Ma, "Adsorption of cadmium (II) ions from aqueous solution by a new low-cost adsorbent-Bamboo charcoal," *Journal of Hazardous Materials*, vol. 177, no. 1-3, pp. 300–306, 2010.

[37] M. Nur-E-Alam, M. Abu Sayid Mia, F. Ahmad, and M. Mafizur Rahman, "Adsorption of chromium (Cr) from tannery wastewater using low-cost spent tea leaves adsorbent," *Applied Water Science*, vol. 8, no. 5, p. 129, 2018.

[38] Y.-J. Zhang, J.-L. Ou, Z.-K. Duan, Z.-J. Xing, and Y. Wang, "Adsorption of Cr(VI) on bamboo bark-based activated carbon in the absence and presence of humic acid," *Colloids and Surfaces A: Physicochemical and Engineering Aspects*, vol. 481, pp. 108–116, 2015.

Hindawi
Journal of Chemistry
Volume 2021, Article ID 9940577, 11 pages
https://doi.org/10.1155/2021/9940577

Research Article

K_2CO_3-Activated Pomelo Peels as a High-Performance Adsorbent for Removal of Cu(II): Preparation, Characterization, and Adsorption Studies

Zheng Liu and Yuling Wei

School of Environmental Science and Engineering, Xiamen University of Technology, Xiamen, China

Correspondence should be addressed to Zheng Liu; liuzh@xmut.edu.cn

Received 18 March 2021; Accepted 5 June 2021; Published 16 June 2021

Academic Editor: Ibrahim H. Alsohaimi

Activated carbons (ACs) were prepared from pomelo peels by K_2CO_3 activation and used as an adsorbent (PAC) for the removal of Cu(II) from aqueous solutions. BET, SEM, and FT-IR were employed for the characterization of the obtained ACs. The optimum ACs were reported at activation temperature of 850°C, activation time of 60 min, and impregnation ratio of 3, which had a high surface area (1213 m^2/g) and total pore volume (0.57 cm^3/g). The resulting ACs were used for the adsorption of Cu(II) from aqueous solutions in the batch mode and yielded a superior adsorption capacity of 139.08 mg/g. The pH of optimum adsorption was determined as 5. Pseudo first-order model, pseudo second-order model, and intraparticle diffusion model were applied to describe the adsorption processes. The adsorption kinetic data were found to follow the pseudo second-order model. The adsorption isotherms data were analyzed using Langmuir, Freundlich, Temkin, and Dubinin–Radushkevich models. The Langmuir model was found to provide the best fit, and the calculated adsorption capacity was 151.35 mg/g.

1. Introduction

Heavy metal contamination in municipal or industrial wastewater has been a global environmental issue [1]. Most heavy metals (e.g., Cr, Mn, Ni, and Cd) can cause serious damage for ecological systems and public health when their concentrations were in excess [2].

Copper (Cu) is a widely used heavy metal and the main raw material of electroplate, electronics, and cable manufactures [3]. It is an indispensable trace metal for the metabolism and human health in low concentration, but chronic exposure or excessive ingestion may lead to Wilson's disease and damage of digestive system, kidney, or liver [4, 5]. The World Health Organization and European Union propose the maximum level of Cu in drinking water is 2 mg/l [6].

There are various techniques for the treatment of Cu from industrial effluents and wastewaters, such as chemical precipitation [7], flocculation [8], membrane filtration [9, 10], ion exchange [11], electrodialysis [12], and flotation [13]. Among numerous treatment processes, activated carbons (ACs) adsorption is widely used because of its simple design, easy accessibility, and high efficiency [14]. The development of cheaper activated carbon is an important part of promoting its widespread use. Consequently, many recent studies focus on activated carbons produced from alternative low-cost waste biomass, such as hazelnut shell [15], *Ceiba pentandra* [16], bamboo [17], kenaf fiber [18], apricot stone [19], and rice husk [14]. Pomelo (*Citrus maxima*) is a widely cultivated citrus fruit in South China and Southeast Asia. China is a large pomelo producer, and about 1.5–2.5 million tons of pomelo peels are released each year [20]. However, most of pomelo peels are thrown away, giving rise to wasting resources and potential contamination.

Following the "treatment of waste by waste" strategy, this study selected pomelo peels as precursor for preparing ACs (PAC, defined as powdered AC prepared from pomelo peels) with two steps. A nonhazardous chemical (potassium

carbonate, K_2CO_3) was used as an activating reagent. The effects of three activation factors were discussed. The physical and chemical characteristics of the prepared PACs were investigated by BET adsorption, SEM, and FT-IR. Besides, the removal mechanisms of Cu(II) were explored by initial pH effects, adsorption isotherms and kinetic studies.

2. Materials and Methods

2.1. Materials and Regents. Pomelo peels were collected from a local fruit shop. The fresh peels were first dried in the sun naturally, followed by drying at 90°C for 24 h. Then they were smashed to 75–180 μm with a small disintegrator (Yongkang Boou 800Y). All chemicals used were purchased from Sinopharm Group and of analytical grade. Copper sulfate ($Cu_2SO_4{\cdot}5H_2O$) and distilled water were used for preparation of solutions contained Cu(II).

2.2. Preparation of PACs. The preparation processes of PACs were primarily including carbonization and activation [21]. In the carbonization process, the dried meal was put in a tubular stove (Hangzhou Zhuochi SK3-2-10-10) with N_2 flow at 550°C for 2 h. After carbonization, the material was impregnated with K_2CO_3 at different mass ratios (chemical: sample) for 2 h and then the mixture was put in a stove for activation at different activation temperature and different activation time (0.5, 1, 2, and 3 h). After reaction, the ACs (PACs) were repeatedly rinsed with 0.1 M HCl solution and distilled water to neutralize superfluous alkali [22]. Finally, PACs were sieved to 75–180 μm after drying at 90°C for 24 h. PACs obtained under different conditions were denoted as PAC*a-b-c*, where *a* (°C) was the activation temperature, *b* (*h*) was the activation time, and *c* was the impregnation ratio.

2.3. Characterization of PACs. The textural characterization was manifested by N_2 adsorption-desorption at -196°C using an automated surface area analyzer (TriStar II 3020). The specific surface area was obtained by the BET isotherm equation in the relative pressure of $P/P_0 = 0.995$. The pore size distributions of micropores (<2 nm) were calculated via the density functional theory (DFT) model. The volumes of mesopores and macropores (>2 nm) were calculated via the Barrett–Joyner–Halenda (BJH) method. The characteristics of the micropores were determined from the t-plot method. The SEM micrographs were using a scanning electron microscope (FEI Inspect F50) under high vacuum conditions. The spot size and acceleration voltage were set at 2.5 and 15 kV, respectively. The Fourier transform infrared (FTIR) spectrum of the PACs surface was investigated by Fourier transform infrared spectroscopy (Nicolet 380) in the range of 4000–400 cm^{-1} wavenumbers. FTIR spectra were recorded using KBr pellet technique with 32 scans at a resolution of 4 cm^{-1}.

2.4. Zeta Potential Measurements. The zeta potential of PACs was carried out as follows: 0.1000 g PACs was added to 20 ml of deionized water. Before adding the adsorbent, 0.1 M HCl was used to adjust the pH ranging from 2 to 5. 0.01 M $NaNO_3$ was used to maintain constant ionic strength of solution [23]. Subsequently, the PACs suspension was stirred in a rotary shaker (30°C, 180 r/min) for 24 h and then filtered by 0.45 μm filtering membrane. Finally, the zeta potential of the filtrate was analyzed by a particle size and zeta potential analyzer (Malvern Zetasizer Nano ZS90).

2.5. Adsorption Studies. For the adsorption experiments, the procedures were conducted as follows: 0.0500 g PACs was added to 200 ml of Cu(II) solution. The Cu(II) solution was prepared by adding the corresponding amount of $Cu_2SO_4{\cdot}5H_2O$ to distilled water. The mixed suspension was stirred in a rotary shaker (30°C, 180 r/min) until the adsorption equilibrium was reached. After reaction, the mixed suspension was filtered by 0.45 μm filtering membrane. The concentration of Cu(II) in solution was analyzed by an ICP-OES (PE DV7000). Experiments were carried out in triplicate.

The amount of Cu(II) adsorbed at equilibrium q_e (mg/g) was figured out by

$$q_e = \frac{(C_0 - C_e) \times V}{W}, \quad (1)$$

where C_0 and C_e (mg/l) were the initial concentration and equilibrium concentration of Cu(II), respectively, V (l) was the volume of Cu(II) solution, and W (g) was the mass of PACs.

2.5.1. Effect of the Initial pHs. The effect of pH on the adsorption capacity was investigated by using 0.0500 g of PAC850-1-3 at 30°C. ACs were added to 200 ml of Cu(II) solution (300 mg/l) with the initial pHs of 2, 3, 4, and 5. The pHs of solutions were measured by a desktop acidometer (Sartorius PB-10). The pHs were adjusted by adding of 0.1 M HCl and 0.1 M NaOH solutions to the initial Cu(II) solutions.

2.5.2. Kinetics and Isothermal Studies. Kinetics and isothermal studies were helpful to understand the adsorption mechanisms. Batch experiments of kinetics were carried out at 30°C with 200 ml of Cu(II) solution (100, 200, and 300 mg/l) at pH 5 using 0.0500 g of PAC850-1-3. The sampling and analysis were conducted at specified time intervals. Batch experiments of isotherms were carried out at 30°C with 200 ml of Cu(II) solution (100, 200, 300 400, and 500 mg/l) at pH 5 using 0.0500 g of PAC850-1-3. The sampling and analysis were conducted at equilibrium.

Several common models were used to fit the kinetics data, and isothermal data and average values were adopted in analysis. The equations, linear forms, and plotting methods of these models were listed in Table 1.

In the table, q_e is the amount of adsorbed Cu(II) (mg/g) at equilibrium; q_t is the amount of adsorbed Cu(II) at time t (mg/g); t is the contact time (min); k_1 is the pseudo first-order rate constant (1/min); k_2 is the pseudo second-order rate constant (g/mg·min); k_3 is the intraparticle diffusion

Table 1: Kinetic and isothermal models used in this study.

Kinetics model	Equation	Linear form	Plot
Pseudo first-order model	$dq_t/dt = k_1(q_e - q_t)$	$\ln(q_e - q_t) = \ln q_e - k_1 t$	$\ln(q_e - q_t)$ vs. t
Pseudo second-order model	$dq_t/dt = k_2(q_e - q_t)^2$	$t/q_t = 1/k_2 q_e^2 + 1/qt$	t/q_t vs. t
Intraparticle diffusion model	$q_t = k_3 t^{0.5} + C_i$	$q_t = k_3 t^{0.5} + C_i$	q_t vs. $t^{0.5}$
Isothermal model			
Langmuir model	$q_e = q_m b C_e / 1 + bC_e$	$C_e/q_e = 1/K_L q_m + 1/q_m C_e$	C_e/q_e vs. C_e
Freundlich model	$q_e = k_F C_e^{1/n}$	$\ln q_e = \ln K_F + 1/n \ln C_e$	$\ln q_e$ vs. $\ln C_e$
Temkin model	$q_e = \ln C_e^{A_T} e^{B_T}$	$q_e = B_T + A_T \ln C_e$	q_e vs. $\ln C_e$
Dubinin–adushkevich (D-R) model	$q_e = q_s e^{-\beta\varepsilon^2}$	$\ln q_e = \ln q_s - \beta\varepsilon^2$	$\ln q_e$ vs. ε^2

rate constant (mg/g·min$^{1/2}$); C_i is the intercept of intraparticle diffusion model; b is Langmuir model constant (l/mg); q_m is theoretical maximal sorption value (mg/g); C_e is the equilibrium concentration of Cu(II) (mg/l); K_L is Langmuir coefficient (l/mg); K_F is Freundlich coefficient ((mg/g)×(l/mg)$^{1/n}$); n is adsorption intensity; A_T and B_T are Temkin coefficients; q_s is the adsorption capacities (mol/g); β is the D-R model constant (mol^2/kJ^2); ε is the Polanyi potential, which was obtained by

$$\varepsilon = \mathrm{RT}\ln\left(1 + \frac{1}{C_e}\right). \quad (2)$$

The average relative error (ARE) was used to assess the fitness of kinetic and isotherm models, which was calculated as

$$\mathrm{ARE}\,(\%) = \frac{1}{n}\sum_{i=1}^{n}\left|\frac{q_{i,cal} - q_{i,\,\exp}}{q_{i,\,\exp}}\right| \times 100, \quad (3)$$

where n is the number of observations in the fit, $q_{i,\,\exp}$ (mg/g) is the observation from experiments, and $q_{i,cal}$ (mg/g) is the estimate from kinetic and isotherm equations.

3. Results and Discussion

3.1. Physicochemical Characteristics of PACs

3.1.1. N_2 Adsorption Isotherms. The adsorption isotherms help to identify the pore structures by adsorbing inert gases. Figure 1 presented the N_2 adsorption-desorption isotherms of PACs prepared under different activation temperatures and impregnation ratios.

According to the isotherm classification proposed by IUPAC, the adsorption isotherms of all samples basically belonged to type I isotherm [24]. When P/P_0 was relatively low (<0.05), the adsorption capacity suddenly increased with the raise of the relative pressure. This phenomenon suggested that there were a huge number of micropores in PACs [25]. In narrow micropores (molecular-sized micropores), enhanced interaction between adsorbent and adsorbate caused micropore filling, which increased the adsorptive capacity at low relative pressures [26].

At higher P/P_0, the isotherms appeared relatively flat, corresponding to monolayer adsorption and micropores with a narrow size range [27, 28]. When the saturation pressure was approached ($P/P_0 > 0.99$), condensation occurred, causing the curve to upwarp. Less obvious hysteresis

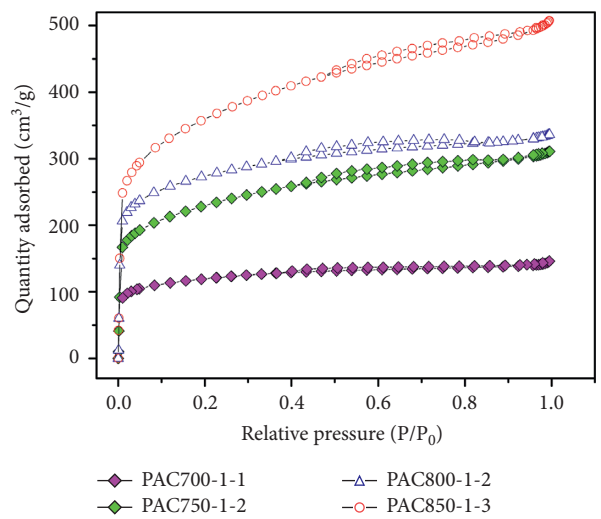

Figure 1: N_2 adsorption-desorption isotherms.

loops of type H4 were usually found in solids with narrow fissure pores. These loops were not clearly observed in Figure 1, suggesting that PACs also had a few mesopores [14].

3.1.2. Pore Structure. The adsorption performances of ACs were connected with specific surface areas and pore volumes. Table 2 presented the effect of activation process on specific surface area and pore volume of PACs. Three common operation parameters were discussed, namely, activation temperature, activation time, and impregnation ratio. The specific surface area of pomelo peel was only 2.15 m^2/g. After the physiochemical process, the specific surface areas of PACs were significantly increased, in the range from 771 to 1213 m^2/g.

PACa-1-2s were used to assess the effects of activation temperature (750, 800, 850, and 900°C) on the textural characteristics of PACs. When the temperature was increased from 750 to 850°C, the specific surface areas increased from 771 to 1006 m^2/g. The effects of activation temperature on the micropore volume and total pore volume followed the same trend. Furthermore, when the activation temperature increased from 750 to 850°C, the ratio of the pore volumes (V_{micro}/V_{total}) increased from 48.5% to 72.1%. However, when the activation temperature increased to 900°C, the specific surface area and V_{micro}/V_{total} decreased, which might be because that the consumption of

Table 2: Textural characteristics of PACs.

Material	Surface area	V_{micro}	V_{total}	V_{micro}/V_{total} (%)
Pomelo peel	2.15	—	0.0019	—
PAC750-1-2	771	0.16	0.33	48.5
PAC800-1-2	885	0.25	0.36	69.4
PAC850-1-2	1006	0.31	0.43	72.1
PAC900-1-2	896	0.23	0.37	62.2
PAC850-0.5-2	853	0.25	0.35	71.4
PAC850-1-2	1006	0.31	0.43	72.1
PAC850-2-2	1039	0.32	0.46	69.6
PAC850-3-2	872	0.22	0.36	61.1
PAC850-1-1	819	0.22	0.35	62.9
PAC850-1-2	1006	0.31	0.43	72.1
PAC850-1-3	1213	0.42	0.57	73.7

K_2CO_3 increased and the internal structure of PACs was destroyed by collapsing. These results were inferred that the appropriate temperature was helpful to the generation of new pores. During the formation of holes, the main reactions were as follows [29]:

$$K_2CO_3 + 2C \longrightarrow 2K + 3CO\ K_2CO_3 \longrightarrow K_2O + CO_2\ K_2O + C \longrightarrow 2K + CO \quad (4)$$

When the activation temperature was over the gasification temperature of potassium (770°C), the gaseous potassium could access the inside of material and consume the carbon atoms on the skeleton, which produced fresh pores.

PAC850-*b*-2s were used to assess the effects of activation time (0.5, 1, 2, and 3 h) on the textural characteristics of PACs. It was obvious the surface areas first rose then declined with increasing activation time. With the increasing activation time, more new holes were constantly generated, resulting in an increasing surface area and pore volume. But with much longer time, excessive burning of pores would occur, and some formed carbon could be enlarged or destroyed, resulting in elimination of surface area and pore volume.

PAC850-1-*c*s were used to assess the effects of impregnation ratio on the textural characteristics of PACs. From Table 2, it could be see that K_2CO_3 was a very efficient activating agent and activated carbons with high porosity were produced through the activation. Table 2 also showed that the impregnation ratio had a great influence on the formation of pores. The surface area of PACs increased from 819 to 1213 m^2/g with increasing the impregnation ratio from 1 to 3. The effects of the impregnation ratio on the micropore volume and total pore volume followed the same trend. It was widely believed that low impregnation ratio caused inadequate contact between activating agent and carbon [30]. Thus, incomplete activation induced limited generation of pores. As the impregnation ratio increased, sufficient contact improved the activation, which was favorable for enlarging pore volume and pore size [31, 32].

3.1.3. Pore Size Distribution. The pore size distribution was an important clue to reveal the adsorption mechanisms of porous materials. Figure 2 illustrated the pore size distributions of PACs. The pores of adsorbing material were usually divided into three categories: micropore (diameter < 2 nm), mesopore (2–50 nm), and macropore (>50 nm) [33]. It could be seen from Figure 2 that all PACs had narrow pore size distributions, including both micropores and mesopores. Most pores of PACs were composed of micropores with sizes ranging from 0.5 to 2.0 nm. All PACs also contained mesopores with narrow range from 2.0 to 8.5 nm. Moreover, Figure 2 presented PACs prepared at different conditions showed discrepant intensity of peaks. Stronger peaks appeared at micropore and mesopore regions of the sample prepared at higher activation temperature and bigger impregnation ratio.

3.1.4. SEM Analysis. The surface morphologies and structural properties of pomelo peel, carbonized pomelo peel, and PAC850-1-3 were investigated via FE-SEM. Figure 3(a) showed the external surface of pomelo peel was dense, neat, and imperforate. After carbonization, the surface was rougher and had some occasional crevices with few bits of pores (Figure 3(b)). This was probably because high temperature pyrolysis caused most organics (organic acid, cellulose, hemicelluloses, lignin, etc.) in pomelo peel to decompose and volatilize, leaving a small number of pores and the cracked surface of carbon.

On the contrary, PAC850-1-3 showed well-formed pores and honeycomb-like structure (Figure 3(c)). This change confirmed the successful preparation of PACs samples with large surface area and high total volume. The pore structures made possible more solutions to access the inside of PACs and were responsible for providing more active sites for adsorbing metal ions.

3.1.5. FTIR Analysis. The FTIR spectrum can provide valuable information about the functional groups on the surface of the material. Figure 4 gave the FTIR spectrum of pomelo peel and PAC850-1-3. It could be seen that PACs presented less and weaker absorption bands than pomelo peel, implying some functional groups presented in the precursor disappeared after physicochemical treatment.

The absorbance peaks of PAC850-1-3 at about 3410 and 2926 cm^{-1} indicated the presence of the stretching vibration of –OH groups (alcohols, phenols, and carboxylic acids) and C–H groups (alkanes), respectively. The peak at 1556 cm^{-1} could be the characteristics of C=O in the quinone structure. The peak of 1042 cm^{-1} suggested the C–O bonds stretching in some oxygen-containing functional groups. The peak of 673 cm^{-1} was ascribed to the out-of-plane bending of the C–H bonds in the arenes [34]. The absorbance peaks at 872 cm^{-1} were ascribed to the out-of-plane deformation of C–H bonds, which indicated that PAC850-1-3 was more inclined to chemisorption process [35].

3.2. Adsorption Studies

3.2.1. Effect of pH. The pH of the solution and the zeta potential of the surface had been identified as the key factors controlling metal ions adsorption because H^+ could compete

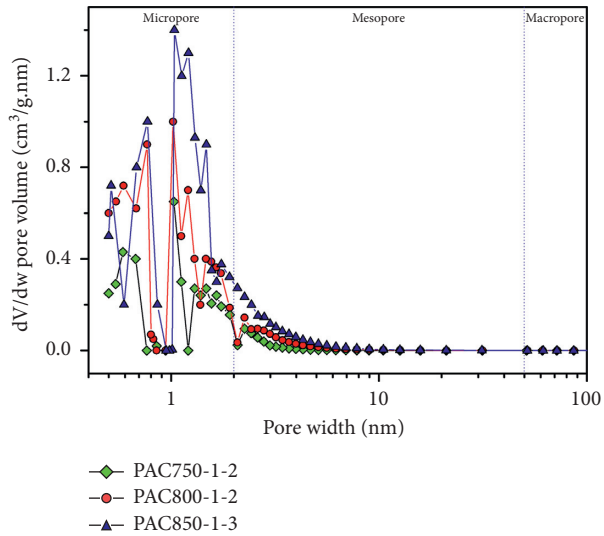

Figure 2: Pore size distribution of PACs.

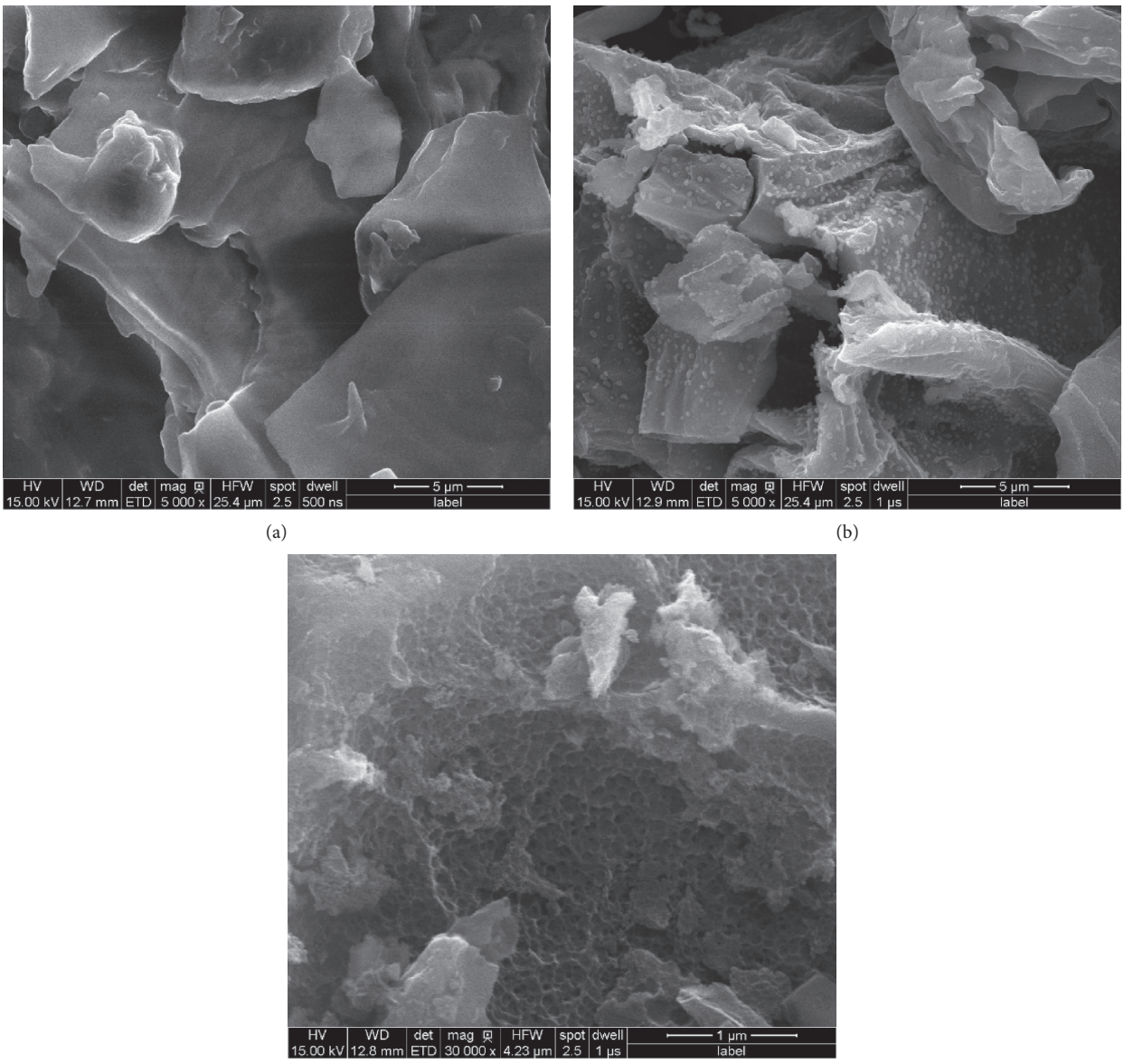

Figure 3: SEM of (a) pomelo peel, (b) carbonized pomelo peel, and (c) PAC850-1-3.

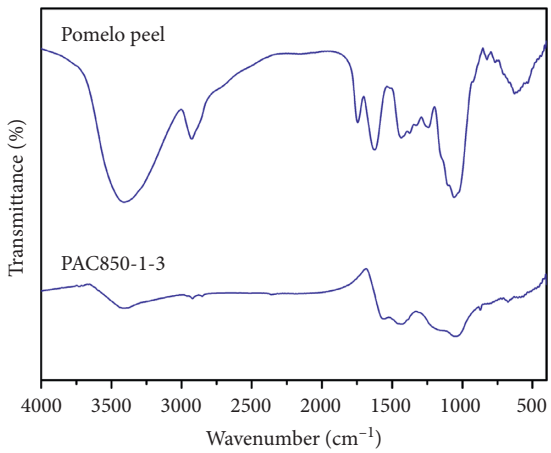

Figure 4: FTIR spectra of pomelo peel and PAC850-1-3.

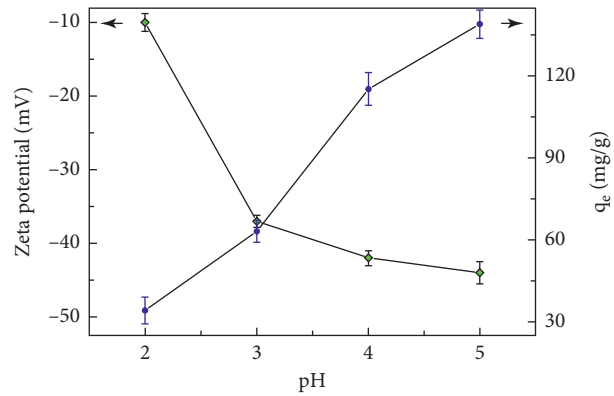

Figure 5: Zeta potential of PAC850-1-3 and the effect of pH on the adsorption capacity of Cu(II) (PACs dose: 0.0500 g; temperature: 30°C; pH: 2, 3, 4, 5; concentration of Cu(II): 100 mg/l). Error bars indicated standard deviation of three replicated experiments.

with metal cations for adsorption sites and the pH of the solution influenced the ionization of functional groups. The zeta potential of PAC850-1-3 and the effect of pH on the adsorption capacity were presented in Figure 5.

As we could see, the zeta potentials of PACs showed negative values in the pH range from 2 to 5. In further evaluation, the zeta potential was roughly −10 mV at pH 2 but fell fast to almost −40 mV at pH 3. As the pH increased from 3 to 5, the zeta potentials slowly descended to the lowest value. Lower zeta potential meant more negatively charged surface, which was in favor of the cations adsorption.

Figure 5 also showed the adsorption capacity of Cu(II) was 34.11 mg/g at pH 2 and then gradually increased to the highest value of 139.08 mg/g at pH 5. Increase in pH beyond 5 could cause precipitation of insoluble metal hydroxides, which would interfere with the adsorption process [36, 37].

When the pH was low, more and faster H^+ could compete with Cu(II) for the adsorption sites in ACs. More H^+ ions made the overall surface charge on PACs become less negative, which impeded the binding of electropositive Cu(II), resulting in lower adsorption. However, with increase in pH, there was a build-up of negatively charged surface, thus making for more Cu(II) removal. The adsorption capacities increased within the pH ranging from 2 to 5, which might be due to partial hydrolyzation of Cu(II). The influence of pH might be attributed to the interactions of Cu(II), $Cu(OH)^+$, and $Cu(OH)_2$ with functional groups at the surface of ACs, which were as follows [38]:

$$\begin{aligned} &R-OH_2^+ \longleftrightarrow R-OH+H^+ \\ &R-OH \longleftrightarrow R-O^- + H^+ \\ &R-O^- + Cu^{2+} \longleftrightarrow R-OCu^+ \\ &R-O^- + Cu(OH)^+ \longleftrightarrow R-OCu(OH) \end{aligned} \tag{5}$$

where R denoted the surface of ACs; $R-O^-$, $R-OH_2^+$, and $R-OH$ denoted different charged hydroxyl functional groups; $R-OCu^+$ and $R-OCu(OH)$ were the formation of the bonding complexes. In addition to the competition between H^+ and Cu(II) at low pH values, fewer deprotonation of functional groups ($R-O^-$, etc.) was adverse to formation of the bonding complexes [39].

Therefore, the best pH for Cu(II) removal was noted to be 5 and all the batch experiments were carried out at this pH.

3.2.2. Adsorption Kinetics. Adsorption kinetics were applied for investigating the efficiency of adsorption at the solid-solution interface. Figure 6 presented that the adsorption of Cu(II) onto PAC850-1-3 demonstrated a rapid velocity at the beginning stage and 50% of the total adsorption occurs within 10 min. This was probably because the adsorption active sites of PACs had not been occupied by Cu(II) at the beginning. Similar result was also reported by Kocabas-Atakli et al. [5]. In that report, the anatase nanoparticles was the adsorbent and the kinetic data of copper also followed the pseudo second-order model. Figure 6 also presented that the adsorbed amount increased with increasing initial concentration of Cu(II). This was probably because higher Cu(II) concentration provided more contact chances between ions and adsorption active sites.

The kinetics data were fitted with three models, which were presented in Figures 7(a)–7(c). Table 3 listed the corresponding kinetics parameters. Clearly, the pseudo second-order model gave higher R^2 and lower ARE, which meant better fit. This indicated that pseudo second-order model was more valid to interpret the adsorption behavior. Similar cases were also reported by other researchers [40, 41]. It could be concluded that chemisorption seemed to be the rate-limiting step which was related to bond forces via electrons sharing or exchange between Cu(II) and PACs.

The intraparticle diffusion model was fitted to understand the diffusion mechanism. As shown in Figure 7(c), all the lines had not passed through the origin, suggesting intraparticle diffusion process was not the rate-limiting step [42]. But intraparticle diffusion played an important part in adsorption process at lower concentration (100 mg/l), for the plots show better linearity. The plots at higher concentration (200 and 300 mg/l) reflected a two-stage process, with initial linear segment followed by plateau (black lines in

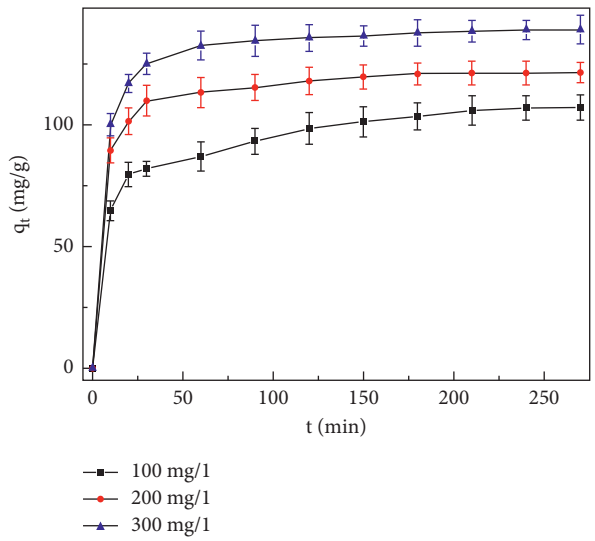

Figure 6: Effects of adsorption time on the adsorption of Cu(II) by PAC850-1-3 (PACs dose: 0.0500 g; temperature: 30°C; pH: 5; volume of of Cu(II) solution: 200 ml; concentration of Cu(II): 100, 200 and 300 mg/l). Error bars indicated standard deviation of three replicated experiments.

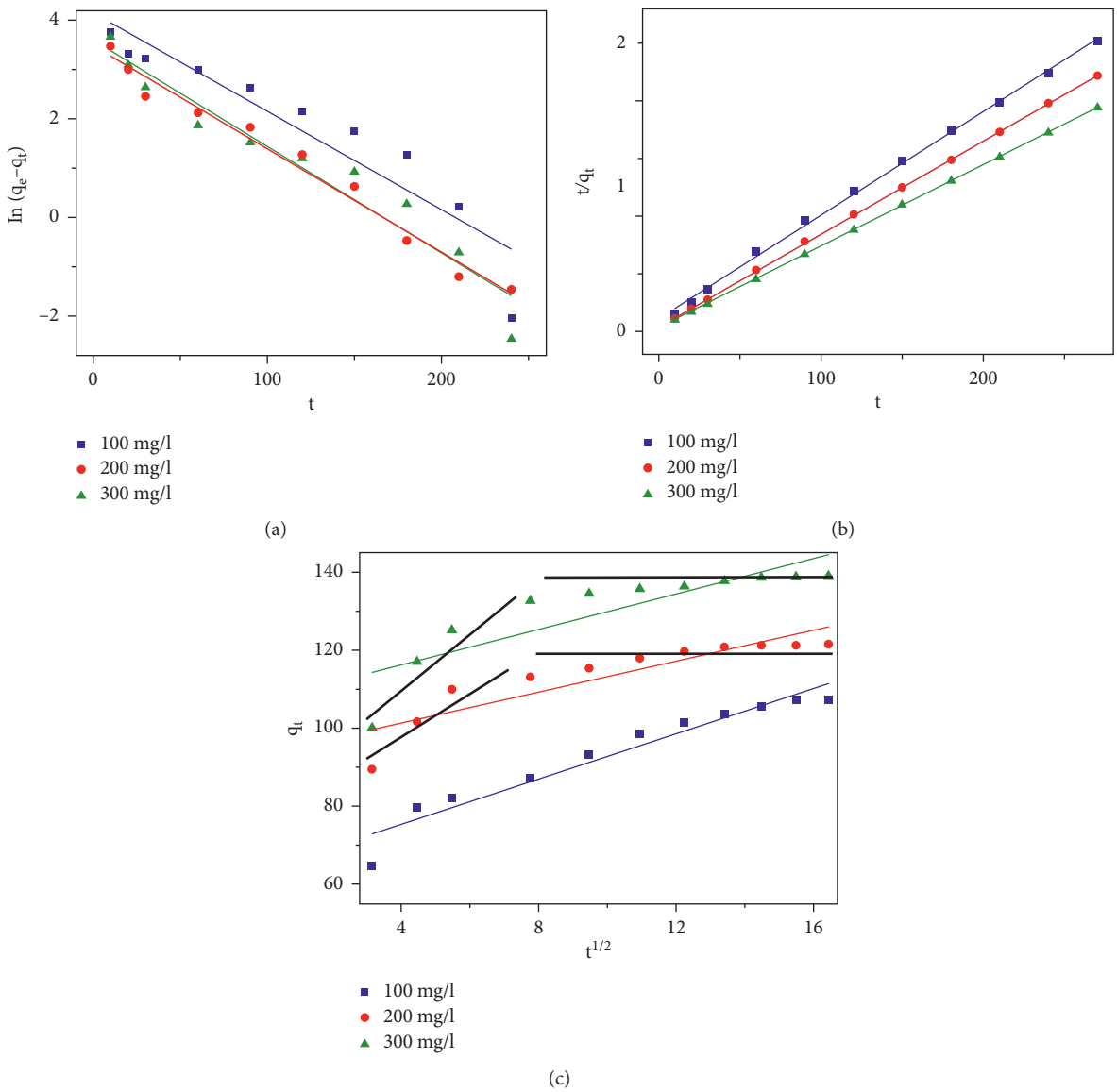

Figure 7: Kinetics of Cu(II) adsorption on PAC850-1-3: (a) pseudo first-order, (b) pseudo second-order, and (c) intraparticle diffusion model (PACs dose: 0.0500 g; temperature: 30°C; pH: 5; volume of of Cu(II) solution: 200 ml; concentration of Cu(II): 100, 200 and 300 mg/l).

Table 3: Parameters of kinetic models for Cu(II) adsorption onto PAC850-1-3.

C_0 (mg/l)				
Pseudo first-order model	$q_{e,cal}$ (mg/g)	k_1 (1/min)	R^2	ARE (%)
100	62.88	0.0199	0.8742	41.3
200	32.63	0.0209	0.9791	73.2
300	36.49	0.0216	0.9369	73.8
Pseudo second-order model				
	$q_{e,cal}$ (mg/g)	k_2 (g/mg·min)	R^2	ARE (%)
100	111.11	0.000749	0.9985	3.7
200	123.46	0.00172	0.9999	1.5
300	140.85	0.00170	1.0000	1.3
Intraparticle diffusion model				
	C (mg/g)	k_3 (mg/g·min$^{1/2}$)	R^2	ARE (%)
100	63.74	2.90	0.9361	4.0
200	93.42	1.98	0.7993	3.6
300	107.12	2.27	0.7389	3.8

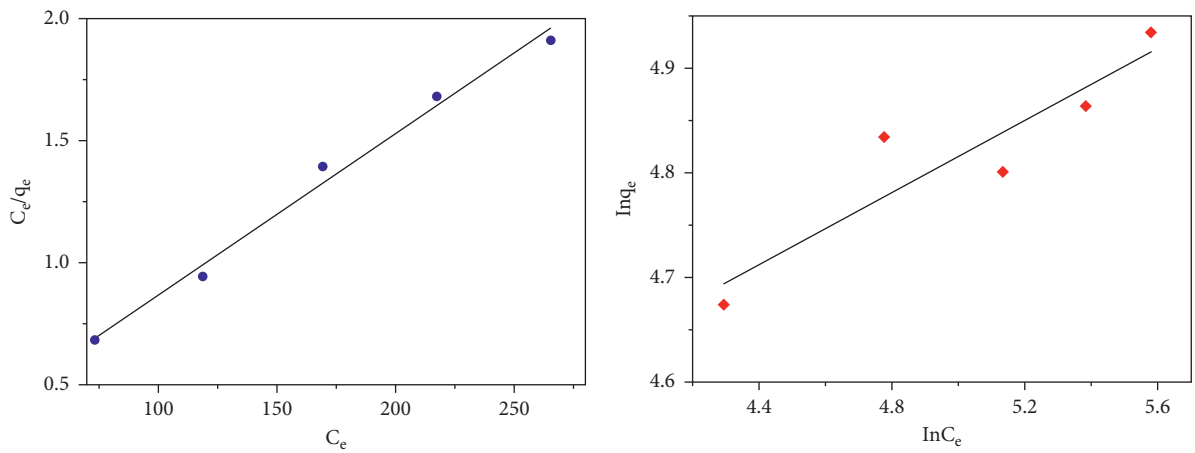

Figure 8: Adsorption isotherms of Cu(II) adsorption on PAC850-1-3: (a) Langmuir and (b) Freundlich (PACs dose: 0.0500 g; temperature: 30°C; pH: 5; volume of of Cu(II) solution: 200 ml; concentration of Cu(II): 100, 200, 300 400 and 500 mg/l).

Figure 7(c)). The initial linear segment implied the exterior surface adsorption, which was a comparatively quick stage. Subsequently, the intraparticle diffusion was quickly arrived and continued to about 70 min. Ultimately, 70 min later the adsorption slowly reached equilibrium. This indicated that the adsorption was a comparatively complicated process. The intercepts of fitted lines of this model gave an understanding of the thickness of boundary layer. The Cu(II) adsorption onto PACs at higher concentration showed greater boundary layer effect.

3.2.3. Adsorption Isotherms. Isothermal adsorption test is a very important way to understand the equilibrium relationship between adsorbate and adsorbent systems at a given temperature. They are also critical for improving the use of adsorbents. Different kinds of adsorption isotherm models have been developed to explicate different isotherm adsorption behavior. In this study, four well-known isothermal adsorption models were served to fit the equilibrium data, namely, Langmuir (Figure 8(a)), Freundlich (Figure 8(b)), Temkin models, and Dubinin–Radushkevich (D-R) model.

The Langmuir model is applied successfully in many monolayer adsorption processes [43, 44]. The Freundlich model is an empirical equation describing multilayer adsorption [45, 46]. The Temkin model also represents multilayer adsorption process considering the thermal effect of adsorption [47]. The D-R model can be used to determine whether the adsorption process was performed physically ($E < 8$ kJ/mol) or chemically ($8 < E < 16$ kJ/mol) [48]. The mean adsorption energy E (kJ/mol) was expressed as

$$E = \frac{1}{\sqrt{-2\beta}}. \tag{6}$$

Table 4 listed the isotherm parameters. The correlation coefficient R^2 was figured out from the corresponding plots in terms of Table 1. Besides, another separation parameter R_L computed from Langmuir isotherm parameters was given as [49]

Table 4: Adsorption isotherm parameters.

Model	Constants			
	q_m	K_L	R^2	ARE (%)
Langmuir	151.35	0.0320	0.990	3.12
	K_F	n	R^2	
Freundlich	52.16	5.804	0.843	3.03
	A_T	B_T	R^2	
Temkin	20.94	19.18	0.840	3.04
	q_s	β	R^2	
D-R	0.00327	$-2.219E-09$	0.845	3.03

Table 5: The comparison of absorption capacity for Cu(II) by PACs and other biomaterials.

Biomaterials	Adsorbent dose, g/ml	pH	q_m, mg/g	Best fit isotherms model	References
Sacha inchi shell	0.1/50	6.00	9.699	Langmuir	[50]
Tomato waste	0.2/50	2–8	22.37	Langmuir	[51]
Beech wood	Unrecorded	4.6–5.0	11–14	Unrecorded	[52]
Lyophilized-bleached almond shell	0.2/50	6	28.7	Langmuir	[53]
Rice straw	0.1/1000	5	29.8	Langmuir	[54]
Lobster shell	0.2/100	2–6	71.4	Langmuir, Freundlich	[55]
Kenaf fiber	0.1/20	5	57.14	Langmuir	[18]
Hazelnut shell	1.0/100	5.0	200	Langmuir, Freundlich	[56]

$$R_L = \frac{1}{1 + C_{0,\max} K_L}, \tag{7}$$

where $C_{0,\max}$ (mg/l) was the highest initial concentration in solution (here $C_{0,\max} = 300$) and K_L (l/mg) had been defined in (2). R_L was an indicator showing the adsorption process was desirable if $0 < R_L < 1$.

Figure 8(a) and Table 4 suggested that Langmuir model fitted better with the isothermal adsorption data ($R^2 = 0.990$ and ARE = 3.12%), when compared to the rest of models. This meant that if a Cu(II) occupied a position, no further adsorption could occur in that site. According to Langmuir model, the maximal monolayer adsorption capacity was calculated to be 151.35 mg/g. It indicated that this adsorbent was a more efficient absorbent than many other biomaterials in Table 5. R_L was calculated to be 0.0943, indicating favorable adsorption of Cu(II). The Freundlich coefficient n also measured the favorability of the adsorption process. In this study, n (5.804) was between 1 and 10, also suggesting favorable adsorption of Cu(II) [16, 57]. Furthermore, D-R model showed that the adsorption of Cu(II) onto PACs was supposed to be a chemisorption process because E had 15.0 kJ/mol, which was in line with the result of kinetics study.

4. Conclusions

Pomelo peel was used to produce activated carbons by K_2CO_3 activation. The removal of Cu(II) by produced ACs was studied in this work. The effects of activation temperature, activation time, and impregnation ratio on the performance of Cu(II) removal were examined. It was observed that there was a large amount of micropores in PACs. The best surface area (1213 m^2/g) and total pore volume (0.57 cm^3/g) were from PAC850-1-3. High temperature was helpful to the generation of more new pores. Appropriate activation time was very important to increase the surface area and pore volume. Higher impregnation ratio was favorable for larger surface area, pore volume, and pore size. Most pores of PACs were composed of micropores with sizes ranging from 0.5 to 2.0 nm. The pH value had a major impact on adsorption capacity and the best pH for adsorption was determined as 5.

Batch adsorption studies showed that the resulting ACs yielded a superior adsorption capacity of 139.08 mg/g. The adsorption process followed the pseudo second-order model at different initial concentrations, suggesting chemisorption seemed to be the rate-limiting step. Langmuir model fitted more closely to the equilibrium data of Cu(II) adsorption, which showed the value of Cu(II) adsorption was 151.35 mg/g. K_2CO_3 was corrosive to equipment, but PACs had a large adsorption capacity and might be considered as a high-performance adsorbent for the removal of Cu(II) from industrial effluents.

Data Availability

The data used to support the findings of this study are available from the corresponding author upon request.

Conflicts of Interest

The authors declare that they have no conflicts of interest.

Acknowledgments

This work was supported by Research Climbing Program of Xiamen University of Technology (XPDKQ19015 and

XPDKT20015) and the Education Department of Fujian Province (JAT200473).

References

[1] M. Hua, S. Zhang, B. Pan, W. Zhang, L. Lv, and Q. Zhang, "Heavy metal removal from water/wastewater by nanosized metal oxides: a review," *Journal of Hazardous Materials*, vol. 211, pp. 317–331, 2012.

[2] N. Dhouibi, H. Binous, H. Dhaouadi, and S. Dridi-Dhaouadi, "Hydrodistillation residues of Centaurea nicaeensis plant for copper and zinc ions removal: novel concept for waste re-use," *Journal of Cleaner Production*, vol. 261, 2020.

[3] M. Mushtaq, H. N. Bhatti, M. Iqbal, and S. Noreen, "Eriobotrya japonica seed biocomposite efficiency for copper adsorption: isotherms, kinetics, thermodynamic and desorption studies," *Journal of Environmental Management*, vol. 176, pp. 21–33, 2016.

[4] A. Arezoo, A. Ahmad, R. Mashallah, and A. Meisam, "Removal of heavy metals from industrial wastewaters: a review," *ChemBioEng Reviews*, vol. 4, no. 1, pp. 1–24, 2017.

[5] Z. O. Kocabas-Atakli and Y. Yurum, "Synthesis and characterization of anatase nanoadsorbent and application in removal of lead, copper and arsenic from water," *Chemical Engineering Journal*, vol. 225, pp. 625–635, 2013.

[6] Lenntech, Drinking Water Tandards, 2020, https://www.lenntech.com/applications/drinking/standards/drinking-water-standards.htm.

[7] X. Zhang, J. Tian, Y. Hu et al., "Selective sulfide precipitation of copper ions from arsenic wastewater using monoclinic pyrrhotite," *Science of the Total Environment*, vol. 705, 2020.

[8] Z. Yang, S. Jia, N. Zhuo, W. Yang, and Y. Wang, "Flocculation of copper(II) and tetracycline from water using a novel pH- and temperature-responsive flocculants," *Chemosphere*, vol. 141, pp. 112–119, 2015.

[9] Y. Bao, X. Yan, W. Du et al., "Application of amine-functionalized MCM-41 modified ultrafiltration membrane to remove chromium (VI) and copper (II)," *Chemical Engineering Journal*, vol. 281, pp. 460–467, 2015.

[10] M. Mohsen-Nia, P. Montazeri, and H. Modarress, "Removal of Cu^{2+} and Ni^{2+} from wastewater with a chelating agent and reverse osmosis processes," *Desalination*, vol. 217, no. 1-3, pp. 276–281, 2007.

[11] S. Edebali and E. Pehlivan, "Evaluation of chelate and cation exchange resins to remove copper ions," *Powder Technology*, vol. 301, pp. 520–525, 2016.

[12] C. Peng, Y. Liu, J. Bi, H. Xu, and A. S. Ahmed, "Recovery of copper and water from copper-electroplating wastewater by the combination process of electrolysis and electrodialysis," *Journal of Hazardous Materials*, vol. 189, no. 3, pp. 814–820, 2011.

[13] H. Polat and D. Erdogan, "Heavy metal removal from waste waters by ion flotation," *Journal of Hazardous Materials*, vol. 148, no. 1-2, pp. 267–273, 2007.

[14] C. Dinh Viet, N.-L. Liu, N. Viet Anh, and C.-H. Hou, "Meso/micropore-controlled hierarchical porous carbon derived from activated biochar as a high-performance adsorbent for copper removal," *Science of the Total Environment*, vol. 692, pp. 844–853, 2019.

[15] E. Demirbas, N. Dizge, M. T. Sulak, and M. Kobya, "Adsorption kinetics and equilibrium of copper from aqueous solutions using hazelnut shell activated carbon," *Chemical Engineering Journal*, vol. 148, no. 2-3, pp. 480–487, 2009.

[16] M. M. Rao, A. Ramesh, G. P. C. Rao, and K. Seshaiah, "Removal of copper and cadmium from the aqueous solutions by activated carbon derived from Ceiba pentandra hulls," *Journal of Hazardous Materials*, vol. 129, no. 1-3, pp. 123–129, 2006.

[17] R. Z. Wang, D. L. Huang, Y. G. Liu et al., "Synergistic removal of copper and tetracycline from aqueous solution by steam-activated bamboo-derived biochar," *Journal of Hazardous Materials*, vol. 384, 2020.

[18] M. R. Razak, N. A. Yusof, A. Z. Aris et al., "Phosphoric acid modified kenaf fiber (K-PA) as green adsorbent for the removal of copper (II) ions towards industrial waste water effluents," *Reactive and Functional Polymers*, vol. 147, Article ID 104466, 2020.

[19] M. Kobya, E. Demirbas, E. Senturk, and M. Ince, "Adsorption of heavy metal ions from aqueous solutions by activated carbon prepared from apricot stone," *Bioresource Technology*, vol. 96, no. 13, pp. 1518–1521, 2005.

[20] L. Xiao, F. Y. Ye, Y. Zhou, and G. H. Zhao, "Utilization of pomelo peels to manufacture value-added products: a review," *Food Chemistry*, vol. 351, Article ID 129247, 2021.

[21] S. W. Choi, J. Tang, V. G. Pol, and K. B. Lee, "Pollen-derived porous carbon by KOH activation: effect of physicochemical structure on CO_2 adsorption," *Journal of CO_2 Utilization*, vol. 29, pp. 146–155, 2019.

[22] A. E. Ogungbenro, D. V. Quang, K. A. Al-Ali, L. F. Vega, and M. R. M. Abu-Zahra, "Synthesis and characterization of activated carbon from biomass date seeds for carbon dioxide adsorption," *Journal of Environmental Chemical Engineering*, vol. 8, Article ID 104257, 2020.

[23] D. Eeshwarasinghe, P. Loganathan, and S. Vigneswaran, "Simultaneous removal of polycyclic aromatic hydrocarbons and heavy metals from water using granular activated carbon," *Chemosphere*, vol. 223, pp. 616–627, 2019.

[24] K. S. W. Sing, "Reporting physisorption data for gas/solid systems with special reference to the determination of surface area and porosity," *Pure and Applied Chemistry*, vol. 54, no. 11, pp. 2201–2218, 1982.

[25] J. Du, L. Liu, L. Zhang, Y. Yu, Y. Zhang, and A. Chen, "Waste chrysanthemum tea derived hierarchically porous carbon for CO_2 capture," *Journal of Renewable And Sustainable Energy*, vol. 9, no. 6, 2017.

[26] R. C. Bansal, M. Goyal, Y. Bao et al., "Application of amine-functionalized MCM-41 modified ultrafiltration membrane to remove chromium (VI) and copper (II)," *Chemical Engineering Journal*, vol. 281, pp. 460–467, 2005.

[27] Z. H. Hu, M. P. Srinivasan, and Y. M. Ni, "Novel activation process for preparing highly microporous and mesoporous activated carbons," *Carbon*, vol. 39, no. 6, pp. 877–886, 2001.

[28] S. Uçar, M. Erdem, T. Tay, and S. Karagöz, "Preparation and characterization of activated carbon produced from pomegranate seeds by $ZnCl_2$ activation," *Applied Surface Science*, vol. 255, no. 21, pp. 8890–8896, 2009.

[29] D. W. McKee, "Mechanisms of the alkali metal catalyzed gasification of carbon," *Fuel*, vol. 62, no. 2, pp. 170–175, 1983.

[30] S. J. Li, K. H. Han, J. X. Li, M. Li, and C. M. Lu, "Preparation and characterization of super activated carbon produced from gulfweed by KOH activation," *Microporous and Mesoporous Materials*, vol. 243, pp. 291–300, 2017.

[31] W. Han, X. Wang, M. Zhu et al., "Melamine modification of spherical activated carbon and its effects on acetylene hydrochlorination," *Journal of Wuhan University of Technology-Materials Science Edition*, vol. 29, pp. 1147–1151, 2014.

[32] J. Li, K. Li, T. Zhang et al., "Development of activated carbon from Windmill palm sheath fiber by KOH activation," *Fibers and Polymers*, vol. 17, pp. 880–887, 2016.

[33] Z. Y. Ryu, J. T. Zheng, M. Z. Wang, and B. J. Zhang, "Characterization of pore size distributions on carbonaceous adsorbents by DFT," *Carbon*, vol. 37, no. 8, pp. 1257–1264, 1999.

[34] S. Mishra, S. S. Yadav, S. Rawat, J. Singh, and J. R. Koduru, "Corn husk derived magnetized activated carbon for the removal of phenol and para-nitrophenol from aqueous solution: interaction mechanism, insights on adsorbent characteristics, and isothermal, kinetic and thermodynamic properties," *Journal of Environmental Management*, vol. 246, pp. 362–373, 2019.

[35] M. I. Sabela, K. Kunene, S. Kanchi et al., "Removal of copper (II) from wastewater using green vegetable waste derived activated carbon: an approach to equilibrium and kinetic study," *Arabian Journal of Chemistry*, vol. 12, no. 8, pp. 4331–4339, 2019.

[36] H. Demiral and C. Güngör, "Adsorption of copper(II) from aqueous solutions on activated carbon prepared from grape bagasse," *Journal of Cleaner Production*, vol. 124, pp. 103–113, 2016.

[37] J. Zhang, H. Fu, X. Lv, J. Tang, and X. Xu, "Removal of Cu(II) fromaqueous solution using the rice husk carbons prepared by the physical activation process," *Biomass and Bioenergy*, vol. 35, no. 1, pp. 464–472, 2011.

[38] X. Wang, X. Liang, Y. Wang et al., "Adsorption of Copper (II) onto activated carbons from sewage sludge by microwave-induced phosphoric acid and zinc chloride activation," *Desalination*, vol. 278, no. 1-3, pp. 231–237, 2011.

[39] F. Bouhamed, Z. Elouear, and J. Bouzid, "Adsorptive removal of copper(II) from aqueous solutions on activated carbon prepared from Tunisian date stones: equilibrium, kinetics and thermodynamics," *Journal of the Taiwan Institute of Chemical Engineers*, vol. 43, no. 5, pp. 741–749, 2012.

[40] D. Kołodyńska, R. Wnętrzak, J. J. Leahy, M. H. B. Hayes, W. Kwapiński, and Z. Hubicki, "Kinetic and adsorptive characterization of biochar in metal ions removal," *Chemical Engineering Journal*, vol. 197, pp. 295–305, 2012.

[41] A. Tomczyk, Z. Sokołowska, and P. Boguta, "Biomass type effect on biochar surface characteristic and adsorption capacity relative to silver and copper," *Fuel*, vol. 278, Article ID 118168, 2020.

[42] H. Demiral and G. Gündüzoğlu, "Removal of nitrate from aqueous solutions by activated carbon prepared from sugar beet bagasse," *Bioresource Technology*, vol. 101, no. 6, pp. 1675–1680, 2010.

[43] P. Y. Ramos, M. T. Munaro, C. C. Triques et al., "Biosorption of binary heavy metal systems: phenomenological mathematical modeling," *Chemical Engineering Journal*, vol. 313, pp. 364–373, 2017.

[44] W. D. M. Souza, W. S. Rodrigues, M. M. S. Lima Filho, J. J. F. Alves, and T. M. B. F. Oliveira, "Heavy metals uptake on Malpighia emarginata DC seed fiber microparticles: physicochemical characterization, modeling and application in landfill leachate," *Waste Management*, vol. 78, pp. 356–365, 2018.

[45] C. Wang, L. Boithias, Z. Ning et al., "Comparison of Langmuir and Freundlich adsorption equations within the SWAT-K model for assessing potassium environmental losses at basin scale," *Agricultural Water Management*, vol. 180, pp. 205–211, 2017.

[46] Z. Zaheer, A. Al-Asfar, and E. S. Aazam, "Adsorption of methyl red on biogenic Ag@Fe nanocomposite adsorbent: isotherms, kinetics and mechanisms," *Journal of Molecular Liquids*, vol. 283, pp. 287–298, 2019.

[47] M. I. Temkin and V. Pyzhev, "Kinetics of ammonia synthesis on promoted iron catalyst," *Acta Physival Chemistry*, vol. 12, pp. 327–356, 1940.

[48] T. E. Köse, H. Demiral, and N. Öztürk, "Adsorption of boron from aqueous solutions using activated carbon prepared from olive bagasse," *Desalination and Water Treatment*, vol. 29, pp. 110–118, 2011.

[49] T. G. Kazi, K. D. Brahman, J. A. Baig, and H. I. Afridi, "A new efficient indigenous material for simultaneous removal of fluoride and inorganic arsenic species from groundwater," *Journal of Hazardous Materials*, vol. 357, pp. 159–167, 2018.

[50] B. Kumar, K. Smita, E. Sánchez, C. Stael, and L. Cumbal, "Andean Sacha inchi (*Plukenetia volubilis L.*) shell biomass as new biosorbents for Pb^{2+} and Cu^{2+} ions," *Ecological Engineering*, vol. 93, pp. 152–158, 2016.

[51] A. . Ş. Yargıç, R. Z. Yarbay Şahin, N. Özbay, and E. Önal, "Assessment of toxic copper(II) biosorption from aqueous solution by chemically-treated tomato waste," *Journal of Cleaner Production*, vol. 88, pp. 152–159, 2015.

[52] S. Vitas, T. Keplinger, N. Reichholf, R. Figi, and E. Cabane, "Functional lignocellulosic material for the remediation of copper(II) ions from water: towards the design of a wood filter," *Journal of Hazardous Materials*, vol. 355, pp. 119–127, 2018.

[53] N. Maaloul, P. Oulego, M. Rendueles, A. Ghorbal, and M. Díaz, "Novel biosorbents from almond shells: characterization and adsorption properties modeling for Cu(II) ions from aqueous solutions," *Journal of Environmental Chemical Engineering*, vol. 5, no. 3, pp. 2944–2954, 2017.

[54] A. K. Sakhiya, I. Aier, S. Pathak et al., "Copper(II) removal from aqua solution using rice straw derived biochar," *Materials Today: Proceedings*, vol. 43, pp. 740–745, 2021.

[55] J. C. Ma, W. Huang, X. S. Zhang, Y. C. Li, and N. Wang, "The utilization of lobster shell to prepare low-cost biochar for high-efficient removal of copper and cadmium from aqueous: sorption properties and mechanisms," *Journal of Environmental Chemical Engineering*, vol. 9, no. 1, Article ID 104703, 2021.

[56] D. D. Milenković, P. V. Dašić, and V. B. Veljković, "Ultrasound-assisted adsorption of copper(II) ions on hazelnut shell activated carbon," *Ultrasonics Sonochemistry*, vol. 16, no. 4, pp. 557–563, 2009.

[57] S. Rangabhashiyam, N. Anu, M. S. Giri Nandagopal, and N. Selvaraju, "Relevance of isotherm models in biosorption of pollutants by agricultural byproducts," *Journal of Environmental Chemical Engineering*, vol. 2, no. 1, pp. 398–414, 2014.

Hindawi
Journal of Chemistry
Volume 2021, Article ID 9978596, 6 pages
https://doi.org/10.1155/2021/9978596

Research Article

Fast and Versatile Pathway in Fabrication of Polyelectrolyte Multilayer Nanofiltration Membrane with Tunable Properties

Ahmad M. Alghamdi

Chemical Engineering Department, Imam Mohammad Ibn Saud Islamic University, Riyadh 11432, Saudi Arabia

Correspondence should be addressed to Ahmad M. Alghamdi; amsalghamdi@imamu.edu.sa

Received 18 March 2021; Revised 15 May 2021; Accepted 1 June 2021; Published 11 June 2021

Academic Editor: Ibrahim H. Alsohaimi

Thin film composite nanofiltration (NF) membranes are relatively new membranes compared to other types of pressure-driven membranes. However, they attract interest from researchers due to their versatility to be used in various applications. In this work, a new class of NF membrane was successfully fabricated through spin-assisted layer-by-layer assembly by depositing alternate layers of branched polyethylenimine (PEI) and poly(sodium 4-styrenesulfonate) (PSS) on ultrafiltration polysulfone (PSF) membrane. The suitability of the fabricated membranes for removal of divalent ions was investigated. It was found that the membrane consisting of $(PEI/PSS)_{10}$–0.05 M NaCl showed $MgCl_2$ rejection rate of 93.95% and permeation flux of 0.9 $L/m^2 \cdot h$ bar during tests performed using a crossflow permeation cell at a crossflow velocity of 0.65 m/s, $MgCl_2$ feed concentration of 6530 ppm, pressure of 10 bar, temperature of 32.5°C, and pH of 6.5. This result suggests that this new fabrication method is suitable for producing polyelectrolyte multilayered (PEM) NF membranes that exhibit comparable membrane performance to commercial ones.

1. Introduction

Among pressure-driven membranes, a nanofiltration (NF) membrane is considered as the most recently developed one. The NF membrane is known for its ability to reject multivalent ions and organic compounds coupled with high permeation flux. Owing to these characteristics, the use of NF particularly in water treatment becomes more and more popular particularly in water treatment applications such as removal of multivalent ions [1, 2], heavy metals [3–5], pesticides [6, 7], dyes [8], and textiles [9].

As for other pressure-driven membranes, NF also suffers from fouling. Rapid fouling film formation causes significant flux decrease which can hurt the operation of this membrane especially in terms of operational cost. In severe cases, it even becomes necessary to replace the membrane. Membrane cleaning and replacement account for up to 6% and 16%, respectively, of the total water treatment costs [10]. Thus, improving the fouling resistance of these membranes has become essential for reducing the above-described costs.

It is generally accepted that the physicochemical properties of membranes, such as their roughness, surface charge, foulant-membrane surface interactions, and hydrophobicity, are the primary factors affecting their fouling characteristics. The primary source of these problems is the membrane material itself. Several common commercial polymers such as poly(ether sulfone) (PES), polyamide (PA), and poly piperazine amide (PPA) are used extensively for NF/reverse osmosis (RO) membranes, making up 91% of the total sales [11]. For instance, PA is used by GE-Osmonics to produce Desal 5 DL®, NF90®, and Desal 51HL®; meanwhile, PES is used by Nitto Denko to fabricate NTR7450®, whereas PPA is used by Toray and Film Tech to prepare UTC-20® and NF-400®, respectively.

All these membranes, and particularly polyamide membranes, are hydrophobic and exhibit relatively rough surfaces. As a result, these NF membranes are especially susceptible to fouling. Unfortunately, research on commercial Reverse Osmosis (RO)/NF membranes from a chemistry viewpoint has been stagnant for some time now,

with there being no major developments in the last couple of decades [11, 12].

It is suggested that, with respect to fouling, both the membrane chemistry and the fabrication technique used play a significant part, as they have a determining effect on the physicochemical properties of the membrane in question. Thus, research efforts in the last two decades have primarily been directed toward the development of novel membrane materials, including inorganic ones, as well as those incorporating nanoparticles and polymers with high hydrophilicity and having smooth surfaces [11].

In order to tackle both fabrication technique and membrane chemistry all at once, it is imperative to try out several new emerging thin film fabrication techniques that truly provide access to control the properties of the film to nanoscale and also offer flexibility from chemistry point of view. Among thin film fabrication techniques, layer-by-layer (LbL) assembly is considered to be the most versatile and most robust technique [13].

In LbL assembly, ultrathin layers with thicknesses of the order of the subnanometer scale can be deposited alternately on a support layer. Hence, the final thickness of the active layer can be fine-tuned to the desired level merely by varying the number of deposition cycles. One can also easily change the membrane surface charge by terminating the assembly process at the deposition of a material with the desired charge (positive, negative, or neutral). For this purpose, typically polyelectrolyte is employed because they are typically hydrophilic and exhibit a charge either positive or negative. This technique itself can utilize various materials including organic, inorganic, or even microorganism.

Principally, there are three approaches for fabricating LbL-assembled films, namely, dipping, spraying, and spinning. Spin-assisted LbL (SA-LbL) assembly is believed to be the fastest method and also the most suitable one for producing membranes with the smoothest surfaces [14, 15]. There have been several works done for the use of conventional dip-LbL in NF application [16–25]; meanwhile, the use of SA-LbL assembly for fabrication of NF membrane is still at infancy. However, our previous works showed that SA-LbL can be successfully used to fabricate this membrane with outstanding properties [26–29].

Based on the above literature review, in this work, spin-assisted LbL (SA-LbL) assembly is utilized for fabricating NF membranes suitable for removing divalent salts such as $MgCl_2$ from water. Also, as part of continuous work in finding the most suitable materials that provide high rejection, high flux, and less susceptible to biofouling, two other polyelectrolytes are used, namely, polystyrenesulfonate (PSS) and poly(ethylene imine) (PEI). Number of layers and pH assembly of polyelectrolyte were studied since PEI is weak polyelectrolyte whose degree of ionization is strongly affected by assembly and external pH.

2. Materials and Methods

2.1. Materials. In this work, branched-polyethylenimine (PEI) with molecular weight of 25,000 and poly(sodium 4-styrenesulfonate) (PSS) with a molecular weight of 70,000 in the form of a 30 wt% in H_2O solution were purchased from Sigma-Aldrich (USA). Extra-pure NaCl was obtained from Scharlau (Spain) while extra-pure $MgCl_2 \bullet 6H_2O$ was obtained from Loba Chemie Pvt. Ltd. (India).

Stock solutions containing 0.02 M polyelectrolytes (PEI and PSS) containing additional NaCl concentration of 0.05 M were prepared. In these experiments, the pH of the PEI and PSS solution were varied to find the optimum condition for membrane preparation.

Polyethersulfone (PES) ultrafiltration (UF) membranes (YMPWSP3001, Sterlitech Corp., USA) with a pore size corresponding to a molecular weight cutoff of 10 kDa were used as the support layers for fabricating the PEM TFC membranes. The PES UF membranes were tested and were found to exhibit a permeation flux of 235.7 $L/m^2 \cdot h$ at a pressure of 10 bar and temperature of 33.5°C. The molecular structures of the various materials used are shown in Figure 1.

2.2. Fabrication of PEM TFC Membranes. The prepared PEI and PSS solutions were alternately deposited on the PES UF membranes using a spin coater (POLOS SPIN150i®, SPS Inc.). Prior to deposition, the PES UF support membrane was pretreated in an air plasma using a plasma cleaner (PDC-32G-2, Harrick Plasma Inc.) as per a procedure described elsewhere [30]. PEI was deposited firstly on the spinning PES support as the first layer. PSS layer was subsequently deposited in a similar manner to complete one cycle of bilayer deposition. The deposition process was performed at a speed of 3000 rpm; this speed was chosen based on a previous study [26], as it helped reduce the gradient in the radial thickness from the center of the support [31]. The PEI and PSS solutions were both deposited at a rate of 0.2 mL/s for 10 s, and the film was let to spin-dried for another 20 s afterward. After every polyelectrolyte deposition, the relatively dry film was then rinsed with deionized (DI) water at a rate of 0.4 mL/s for 20 s to remove any weakly bonded polyelectrolyte molecules that might remain on the surface. This was followed by spin-drying for 20 s. The resulting membranes were labelled as $(PEI/PSS)_x$ where "x" indicates the number of bilayers. The NaCl concentration in the two polyelectrolyte solutions were the same at 0.05 M optimized value from our previous work [28, 29].

2.3. Permeation Tests. Permeation tests were performed using a crossflow permeation cell (Innovator® CF016, Sterlitech Corporation). The CF016 system has an active membrane surface area of 20.6 cm^2. The conditions for the permeation tests were as follows: pressure of 10 bar, feed temperature of 32.39 ± 0.27°C, cross flow velocity (CFV) of 0.65 m/s, and $MgCl_2$ concentration of 6578.21 ± 69.2 ppm. Meanwhile, the pH of the feed solution remained stable at approximately 6.49 ± 0.11 without requiring any adjustments. These tests were performed for 5 h, and the operation conditions were measured every hour.

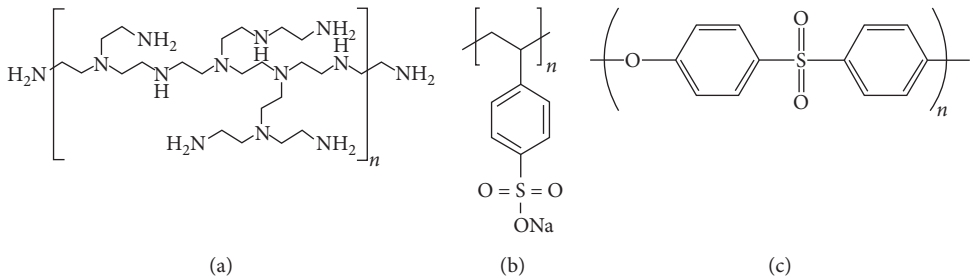

Figure 1: Molecular structures of materials used to synthesize PEM TFC membranes: (a) PEI, (b) PSS, and (c) PES.

3. Results and Discussion

PEM membranes consisting of branched PEI/PSS bilayers were fabricated utilizing SA-LbL assembly method on PES UF membrane supports. The resulting membranes were similar to TFC membranes. The multilayer PEI/PSS acted as the active layer for rejecting the salt, while the UF PES support provided the mechanical strength to the overall membrane structure. PSS is a strong polyelectrolyte with a pKa of 2.1 at room temperature [32], and its degree of ionization remains constant over a wide range of pH values [33], whereas PEI is weak polyelectrolyte which means the degree of ionization is strongly affected by its pH.

3.1. Effect of Assembly pH on Membrane Performance. As previously mentioned, PEI dissociation in an aqueous solution is a function of pH; meanwhile, the dissociation of polyelectrolyte affects its conformation and multilayer structure. Thus, it is imperative to investigate the effect of assembly pH on membrane performance, i.e., permeate flux and rejection rate. In this work, not only assembly pH of PEI solution was studied, but also that of PSS and the rinse solution were studied too. Previous study by Lutkenhaus et al. [34] provides a valuable in-depth analysis for the effect of assembly pH of linear PEI (LPEI) on structure of polyelectrolyte multilayer consists of LPEI/PAA.

Figure 2 shows significant improvement of permeability without severely compromising the rejection rate of the membrane when the assembly pH of PEI was kept at 3.5 and that of PSS was changed from 8 to 3.5. This trend is even more pronounced when the water rinse pH was also brought to the same level. This trend implies that external pH also affects the conformation of already deposited PEI.

When the assembly pH of PEI was at 3.5, PEI was in highly ionized state and adopted less coiled conformation; meanwhile, PSS will always have highly flat conformation owing to its fully ionized condition at all pH.

The combination of both polyelectrolytes at the pH for PEI/PSS/water of 3.5/8/7, respectively, is expected to show PEM with higher permeability. However, in fact, it showed the lowest permeability. This observation showed that the external pH also has significant impact. The water and PSS that carry more basic pH will penetrate the already deposited PEI layer and alter PEI ionization state to be less ionized. This results in changing of internal structure and increase of layer thickness. In the end, it provides more barrier for water transport across the film. The opposite behavior was noticed when the pH of rinsing water and PSS were adjusted at the same pH as that of PEI. In this case, PEI chain conformation remains flat and results in higher permeability, whereas when the pH of PEI was adjusted at more basic pH, PEI chain became less ionized and adopted more coiled structure. Therefore, PEM film became thicker and provided less permeability.

Rejection mechanism of the NF membrane is somewhat more complex, particularly for charged solutes as used in this work. It is generally known that there are two contributing mechanisms, i.e., Donnan potential and steric hindrance in the rejection of charged solutes. When the layer was prepared from less ionized PEI, more PEI molecules are needed to compensate the charges of fully ionized PSS. This results in denser film compared to that prepared from highly ionized PEI. The denser film produces higher salt rejection.

3.2. Effect of Number of Bilayers on Membrane Performance. Number of bilayers deposited on membrane is also important parameter which determines the membrane performance. Figure 3 shows the changes in the permeation flux and salt rejection rate as the number of bilayers was increased from 5, 8, 10, and then 20. It shows that as the number of bilayers was increased, the permeate flux decreased. The flux decline can be affected by several things such as layer thickness, effective pore radius, and porosity. However, layer thickness contributes the most significant effect. It is generally known that the permeation flux is inversely proportional to the membrane thickness. Thus, when more layers were added, the layer thickness increased and that resulted in the decrease of the flux. The flux decrease then becomes stagnant as more number of layers were deposited, implying the linear growth of PEI/PSS film as reported somewhere else [35].

Figure 3 also shows the increase of rejection rate as the number of layers was increased. This trend was due to improvement in surface coverage. This study also suggests that steric hindrance and Donnan potential play an important role in rejection mechanism in the case of NF membrane. Donnan potential effect has already taken place regardless of the number of layers; meanwhile, the steric hindrance effect becomes more evident as the surface coverage and layering quality improved through more layer deposition. This rejection still improved up to a certain number of layers, i.e., around 10 bilayers, and became

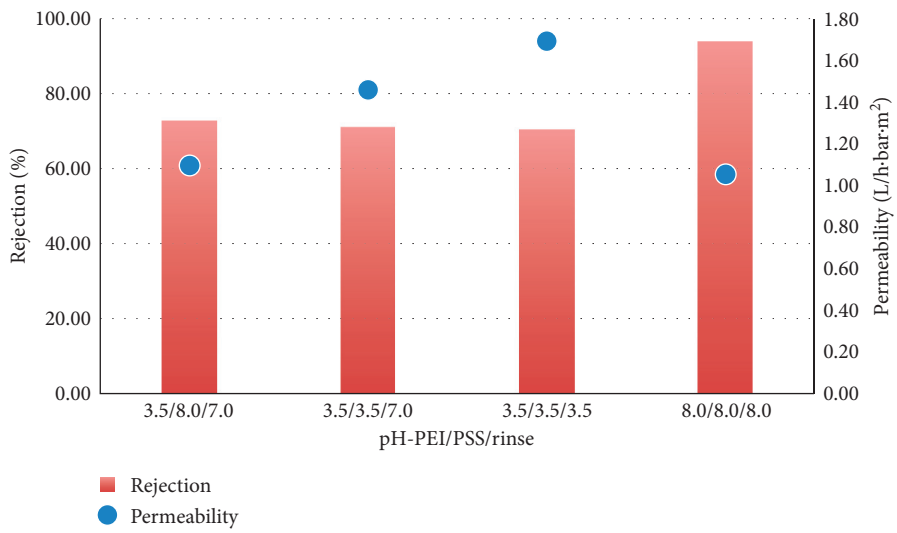

Figure 2: Effect of solution pH on performance of $(PEI/PSS)_{35}$ (testing condition: $P = 10$ bar, $T = 32.08 \pm 0.3^{\circ}C$, CFV = 0.65 m/s, $MgCl_2$ concentration = 1345.6 ± 66.6 ppm, and pH = 6.52 ± 0.06).

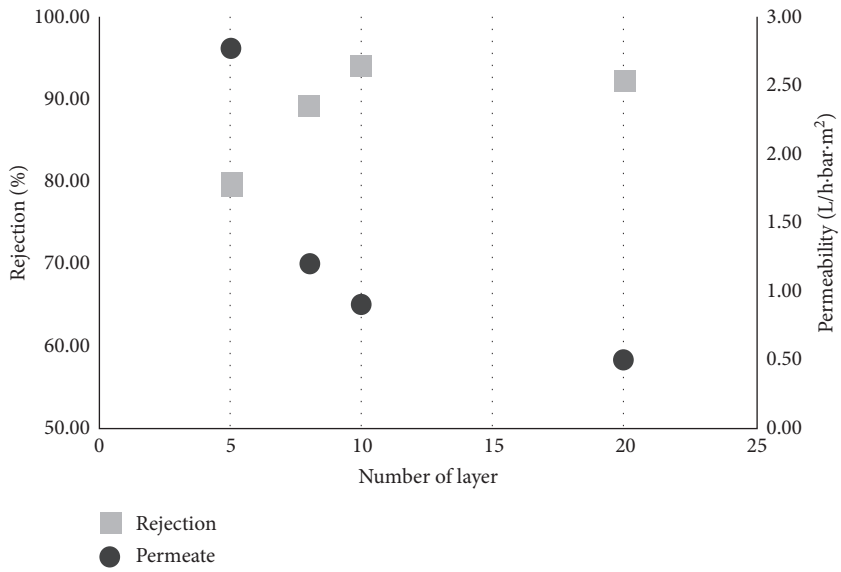

Figure 3: Effect of number of deposited PEI/PSS bilayers on salt rejection rate and permeability ($P = 10$ bar, $T = 32.39 \pm 0.27^{\circ}C$, CFV = 0.65 m/s, $MgCl_2$ concentration = 6578.21 ± 69.29 ppm, and pH = 6.49 ± 0.11).

Table 1: NF membrane performance comparison.

Membrane material	Preparation method	Rejection (%)	Permeability ($L/m^2 \cdot h$ bar)	Testing condition	Reference
$(PEI/PSS)_{35}$-PES	Spin	93.8	1.05	10 bar, 1345 ppm $MgCl_2$.	This work
$(PEI/PSS)_{10}$-PES	Spin	93.5	0.9	10 bar, 6600 ppm $MgCl_2$.	This work
$(PVA/PVS)_{60}$-PAN/PET	Dip	98.5	0.089	10 bar, 952.1 ppm $MgCl_2$.	[17]
$(PSS/PAH)_5$-porous alumina	Dip	95	7.38	4.8 bar, 1000 ppm $MgCl_2$	[25]
Polyamide	Interfacial polymerization using PEI/TMC	92.2	2.8	4 bar, 1000 ppm $MgCl_2$	[36]
NF90 (Film Tech)	Interfacial polymerization	89	4.37	10 bar, 6600 ppm $MgCl_2$	This work
SBNF (Trisep)	Cellulose acetate	86.14	1.62	10 bar, 600 ppm $MgCl_2$	[28]

stagnant afterward. It indicated that at that number of layers, the support has been completely covered.

3.3. Comparison with Other NF Membranes. In this section, the performance of our membrane is compared with other membranes either fabricated using LbL assembly or other techniques as can be seen in Table 1. As shown, membrane produced in this work is comparable to those membranes even when it was tested at 6600 ppm $MgCl_2$, and the membrane still shows stable performance.

4. Conclusions

In this study, PEM TFC NF membranes consist of PEI/PSS were successfully fabricated using SA-LbL assembly. The fabricated membrane achieved comparable performance with commercial membrane such as NF90 which was tested at the same condition showed rejection rate of 89% and permeate permeability of 4.37 L/h bar·m^2. Meanwhile, $(PEI/PSS)_{10}$–0.05 achieved rejection rate of 93.95% and permeate permeability of 0.9 L/h bar·m^2.

In conclusion, the proposed membrane fabrication method is promising, as this method is not limited to a certain type of material. A range of materials, including organic and inorganic materials and even microorganisms have been employed to create thin layers using the conventional dip-LbL assembly technique for various applications. There is still huge room for study and research in this type of membrane including optimization of preparation condition, selection of membrane materials, stability, and so on. Thus, the participation from researchers all over the world is urgently required.

Data Availability

All the data that support the findings of this study are displayed in this manuscript.

Conflicts of Interest

The author declares no conflicts of interest.

Acknowledgments

This project was funded by the National Plan for Science, Technology, and Innovation (MAARIFAH), King Abdulaziz City for Science and Technology, the Kingdome of Saudi Arabia, award #: WAT68-08-R. The author also acknowledges Dr. Farid Fadhillah for his valuable analysis and discussion.

References

[1] B. Van der Bruggen, A. Koninckx, and C. Vandecasteele, "Separation of monovalent and divalent ions from aqueous solution by electrodialysis and nanofiltration," *Water Research*, vol. 38, no. 5, pp. 1347–1353, 2004.

[2] K. Gu, S. Wang, Y. Li, X. Zhao, Y. Zhou, and C. Gao, "A facile preparation of positively charged composite nanofiltration membrane with high selectivity and permeability," *Journal of Membrane Science*, vol. 581, pp. 214–223, 2019.

[3] X.-Y. Gong, Z.-H. Huang, H. Zhang et al., "Novel high-flux positively charged composite membrane incorporating titanium-based MOFs for heavy metal removal," *Chemical Engineering Journal*, vol. 398, Article ID 125706, 2020.

[4] B. A. M. Al-Rashdi, D. J. Johnson, and N. Hilal, "Removal of heavy metal ions by nanofiltration," *Desalination*, vol. 315, pp. 2–17, 2013.

[5] J. Tian, H. Chang, S. Gao, and R. Zhang, "How to fabricate a negatively charged NF membrane for heavy metal removal via the interfacial polymerization between PIP and TMC?" *Desalination*, vol. 491, Article ID 114499, 2020.

[6] K. V. Plakas and A. J. Karabelas, "Removal of pesticides from water by NF and RO membranes—a review," *Desalination*, vol. 287, pp. 255–265, 2012.

[7] H. Karimi, A. Rahimpour, and M. R. Shirzad Kebria, "Pesticides removal from water using modified piperazine-based nanofiltration (NF) membranes," *Desalination and Water Treatment*, vol. 57, no. 52, pp. 24844–24854, 2016.

[8] J. H. Mo, Y. H. Lee, J. Kim, J. Y. Jeong, and J. Jegal, "Treatment of dye aqueous solutions using nanofiltration polyamide composite membranes for the dye wastewater reuse," *Dyes and Pigments*, vol. 76, no. 2, pp. 429–434, 2008.

[9] A. Akbari, S. Desclaux, J. C. Remigy, and P. Aptel, "Treatment of textile dye effluents using a new photografted nanofiltration membrane," *Desalination*, vol. 149, no. 1–3, pp. 101–107, 2002.

[10] N. L. Le and S. P. Nunes, "Materials and membrane technologies for water and energy sustainability," *Sustainable Materials and Technologies*, vol. 7, pp. 1–28, 2016.

[11] K. P. Lee, T. C. Arnot, and D. Mattia, "A review of reverse osmosis membrane materials for desalination-development to date and future potential," *Journal of Membrane Science*, vol. 370, no. 1-2, pp. 1–22, 2011.

[12] R. J. Petersen, "Composite reverse osmosis and nanofiltration membranes," *Journal of Membrane Science*, vol. 83, no. 1, pp. 81–150, 1993.

[13] G. Decher, "Fuzzy nanoassemblies: toward layered polymeric multicomposites," *Science*, vol. 277, no. 5330, pp. 1232–1237, 1997.

[14] J. Cho, K. Char, J.-D. Hong, and K.-B. Lee, "Fabrication of highly ordered multilayer films using a spin self-assembly method," *Advanced Materials*, vol. 13, no. 14, pp. 1076–1078, 2001.

[15] P. A. Chiarelli, M. S. Johal, J. L. Casson, J. B. Roberts, J. M. Robinson, and H.-L. Wang, "Controlled fabrication of polyelectrolyte multilayer thin films using spin-assembly," *Advanced Materials*, vol. 13, no. 15, pp. 1167–1171, 2001.

[16] L. Krasemann and B. Tieke, "Selective ion transport across self-assembled alternating multilayers of cationic and anionic polyelectrolytes," *Langmuir*, vol. 16, no. 2, pp. 287–290, 2000.

[17] W. Jin, A. Toutianoush, and B. Tieke, "Use of polyelectrolyte layer-by-layer assemblies as nanofiltration and reverse osmosis membranes," *Langmuir*, vol. 19, no. 7, pp. 2550–2553, 2003.

[18] J. J. Harris, J. L. Stair, and M. L. Bruening, "Layered polyelectrolyte films as selective, ultrathin barriers for anion transport," *Chemistry of Materials*, vol. 12, no. 7, pp. 1941–1946, 2000.

[19] B. W. Stanton, J. J. Harris, M. D. Miller, and M. L. Bruening, "Ultrathin, multilayered polyelectrolyte films as nanofiltration membranes," *Langmuir*, vol. 19, no. 17, pp. 7038–7042, 2003.

[20] J. L. Stair, J. J. Harris, and M. L. Bruening, "Enhancement of the ion-transport selectivity of layered polyelectrolyte

membranes through cross-linking and hybridization," *Chemistry of Materials*, vol. 13, no. 8, pp. 2641–2648, 2001.

[21] S. U. Hong, R. Malaisamy, and M. L. Bruening, "Optimization of flux and selectivity in Cl^-/SO_4^{2-} separations with multilayer polyelectrolyte membranes," *Journal of Membrane Science*, vol. 283, no. 1–2, pp. 366–372, 2006.

[22] R. Malaisamy and M. L. Bruening, "High-flux nanofiltration membranes prepared by adsorption of multilayer polyelectrolyte membranes on polymeric supports," *Langmuir*, vol. 21, no. 23, pp. 10587–10592, 2005.

[23] H. Deng, Y. Xu, B. Zhu, X. Wei, F. Liu, and Z. Cui, "Polyelectrolyte membranes prepared by dynamic self-assembly of poly (4-styrenesulfonic acid-co-maleic acid) sodium salt (PSSMA) for nanofiltration (I)," *Journal of Membrane Science*, vol. 323, no. 1, pp. 125–133, 2008.

[24] Q. Nan, P. Li, and B. Cao, "Fabrication of positively charged nanofiltration membrane via the layer-by-layer assembly of graphene oxide and polyethylenimine for desalination," *Applied Surface Science*, vol. 387, pp. 521–528, 2016.

[25] L. Ouyang, R. Malaisamy, and M. L. Bruening, "Multilayer polyelectrolyte films as nanofiltration membranes for separating monovalent and divalent cations," *Journal of Membrane Science*, vol. 310, no. 1–2, pp. 76–84, 2008.

[26] F. Fadhillah, S. M. Javaid Zaidi, Z. Khan, M. Khaled, and P. T. Hammond, "Reverse osmosis desalination membrane formed from weak polyelectrolytes by spin assisted layer by layer technique," *Desalination and Water Treatment*, vol. 34, no. 1–3, pp. 44–49, 2011.

[27] F. Fadhillah, S. M. Javaid Zaidi, Z. Khan, M. Khaled, F. Rahman, and P. Hammond, "Development of multilayer polyelectrolyte thin-film membranes fabricated by spin assisted layer-by-layer assembly," *Journal of Applied Polymer Science*, vol. 126, no. 4, pp. 1468–1474, 2012.

[28] F. Fadhillah, A. M. Alghamdi, M. D. Alsubei, and S. A. Aljlil, "Synthesis of protein-fouling-resistance polyelectrolyte multilayered nanofiltration membranes through spin-assisted layer-by-layer assembly," *Journal of King Saud University—Engineering Sciences*, vol. 33, no. 2, pp. 81–87, 2021.

[29] A. M. Alghamdi and F. Fadhillah, "Thin film composite polyelectrolyte multilayer nanofiltration membrane fabricated using spin assisted layer by layer assembly: application of solution diffusion film model," *Communications in Science and Technology*, vol. 5, no. 1, pp. 10–15, 2020.

[30] K. S. Kim, K. H. Lee, K. Cho, and C. E. Park, "Surface modification of polysulfone ultrafiltration membrane by oxygen plasma treatment," *Journal of Membrane Science*, vol. 199, no. 1–2, pp. 135–145, 2002.

[31] A. Zhuk, V. Selin, I. Zhuk, B. Belov, J. F. Ankner, and S. A. Sukhishvili, "Chain conformation and dynamics in spin-assisted weak polyelectrolyte multilayers," *Langmuir*, vol. 31, no. 13, pp. 3889–3896, 2015.

[32] J. E. Yoo, K. S. Lee, A. Garcia et al., "Directly patternable, highly conducting polymers for broad applications in organic electronics," *Proceedings of the National Academy of Sciences*, vol. 107, no. 13, pp. 5712–5717, 2010.

[33] C. Wu, L. Zhao, and Y. Zhang, "pH-responsive nanofiltration membranes based on porphyrin supramolecular self-assembly by layer-by-layer technique," *RSC Advances*, vol. 7, no. 75, pp. 47397–47406, 2017.

[34] J. L. Lutkenhaus, K. McEnnis, and P. T. Hammond, "Nano- and microporous layer-by-layer assemblies containing linear poly(ethylenimine) and poly(acrylic acid)," *Macromolecules*, vol. 41, no. 16, pp. 6047–6054, 2008.

[35] S. Singh, A. Junghans, M. J. Waltman, A. Nagy, R. Iyer, and J. Majewski, "Neutron reflectometry characterization of PEI-PSS polyelectrolyte multilayers for cell culture," *Soft Matter*, vol. 8, no. 45, pp. 11484–11491, 2012.

[36] Y.-C. Chiang, Y.-Z. Hsub, R.-C. Ruaan, C.-J. Chuang, and K.-L. Tung, "Nanofiltration membranes synthesized from hyperbranched polyethyleneimine," *Journal of Membrane Science*, vol. 326, no. 1, pp. 19–26, 2009.

Hindawi
Journal of Chemistry
Volume 2021, Article ID 5841066, 11 pages
https://doi.org/10.1155/2021/5841066

Research Article

Mesoporous $LaFeO_3$: Synergistic Effect of Adsorption and Visible Light Photo-Fenton Processes for Phenol Removal from Refinery Wastewater

Thi To Nga Phan,[1] **Hong Lien Nguyen**,[1] **Van Tuyen Le**,[1] **Chi Nhan Phan**,[2] **and Thanh Huyen Pham**[1]

[1]*Department of Organic and Petrochemical Technology, School of Chemical Engineering, Hanoi University of Science and Technology, Hanoi, Vietnam*
[2]*Center for Chemical Accident Response and Safety, Vietnam Chemicals Agency, Ministry of Industry and Trade of the Socialist Republic of Vietnam, Hanoi, Vietnam*

Correspondence should be addressed to Thi To Nga Phan; nga.phanthito@hust.edu.vn

Received 28 April 2021; Revised 10 May 2021; Accepted 25 May 2021; Published 3 June 2021

Academic Editor: Ibrahim H. Alsohaimi

Mesoporous $LaFeO_3$ as a visible light-driven photocatalyst was prepared by a nanocasting method using mesoporous silica (SBA-15) as a hard template. The as-prepared $LaFeO_3$ photocatalyst was characterized by X-ray diffraction (XRD), scanning electron microscopy (SEM), transmission electron microscopy (TEM), N_2 adsorption-desorption, X-ray photoelectron spectroscopy (XPS), and optical absorption spectra. The characterization studies and experimental results showed that $LaFeO_3$ with porous structure caused by the removal of SBA-15 hard template could enhance the specific surface area of the resulting photocatalyst, which improves the phenol adsorption ability of the photocatalyst and in turn enhances its photo-Fenton catalytic activity. The photo-Fenton catalytic activity of the photocatalyst was investigated by photo-Fenton degradation of aqueous phenol under visible light irradiation. The effects of catalyst dosage, H_2O_2 concentration, and solution pH on the photo-Fenton catalytic degradation of phenol using mesoporous $LaFeO_3$ were studied and optimized. Under the optimal conditions of 20 mg L^{-1} phenol, 1.0 g L^{-1} catalyst, and 10 mM H_2O_2 at pH = 5, the photo-Fenton degradation of phenol (93.47%) was achieved in 180 min under visible light irradiation. Furthermore, our results proved the stability and reusability of mesoporous $LaFeO_3$ and revealed its catalytic mechanism for the photo-Fenton degradation of phenol.

1. Introduction

Untreated wastewater released from many industries such as paper making; petrochemical, textile, and flavouring agents; and petroleum industry contains high phenol concentrations. Phenol is considered as a hazardous and lethal pollutant that could be one of the main sources of harm to our ecosystem and human health [1]. The US Environmental Protection Agency (USEPA) has listed phenol as a foremost contaminant due to its poor degradability and high toxicity and suggested a permissible limit of phenol deposition less than 0.5 ppm in wastewater [2, 3]. In this frame, strategies for wastewater remediation of phenol are extremely essential.

Various technologies have been recently developed for wastewater treatment [4–6]. Wang et al. investigated the use of $LaCu_{0.5}Co_{0.5}O_3$ perovskite intercalated montmorillonite and g-C_3N_4 nanocomposites on microwave-induced H_2O_2 catalytic degradation of bisphenol A [7]. This technique shows several advantages such as fast reaction rate, rapid selective heating, efficient degradation of a variety of organic contaminants, and no secondary pollution [7, 8]. Meanwhile, adsorption is also considered as a promising method for wastewater treatment due to its convenience, cost-

effectiveness, simple operation, and environmental reasons [6]. In order to treat phenol-containing wastewater, several methods have been employed such as biological, stripping, and adsorption processes; however, these methods did not allow completely mineralizing phenol due to its recalcitrant nature [9]. Therefore, high-efficiency technologies such as Advanced Oxidative Processes (AOPs) should be applied. AOPs are based on the generation of hydroxyl radicals, very strong oxidizing species, that are able to chemically degrading a wide range of organic pollutants into innocuous products and in turn reduce the levels of pollution in wastewater [10, 11]. AOPs consist of photocatalysis, UV, UV/O_3, UV/H_2O_2, O_3/H_2O_2, Fenton, photo-Fenton processes, and catalytic wet peroxide oxidation [12–14]. Among these AOPs, the photo-Fenton process has been found to be the most promising method in terms of the process efficiency based on organic contaminants removal and operation cost [15]. Recently, the utilization of solar energy appears to be an effective strategy for addressing environmental concerns and energy crises [16–18]. Considering the use of solar power, semiconductor photocatalysts, especially iron-containing photocatalysts with narrow band gap energy belonging to the perovskite family, have been developed to decompose organic pollutants under visible light irradiation [19–22].

As one of the commonly iron-contained perovskite oxides, $LaFeO_3$ is considered as a promising visible light-driven photocatalyst for the photo-Fenton degradation of organic pollutants [19, 23–26]. During the photo-Fenton reaction, the organic pollutants could be oxidized by the attack of hydroxyl radicals; it is, therefore, necessary to improve the contact area between the active sites on to photocatalyst surface and organic compounds. However, the practical applications of the perovskite materials are limited due to the fact that they owe large particle size and small specific surface area causing by the traditional preparation methods such as sol-gel process, coprecipitation, and solution combustion [27]. Therefore, many strategies have been developed to overcome this shortcoming by improving their surface area via several novel methods, including the modified sol-gel process [28], nanocasting strategy [29, 30], polystyrene added sol-gel [31], and biotemplate method [32]. Of these methods, the nanocasting pathway using a hard template has attracted recent research interest due to its unique features such as controlled morphology and texture and highly crystallized walls of target materials [33]. Kaliaguine and coworkers prepared a series of perovskite oxides with the formula $LaBO_3$ (B = Mn, Co, Fe) via the nanocasting method [30]. The resulting samples exhibited extremely high specific surface areas, which are in a range of 110–155 $m^2\ g^{-1}$. Wang et al. synthesized mesoporous $LaCoO_3$ by a similar method to that of Kaliaguine's group [29]. The results showed that $LaCoO_3$ possessed a specific surface area of 96.7 $m^2\ g^{-1}$ which is much higher than that synthesized by the conventional citrate method. Interestingly, all the hard templates used in these studies are mesoporous silica. The enhancement of the specific surface area of materials is believed to play an important role in the transportation of organic pollutants to active sites on its surface, improvement of its adsorption capability, and catalytic degradation [34].

In this work, the mesoporous $LaFeO_3$ photocatalyst was prepared by a nanocasting method using mesoporous silica (SBA-15) as a hard template. After filling the $LaFeO_3$ precursor into mesoporous channels of SBA-15, the hard template was then leached by NaOH solution. The adsorption capability and photo-Fenton-like catalytic activity for phenol removal over mesoporous $LaFeO_3$ were systematically studied. The effects of different operational parameters were investigated to determine the highest phenol removal efficiency. To the best of our knowledge, no such work has been previously published.

2. Materials and Methods

2.1. Materials. Tetraethyl orthosilicate ($Si(OC_2H_5)_4$; 99%), pluronic P123 ($EO_{20}PO_{70}O_{20}$; $M_n \sim 5800$), lanthanum nitrate hexahydrate ($La(NO_3)_3.6H_2O$; 99.9%), iron nitrate nonahydrate ($Fe(NO_3)_3.9H_2O$; ≥98%), citric acid ($C_6H_8O_7.H_2O$; 99.9%), hydrogen peroxide (H_2O_2; 30 wt%), and phenol (C_6H_5OH; 99.5%) were purchased from Sigma-Aldrich. Other chemicals were obtained from our lab in Vietnam. All chemicals were used without additional purifications.

2.2. Photocatalyst Preparation

2.2.1. Synthesis of Hard Template SBA-15. The hard template (HT) was synthesized according to Zhao's research [35]. 3.5 g of P123 was firstly dissolved in 100 mL of 1.5 M HCl under vigorous stirring for 2 h. Subsequently, 8.5 g of TEOS was added to the above solution and the resulting solution was kept at room temperature for 15 h. After that, the final mixture was allowed to stir at 40°C for 24 h before transferring into a Teflon-lined autoclave for hydrothermal treatment at 90°C for 48 h. The obtained solid product was filtered and rinsed with DI water several times before being dried at 80°C in an oven overnight. The obtained SBA-15 powder was then calcined in the air from 25°C to 550°C for 6 h (heating rate of 1°C/min^{-1}).

2.2.2. Synthesis of Mesoporous $LaFeO_3$ (LFO-RHT). Mesoporous $LaFeO_3$ (LFO-RHT) was prepared by the nanocasting method. Typically, 1.241 g of $La(NO_3)_3.6H_2O$, 1.158 g of $Fe(NO_3)_3.9H_2O$, and 1.205 g of citric acid were added to 5 mL of DI water. The mixture was kept on stirring for 3 h at ambient temperature, after which 1 g of SBA-15 was added. This resulting solution was continuously stirred at 70°C for 3 h and then dried at 350°C in an oven for 12 h. The SBA-15 filled with LFO was obtained by calcination at 700°C for 6 h. To remove the SBA-15 hard template, the obtained powder was treated with NaOH 8 M solution at 80°C for 4 h. Finally, the powders were centrifuged, washed with deionized water several times, and then dried in the oven at 60°C overnight. The resulting sample was named LFO-RHT. For comparison, pure LFO was synthesized using the similar method above in the absence of SBA-15 and used

to compare with LFO-RHT in the photo-Fenton degradation of phenol.

2.3. Characterization of Materials. Powder X-ray diffraction (XRD) patterns of samples were collected on a Bruker D8 diffractometer (Bruker, USA) using CuKα as radiation. The data was collected in 2θ range 10–80° with a step size of 0.02°/s. Scanning electron microscopy (SEM) (Zeiss 1555 VP-FESEM, Germany) was used to examine the surface morphology of the sample. Transmission electron microscopy (TEM) was taken using HRTEM (H7500, HITACHI). X-ray photoelectron spectroscopy of the target sample was taken on an X-ray photoelectron spectrometer (XPS, Kratos AXIS Ultra DLD, UK). The nitrogen adsorption-desorption isotherms were measured at 77 K on MICROMERITICS 2020 analyzer (Micromeritics, USA). The surface areas of samples were determined by using the Brunauer–Emmett–Teller (BET) method. The optical absorption spectra were recorded from 200 to 800 nm on a PerkinElmer LAMBDA 750 UV/Vis/NIR spectrophotometer (PerkinElmer, USA).

2.4. Removal of Phenol over LFO-RHT. The photo-Fenton experiments were carried out in a 250 ml cylindrical glass reactor with 70 mm in diameter and 115 mm in length. To avoid heating inside the reactor, it was surrounded by a circulating water jacket. A Xenon arc lamp of 300 W (LOT-Quantum Design) was used with a 400 nm cut-off filter as the source of visible light irradiation. 100 ml phenol solution of 20 mg L^{-1} and LFO-RHT was prepared and added to the reactor. Prior to light irradiation, the suspension was magnetically stirred in the dark for 60 min to reach an adsorption-desorption equilibrium of phenol onto LFO-RHT. To perform the photo-Fenton-like reaction, 1 ml H_2O_2 aqueous solution was dispersed in the suspension and the lamp was turned on to commence the photo-Fenton reaction. A small amount of sample was extracted from the reactor every 15 min and centrifuged for measurement.

2.5. Analytical Method. Perkin Elmer Lambda 750 UV–Vis spectrophotometer was used as the analytical technique for confirming the concentration of phenol. The maximum absorbance wavelength of phenol was found at 272 nm. The photo-Fenton degradation efficiency (%) was evaluated as follows:

$$\text{degradation efficiency (\%)} = \left(1 - \frac{C_t}{C_1}\right) \times 100\%, \quad (1)$$

where C_1 and C_t are the phenol concentrations before the photo-Fenton degradation and after time t in the photo-Fenton reaction, respectively.

To understand the degradation kinetics of phenol, the pseudo-first-order model was used (Mahmoodi et al., 2006):

$$-\ln \frac{C_t}{C_1} = kt. \quad (2)$$

where C_t is the concentration of phenol after time t in the photo-Fenton reaction and k is the pseudo-first-order rate constant. The rate constant (k) was calculated from the slope of the plot of ln (C_t/C_1) versus time.

The total removal rate of phenol was calculated as

$$\text{Removal rate (\%)} = \left(1 - \frac{C_i}{C_0}\right) \times 100\%, \quad (3)$$

where C_0 is the phenol concentrations before starting adsorption and C_i is the phenol concentrations after time i during the adsorption-photo-Fenton degradation process.

2.6. Reusability Experiments. The reusability of the photocatalyst was performed by repeating the photo-Fenton degradation tests (four times) under the above similar reaction conditions.

3. Results and Discussion

3.1. Material Characterization. The wide-angle XRD patterns of LFO and LFO-RHT are shown in Figure 1(a) and the XRD patterns of SBA-15 and LFO-RHT at low angles are included in Figure 1(b). As can be seen clearly from the low angle XRD, SBA-15 showed a strong characteristic peak at $2\theta = 1°$ and two small diffraction peaks at $2\theta = 1.7$ and 1.9° that could be assignable to the (100), (110), and (200) plane of SBA-15 [36], confirming the success in the synthesis of hard template SBA-15. As expected, in the wide-angle XRD pattern of the LFO-RHT, several characteristic peaks appeared at 2θ of 22.6, 32.2, 39.6, 46.3, 52.0, 57.4, 67.4, 72.0, and 76.7°, which are identical to those in the XRD pattern of our synthesized LFO [37]. The sample LFO-RHT exhibited the characteristic diffraction peaks indexable to the orthorhombic structure of LFO (JCPDS no. 37-1493). Note that the small-angle XRD of LFO-RHT (the inset in Figure 1(b)) showed the diffraction peak that could be indexed to the lattice plane (100) of SBA-15. Although the peak intensity was much lower than that of SBA-15, it still confirmed the existence of the SBA-15 hard template which was not able to be completely removed by NaOH solution [29, 30].

The general morphologies of LFO and LFO-RHT before and after alkali leaching are presented in Figures 2(a)–2(c). LFO is composed of nanosized particles, aggregating into large clumps, as shown in Figure 2(a). As can be seen in Figure 2(b), prior to removing SBA-15 by NaOH solution, the LFO-RHT sample showed agglomerated irregular shaped particles with the diameter in a range of 40–150 nm whilst the morphology of LFO-RHT after the removal of SBA-15 exhibited porous architecture with mesopores diameters in the range of 10–200 nm that were interconnected together (Figure 2(c)). This implies that the filling in the porous structure of SBA-15 and then removing of the SBA-15 hard template have significant influences on the morphology of LFO-RHT. TEM image in Figure 2(d) confirmed the porous structure of LFO-RHT after removing the SBA-15 hard template.

The nitrogen adsorption-desorption isotherms and BJH pore size distribution curves of LFO-RHT are shown in Figure 3. The N_2 adsorption-desorption isotherm curves of LFO-RHT showed a type IV isotherm with H_2-hysteresis

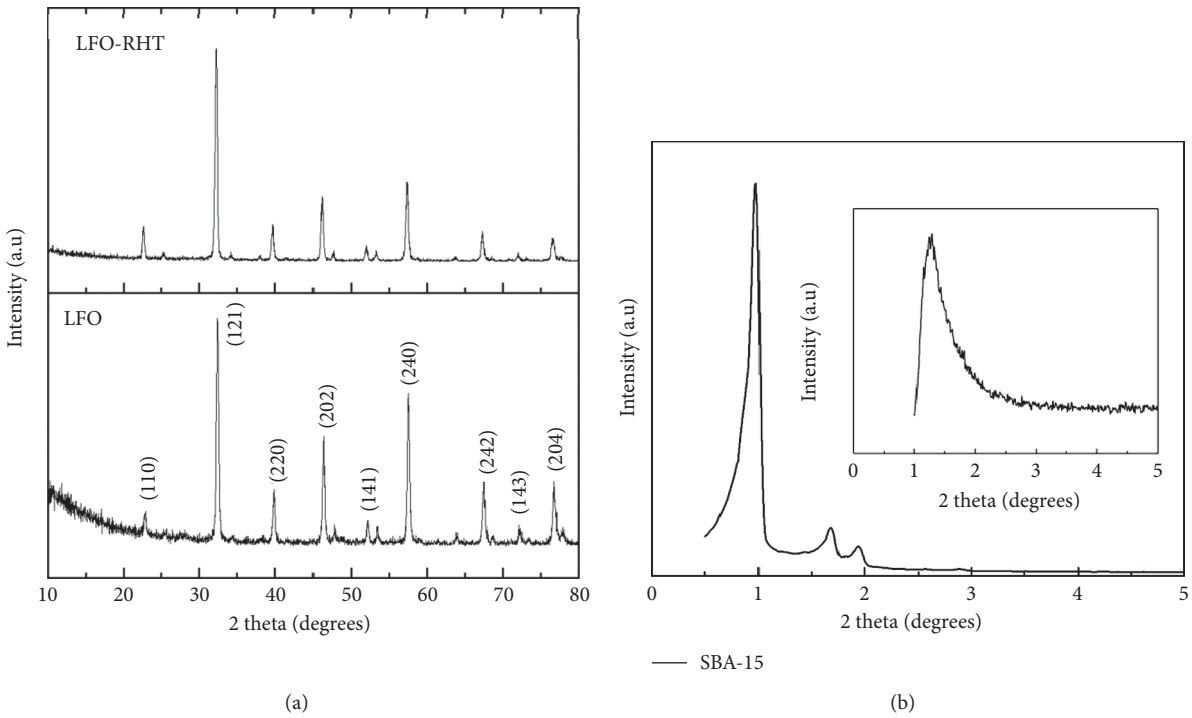

Figure 1: (a) XRD patterns of LFO and LFO-RHT and (b) XRD pattern of SBA-15 at low angles (the inset: XRD patterns of LFO-RHT at low angles).

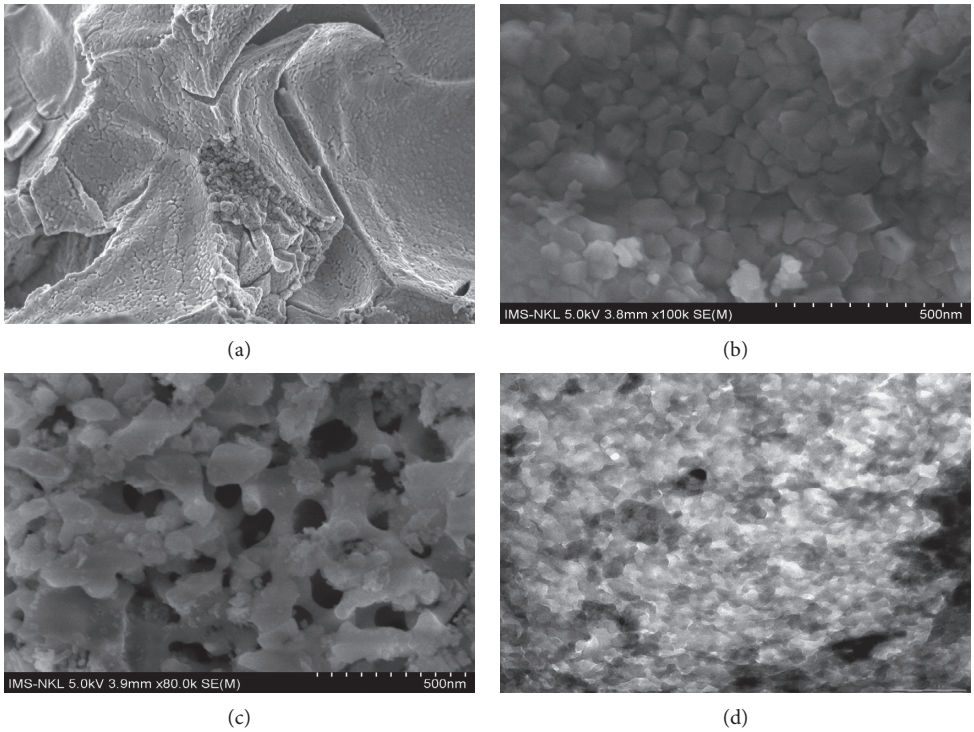

Figure 2: SEM images of (a) LFO, (b-c) LFO-RHT before and after removing SBA-15 hard template; and (d) TEM images of LFO-RHT.

loop appearing in a relative pressure range of 0.4–1 [5], as depicted in Figure 3(a). This suggests the characteristic of the presence of mesopores in the LFO-RHT sample due to the removal of the hard template [33, 38]. It can be seen from Figure 3(b) that the LFO-RHT exhibited a broad pore size distribution with bimodal mesopores peaks at around 10 and 50 nm. The LFO-RHT samples possessed larger specific areas ($48.75\,m^2\ g^{-1}$) than the pure LFO sample ($8.06\,m^2\ g^{-1}$),

which was advantageous to provide more active sites for the adsorption and photo-Fenton degradation to take place and enhancing removal efficiency. In literature, Zhang et al. also reported the improved specific surface area of mesoporous $LaCoO_3$ preparing by the nanocasting method [29]. The textual properties of LFO-RHT are listed in Table 1.

To estimate the surface elemental composition and the valence states of principle elements in LFO-RHT, the XPS spectra of LFO-RHT were investigated. The results presented in Figure 4 revealed the presence of La, Fe, and O elements in the LFO-RHT sample. The La 3d spectrum was examined to evidence the valence of La in Figure 4(a). The main two peaks at around 834 and 850 eV were assigned to La $3d_{5/2}$ and La $3d_{3/2}$ of La^{3+} [24]. The appearance of two peaks at around 710 and 728 eV, consigning to the binding energies of $Fe2p_{3/2}$ and Fe $2p_{1/2}$ on the Fe2p XPS spectrum (Figure 4(b)), implies the existence of Fe^{3+} oxidation state [39]. Figure 4(c) depicts the O 1s spectrum with two major peaks centering at around 528 and 531 eV, which were attributed to the crystal lattice oxygen and chemisorbed oxygen species, respectively [23].

As is well known that the performances of photocatalysts are highly related to their optical properties [40], Figure 5 illustrates the UV-Vis absorption spectra and the corresponding band gap energy of LFO-RHT. The band gap value was calculated from the interception of a linear fit to the low-energy side in a plot of $[F(R)hv]^2$ versus hv based on the following equation [41]:

$$F(R) = \frac{(1-R)^2}{2R}, \tag{4}$$

where hv is the energy of the incident photon, $F(R)$ is the Kubelka Munk function, and R is reflectance.

It can be seen from Figure 5(a) that the absorption spectra of LFO-RHT showed strong absorption in the visible region (400–800 nm). In Figure 5(b), the band gap value of LFO-RHT was estimated to be 1.96 eV, implying its suitability for photodegradation of pollutants under visible light irradiation.

3.2. Photo-Fenton Catalytic Degradation of Phenol

3.2.1. Effect of Different Catalysts on the Removal of Phenol. The removal of phenol using LFO and LFO-RHT via adsorption and photo-Fenton degradation under visible light irradiation is presented in Figure 6(a). It can be found that the tests utilizing no catalyst showed phenol removal of 0% in the absence of H_2O_2 and 8.9% in the presence of H_2O_2. Meanwhile, the LFO sample removed 1.4% and 73.50% of phenol via dark adsorption and photo-Fenton degradation, respectively. Interestingly, the adsorption capacity and photo-Fenton catalytic performance of LFO-RHT were considerably improved in comparison with LFO. The phenol removal rate after 60 min adsorption and 180 min visible light exposure were 12.7% and 94.7%, respectively. This could be attributed to the enhancement of dark adsorption thanks to the mesoporous structure of LFO-RHT, which then facilitates the subsequent photo-Fenton degradation of phenol under visible light irradiation [42]. The dynamics analysis of the phenol photo-Fenton degradation was studied as well. To better understand the reaction kinetic of phenol degradation, the pseudo-first-order model was applied. As can be seen from the pseudo-first-order kinetics in Figure 6(b), LFO-RHT exhibited higher apparent rate constants which are 0.0192 and 2.1 times over that of LFO, implying its faster photo-Fenton degradation rate and better photo-Fenton catalytic activity. Obviously, the modification of the morphology and texture can enhance the photo-Fenton catalytic activity of pure catalyst of $LaFeO_3$.

Figure 6(c) shows the time-dependent absorbance spectrum of LFO-RHT in the phenol photo-Fenton degradation. When irradiation time increased, the absorption maximum of phenol at $\lambda = 272$ nm gradually decreased. There was a slight change in the absorption maximum for LFO-RHT after 120 min exposure to visible light.

3.2.2. Effect of Parameters on the Photo-Fenton Degradation of Phenol. The effects of catalyst dosage, H_2O_2 concentration, and initial pH solution on the photo-Fenton degradation of phenol versus irradiation time are presented in Figures 7(a)–7(c). Figure 7(a) indicates that the photo-Fenton degradation efficiency increased with an increase of catalyst dosage. It could be ascribed to the increase of the number of active sites on the photocatalyst surface and subsequently the formation of hydroxyl radicals. A similar trend has been reported in Wei's study [43]. The highest degradation rate of 94.7% (corresponding total removal rate of 95.37%) was obtained at catalyst loading of 1 g L^{-1} and then decreased. A possible reason is that, as the catalyst dosage increases, the reaction suspension becomes more turbidity, leading to reducing the penetration of visible light into it and in turn decreasing the generation of OH radicals [42]. The observed pseudo-first-order reaction rate constant k for phenol degradation at the catalyst dosages of 0.5, 0.8, 1.0, and 1.2 g L^{-1} were 0.0146, 0.0179, 0.0192, and 0.0082 min^{-1}, respectively. Yu et al. reported similar observations for the photo-Fenton degradation of phenol by using Fe_3O_4-GO nanocomposite [44]. Therefore, 1 g L^{-1} was identified as the optimal catalyst dosage for the photo-Fenton degradation of phenol using LFO-RHT in our work.

In the heterogeneous photo-Fenton system, the influence of H_2O_2 concentration is important for the degradation of phenol because the amount of formed OH radicals depends on the H_2O_2 concentration [45]. In general, H_2O_2 concentration has effects on the photo-Fenton reaction via the following two opposing cases: (i) as the H_2O_2 concentration was increased, the phenol removal rate was enhanced due to the increasing of OH radicals which are available for a phenol attack; (ii) at higher concentration of H_2O_2, the excess amount H_2O_2 in the reaction solution could react with OH radicals to produce less reactive hydroperoxyl radicals (HO_2) (the following equation) and in turn lower photo-Fenton degradation efficiency [46]:

$$OH + H_2O_2 \longrightarrow HO_2 + H_2O \tag{5}$$

As can be seen in Figure 7(b), a maximum total removal rate of 95.37% was achieved with an optimal value of H_2O_2

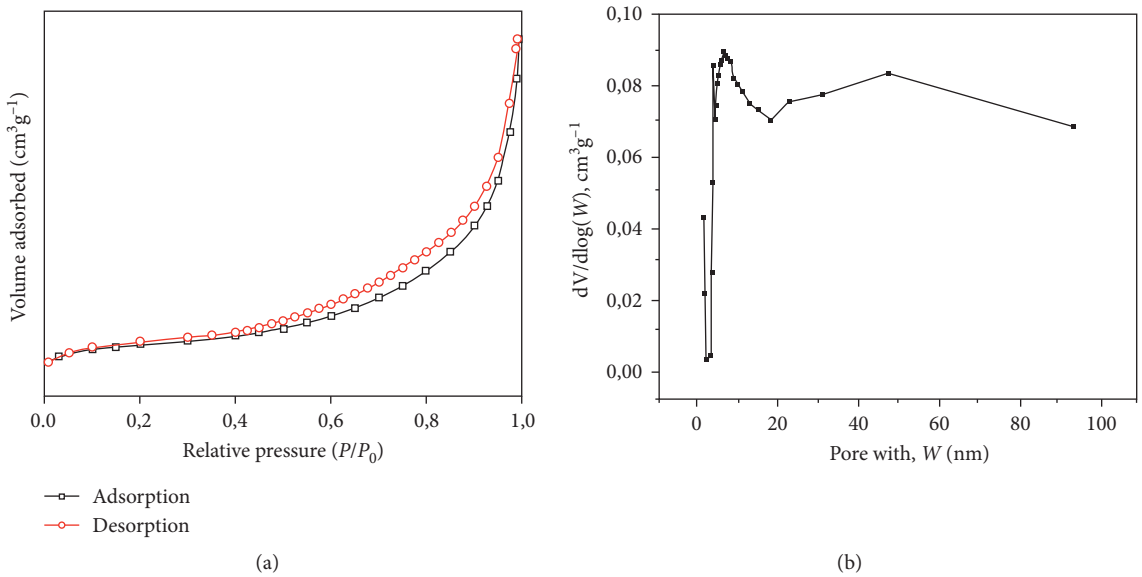

Figure 3: (a) N_2 adsorption-desorption isotherm and (b) BJH pore size distribution of LFO-RHT.

Table 1: Characteristics of LFO-RHT and LFO samples.

Sample	Structural property		
	BET specific surface area (m^2 g^{-1})	Pore volume (cm^3 g^{-1})	Pore size (nm)
LFO-RHT	48.75	0.142	7.87
LFO	8.06	0.028	11.43

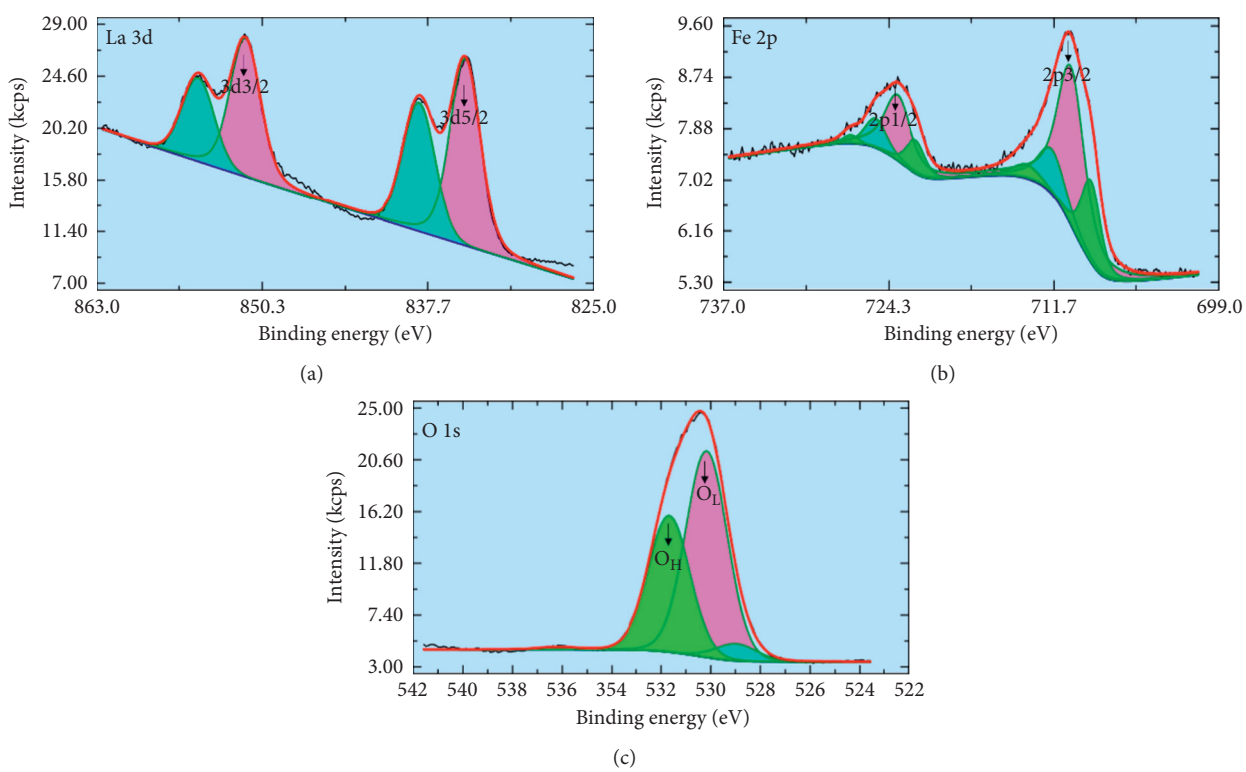

Figure 4: XPS spectra of (a) La 3d, (b) Fe 2p, and (c) O 1s for LFO-RHT.

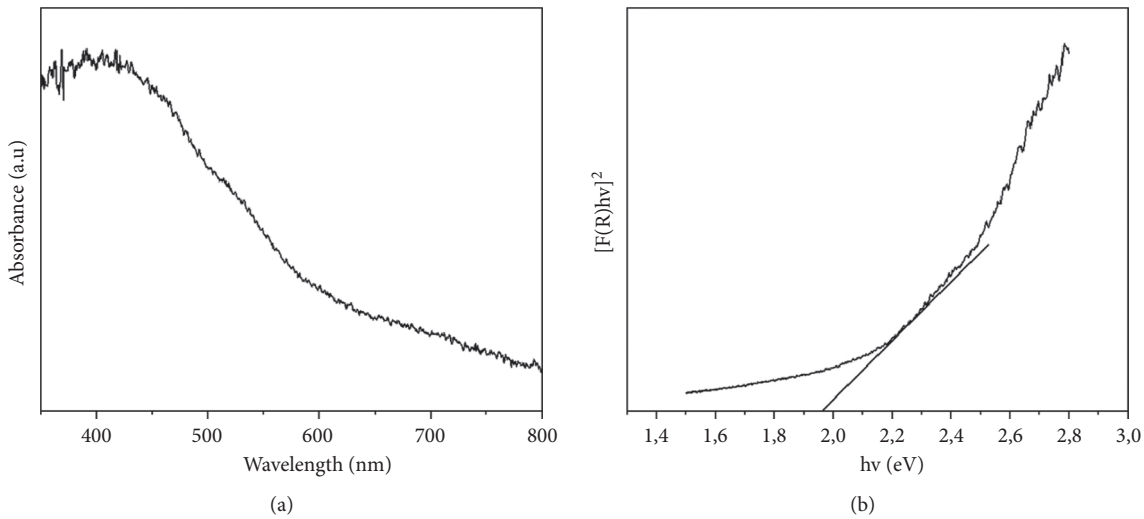

Figure 5: (a) UV-Vis absorption spectra and (b) corresponding [F (R) hv]2 versus hv plot.

concentration of 10 mM. However, a decrease of phenol total removal rate by 6.98% was observed when further increasing the concentration of H_2O_2 to 20 mM. The fitting of photo-Fenton catalytic degradation data in Figure 7(b) showed that the reaction rate constants k for phenol degradation in 5 mM, 10 mM, 15 mM, and 20 mM H_2O_2 were 0.0091, 0.0192, 0.0130, and 0.0123 min^{-1}, respectively.

Industrial wastewater could be acidic or basic medium due to its discharging from different industrial activities and thus the effect of pH should be studied. The effect of initial solution pH on phenol photo-Fenton degradation is presented in Figure 7(c). The phenol degradation rate via the photo-Fenton process decreased with increasing pH values, which is consistent with the previous reports [44, 47]. It can be observed that the maximum photo-Fenton degradation of phenol of 94.7% was achieved at pH 5.0 while the degradation rate dropped to 90.8% at pH = 8 and 86.7% at pH = 10. The pseudo-first-order reaction rate constant k was found to be the highest (0.0192 min^{-1}) at pH = 5 as compared with 0.0146, 0.0131, and 0.0112 min^{-1} when at pH = 3, 8, and 10, respectively. This could be explained by the changes in the surface charge of LFO-RHT, the dissociation of phenol, and the generation of hydroxyl radicals during the photo-Fenton reaction. As can be seen from Figure S1, the pH of point zero of charge (pH_{pzc}) of LFO-RHT is 6.05 which is determined by using the pH drift method [29]. At pH below the pH_{pzc} (pH = 3 and 5), the surface of the LFO-RHT is positively charged, whilst at pH above the pH_{pzc} (pH = 8 and 10), it is negatively charged. Meanwhile, phenol is in a molecular form at a neutral or weakly alkaline solution and in phenoxide ion $C_6H_5O^-$ structure at high pH values due to its dissociation [47]. Therefore, at low pH values, there is no electrostatic repulsion between the positively charged surface of LFO-RHT and phenol species. Moreover, the generation of hydroxyl radicals was found to be easier in an acidic medium than in a neutral or basic medium [42]. Noting that, as the solution is too acidic (pH = 3), the excess H^+ ions could react with hydroxyl radicals OH in the solution, leading to a deterioration in the degradation rate [17]. Thus, the highest degradation rate was observed at pH = 5. At pH = 8 and 10, the negatively charged surfaces of LFO-RHT might hinder the adsorption of anion phenoxide species due to the repulsive force, causing a slight decrease in the phenol degradation rate. Jiang and coworkers have reported a similar observation [48]. From a practical application point of view, the degradation of phenol at pH = 5 would be an environmentally friendly process because the pH of the phenol-containing industrial effluents is around 5.

Based on the above results, a possible photo-Fenton catalytic mechanism using LFO-RHT was proposed, as follows:

$$\equiv Fe^{III} + H_2O_2 \longrightarrow Fe^{III}H_2O_2 \quad (6)$$

$$\equiv Fe^{III} + H_2O_2 \longrightarrow Fe^{II} + HO_2 + H^+ \quad (7)$$

$$\equiv Fe^{III} + HO_2 + H^+ \longrightarrow Fe^{II} + O_2 + 2H^+ \quad (8)$$

$$\equiv Fe^{II} + H_2O_2 \longrightarrow Fe^{III} + OH + OH^- \quad (9)$$

$$LFO - RHT + hv \longrightarrow LFO - RHT\left(e^- + h^+\right) \quad (10)$$

$$H_2O_2 + e^- \longrightarrow OH + OH^- \quad (11)$$

$$OH + \text{phenol} \longrightarrow \text{degradation products} \quad (12)$$

As is well known during Fenton-like reaction, the interfacial Fe atoms (denoted as $\equiv Fe^{III}$) of LFO-RHT photocatalyst can react with H_2O_2 to generate OH radicals (equations (6)–(9)) which can directly oxidize phenol to degradation products (equation (12)) [22]. Under visible light irradiation, the LFO-RHT photocatalyst undergoes charge separation which produces electrons (e^-) and holes ($\underline{h}^+$) simultaneously (equation 10). Then, the electron is trapped by H_2O_2 to form the OH as well (equation (11)) [17]. Therefore, the considerable improvement in the rate of phenol removal benefits from the synergism of photocatalysis and heterogeneous Fenton-like reaction.

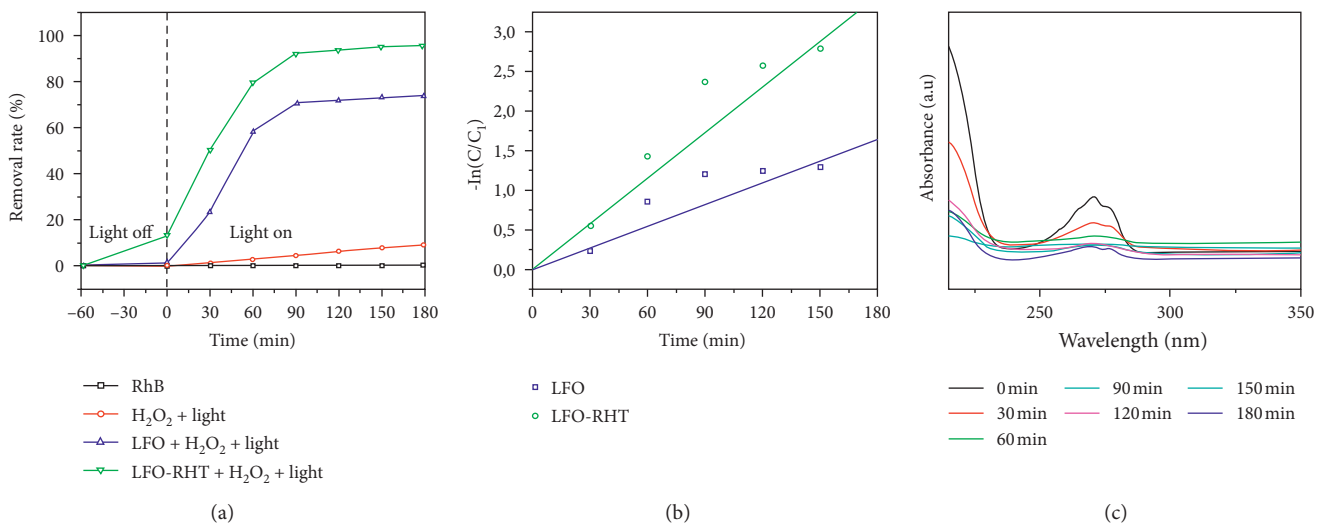

Figure 6: (a) Removal of phenol by adsorption and photo-Fenton reaction using LFO and LFO-RHT catalysts; (b) plots of –ln ($C/C1$) versus irradiation time; and (c) temporal UV-Vis spectral change of phenol aqueous solution versus irradiation time in the photo-Fenton reaction (test conditions: temperature = 25°C; phenol concentration = 20 mg L^{-1}; catalyst dosage = 1 g L^{-1}; H_2O_2 concentration = 10 mM; pH = 5).

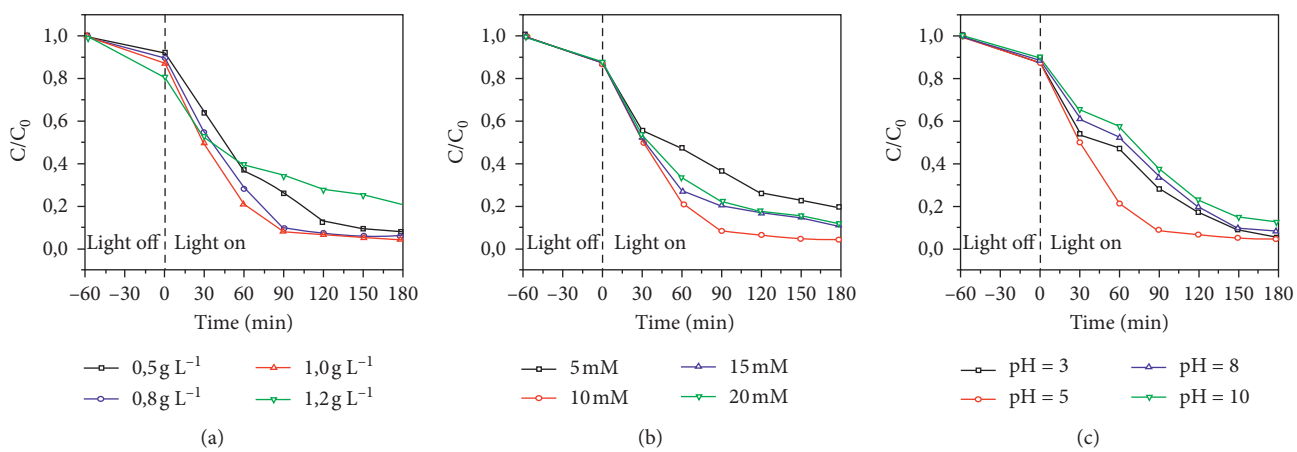

Figure 7: (a) Effect of catalyst dosage (H_2O_2 concentration = 10 mM); (b) H_2O_2 concentration; and (c) initial solution pH (H_2O_2 concentration = 10 mM) on photo-Fenton degradation of phenol (reaction conditions (if not specified): temperature = 25°C, catalyst dosage = 1 g L^{-1}, initial phenol concentration = 20 mg L^{-1}, and initial solution pH = 5).

3.3. Reusability of LFO-RHT Catalyst. Photocatalytic stability is considered as one of the important criteria in evaluating photocatalyst performances. In order to explore the reusability of the as-synthesized catalyst, the stability of the LFO-RHT photocatalyst was evaluated by successive experiments, as shown in Figure 8(a). Obviously, LFO-RHT showed good stability for the photo-Fenton degradation of phenol under visible light irradiation and has no significant loss of activity after 4 recycles. At the fourth experiment, the photo-Fenton degradation rate of phenol is up to 93.47% after 180 min exposure to visible light irradiation, which is relatively similar to the first run (94.7%). Moreover, a comparison of XRD diffraction patterns of the fresh and after 4 recycles of LFO-RHT was performed as shown in Figure 8(b). It was found that there are no significant changes between these two samples, suggesting the stability of LFO-RHT during reaction, which indicates that the LFO-RHT is a stable and reusable photocatalyst in wastewater treatment.

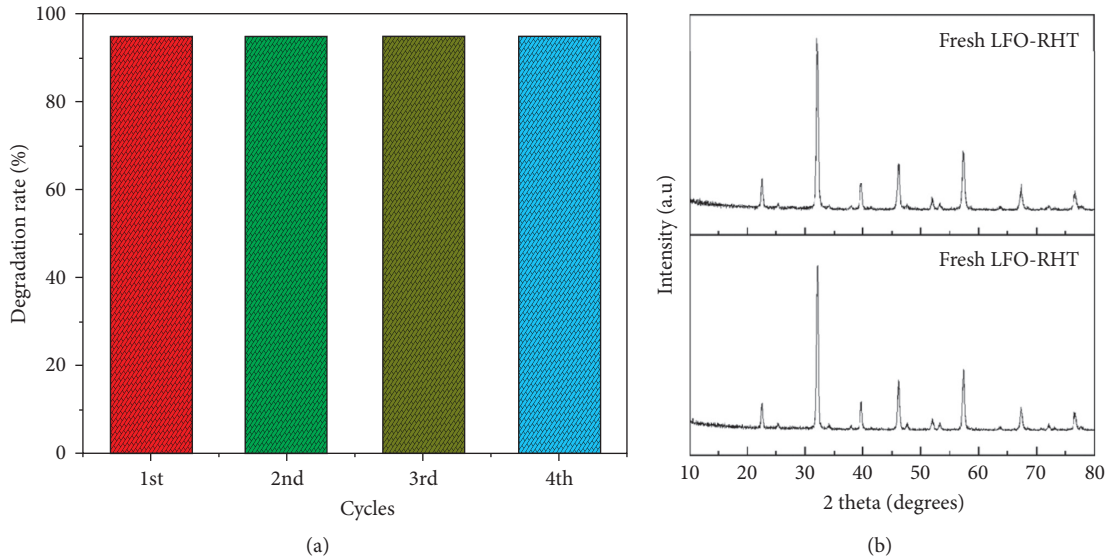

Figure 8: (a) The regeneration and reusability of LFO-RHT for the photo-Fenton degradation of phenol over 4 cycles and (b) XRD patterns of LFO-RHT before and after 4 cycles of photo-Fenton degradation test.

4. Conclusions

Mesoporous $LaFeO_3$ particles with pure perovskite phase have been synthesized via a nanocasting process. Characterization and experimental results showed that $LaFeO_3$ with porous structure could improve the phenol adsorption ability of the photocatalyst and in turn enhance its photo-Fenton catalytic activity, implying synergistic effects of adsorption, and the photo-Fenton process is a good technique for phenol removal. Effects of catalyst dosage, H_2O_2 concentration, and initial solution pH on the photo-Fenton degradation of phenol were systematically investigated. Furthermore, our results proved that mesoporous $LaFeO_3$ exhibited good photo-Fenton catalytic activity and stability even after four cycles and proposed its photo-Fenton catalytic mechanism for the degradation of phenol under visible light.

Data Availability

The data used to support the findings of this study are available from the corresponding author upon request.

Conflicts of Interest

There are no conflicts of interest to declare.

Acknowledgments

This research was funded by the Hanoi University of Science and Technology (HUST) under Project no. T2020-SAHEP-029.

Supplementary Materials

Figure S1: the pH of point of zero charge of LFO-RHT. (*Supplementary Materials*)

References

[1] B. Diya'uddeen, S. R. Pouran, A. R. A. Aziz, S. M. Nashwan, W. M. A. W. Daud, and M. G. Shaaban, "Hybrid of Fenton and sequencing batch reactor for petroleum refinery wastewater treatment," *Journal of Industrial and Engineering Chemistry*, vol. 25, pp. 186–191, 2015.

[2] F. Adam, J. Andas, and I. A. Rahman, "A study on the oxidation of phenol by heterogeneous iron silica catalyst," *Chemical Engineering Journal*, vol. 165, no. 2, pp. 658–667, 2010.

[3] G. M. Salcedo, L. Kupski, J. L. de Oliveira Arias, S. C. Barbosa, and E. G. Primel, "Bojuru sand as a novel catalyst for refinery wastewater treatment and phenol degradation by heterogeneous photo catalysis," *Journal of Photochemistry and Photobiology A: Chemistry*, vol. 402, Article ID 112796, 2020.

[4] X. Zhang, J. Chen, S. Jiang et al., "Enhanced photocatalytic degradation of gaseous toluene and liquidus tetracycline by anatase/rutile titanium dioxide with heterophase junction derived from materials of Institut Lavoisier-125(Ti): degradation pathway and mechanism studies," *Journal of Colloid and Interface Science*, vol. 588, pp. 122–137, 2021.

[5] Y. Wang, R. Wang, N. Lin, Y. Wang, and X. Zhang, "Highly efficient microwave-assisted Fenton degradation bisphenol A using iron oxide modified double perovskite intercalated montmorillonite composite nanomaterial as catalyst," *Journal of Colloid and Interface Science*, vol. 594, pp. 446–459, 2021.

[6] Y. Wang, N. Lin, Y. Gong, R. Wang, and X. Zhang, "Cu-Fe embedded cross-linked 3D hydrogel for enhanced reductive removal of Cr(VI): characterization, performance, and mechanisms," *Chemosphere*, vol. 280, Article ID 130663, 2021.

[7] Y. Wang, R. Wang, L. Yu, Y. Wang, C. Zhang, and X. Zhang, "Efficient reactivity of LaCu0.5Co0.5O3 perovskite intercalated montmorillonite and g-C3N4 nanocomposites in microwave-induced H2O2 catalytic degradation of bisphenol A," *Chemical Engineering Journal*, vol. 401, Article ID 126057, 2020.

[8] L. Hu, P. Wang, G. Zhang et al., "Enhanced persulfate oxidation of organic pollutants and removal of total organic

carbons using natural magnetite and microwave irradiation," *Chemical Engineering Journal*, vol. 383, Article ID 123140, 2020.

[9] O. B. Ayodele, J. K. Lim, and B. H. Hameed, "Degradation of phenol in photo-Fenton process by phosphoric acid modified kaolin supported ferric-oxalate catalyst: optimization and kinetic modeling," *Chemical Engineering Journal*, vol. 197, pp. 181–192, 2012.

[10] L. Di, H. Yang, T. Xian, X. Liu, and X. Chen, "Photocatalytic and photo-Fenton catalytic degradation activities of Z-scheme Ag2S/BiFeO3 heterojunction composites under visible-light irradiation," *Nanomaterials*, vol. 9, no. 3, p. 399, 2019.

[11] V. Kavitha and K. Palanivelu, "The role of ferrous ion in Fenton and photo-Fenton processes for the degradation of phenol," *Chemosphere*, vol. 55, no. 9, pp. 1235–1243, 2004.

[12] M. Antonopoulou, E. Evgenidou, D. Lambropoulou, and I. Konstantinou, "A review on advanced oxidation processes for the removal of taste and odor compounds from aqueous media," *Water Research*, vol. 53, pp. 215–234, 2014.

[13] Y. Yang, W. Ji, X. Li et al., "Insights into the degradation mechanism of perfluorooctanoic acid under visible-light irradiation through fabricating flower-shaped Bi5O7I/ZnO n-n heterojunction microspheres," *Chemical Engineering Journal*, vol. 420, Article ID 129934, 2021.

[14] Y. Yang, Z. Zheng, M. Yang et al., "In-situ fabrication of a spherical-shaped Zn-Al hydrotalcite with BiOCl and study on its enhanced photocatalytic mechanism for perfluorooctanoic acid removal performed with a response surface methodology," *Journal of Hazardous Materials*, vol. 399, Article ID 123070, 2020.

[15] A. Babuponnusami and K. Muthukumar, "Degradation of Phenol in Aqueous Solution by Fenton, Sono-Fenton and Sono-photo-Fenton Methods degradation of phenol in aqueous solution by fenton, sono-fenton and sono-photo-fenton methods," *CLEAN - Soil, Air, Water*, vol. 39, no. 2, pp. 142–147, 2011.

[16] F. Chen, W. An, L. Liu, Y. Liang, and W. Cui, "Highly efficient removal of bisphenol A by a three-dimensional graphene hydrogel-AgBr@rGO exhibiting adsorption/photocatalysis synergy," *Applied Catalysis B: Environmental*, vol. 217, pp. 65–80, 2017.

[17] T. Huang, J. Zhu, S. Ge, T. Guo, C. Jiang, and L. Xie, "Synthesis of novel CdSe QDs/BiFeO3 composite catalysts and its application for the photo-Fenton catalytic degradation of phenol," *Journal of Environmental Chemical Engineering*, vol. 8, no. 5, Article ID 104384, 2020.

[18] P. Garcia-Muñoz, F. Fresno, C. Lefevre, D. Robert, and N. Keller, "Highly robust La1-xTixFeO3 dual catalyst with combined photocatalytic and photo-CWPO activity under visible light for 4-chlorophenol removal in water," *Applied Catalysis B: Environmental*, vol. 262, Article ID 118310, 2020.

[19] Q. Feng, J. Zhou, W. Luo, L. Ding, and W. Cai, "Photo-Fenton removal of tetracycline hydrochloride using LaFeO3 as a persulfate activator under visible light," *Ecotoxicology and Environmental Safety*, vol. 198, Article ID 110661, 2020.

[20] B. Palas, G. Ersöz, and S. Atalay, "Photo Fenton-like oxidation of Tartrazine under visible and UV light irradiation in the presence of LaCuO3 perovskite catalyst," *Process Safety and Environmental Protection*, vol. 111, pp. 270–282, 2017.

[21] Y. Jia, C. Wu, D.-H. Kim et al., "Nitrogen doped BiFeO3 with enhanced magnetic properties and photo-Fenton catalytic activity for degradation of bisphenol A under visible light," *Chemical Engineering Journal*, vol. 337, pp. 709–721, 2018.

[22] P. Garcia-Muñoz, F. Fresno, C. Lefevre, D. Robert, and N. Keller, "Synergy effect between photocatalysis and heterogeneous photo-Fenton catalysis on Ti-doped LaFeO3 perovskite for high efficiency light-assisted water treatment," *Catalysis Science & Technology*, vol. 10, no. 5, pp. 1299–1310, 2020.

[23] Y. Ye, H. Yang, H. Zhang, and J. Jiang, "A promising Ag2CrO4/LaFeO3 heterojunction photocatalyst applied to photo-Fenton degradation of RhB," *Environmental Technology*, vol. 41, no. 12, pp. 1486–1503, 2020.

[24] S. Guan, H. Yang, X. Sun, and T. Xian, "Preparation and promising application of novel LaFeO3/BiOBr heterojunction photocatalysts for photocatalytic and photo-Fenton removal of dyes," *Optical Materials*, vol. 100, Article ID 109644, 2020.

[25] S. Guan, R. Li, X. Sun, T. Xian, and H. Yang, "Construction of novel ternary Au/LaFeO3/Cu2O composite photocatalysts for RhB degradation via photo-Fenton catalysis," *Materials Technology*, pp. 1–13, 2020.

[26] A. Alpay, Ö. Tuna, and E. B. Simsek, "Deposition of perovskite-type LaFeO3 particles on spherical commercial polystyrene resin: a new platform for enhanced photo-Fenton-catalyzed degradation and simultaneous wastewater purification," *Environmental Technology & Innovation*, vol. 20, Article ID 101175, 2020.

[27] T. T. N. Phan, A. N. Nikoloski, P. A. Bahri, and D. Li, "Enhanced removal of organic using LaFeO3-integrated modified natural zeolites via heterogeneous visible light photo-Fenton degradation," *Journal of Environmental Management*, vol. 233, pp. 471–480, 2019.

[28] Y. Ji, Y. Xie, L. Zheng, and F. Xu, "Efficient activation of peroxymonosulfate by porous Co-doped LaFeO3 for organic pollutants degradation in water," *Journal of Solid State Chemistry*, vol. 297, Article ID 122077, 2021.

[29] Y. Wang, J. Ren, Y. Wang et al., "Nanocasted synthesis of mesoporous LaCoO3 perovskite with extremely high surface area and excellent activity in methane combustion," *The Journal of Physical Chemistry C*, vol. 112, no. 39, pp. 15293–15298, 2008.

[30] M. M. Nair, F. Kleitz, and S. Kaliaguine, "Kinetics of methanol oxidation over mesoporous perovskite catalysts," *ChemCatChem*, vol. 4, no. 3, pp. 387–394, 2012.

[31] J. Wang, H. Guo, Y. Liu, W. Li, and B. Yang, "Peroxymonosulfate activation by porous BiFeO3 for the degradation of bisphenol AF: non-radical and radical mechanism," *Applied Surface Science*, vol. 507, Article ID 145097, 2020.

[32] Y. Wang, L. Wang, R. Liu, and X. Li, "Casein templated synthesis of porous perovskite and its application in visible-light photocatalytic degradation of methylene blue," *Materials Science in Semiconductor Processing*, vol. 103, Article ID 104597, 2019.

[33] R. Zhang, P. Li, N. Liu, W. Yue, and B. Chen, "Effect of hard-template residues of the nanocasted mesoporous LaFeO3with extremely high surface areas on catalytic behaviors for methyl chloride oxidation," *Journal of Materials Chemistry A*, vol. 2, no. 41, pp. 17329–17340, 2014.

[34] H. Li, J. Zhu, P. Xiao et al., "On the mechanism of oxidative degradation of rhodamine B over LaFeO3 catalysts supported on silica materials: role of support," *Microporous and Mesoporous Materials*, vol. 221, pp. 159–166, 2016.

[35] D. Zhao, Q. Huo, J. Feng, B. F. Chmelka, and G. D. Stucky, "Nonionic triblock and star diblock copolymer and oligomeric surfactant syntheses of highly ordered, hydrothermally stable, mesoporous silica structures," *Journal of the American Chemical Society*, vol. 120, no. 24, pp. 6024–6036, 1998.

[36] M. Kruk, M. Jaroniec, C. H. Ko, and R. Ryoo, "Characterization of the porous structure of SBA-15," *Chemistry of Materials*, vol. 12, no. 7, pp. 1961–1968, 2000.

[37] T. T. N. Phan, A. N. Nikoloski, P. A. Bahri, and D. Li, "Adsorption and photo-Fenton catalytic degradation of organic dyes over crystalline LaFeO3-doped porous silica," *RSC Advances*, vol. 8, no. 63, pp. 36181–36190, 2018.

[38] Y. Wang, l. Yu, R. Wang, Y. Wang, and X. Zhang, "Reactivity of carbon spheres templated Ce/LaCo0.5Cu0.5O3 in the microwave induced H2O2 catalytic degradation of salicylic acid: characterization, kinetic and mechanism studies," *Journal of Colloid and Interface Science*, vol. 574, pp. 74–86, 2020.

[39] Y. Song, S. Xue, G. Wang et al., "Enhanced photocatalytic decomposition of an organic dye under visible light with a stable LaFeO3/AgBr heterostructured photocatalyst," *Journal of Physics and Chemistry of Solids*, vol. 121, pp. 329–338, 2018.

[40] Y. Wang, F. Qin, Z. Yi et al., "Effect of slit width on surface plasmon resonance," *Results in Physics*, vol. 15, Article ID 102711, 2019.

[41] B. M. Pirzada and Pushpendra, B. S. Kunchala, Synthesis of LaFeO3/Ag2CO3 nanocomposites for photocatalytic degradation of Rhodamine B and p-Chlorophenol under natural sunlight," *ACS Omega*, vol. 4, no. 2, pp. 2618–2629, 2019.

[42] T. T. N. Phan, A. N. Nikoloski, P. A. Bahri, and D. Li, "Optimizing photocatalytic performance of hydrothermally synthesized LaFeO3 by tuning material properties and operating conditions," *Journal of Environmental Chemical Engineering*, vol. 6, no. 1, pp. 1209–1218, 2018.

[43] X. Wei, H. Wu, G. He, and Y. Guan, "Efficient degradation of phenol using iron-montmorillonite as a Fenton catalyst: importance of visible light irradiation and intermediates," *Journal of Hazardous Materials*, vol. 321, pp. 408–416, 2017.

[44] L. Yu, J. Chen, Z. Liang, W. Xu, L. Chen, and D. Ye, "Degradation of phenol using Fe3O4-GO nanocomposite as a heterogeneous photo-Fenton catalyst," *Separation and Purification Technology*, vol. 171, pp. 80–87, 2016.

[45] J. Feng, X. Hu, P. L. Yue, H. Y. Zhu, and G. Q. Lu, "Degradation of azo-dye orange II by a photoassisted Fenton reaction using a novel composite of iron oxide and silicate nanoparticles as a catalyst," *Industrial and Engineering Chemistry Research*, vol. 42, no. 10, pp. 2058–2066, 2003.

[46] H. Kusic, N. Koprivanac, A. Bozic, and I. Selanec, "Photo-assisted Fenton type processes for the degradation of phenol: a kinetic study," *Journal of Hazardous Materials*, vol. 136, no. 3, pp. 632–644, 2006.

[47] M. Khraisheh, L. Wu, A. a. H. Al-Muhtaseb, A. B. Albadarin, and G. M. Walker, "Phenol degradation by powdered metal ion modified titanium dioxide photocatalysts," *Chemical Engineering Journal*, vol. 213, pp. 125–134, 2012.

[48] Z. Jiang, L. Wang, J. Lei, Y. Liu, and J. Zhang, "Photo-Fenton degradation of phenol by CdS/rGO/Fe2+ at natural pH with in situ-generated H2O2," *Applied Catalysis B: Environmental*, vol. 241, pp. 367–374, 2019.

Hindawi
Journal of Chemistry
Volume 2021, Article ID 7248402, 9 pages
https://doi.org/10.1155/2021/7248402

Research Article

Treatment of Cutting Oil-in-Water Emulsion by Combining Flocculation and Fenton Oxidation

Chu Thi Hai Nam,[1] **Nguyen Thi Thu Hien**,[2] **Nguyen Thi Thu Huyen**,[1] **Hoang Huu Hiep**,[1] **and Nghiem Thi Thuong**[1]

[1]*School of Chemical Engineering, Hanoi University of Science and Technology, No. 1 Dai Co Viet, Hanoi, Vietnam*
[2]*Institute of Chemistry, Vietnam Academy of Science and Technology, 18 Hoang Quoc Viet, Hanoi, Vietnam*

Correspondence should be addressed to Nghiem Thi Thuong; thuong.nghiemthi@hust.edu.vn

Received 21 April 2021; Revised 11 May 2021; Accepted 22 May 2021; Published 28 May 2021

Academic Editor: Ibrahim H. Alsohaimi

Recently, the disposal of waste oil-in-water cutting emulsion has become an urgent issue because of its extremely high chemical oxygen demand (COD). The present work focuses on treating the waste cutting emulsion generated from the Samsung Thai-Nguyen factory in Vietnam. This work used multistage methods to treat the waste cutting emulsion to meet the wastewater disposal requirement and characterize the oil recovered. The multistage methods consist of the flocculation method (stage 1) and Fenton oxidation (stage 2). The wastewater after stage 1 treatment has a COD reduction efficiency of 98.24% at the condition of pH 5, $Al_2(SO_4)_3$ 2 g/L, C-PAM 12 mg/L, stirring speed 50 rpm, and stirring time 15 minutes. At that condition, the COD value decreased from 147200 mg/L to 2484 mg/L. After stage 2, the COD value further decreased from 2484 mg/L to 85.4 mg/L with total COD removal efficiency increasing to 99.9% at the optimum conditions of pH 3, $H_2O_2 : FeSO_4$ concentration ratio of 10 : 1, and $FeSO_4$ concentration of 14.04 g/L. After the stage 2 treatment, the wastewater with the COD value of 85.4 mg/L and BOD_5 value of 30 mg/L satisfied the Vietnam standard grade B and grade A, respectively, for industrial wastewater. The oil recovered from the treatment has a heating value of 38095 ± 8 kJ/kg, and thus, it could be reusable as fuel gas.

1. Introduction

Metal cutting emulsions or cutting fluids play an important role in the machining process. They are frequently used in metalworking industries for several reasons, such as lubricating and cooling the machine. It also helps to increase the cutting tool efficiency and its lifetime and improve the surface of the workpiece and protect them from corrosion [1, 2]. Among various types of cutting emulsions, oil-in-water emulsions are the most preferred in the industry due to their longer period and easier preparation [3, 4]. These emulsions are formed by blending oil and water for about 3–15% oil concentration and the emulsifiers for more stable emulsion [5].

Despite their huge advantages, cutting emulsions is becoming the main source of oil-contaminated wastewater in metal industries. They contain chemical ingredients toxic to human health and cause some symptoms such as skin irritation, respiratory diseases, or cancers [6]. The composition of the used cutting emulsion was probably denatured and become more toxic than before using. If disposal techniques are not appropriate, they will lead to secondary contamination and harm to the environment. The serious issues on the treatment were due to the complicated composition and the high volume of the wastewater disposal. It is estimated that more than 1000 million gallons of the cutting emulsions are disposed of each year in the USA, and the amount of wastewater may increase a lot after using [7, 8]. It brings about more challenges for the treatment to meet the requirement of the standard for discharging fluids.

There are many methods used for the treatment of the O/W cutting emulsion. They are physical separation [9], chemical treatment [10, 11], biodegradation [12, 13], and advanced oxidation process (AOP) [14, 15]. In recent years,

AOP is gaining attention for its high efficiency, simple process, and ability to handle nonbiodegradable fluids. AOP is a technology that uses hydroxyl free radicals ($^{\bullet}OH$) that break down toxic organic compounds into harmless compounds such as CO_2 and water [16, 17]. The Fenton method is being most widely applied with a series of advantages such as no need for stimulating reactive energy, easy-to-obtain chemicals, fast processing time, and high efficiency [17]. In general, the Fenton oxidation process consists of the primary reaction between H_2O_2 and Fe^{2+} in an acidic medium to generate $OH^{\bullet}$, the radical species necessary for organic pollutant degradation. The reaction mechanism is complex followed by equations (1)–(7) [18, 19]. It demonstrates that the Fenton process is closely dependent on the pH of solution, ferric concentration, and hydrogen peroxide concentration. Therefore, to obtain the best treatment by Fenton oxidation, it is necessary to determine the suitable conditions for the treatment:

$$H_2O_2 + Fe^{2+} \longrightarrow Fe^{3+} + OH^{\bullet} + OH^{-} \quad (1)$$

$$Fe^{2+} + H_2O_2 \longrightarrow Fe^{2+} + HO_2^{\bullet} + H^{+} \quad (2)$$

$$OH^{\bullet} + H_2O_2 \longrightarrow HO_2^{\bullet} + H_2O \quad (3)$$

$$OH^{\bullet} + Fe^{2+} \longrightarrow Fe^{3+} + OH^{-} \quad (4)$$

$$Fe^{3+} + HO_2^{\bullet} \longrightarrow Fe^{2+} + O_2 + H^{+} \quad (5)$$

$$Fe^{3+} + HO_2^{\bullet} + H^{+} \longrightarrow Fe^{3+} + H_2O_2 \quad (6)$$

$$HO_2^{\bullet} + HO_2^{\bullet} \longrightarrow H_2O_2 + O_2 \quad (7)$$

Previous work reported that the combinations of several methods lead to enhanced treatment. For instance, the electrochemical method could be combined with membrane filtration [20, 21]. Another work from Kaur and Sodhi reported treating cutting emulsion by adsorption from the agricultural waste [22]. Su et al. reported that a combination of flocculation and absorption by the heterogeneous Fenton system could remove 99.8% of chemical oxygen demand (COD) for wastewater [23]. However, the heterogeneous Fenton system is very difficult to apply at a larger scale due to the high cost and difficulty to scale up. The demand for cheap and efficient methods to treat waste-cutting emulsion is still more urgent. If the oil concentration is too high, it is necessary to recover and recycle the separated oil.

In this work, the aim is to treat cutting fluids discharged from Samsung Thai-Nguyen company in Vietnam to pass the Vietnam standard for treated wastewater. COD was selected as the target standard for the treatment. At first, the cutting emulsion was characterized to determine some physiochemistry properties. Secondly, stage 1 was carried out by the flocculation method using flocculants. Then, it is treated further using a homogenous Fenton process to increase the treatment's efficiency at a large scale. A flotation technique was applied to obtain a better recovery of oil. The flocculation was selected due to the suitability and low cost as compared to other methods. Also, at high COD of the cutting emulsion, the flocculation will remove oils, a major cause of the high COD of cutting emulsion wastewater. Two flocculation agents that are $Al_2(SO_4)_3$ and cationic polyacrylamide (C-PAM) were used. C-PAM is a positively charged organic polymer used as a water treatment flocculant aid [23]. The Fenton oxidation was selected as stage 2 for the treatment. The hydroxyl radical produced from advanced oxidation can decompose the residual oil and other contaminants into harmless substances such as CO_2 and water [24].

2. Experimental

2.1. Characterization of Oil-in-Water Emulsion. Cutting emulsions were provided by Samsung Thai-Nguyen, Vietnam. The oil concentration in the emulsion was determined by the steam distillation method. The heat value of the recovered oil was determined with Parr 6300 (USA) according to ASTM D240. The pH of the sample was determined using Titra Lab machine, TIM 900 of France. Particle size distribution and zeta potential of the emulsion were determined by dynamic laser scattering technique using Horiba SZ-100.

2.2. Stage 1: Flocculation Process. Stage 1 treatment of waste cutting O/W emulsion by flocculation method was conducted as follows: first, $Al_2(SO_4)_3$ (initial concentration of 35 wt.%) was added slowly into a beaker containing about 200 mL of waste cutting emulsion under constant stirring. Simultaneously, the pH of the reaction was adjusted using NaOH 1 M or H_2SO_4 0.5 M and continued stirring for 5 minutes. After that, C-PAM (initial concentration of 0.2 wt.%) was injected under gentle stirring for 15 minutes. The oil and the sludge were separated with a separating funnel, and the oil was recovered. The water after filtration was bubbled for 30 minutes (with air compression at pressure $P = 5$ bar, gas flow 5 mL/min) and filtered again. COD of the wastewater after this step was determined to evaluate the COD removal efficiency of the process. The detailed procedure is given in Figure 1.

2.3. Stage 2: Fenton Oxidation. The wastewater after stage 1 was subjected to stage 2 treatment with Fenton oxidation as shown in Figure 1. About 100 mL of the cutting emulsion was placed in a beaker under stirring. The pH of the solution was adjusted with H_2SO_4 0.5 M, then, adding iron (II) sulfate salt ($FeSO_4.7H_2O$) with content 14.04 (g/L) followed by hydroperoxide solution (H_2O_2, 30 wt.%). The reaction was allowed to proceed for 20 minutes. After completing the reaction, the pH of the solution was neutralized to 7 using NaOH 1 M (to meet the requirement before discharging into the environment) and stirred for 2 hours to remove the residual H_2O_2, letting it set down for another 3 hours before filtration. The clear solution after filter was subjected to COD measurement.

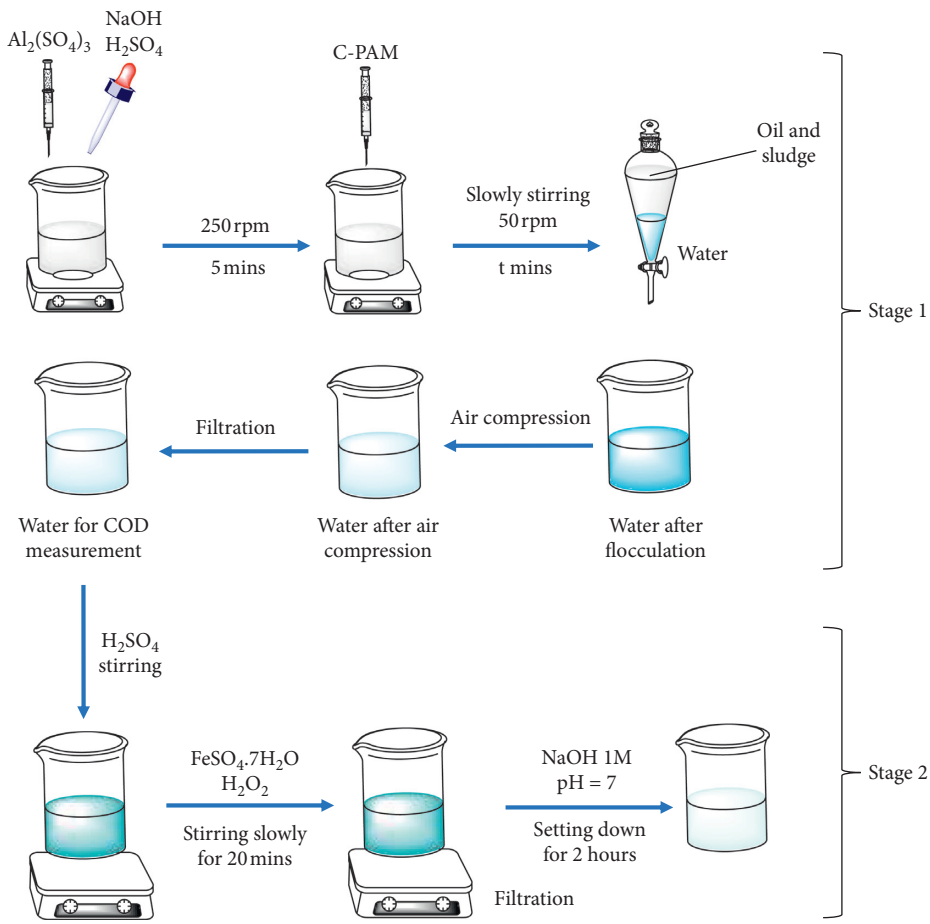

Figure 1: Treatment process with stage 1 (flocculation) and stage 2 (Fenton oxidation).

2.4. Determination of COD. The chemical oxygen demand (COD) is the quantity of oxygen required to oxidize the organic compounds in a wastewater sample. In this work, the organic compounds are oxidized by potassium dichromate in sulfuric acid solution 0.5 M at reflux temperature. Silver sulfate is used as a catalyst and mercuric sulfate is added to prevent the effect of chloride substance. The excess dichromate is titrated with standard ferric ammonium sulfate, using ferroin as an indicator. The COD of wastewater after treatment was determined as the following equation:

$$\mathrm{COD} = \frac{8000.C.(V_1 - V_2)}{V_0}\left(\frac{\mathrm{mg}}{\mathrm{L}}\right), \tag{8}$$

in which C is the concentration of ferric ammonium sulfate (mol/L), V_0 is the volume of wastewater sample before dilution (mL), V_1 is the volume of ferric ammonium sulfate to titrate the blank sample (mL), and V_2 is the volume of ferric ammonium sulfate to titrate the sample (mL).

2.5. Determination of BOD. Biochemical oxygen demand (BOD) is the amount of oxygen taken up by the microorganisms that decompose the organic compounds in wastewater. In this case, BOD represents the type of organic water pollution. BOD is calculated by keeping a sample of water containing a known amount of oxygen for five days at 20°C according to the method described in TCVN 7325 (ISSO 5814) and the formula is shown as follows:

$$\mathrm{BOD}_5 = \left[(p_1 - p_2) - \frac{V_t - V_s}{V_t}(p_3 - p_4)\right]\frac{V_t}{V_s}, \tag{9}$$

in which p_1 is the dissolved oxygen concentration of the solution at zero (mg/L), p_2 is the dissolved oxygen concentration of the sample solution after 5 days (mg/L), p_3 is the dissolved oxygen concentration of the blank solution at zero (mg/L), p_4 is the dissolved oxygen concentration of the blank solution after 5 days (mg/L), V_s is the volume of the original sample (mL), and V_t is the total volume of the sample (mL).

3. Results and Discussion

3.1. Characterization of Waste Cutting Emulsion. Characterization of the waste cutting emulsion was performed to determine its characteristic physiochemical parameters. Figure 2 shows the appearance of the emulsion, its size distribution, and zeta potential. Several parameters characteristics for the emulsion are shown in Table 1.

As can be seen, the emulsion has a milky white color with an oil concentration of 5.35%. The size distribution of the

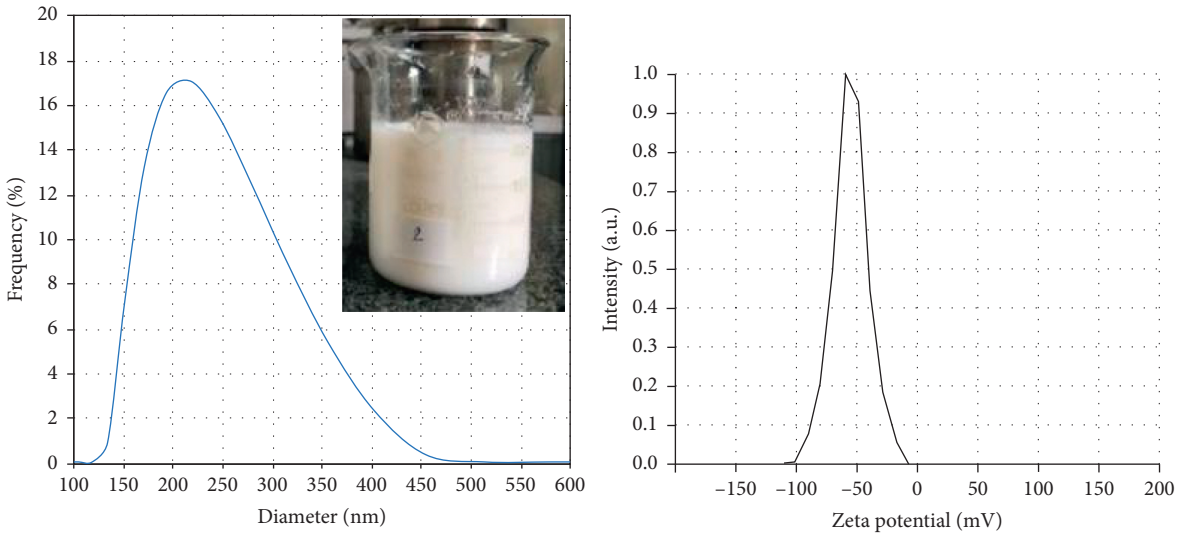

Figure 2: Size distribution and zeta potential of waste cutting emulsion.

Table 1: Characteristic parameters for waste cutting O/W emulsion.

Parameter	Value
Oil concentration, %	5.35 ± 0.22
pH	8.721 ± 0.005
COD, mg/L	147200 ± 100
Particle size (mean), nm	216.7 ± 3.4
Zeta potential, mV	−53.3 ± 1.4

emulsion was unimodal with an average size of oil drops of about 216.7 nm. It indicated that the oil droplets were very small and evenly distributed in the water phase. The stability of the emulsion was evaluated by zeta potential. The zeta potential of the O/W emulsion was −53.3 mV, suggesting that the oil droplet surface is a negative charge. The high negative zeta potential of the O/W emulsion subsequently enhanced the stability of the emulsion. In this case, if they were discharged into the environment, it would not be easy to treat them. In addition, due to the very high COD value, it is necessary to combine several methods for the treatment to obtain the maximum decrease in COD value before discharging into the environment.

3.2. Results from Stage 1: Flocculation Treatment. The flocculation treatment of the oil cutting emulsion was carried out using $Al_2(SO_4)_3$ and cationic polyacrylamide (C-PAM) as the flocculant and flocculant aid, respectively. Several factors will be investigated, including pH, the dosage of $Al_2(SO_4)_3$, and the dosage of C-PAM. The flotation will be used during the flocculation process to increase the efficiency of the oil-water separation.

3.2.1. Effect of pH. Effect of pH on the treatment of emulsions using $Al_2(SO_4)_3$ and C-PAM as a flocculant and flocculant aid was performed at the same dosages of $Al_2(SO_4)_3$ (3.5 g/L), C-PAM (10 mg/L), stirring speed (80 rpm), and stirring time (25 minutes). The pH was adjusted from 3 to 10. The efficiency of the treatment was evaluated through COD reduction.

Table 2 shows the COD of wastewater after treatments at various dosages and pH conditions. As can be seen, the treatment using the only $Al_2(SO_4)_3$ as a flocculant achieved the best efficiency at pH equal to 5. The COD value for treated water was 5024 mg/L, corresponding to the COD removal efficiency of 96.58%. Simultaneously, the flocculation treatment with $Al_2(SO_4)_3$ and C-PAM gets the best efficiency at a pH of 5. In this case, the COD value of water after the treatment was 4168 mg/L. This is the lowest COD value among all the treatment conditions. The highest COD removal efficiency of 97.17% was obtained.

The dependence of pH on the flocculation pretreatment is depicted in Figure 3. It illustrated that when increasing pH from 3 to 5, the treatment efficiency increased. The best pH for the flocculation pretreatment was around 5 to 6. At pH higher than 6, the efficiency of the treatment decreased.

The effect of pH on the flocculation treatment may probably be explained due to the formation of colloidal particles from $Al_2(SO_4)_3$ as flocculant. In the water medium, aluminum sulfate was dissociated into Al^{3+} cation. Then, ion Al^{3+} was hydrolyzed to produce several common colloidal particles, such as $Al(OH)^{2+}$, $Al(OH)_2{}^{+}$, and $Al(OH)_4{}^{-}$, or solid polymer colloidal particles, $Al_2(OH)_2{}^{4+}$, $Al_3(OH)_4{}^{5+}$, $Al_{13}O_4(OH)_{24}{}^{7+}$, and $Al(OH)_3$ [25], in which $Al_{13}O_4(OH)_{24}{}^{7+}$ is known as the best coagulant agent among all. However, the amount of the solid polymer colloidal particles (i.e., $Al_2(OH)_2{}^{4+}$, $Al_3(OH)_4{}^{5+}$, and $Al_{13}O_4(OH)_{24}{}^{7+}$) is less than the common colloidal particles.

On the other hand, the hydrolysis of Al^{3+} ion is suppressed in the acidic medium (pH from 3 to 4). Only a small amount of Al^{3+} ion was hydrolyzed to form colloidal flocculant agents. Thus, the COD removal efficiency obtained in this case was not so high. When the pH of the medium increased to 5 and 6, the hydrolysis of Al^{3+} increased favorably. Various colloidal particles, such as $Al(OH)^{2+}$ and

Table 2: COD values and COD removal efficiencies of wastewater after treatment at various dosages and pH (stirring speed 80 ppm, stirring time 25 minutes).

pH	$Al_2(SO_4)_3$ (g/L)	C-PAM (mg/L)	COD of treated water (mg/L)	COD removal efficiency (%)
3	3.5	0	7284	95.05
	3.5	10	5582	96.20
4	3.5	0	5704	96.12
	3.5	10	4878	96.68
5	3.5	0	5024	96.58
	3.5	10	4164	97.17
6	3.5	0	5092	96.54
	3.5	10	4298	97.08
7	3.5	0	5512	96.25
	3.5	10	4749	96.67
8	3.5	0	6022	95.91
	3.5	10	4934	96.64
9	3.5	0	9682	93.42
	3.5	10	7012	95.34
10	3.5	0	12268	91.66
	3.5	10	11842	91.95

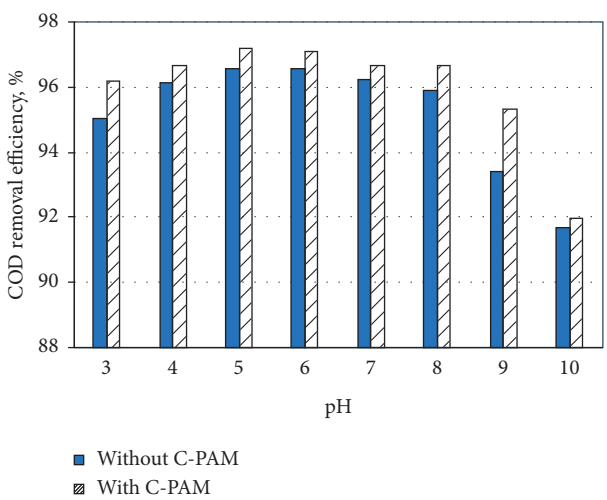

Figure 3: COD removal efficiency with and without C-PAM (10 mg/L) ($[Al_2(SO_4)_3] = 3.5$ g/L, stirring speed 80 rpm, stirring time 25 minutes).

$Al(OH)_2^+$, were formed. Besides, some polymer colloidal particles with high positive oxygen numbers, that is, $Al_2(OH)_2^{4+}$, $Al_3(OH)_4^{5+}$, and $Al_{13}O_4(OH)_{24}^{7+}$, could be formed via the condensation process. The formation of these polymer colloidal particles helps to neutralize suspended particles and oil particles in the emulsion more efficiently.

At a basic pH medium (pH from 7 to 10), the hydrolysis equilibrium moved to the right to form the positive charge particles. So far, the hydrolysis of Al^{3+} resulted in the formation of $Al(OH)_3$ precipitate. These precipitated $Al(OH)_3$ will absorb a small number of positive charge ions from the water medium, giving a small reduction in treatment efficiency. When pH is higher than 8, $Al(OH)_3$ interacted with OH^- to form AlO_2^- anion. It will further stabilize the O/W emulsion due to the same electrical charge with oil droplets. Consequently, the COD removal efficiency decreased at pH from 7 to 10.

From Figure 3, when $Al_2(SO_4)_3$ and C-PAM were used, COD treatment efficiency increases by about 20% compared to when using $Al_2(SO_4)_3$ alone. It was because C-PAM is a cationic polymer macromolecule. It will decrease the negative charge of oil droplets and increase the speed of the sedimentation process. Thus, the optimum condition for the pretreatment process was at pH 5, $Al_2(SO_4)_3$ dosage of 3.5 g/L, C-PAM dosage of 10 mg/L, stirring speed 80 rpm, and stirring time of 25 minutes. The best treatment efficiency was 97.17%, corresponding to the reduction in COD of wastewater from 147200 mg/L to 4164 mg/L.

3.2.2. Effect of $Al_2(SO_4)_3$. The effect of the dosage of $Al_2(SO_4)_3$ on the COD removal efficiency was investigated at the conditions as follows: pH 5, C-PAM of 10 ppm, stirring speed of 80 rpm, and stirring time of 25 minutes. The amount of $Al_2(SO_4)_3$ was adjusted from 0.5 to 5 g/L. Figure 4 shows the result obtained.

As we can see, the treatment efficiency reached the highest at the $Al_2(SO_4)_3$ concentration of 2 g/L. In particular, COD value reduced to 3527 mg/L, yield 97.6%. At the concentration of $Al_2(SO_4)_3$ higher than 2 g/L, the removal efficiency decreased. It may be because, at the concentration of 2 g/L, the cations generated from hydrolysis of Al^{3+} and C-PAM were enough to neutralize the oil droplets in the emulsion. At $Al_2(SO_4)_3$ concentration less than 2 g/L, the cation was not neutralized completely during the flocculation process. Therefore, the electrostatic interaction force between the oil droplets may still be large; thus, the emulsion is still stable, yielding the low treatment efficiency. Similarly, when the $Al_2(SO_4)_3$ concentration is higher than 2 g/L, the cation is hydrolyzed excessively, giving an excess of positive charge. At this time, the emulsion is reversely stabilized; thus, the treatment efficiency decreased.

3.2.3. Effect of C-PAM. The concentration of C-PAM used for the treatment was varied from $2 \div 20$ mg/L. Figure 5

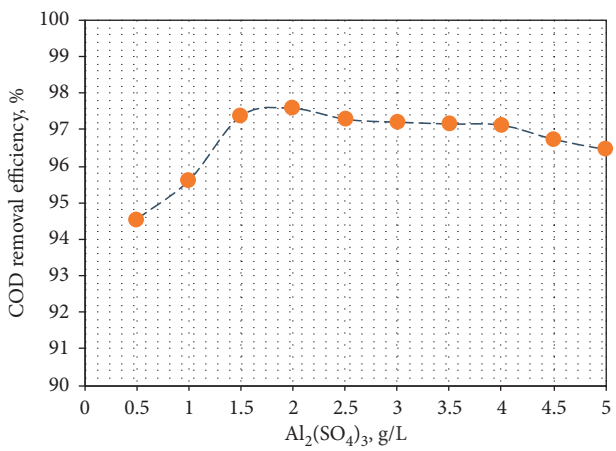

Figure 4: Effect of $Al_2(SO_4)_3$ dosages on COD removal efficiency (pH 5, C-PAM: 10 mg/L, stirring speed 80 rpm, and stirring time 25 minutes).

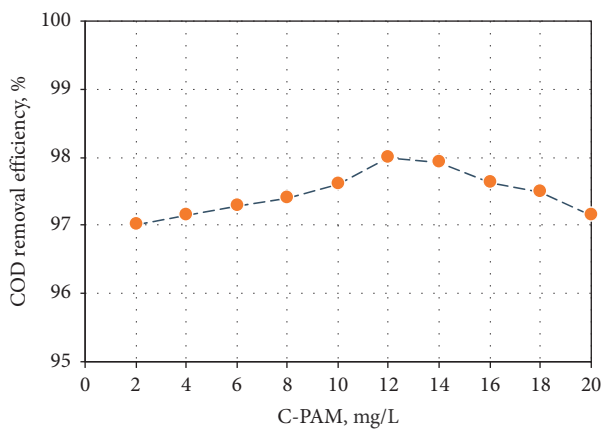

Figure 5: COD removal efficiencies at different C-PAM concentrations ($[Al_2(SO_4)_3] = 2$ g/L, stirring speed 80 rpm, stirring time 25 minutes).

shows the effect of C-PAM concentration on the COD removal at the conditions: pH = 5, $Al_2(SO_4)_3$ 2 g/L, stirring speed 80 rpm for 25 minutes. At the C-PAM concentration of 12 mg/L, COD reduced to the lowest value, that is, 3020 (mg/L), corresponding to the highest yield of 97.98%. It may be because that the C-PAM content of 12 mg/L is the optimum amount of the C-PAM needs to attach to the oil droplets. When the amount of C-PAM is less than 12 mg/L, the number of polymer molecules is not enough to cover the oil particles' surface. Therefore, there existed a vacant position that has not been neutralized. The repulsion force made the emulsion difficult to be coagulated. Hence, COD is still high. When the amount of C-PAM is higher than 12 mg/L, the particle surface is saturated with C-PAM molecules. And therefore, the surface of oil droplets again was stabilized.

3.2.4. Effect of Stirring Rate. During the flocculation process, the stirring rate is a very important factor that affects the COD removal. In this work, we investigate the stirring rate

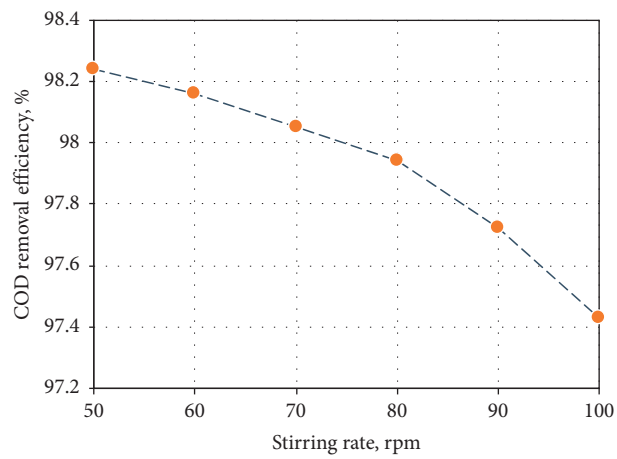

Figure 6: Effect of stirring rate on COD removal efficiency (C-PAM 12 mg/L, $[Al_2(SO_4)_3]$ 2 g/L, stirring time 25 minutes).

from 50 to 100 rpm for about 25 minutes. Figure 6 shows the results about the effect of stirring on the removal efficiency. As we can see, the highest COD removal efficiency was obtained at the speed of 50 rpm. The COD value decreased to 2568 mg/L with regard to the COD removal efficiency of 98.24%. At a higher stirring rate, the oil droplet was more separated due to the strong stirring force. The aggregation of the oil droplets decreased under a high stirring speed. The stirring rate of 50 rpm was enough for the attraction force to form large aggregates necessary for coagulation.

3.2.5. Effect of Stirring Time. The slow stirring step may affect the flocculation treatment. The time for stirring was altered from 5 to 55 minutes under the condition, that is, pH 5, $Al_2(SO_4)_3$ 2 g/L, C-PAM 12 mg/L, and stirring speed 50 rpm. The obtained results are given in Table 3.

From the results, when the stirring time is less than 15 minutes, the collision between the oil droplets was not enough to form larger oil droplets. However, if the stirring time is longer than 15 minutes, the large oil droplets may be broken into smaller ones. It may prevent the cumulation of oil from the wastewater. Therefore, the optimum stirring time is determined to be 15 minutes. At that condition, the COD of wastewater obtained was 2484 mg/L, equivalent to the COD removal efficiency of 98.31%.

Overall, after stage 1 treatment with flocculation, the COD of waste cutting emulsion decreased from 147200 mg/L to 2484 mg/L under the optimum condition: pH 5, $Al_2(SO_4)_3$ 2 g/L, C-PAM 12 mg/L, stirring speed 50 rpm, and stirring time 25 minutes. This treated wastewater will be used for further treatment (step 2) with Fenton oxidation.

3.2.6. Heat Value of Oil Recovered. The oil recovered after the flotation process was characterized by determining the heat value. The heat value of the oil recovered was 38095 ± 8 kJ/kg. This value is comparable to the heat value of biodiesel (~41000 kJ/kg) [26] and higher than that of brown coal (~19575 kJ/kg) [27]. It shows that the used oil could be recycled and used as fuel gas for heat generation. It will

Table 3: COD value and COD removal efficiency.

Stirring time (minutes)	COD (mg/L)	COD removal efficiency (%)
5	2938	98.00
15	2484	98.31
25	2586	98.24
35	2702	98.16
45	2768	98.12
55	2992	97.96

increase the cost-effectiveness for the treatment of cutting waste oil emulsion containing high oil concentration.

3.3. Result for Stage 2 Treatment by Fenton Process

3.3.1. Effect of $H_2O_2/FeSO_4$ Concentration Ratio. The concentration ratio $H_2O_2 : FeSO_4$ was varied from 3 : 1 to 15 : 1 at the same conditions: initial pH of 3 and $FeSO_4$ concentration of 11.23 (g/L). The results are shown in Figure 7.

Figure 7 shows that the concentration ratio of $H_2O_2 : FeSO_4$ increased from 3 : 1 to 10 : 1, and the COD removal increased. It is found that COD decreased when the concentration ratio increased to 12 : 1 and 15 : 1. Hence, the optimum concentration ratio of $H_2O_2 : FeSO_4$ was 10 : 1. The lowest COD value obtained was 172.2 (mg/L), with a COD removal efficiency of 93.06%. This observation may be explained as follows: at lower $H_2O_2 : FeSO_4$ concentration ratios, the H_2O_2 was not enough to oxidize the organic pollutants; therefore, the COD removal was low. However, when concentration ratios were too high, H_2O_2 may contribute to the COD and exhibit as hydroxyl radical scavenger [19, 28, 29] as shown by equation (3). The product, hydroperoxyl radical, is an oxidizing radical, but its oxidizing ability is lower than that of hydroxyl radical ($OH^{\bullet}$), leading to a decrease in treatment efficiency. Therefore, the suitable concentration ratio between H_2O_2 and $FeSO_4$ was applied for the next treatment step.

3.3.2. Effect of $FeSO_4$ Concentration. The concentration of $FeSO_4$ was varied from 8.42 to 19.66 g/L for the treatment of the emulsion and the result is shown in Figure 8.

The effect of $FeSO_4$ concentration on the treatment was performed at the conditions as follows: pH 3 and the ratio $H_2O_2 : FeSO_4$ of 10 : 1. The optimum $FeSO_4$ concentration was determined to be 14.04 g/L, with the lowest COD value of 84.1 mg/L, achieving 96.61% removal efficiency. At the concentration of $FeSO_4$ less than 14.04 g/L, it was not enough to catalyze the H_2O_2 degradation to form $OH^{\bullet}$ radical. However, with too much $FeSO_4$, more radicals were lost by the excess of ion Fe^{2+} due to the reaction (4). Therefore, a suitable amount of $FeSO_4$ was important to accelerate the Fenton reaction for the treatment.

3.3.3. Effect of pH. For the Fenton reaction, the pH is a critical factor, since it affects the generation of radical. In this work, the pH of the treatment was investigated ranging from 2 to 5. The result for the effect of pH is plotted in Figure 9.

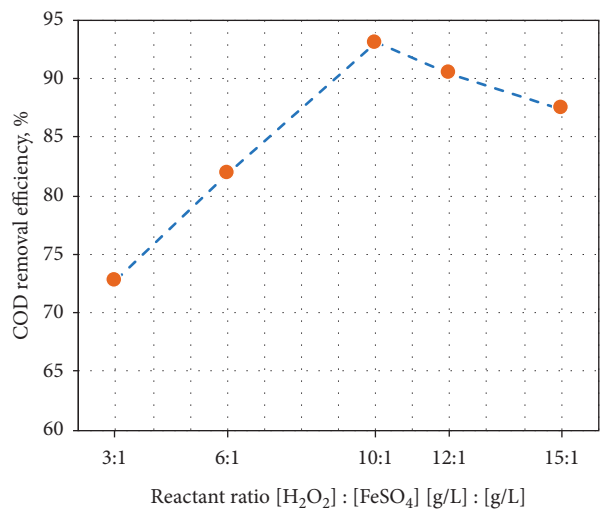

Figure 7: COD removal efficiency at different $H_2O_2 : FeSO_4$ concentration ratios.

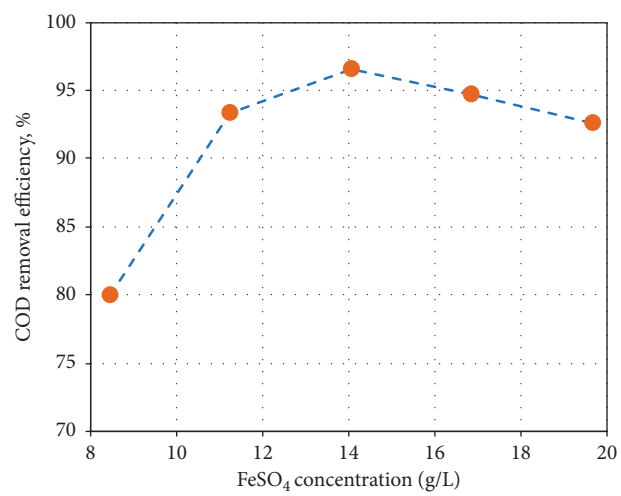

Figure 8: COD removal efficiency at different $FeSO_4$ concentrations (g/L).

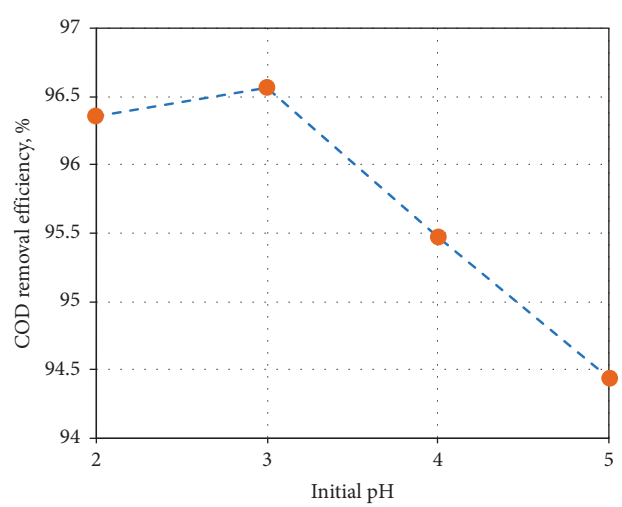

Figure 9: COD removal efficiency at different initial pHs.

Table 4: COD and BOD5 of the waste cutting oil after stage 1 and stage 2 treatment.

Parameter	Stage 1+ stage 2 treatment	Standard A	Standard B
COD (mg/L)	85.4	75	150
BOD_5 (mg/L)	30	30	50

As we can see, the low pH value gave higher COD removal efficiency than at the high pH. In particular, the best COD removal was obtained at a pH of 3, with the lowest COD value of 85.4 mg/L. The COD efficiency was 96.56%. It could be explained that when pH is higher than 3, ion Fe^{3+} may tend to dissociate with water to form $Fe(OH)_3$ (equations (10)–(12)) and, therefore, it produced less $OH^{\bullet}$ radical. At pH less than 3, the amount of $OH^{\bullet}$ radical was decreased due to hydrate ion formation, that is, $[Fe(H_2O)_6]^{2+}$, which reacts slowly with H_2O_2 [30]. Another possibility is that, at low pH, H^+ ion will act as a hydroxyl radical scavenger as shown by equation (13) [30]:

$$Fe^{3+} + H_2O \longrightarrow FeOH^{2+} + H^+ \quad (10)$$

$$FeOH^{2+} + H_2O \longrightarrow Fe(OH)^{1+} + H^+ \quad (11)$$

$$Fe(OH)^{1+} + H_2O \longrightarrow Fe(OH)_3 + H^+ \quad (12)$$

$$H^+ + OH^{\bullet} + 1e \longrightarrow H_2O \quad (13)$$

Thus, the best condition for treatment by the Fenton process was pH 3, concentration ratio $H_2O_2 : FeSO_4$ of 10 : 1, and $FeSO_4$ concentration of 14.04 g/L. At that condition, the COD of wastewater obtained was 85.4 mg/L.

Table 4 shows COD and BOD_5 of wastewater after the treatment compared to Vietnam standard A and standard B for wastewater. As can be seen, the COD of the wastewater from cutting emulsion meets standard B, and the BOD_5 value meets the requirement of standard A. It showed that the treatment utilized in the present work could treat efficiently the waste-cutting emulsion. Thus, the wastewater could be discharged into the environment without any concern.

4. Conclusions

The waste oil-in-water cutting fluids were effectively treated in this work by combining the flocculation and Fenton processes. Under the best condition, the COD value was reduced from 147200 mg/L to 2484 mg/L after stage 1, flocculation treatment, and to 85.4 mg/L after stage 2, Fenton process. The COD removal efficiency of the overall treatment process was up to 99.94%. The COD and BOD_5 values of the treated wastewater sample satisfied grade B and grade A level for industrial wastewater standards of Vietnam. Our result demonstrated that a combination of conventional flocculation and traditional homogenous Fenton process could be practically applied for the large-scale treatment of waste cutting emulsion. The cost may be minimized by using cheap chemical reagents and simple setting equipment. Moreover, with the support of the flotation technique, the oil was accumulated more effectively. It could be recovered and utilized as fuel gas for heat generation.

Data Availability

The data used to support the findings of this study are available from the corresponding author upon request.

Conflicts of Interest

The authors declare that there are no conflicts of interest regarding the publication of this paper.

Acknowledgments

This research was funded by the Hanoi University of Science and Technology (HUST) under project no. T2020-SAHEP-030.

References

[1] W. F. Sales, A. E. Diniz, and Á. R. Machado, "Application of cutting fluids in machining processes," *Journal of the Brazilian Society of Mechanical Sciences*, vol. 23, no. 2, 2001.

[2] E. Benedicto, D. Carou, and E. M. Rubio, "Technical, economic and environmental review of the lubrication/cooling systems used in machining processes," *Procedia Engineering*, vol. 184, pp. 99–116, 2017.

[3] Cutting fluids-monitoring and maintenance, Technical Information [online]. Available: https://www.fuchs.com/fileadmin/schmierstoffe/Prospekte/FTI/Cutting-Fluids-Monitoring-and-Maintenance.pdf.

[4] A. Bhattacharya and D. Senapati, "Biocides for metal working fluids: India outlook," Lube: The European Lubricants Industry Magazine, Minneapolis, MN, USA, 2017.

[5] W. Grzesik, "Cutting fluids, advanced machining processes of metallic materials," *Theory, Modelling, and Applications*pp. 183–195, Second edition, 2017.

[6] Safety & Health Assessment & Research for Prevention (SHARP), "Metalworking fluids: a resource for employers and health & safety personnel in Washington state," Technical Report Number 46-2-2007, SHARP, Washington, DC, USA, 1997.

[7] V. P. Astakhov, "Environmentally friendly near-dry machining of metals, metalworking fluids (mwfs) for cutting and grinding," in *Woodhead Publishing Series in Metals and Surface Engineering, Metalworking Fluids (MWFs) for Cutting and Grinding*, V. P. Astakhov and S. Joksch, Eds., Woodhead Publishing, Cambridge, UK, pp. 135–200, 2012.

[8] S. Feng and M. Hattori, "Cost and process information modeling for dry machining," in *Proceedings of the International Workshop on Environment and Manufacturing*, Novi Sad, Serbia, July 2000.

[9] W. Grzesik, "Cutting fluids," in *Advanced Machining Processes of Metallic Materials*, W. Grzesik, Ed., pp. 141–148, Elsevier, Amsterdam, Netherlands, 1st edition, 2008.

[10] K. Bensadok, M. Belkacem, and G. Nezzal, "Treatment of cutting oil/water emulsion by coupling coagulation and dissolved air flotation," *Desalination*, vol. 206, no. 1–3, pp. 440–448, 2007.

[11] "Demulsification of cutting oil emulsion by electro-oxidation process: batch and continuous mode," *Journal of The Electrochemical Society*, vol. 164, no. 13, pp. 496–504, 2017.

[12] A. Dermouchi, T. Lendormi, A. Sihem, J. L. Lanoiselle, and B. L. Mossaab, "Cutting oil emulsion anaerobic biodegradation: electrocoagulation pretreatment effect," *Chemical Engineering Transactions*, vol. 64, pp. 565–570, 2018.

[13] A. Muszyński and M. Łebkowska, "Biodegradation of used metalworking fluids in wastewater treatment," *Polis Journal of Environmental Studies*, vol. 14, no. 1, pp. 73–79, 2005.

[14] Y. Mokhbi, K. Korichi, and Z. Akchiche, "Combined photocatalytic and Fenton oxidation for oily wastewater treatment," *Applied Water Science*, vol. 9, no. 2, p. 35, 2019.

[15] Y. A. Mustafa, A. I. Alswared, and M. Ebrahim, "Removal of oil from wastewater by advanced oxidation process/homogeneous process," *Journal of Engineering*, vol. 19, no. 6, pp. 686–694, 2013.

[16] M. M. Amin, M. M. G. Mofrad, H. Pourzamani, S. M. Sebaradar, and K. Ebrahim, "Treatment of industrial wastewater contaminated with recalcitrant metal working fluids by the photo-Fenton process as post-treatment for DAF," *Journal of Industrial and Engineering Chemistry*, vol. 45, pp. 412–420, 2016.

[17] C. Feng, H. Sun, M. K. Camarillo, and W. Stringfellow, "Treatment of oil–water emulsion from the machinery industry by Fenton's reagent," *Water Science and Technology*, vol. 71, no. 12, pp. 1884–1892, 2015.

[18] A. G. Gutierrerz-Mata, S. Velazquez-Martinez, A. Alvarez-Gallegos et al., "Recent overview of solar photocatalysis and solar photo-Fenton processes for wastewater treatment," *International Journal of Photoenergy*, vol. 201727 pages, Article ID 8528063, 2017.

[19] A. Babuponnusami and K. Muthukumar, "A review on Fenton and improvements to the Fenton process for wastewater treatment," *Journal of Environment Chemical Engineering*, vol. 2, no. 1, pp. 557–572, 2013.

[20] P. Chen, D. Yin, P. Song et al., "Demulsification and oil recovery from oil-in-water cutting fluid wastewater using electrochemical micromembrane technology," *Journal of Cleaner Production*, vol. 244, 2020.

[21] M. Kobya, P. I. Omwene, and Z. Ukundimana, "Treatment and operating cost analysis of metalworking wastewaters by a continuous electrocoagulation reactor," *Journal of Environmental Chemical Engineering*, vol. 8, 2020.

[22] S. Kaur and A. K. Sodhi, "A study on removal of cutting oil from wastewater by using agricultural wastes," *Materials Today: Proceedings*, vol. 32, no. 4, pp. 719–727, 2020.

[23] C. Su, G. Cao, S. Lou et al., "Treatment of cutting fluid waste using activated carbon fiber supported nanometer iron as a heterogeneous fenton catalyst," *Scientific Reports*, vol. 8, p. 10650, 2018.

[24] S. Khan, M. Sayed, M. Sohail, L. A. Shah, and M. A. Raja, "Advanced oxidation and reduction processes," in *Advances in Water Purification Techniques*, S. Ahuja, Ed., Elservier, Amsterdam, Netherlands, pp. 135–164, 2019.

[25] O. P. Sahu and P. K. Chaudhari, "Review on chemical treatment of industrial waste water," *Journal of Applied Science and Environment Management*, vol. 17, no. 2, pp. 241–257, 2013.

[26] R. Karmakar, A. Rajor, K. Kundu, and N. Kumar, "A comparative study of the fuel characteristics between algal biodiesel and petro-diesel," *Bioresource Utilization and Bioprocess*, pp. 49–55, 2020.

[27] E. S. Hasan, M. Jahiding, M. Mashuni, W. Ilmawati, W. Wati, and I. N. Sudiana, "Proximate and the calorific value analysis of brown coal for high-calorie hydrid briquette application," *Journal of Physics Conference Series*, vol. 846, no. 1, p. 012022, 2017.

[28] A. Eslami, F. Mehdipour, K.-Y. A. Lin, H. Sharifi Maleksari, F. Mirzaei, and F. Ghanbari, "Sono-photo activation of percarbonate for the degradation of organic dye: the effect of water matrix and identification of by-products," *Journal of Water Process Engineering*, vol. 33, Article ID 100998, 2020.

[29] F. Ghanbari, A. Hassani, S. Wacławek et al., "Insights into paracetamol degradation in aqueous solutions by ultrasound-assisted heterogeneous electro-Fenton process: key operating parameters, mineralization and toxicity assessment," *Separation and Purification Technology*, vol. 266, no. 1, Article ID 118533, 2021.

[30] S. Giannakis, K.-Y. A. Lin, and F. Ghanbari, "A review of the recent advances on the treatment of industrial wastewaters by sulfate radical-based Advanced Oxidation Processes (SR-AOPs)," *Chemical Engineering Journal*, vol. 406, no. 15, Article ID 127083, 2021.

Hindawi
Journal of Chemistry
Volume 2021, Article ID 9981738, 13 pages
https://doi.org/10.1155/2021/9981738

Research Article

Removal of Antibiotics from Real Hospital Wastewater by Cold Plasma Technique

Phuong Thi Thanh Nguyen,[1,2] **Hieu Trung Nguyen**,[3] **Uyen Nhat Phuoc Tran**,[2] **and Ha Manh Bui**[4]

[1]*Institute for Environment and Resources, Vietnam National University, Ho Chi Minh 700000, Vietnam*
[2]*Institute of Biotechnology, Vanhien University, Ho Chi Minh 700000, Vietnam*
[3]*Institute of Applied Technology, Thu Dau Mot University, Thu Dau Mot 750000, Binh Duong, Vietnam*
[4]*Institute of Environmental Sciences, Nguyen Tat Thanh University, Ho Chi Minh 700000, Vietnam*

Correspondence should be addressed to Ha Manh Bui; manhhakg@yahoo.com.vn

Received 18 March 2021; Accepted 3 May 2021; Published 20 May 2021

Academic Editor: Abdullah Aldawsari

Hospital wastewater contains a complex mixture of bioactive substances and microorganisms that are deleterious to humans and aquatic animals. In this study, four antibiotics, namely, ofloxacin, ciprofloxacin, cefuroxime, and amoxicillin, respectively, from the wastewater of seven hospitals in Ho Chi Minh City, Vietnam, were monitored. The results revealed that the wastewater from these hospitals is contaminated with at least one of the antibiotics. In addition, the degradation capacity of the antibiotics by the wastewater treatment plant at one of the hospitals by the cold plasma technique was investigated. Furthermore, effects of the variation in pH, interelectrode distance, applied voltage, and reaction time on the removal efficiency were investigated in terms of the reduction in antibiotics concentration, COD, and ammonia. Ciprofloxacin, cefuroxime, COD, and ammonia were almost eliminated, while ofloxacin and amoxicillin were reduced by more than 72% under optimum conditions (initial pH of 10, reaction time of 15 min, applied voltage of 30 kV, and interelectrode distance of 10 mm). All of these factors affected the removal efficiency. The removal efficiency was most robust in the first 5 min, and it increased with the increase in the reaction time. However, the removal efficiency tended to saturate over time, while it decreased with the increase in the reaction time. With an applied voltage of 30 kV onwards, the removal efficiency was not significantly different. Most of the pollutants were predominately eliminated under slightly alkaline conditions (pH of ~10). In addition, primary oxidants in the aqueous phase, such as O_3, H_2O_2, and ·OH, were generated. Besides, the obtained results also revealed that the decomposition of ciprofloxacin and cefuroxime follows the first-order reaction kinetics; meanwhile, the third-order reaction kinetics was most likely for the decomposition of ofloxacin and amoxicillin.

1. Introduction

As one of the sources of waste, hospital wastewater (HWW), which contains a high concentration of detergents, disinfectants, hormones, and even antibiotic compounds, causes severe environmental pollution. The presence of these compounds in HWW poses an adverse threat to living organisms. Several studies have reported that these antibiotics and their residues pose a substantial toxic risk to aquatic organisms [1]. Moreover, antibiotic residues can accelerate the production of antibiotic-resistant bacteria and antibiotic-resistant genes even at low concentrations, which could be a major threat to public health globally [2, 3]. Extensive studies have reported that antibiotic compounds originating from HWW can be transported to ponds, rivers, and wastewater treatment plants [4]. Therefore, these compounds must be eliminated before their discharge into sewage systems. Several methods have been developed to eliminate these compounds in HWW. Conventional processes such as coagulation, aerotank, and adsorption have been applied for the treatment of real HWW; however, these methods are not adequate to remove contaminants [5–7].

Some advanced oxidation processes (AOPs), including photocatalysis [8, 9], ozone treatment [10], activated persulfate [11, 12], electro-Fenton process [13], and an electron-beam process [14–16], have successfully mitigated the pollutants present in synthetic HWW; however, these AOPs exhibit practical limitations when used on an industrial scale.

Recently, the application of cold plasma—one of the AOPs—has attracted considerable attention for wastewater treatment due to its efficiency, less chemical requirements, and low sludge production [17]. Cold plasma has been employed for the degradation of recalcitrant pollutants in the wastewater generated from pesticide production [18], a slaughterhouse [19], textiles [20], and pharmaceuticals [21–24].

Under aqueous conditions, cold plasma typically generates strongly reactive free radicals or molecules *in situ*, such as hydroxyl radicals (·OH), hydrogen radicals (·H), hydrated electrons (e^-), hydrogen peroxide (H_2O_2), ozone (O_3), and even UV light [18] by the following process [25].

$$H_2O \longrightarrow^{\text{Cold plasma}} \cdot OH + e^- + H\cdot + H_2O_2 + H_3O^+ + O_3 + UV \quad (1)$$

The as-formed powerful oxidants can decompose and mineralize organic pollutants into carbon dioxide and water. Some studies have reported that cold plasma is an efficient technology for the removal of antibiotics. Lou et al. [26] have reported that the use of only dielectric barrier discharge (DBD), a type of cold plasma, can degrade >80% chloramphenicol in contaminated soil. Kim et al. [27] have employed a DBD system and reported the removal of 9 antibiotic compounds, namely, lincomycin, ciprofloxacin, enrofloxacin, chlortetracycline, oxytetracycline, sulfathiazole, sulfamethoxazole, sulfamethazine, and trimethoprim, respectively, from a synthesis solution, with removal efficiencies varying from 60% to 90%. In addition, Sarangapani et al. have employed cold plasma for the high-efficiency mitigation of two widely used antibiotics (i. e., ofloxacin and ciprofloxacin, respectively) from water and meat effluents [21]. The results revealed that cold plasma successfully degrades the examined antibiotics and that plasma treatment considerably reduces the activity of both antibiotics. The authors indicated that the advantages of cold plasma treatment include the oxidation or reduction of pollutants into biodegradable compounds without environmental risks, and the method can be an effective, ecofriendly, and economically promising technology for the treatment of wastewater in practical applications. Although these techniques can reduce the organic compounds in aqueous solutions, studies on removing these contaminants from real HWW are not available.

In this study, contamination by four widely used antibiotics (such as ofloxacin, ciprofloxacin, cefuroxime, and amoxicillin, respectively) from the wastewater of seven hospital treatment plants in Vietnam was investigated. Next, the application of cold plasma to eliminate these pollutants from the wastewater of one representative hospital was investigated. Furthermore, the effects of four factors, i. e., pH, interelectrode distance, voltage, and reaction time, respectively, were examined by reducing the antibiotic concentration, COD, and ammonia. To the best of our knowledge, this is the first study to discuss the application of cold plasma for the treatment of hospital wastewater in Vietnam.

2. Methodology

2.1. Wastewater and Chemicals. Wastewater was obtained from equalization tanks at seven hospital wastewater treatment plants (i. e., National Hospital of Odonto-Stomatology, Oncology Hospital, Thong Nhat Hospital, Hung Vuong Hospital, General Saigon Hospital, Binh Dan Hospital, and Gia Dinh Hospital, respectively) in Ho Chi Minh City, Vietnam (Figure S1). The wastewater was collected in glass containers and preserved at 4°C for treatment by cold plasma.

Analytical-grade standards of ofloxacin, ciprofloxacin, cefuroxime, and amoxicillin (>98% purity) were used. In addition, HPLC solvents, such as methanol, acetonitrile, ethyl acetate, ammonium hydroxide solution (NH_4OH), acetic acid (AcOH), formic acid (HCOOH), and other chemicals were of analytical grade. The chemicals and solutions were kept in the dark and stored at 4°C.

2.2. The Cold Plasma Reactor Model. Figure 1 shows the schematic of a plasma reactor model, including plumbing, a reaction chamber, sewage tanks, water pumps, gas pumps, flowmeters, pump control valves, and switches. A gas mass flow meter and controllers were used to introduce air into the reactor chamber. The height and volume of the reaction chamber were 30 cm and 1500 mL, respectively, which was designed with one inlet and one outlet. The water inlet was placed 12 cm from the bottom, and water was allowed to flow from the bottom up—the volume of the reaction zone was 600 mL. The experiment was designed with plasma electrodes, including two SUS304 stainless-steel electrodes and a pointed tip anode electrode submerged in water. A rectangular design (30 × 25 × 3 mm) on a perforated electrode plate with a diameter of 4 mm served as the negative electrode. The top of the reaction chamber was a threaded lock cap comprising an insulating plastic, which fixed two electrodes of the model. A rectangular box composed of acrylic plastic with a volume of 2000 mL served as the reservoir for the output effluent.

2.3. Experimental Design and Procedure. Plasma treatment experiments were conducted on the basis of the single-factor design, i. e., in every series of experiments; only one independent factor was varied, whereas all other factors were maintained constant. Table S1 shows the parameters and their value ranges with the following initial conditions: initial pH of 6.7, the reaction time of 15 min, the distance between two electrodes of 20 mm, and applied voltage in the range of 15–35 kV at constant antibiotic concentrations for the examination of the wastewater from the General Saigon hospital. A total of four series were conducted to evaluate all

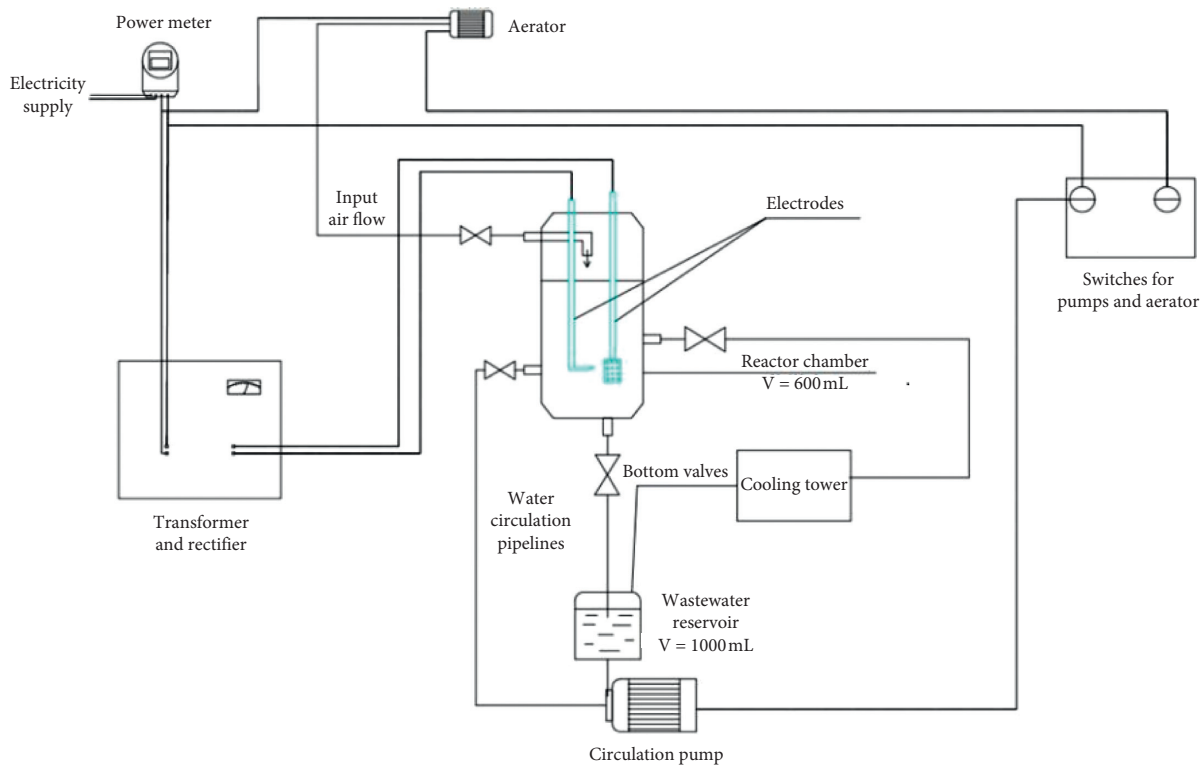

Figure 1: The cold plasma reactor chamber.

factors. Moreover, the formation of O_3, H_2O_2, and ·OH were investigated by the variation in the pH and reaction time under optimum conditions (the distance between the two electrodes was 10 mm, and the applied voltage was 30 kV).

In each run, 600 mL of the wastewater from General Saigon hospital (which was adjusted to the desired pH) was added to the reaction chamber at the established gap between two electrodes, followed by locking the two valves at the bottom and the cooling tower. Then, the air was fed into the chamber at a constant flow rate of 4 L/min, the power supply was switched on, and the applied voltage was adjusted to the required values. After the desired reaction time, aliquots of the treated wastewater were sampled through the bottom discharge and analyzed.

2.4. Analysis Method. A Shimadzu HPLC system (Model 20AT) equipped with a UV detector was utilized to monitor the antibiotics extracted from the wastewater using solid-phase microextraction method as follows. About 5 μL of the analyte solution was injected into the HPLC valve using a 25 mm Puradisc syringe (sterile and free of endotoxins, 0.2 μm PES Filter Media) and a Terumo syringe (5 mL) at room temperature ($25 \pm 2^{\circ}$C). The target analyzed compounds were separated on a Phenomenex Luna reverse phase (RP-18) column (250 mm × 4.6 mm) packed with a C18 stationary phase having a particle size of 5 μm.

The pollution and pathogenic microorganism parameters in HWW before and after treatment, such as pH, COD, TSS, sulfide, ammonium, nitrate, phosphate, plant and animal fats and oils, coliforms, *Salmonella*, *Shigella*, and *Vibrio* cholera, were analyzed according to the American Public Health Association [28]. Meanwhile, O_3, H_2O_2, and ·OH generated in wastewater also were determined by standard methods [28–30]. Results were expressed as the mean of triplicate measurements, and statistical analyses were performed using Microsoft Excel software release 2010 (Microsoft Corp., USA).

3. Results and Discussion

3.1. Characteristics of Hospital Wastewater. All of the HWW samples were contaminated with COD in the range from 191 to 539 mg/L, while coliforms ranged from 1.5×10^5 to 1.4×10^7 CFU/100 mL, and the other parameters were above the stipulated standards in some hospitals. Some antibiotics were detected in the wastewater; in particular, all four parameters were detected in the wastewater of the General Saigon hospital. These results revealed that contaminants are detected in most surveyed hospitals and are deleterious to residents (Table S2). Owing to the presence of all four contaminant antibiotics, the wastewater from the General Saigon hospital was selected for the plasma treatment experiment. The degradation efficiencies of the antibiotics from the hospital's wastewater treatment plant by the cold plasma technique were evaluated via the investigation of the effects of applied voltage, reaction time, pH, and the interelectrode distance of the plasma reactor on the concentration of the four antibiotics in the effluents. In addition, the formation of oxidizing species, such as O_3, H_2O_2, and·OH, was investigated to clarify the degradation mechanism of cold plasma.

3.2. Plasma Treatment

3.2.1. Effect of Applied Voltage. The effect of the applied voltage on the degradation of the antibiotics was investigated by conducting experiments at applied voltages of 15, 20, 25, 30, and 35 kV by maintaining the distance between two electrodes at 20 mm and the initial pH value at ~6.7 (background value of the General Saigon hospital wastewater) for a reaction time of 15 min. With the increase in the applied voltage, the removal efficiency of antibiotics, COD, and ammonia by cold plasma treatment increased (Figure 2); however, the efficiencies were different for each antibiotic. Ciprofloxacin, cefuroxime, COD, and ammonia were mostly eliminated at an applied voltage of ≥25 kV, while no clear difference in the removal efficiency was observed with the further increase in the applied voltage to 35 kV (Figures 2(b)–2(f)). The finding might be related to the low concentration of ciprofloxacin (1.052 mg/L) and cefuroxime (0.273 mg/L) and the facile oxidizing substances that contribute to the COD in the HWW sample. That is, an applied voltage of 25 kV is adequate to release sufficient oxidants (·OH, O_3, and H_2O_2) for eliminating ciprofloxacin, cefuroxime, COD, and ammonia during the plasma process [31]. On the contrary, at an applied voltage of 35 kV, the highest removal efficiencies of 50.22% and 35.40% were observed for ofloxacin and amoxicillin, respectively (Figures 2(a) and 2(d)). The highest applied voltage can be attributed to the generation of an increased number of reactive species at a higher applied voltage. However, the low removal efficiencies mentioned above may be explained by inadequate oxidant products for removing high concentrations of ofloxacin (41.23 mg/L) and amoxicillin (23.58 mg/L). The increase in the removal efficiency with an adequate increase in the applied voltage is consistent with the results reported by Sarangapani et al. [21]; in their study, the authors have reported that with the rise in the voltage from 70 to 80 kV, the plasma degradation efficiency increased from 75% to 89% for ciprofloxacin and from 88% to 92% for ofloxacin. Even at an applied voltage of 35 kV, the highest removal efficiency was observed for ofloxacin and amoxicillin; however, the difference in removal efficiencies was not significant between the applied voltages of 30 kV and 35 kV. Moreover, to optimize the experimental conditions and reduce energy for plasma treatment (saving time and safety), an applied voltage of 30 kV was selected for subsequent experiments.

3.2.2. Effect of Reaction Time. Experiments were conducted at reaction times of 5, 10, 15, 20, and 25 min with a distance between two electrodes of 20 mm, an applied voltage of 30 kV, and a natural pH value (6.6). With the increase in the reaction time, the degradation efficiency increased (Figure 3); however, similar to the effect of the applied voltage, the results revealed that ciprofloxacin and cefuroxime are rapidly degraded in the first 10 min (>90%) and reach a plateau until the reaction is completed (Figures 3(b) and 3(c)); this trend also was observed in the case of COD and ammonia at a reaction time of 15 min (Figures 3(e) and 3(f)). This result is consistent with the following theory: the reaction time exhibited a positive effect on the degradation of organic compounds in the plasma process. With the increase in the reaction time, the disturbing process is strong, the reaction occurs rapidly, and organic substances are exposed to strong oxidizing substances [32]. However, with the increase in the reaction time to greater than 15 min, the degradation efficiency remained stable. It is hypothesized that with the further increase in the reaction time, the number of intermediate products (between the formed oxidants and antibiotics) increases, which are competing with antibiotics; hence, the degradation efficiency decreases. Meanwhile, a different trend in degradation efficiencies was observed in the case of ofloxacin and amoxicillin (Figures 3(a) and 3(d)), where their efficiencies reached peak values at a reaction time of 30 min. This might result in the presence of inadequate concentrations of oxidants (such as ·OH, O_3, and H_2O_2) to remove high concentrations of ofloxacin and amoxicillin from wastewater. This pattern of results is consistent with the previous study of Kim et al. [27], where plasma was used to degrade enrofloxacin in an aqueous solution. The author revealed that the decomposition of 1 mg/L of enrofloxacin could be completed only within 20 min, while around 30 min is required to reduce the concentration of the same compound from 5 mg/L to 1 mg/L. In terms of removal efficiency, a reaction time of 30 min was optimum for subsequent experiments. However, excluding ofloxacin and amoxicillin, all of the six parameters and *coliforms* (data not shown) were entirely eliminated during 15 min. Furthermore, the shortened reaction time ensures savings in operational costs. Hence, a reaction time of 15 min reaction is selected for subsequent experiments.

3.2.3. Effect of the Initial pH. Effects of the initial pH on the removal of antibiotics by cold plasma were investigated in the range from 7 to 10. The distance between the two electrodes and applied voltage was maintained constant at 20 mm and 30 kV, respectively, during a reaction time of 15 min for all experiments. With the increase in the initial pH from 7 to 10, the overall removal efficiencies increased for all pollutants by cold plasma treatment (Figure 4). These results are in agreement with those reported in recent studies where an increase in the pH accelerates the formation of ·OH due to the decrease in the ·OH redox potential according to the Nernst equation [33, 34]:

$$\mathbf{E}^0 = E^0_{\mathbf{HO^{\bullet}/H_2O_2}} - 0.059\,\mathbf{pH}. \quad (2)$$

In other words, the redox potential of ·OH might slightly decrease from 2.39 to 2.21 with the increase in the pH from 7 to 10 [33]. At a constant applied voltage, the decrease in the redox potential can enhance ·OH production; hence, the oxidant can react with an increased amount of pollutants in wastewater, leading to increased removal efficiencies. Panorel et al. [24] have reported that the oxidation efficiency of paracetamol under alkaline conditions (52 g/kW·h) is substantially greater than that under acidic conditions (28 g/kW·h). With the increase in the initial pH, even the overall removal efficiencies of

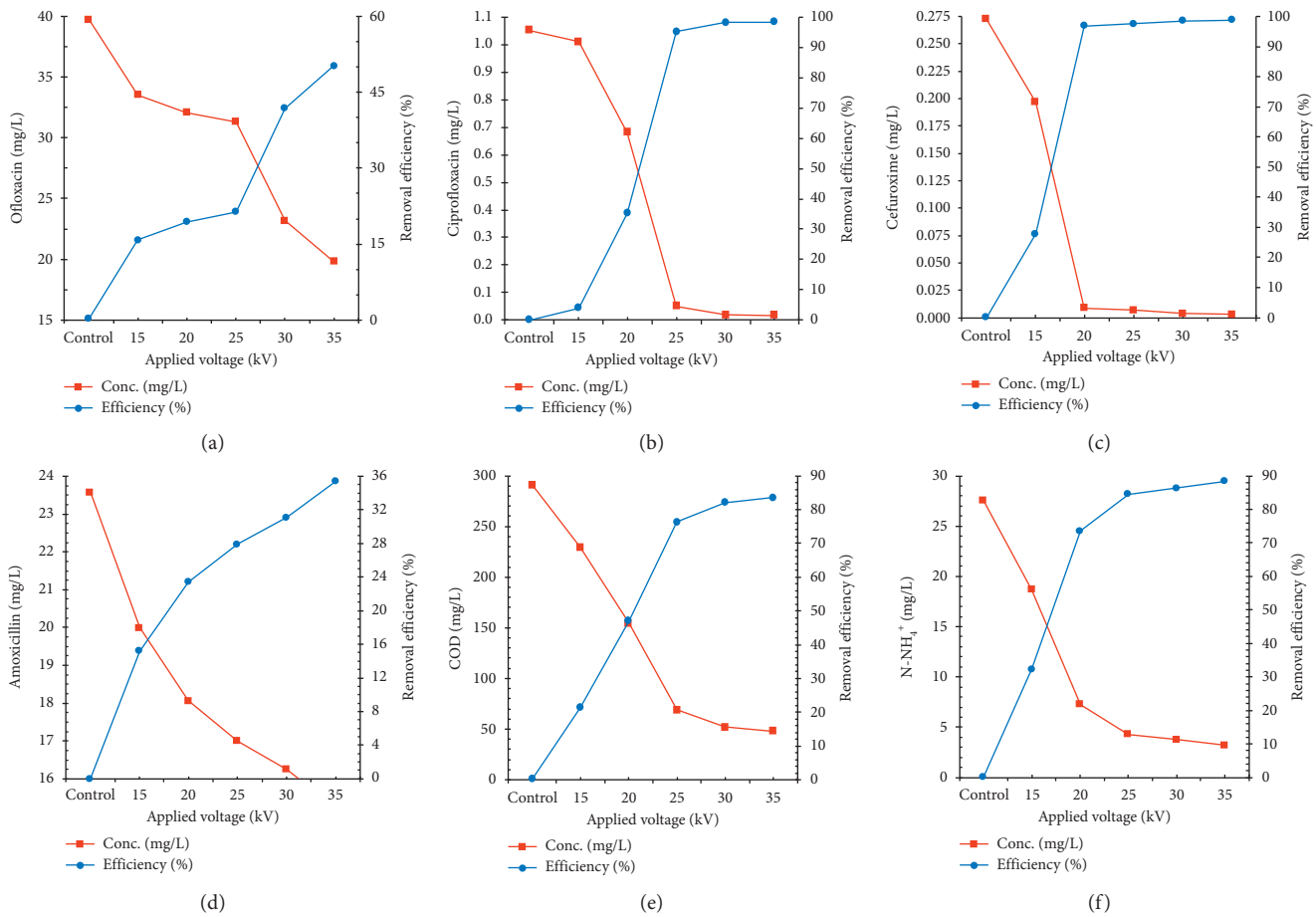

Figure 2: Effect of the applied voltage on the degradation efficiency of the four antibiotics, i.e., (a) ofloxacin, (b) ciprofloxacin, (c) cefuroxime, and (d) amoxicillin, respectively, as well as (e) COD and (f) ammonia removal.

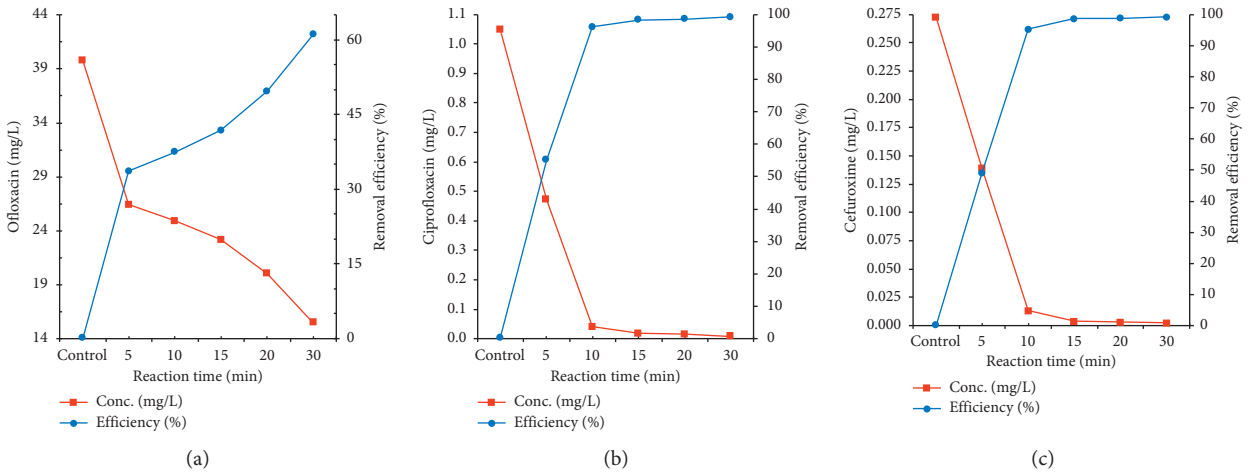

Figure 3: Continued.

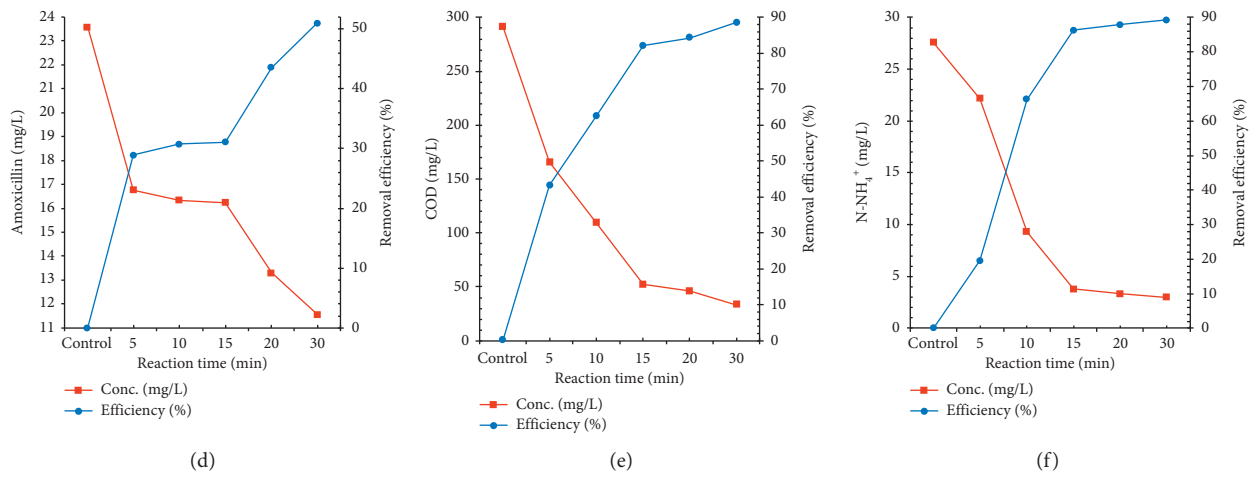

Figure 3: Effect of the reaction time on the degradation efficiency of four antibiotics, namely, (a) ofloxacin, (b) ciprofloxacin, (c) cefuroxime, and (d) amoxicillin, respectively, as well as (e) COD and (f) ammonia removal.

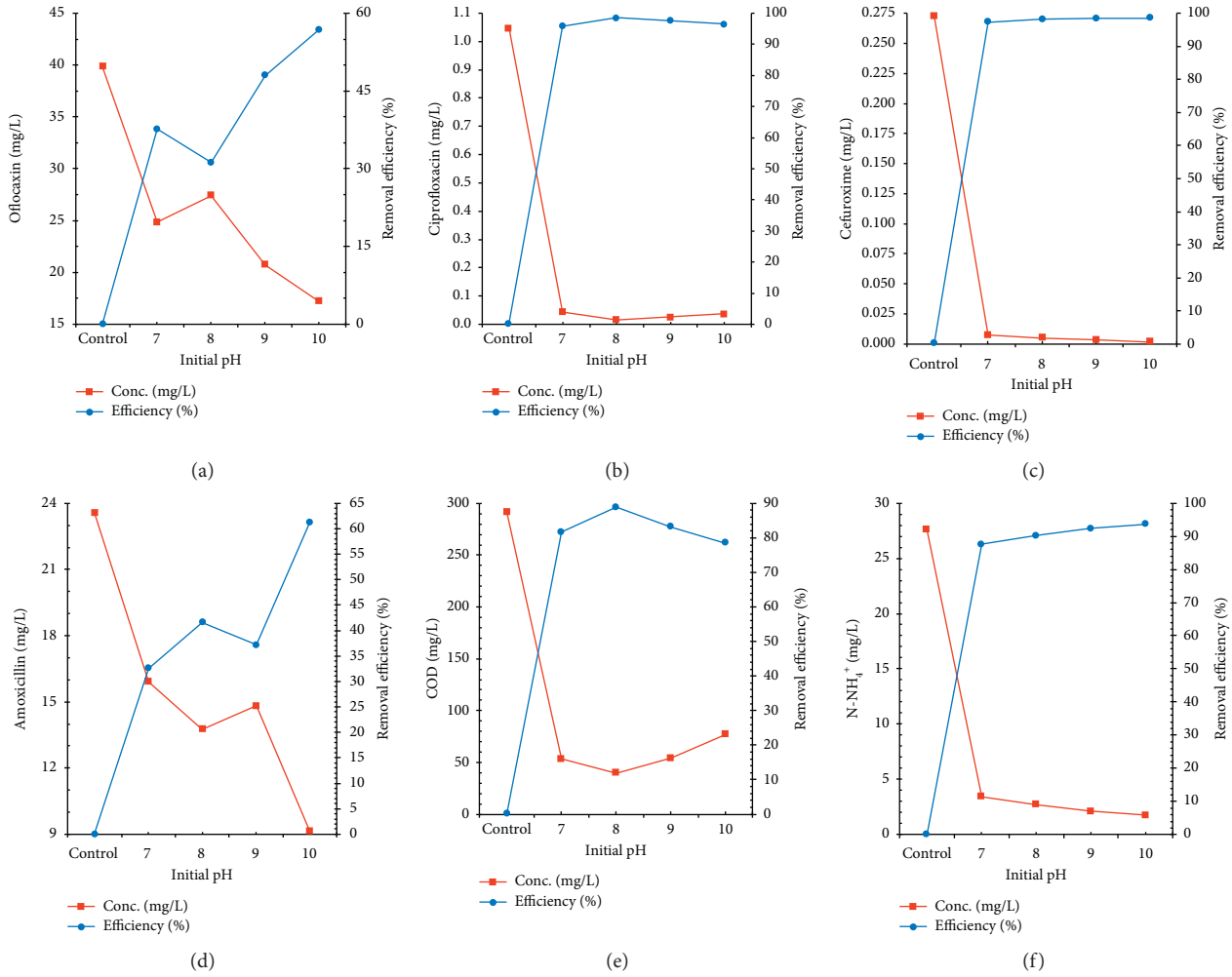

Figure 4: Effect of the pH on the degradation efficiency of four antibiotics, namely, (a) ofloxacin, (b) ciprofloxacin, (c) cefuroxime, and (d) amoxicillin, respectively, as well as (e) COD and (f) ammonia removal. Effect of the interelectrode distance of the plasma reactor.

these antibiotics, COD, and ammonia increased. Three trends were observed during this treatment. In the case of ofloxacin and amoxicillin (Figures 4(a) and 4(d)), the variation in the removal efficiencies or breakpoint at pH 8 (ofloxacin 31.18%) and 9 (amoxicillin 41.63%) was possibly related to the existing forms of the two antibiotics [35]. Notably, at pH values of 8 and 9, the two antibiotics were dominated by negatively charged forms due to their higher pH values than the pKa values of the compounds. These forms could ineffectively react with ·OH; hence, removal efficiencies decrease [35, 36]. All of the ciprofloxacin, cefuroxime, and COD (Figures 4(b)–4(e)) were completely degraded (~90%) at pH 8; the further increase in the pH led to the slight reduction in the removal efficiency because, at a higher pH of 8, the two antibiotics could be negatively charged forms, leading to decrease in the removal efficiency [37]. With the increase in the pH, ammonia in the wastewater was eliminated extremely rapidly (>90%) (Figure 4(f)). Two mechanisms were involved; first, the extent of oxidation of ammonia to nitrite or nitrate is increased by the produced oxidants under alkaline conditions as mentioned above; second, N-NH_4^+can be transformed easily to NH_3, which can evaporate under alkaline conditions during cold plasma treatment. These complex trends with the variation in pH during cold plasma treatment were in good agreement with those reported in previous studies [18, 27, 32]. A pH of 10 satisfied all parameters to attain the highest removal efficiency; therefore, this pH is selected for subsequent experiments.

A previous study has reported that the interelectrode distance in the plasma reactor can determine the amount of the formed ·OH [38], thereby affecting the degradation efficiency. The experiment was conducted by utilizing various electrode distances of 10–30 mm, pH 10, and an applied voltage of 30 kV for a reaction time of 15 min. Figure 5 shows the relationship between the pollutant concentration and removal efficiency to the electrode distance. The removal efficiency even slightly varied at an interelectrode distance of 25 mm for ofloxacin (Figure 5(a)) and at that of 30 mm for the other antibiotics (Figures 5(b)–5(d)); hence, the increase in the interelectrode distance leads to the significant decrease in the antibiotic removal efficiency. At an interelectrode distance of 10 mm, the highest antibiotic removal efficiencies reached 72.13%, 99.60%, 99.20%, and 75.80% for ofloxacin, ciprofloxacin, cefuroxime, and amoxicillin, respectively. The decrease in the removal efficiency with the increase in the electrode distances can be explained as follows: with the increase in the interelectrode distance, the possibility of electrical discharge is reduced, leading to the decrease in the electric-field energy generated to create the plasma and subsequently low production of oxidants during the plasma process. These results are consistent with those reported in some previous studies [17, 38, 39]; these studies indicated that a suitable two-electrode spacing from 8 to 20 mm not only improves the formation of oxidants but also accelerates the temperature during the plasma process, leading to the mitigation of a high concentration of pollutants. In the case of COD and ammonia, with the increase in the interelectrode distance, even the removal efficiency decreased, albeit with an insignificant decrease. The highest removal efficiencies of 84.23% and 98.60% for COD and ammonia were observed at an interelectrode distance of 10 mm, respectively, while the lowest values of 73.17% and 76.40%, respectively, were observed at an interelectrode distance of 30 mm. These results demonstrated the effectiveness of the plasma process for the disinfection of HWW. Hence, an interelectrode distance of 10 mm may be a suitable alternative for subsequent experiments for oxidant formation during the plasma process.

3.3. Formation of Oxidizing Agents O_3, H_2O_2, and ·OH. As mentioned above, cold plasma generates several oxidizing species, such as radicals (·OH, ·H) and molecules (O_3 and H_2O_2); among these species, the hydroxyl radical is considered to be a powerful nonselective oxidant [25]. The process formed free ·OH as O_3 was dissolved in water-based eqs (3)–(10):

$$O_2 + e^- \longrightarrow 2O + e^- \tag{3}$$

$$O_2 + O\cdot \longrightarrow O_3 \tag{4}$$

$$O_3 + OH^- \longrightarrow O_3^{\cdot -} + \cdot OH \tag{5}$$

$$O_3^{\cdot -} \longrightarrow O^{\cdot -} + O_2 \tag{6}$$

$$O^{\cdot -} + H_2O \leftrightarrow \cdot OH + OH^- \tag{7}$$

$$3O_3 + H_2O \longrightarrow 2\cdot OH + 4O_2 \tag{8}$$

$$O_3 + HO_{2\cdot} \longrightarrow \cdot OH + O_2O_2^- \tag{9}$$

$$HO_{2\cdot} + HO_{2\cdot} \longrightarrow H_2O_2 + O_2 \tag{10}$$

$$H_2O_2 + O_3 \longrightarrow \cdot OH + O_2 + \cdot HO_2 \tag{11}$$

Hydroxyl radicals were formed by a collision between energetic electrons and H_2O vapour molecules.

$$e^- + H_2O \longrightarrow \cdot OH + H\cdot + e^- \tag{12}$$

In addition, ·OH radicals were formed by the reaction between oxygen and water vapour molecules.

$$O_2 + 2H_2O \longrightarrow 2\cdot OH + 2\cdot OH \tag{13}$$

Recombination of free radicals also possibly decreased the mitigation capacity according to the following equations (14) and (15) [40].

$$\cdot OH + \cdot OH \longrightarrow H_2O_2 \tag{14}$$

$$HO_2 + \cdot OH \longrightarrow O_2 + H_2O \tag{15}$$

Experimentswere conducted to investigate the effects of pH and reaction time on the formation of O_3, H_2O_2 and·OH.

3.4. Effect of pH on the Formation of O_3, H_2O_2, and ·OH. The content of oxidizing agents generated by variation in the pH value (4, 6, 8, 10, and 12) while simultaneously

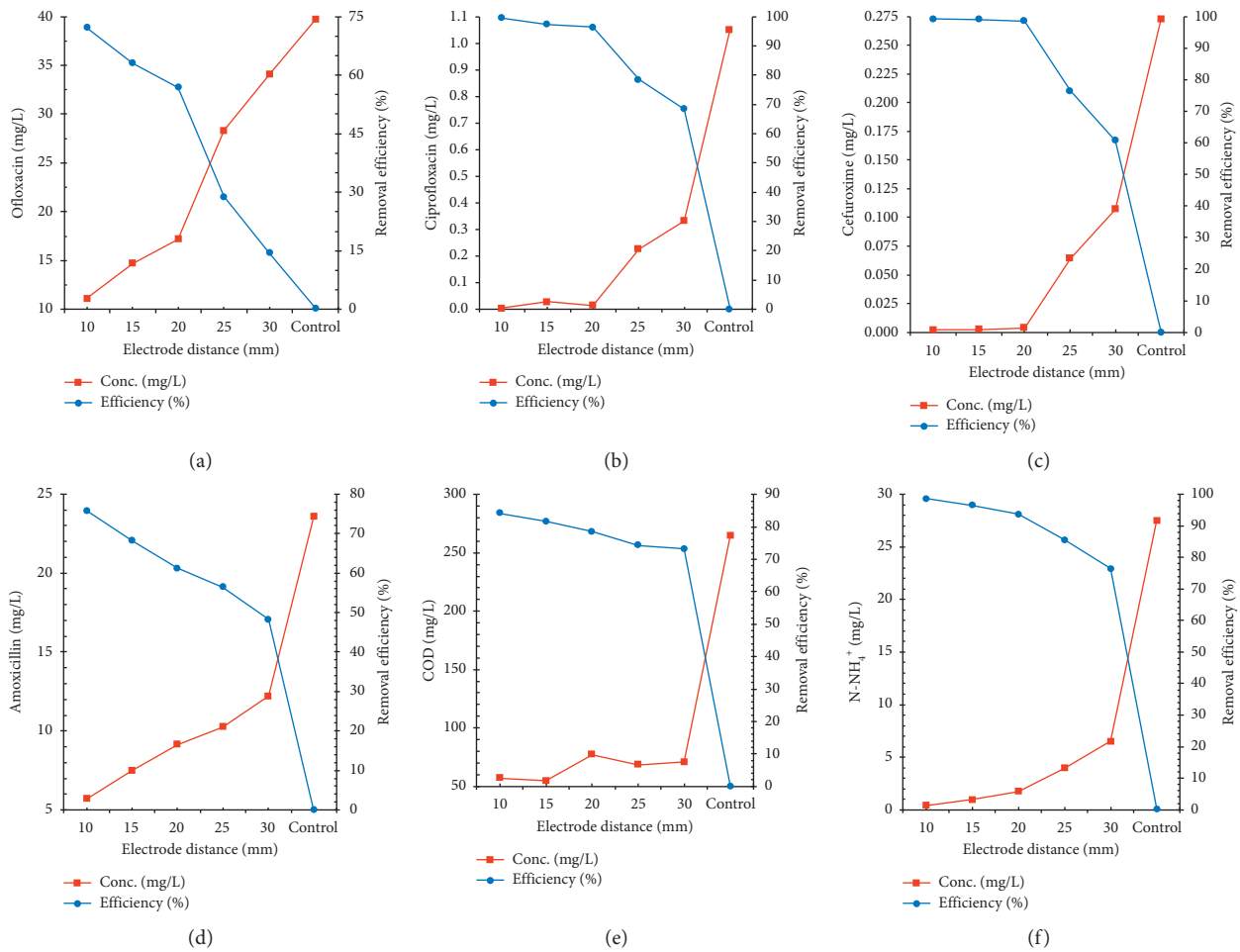

Figure 5: Effect of the interelectrode distance in the plasma reactor on the degradation efficiency of four antibiotics, namely, (a) ofloxacin, (b) ciprofloxacin, (c) cefuroxime and (d) amoxicillin, respectively, as well as (e) COD and (f) ammonia removal.

maintaining the other parameters constant, i. e., an applied voltage of 30 kV, a reaction time of 15 min, and an interelectrode distance of 10 mm. As can be observed in Figures 6(a) and 6(b), with the increase in the pH from acidic to alkaline conditions (3.4 mM and 0.05 mM), the highest concentrations of ozone and H_2O_2were observed, with the highest detected under acidic conditions (4.8 mM and 0.18 mM), and the decomposition rate of these compounds sharply increased. These results are in good agreement with those reported by Kuo et al. [41], where the author reported that in the plasma process, with the increase in pH, the reaction between ozone and H_2O_2 can be accelerated to produce ·OH (a stronger oxidant), as shown in equation (11), leading to the decrease in the concentrations of ozone and H_2O_2 in the aqueous phase. These explanations can be confirmed by the predominant formation of ·OH under alkaline conditions (Figure 6(c)): with the increase in the pH from 4 to 6, the ·OH concentration only slightly increased from 0.052 mM to 0.06 mM. Nevertheless, with the increase in the pH to 10 (0.215 mM), the ·OH concentration dramatically increased. The sudden drop in the ·OH concentration to 0.17 mM at pH 12 may be explained by the fact that most of the ·OH reacted with pollutants in the wastewater. These results also again demonstrated the enhanced formation and removal efficiency of ·OH under alkaline conditions by the Nernst equation [33].

3.5. Effects of the Reaction Time on the Formation of O_3, H_2O_2, and ·OH. Reaction time was directly related to the formation of active radicals; hence, its effect on the production of radicals is examined. The reaction time was adjusted from 2 min to 10 min while simultaneously maintaining an applied voltage of 30 kV, a pH of 10, and an interelectrode distance of 10 mm. At a long reaction time, the O_3 concentration increased (Figure 7(a)). At a reaction time of 2 min, the ozone concentration was 1.2 mM, which slightly increased at a reaction time of 3 min. The generated ozone concentration was 3.9 mM (greater than 3.2 times), while the reaction time increased only by 1 min. At a reaction time of 10 min, the ozone concentration was 8.0 mM (6.7 times greater than that observed in 2 min). Similar trends observed for the formation of H_2O_2 (Figure 7(b)): the H_2O_2 concentration notably increased from 0.076 mM at 2 min to 0.23 mM at 5 min. The H_2O_2 concentration was 0.076 mM at a reaction time of 2 min. With the further increase in

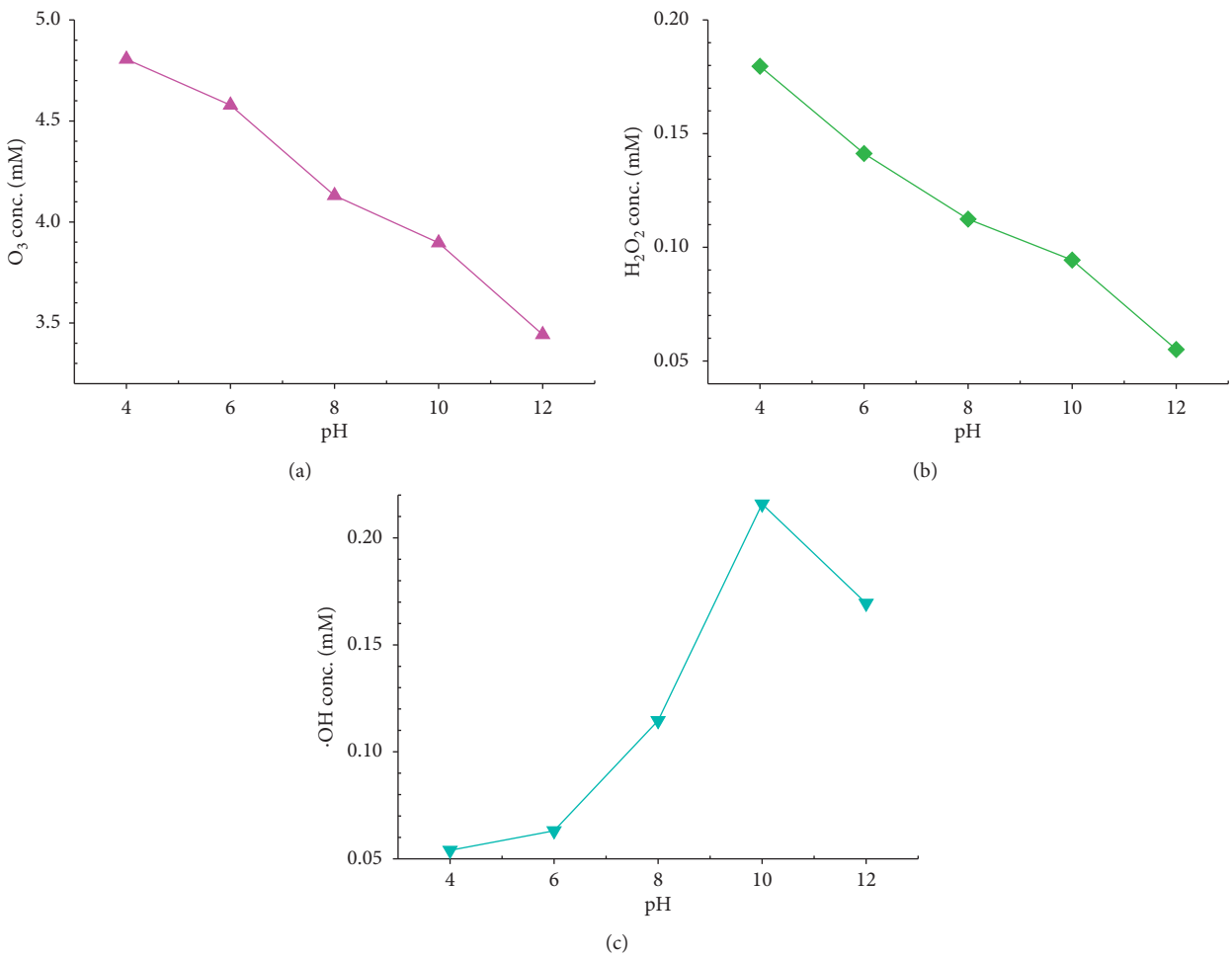

Figure 6: Effect of pH on the formation of (a) O_3, (b) H_2O_2, and (c) ·OH.

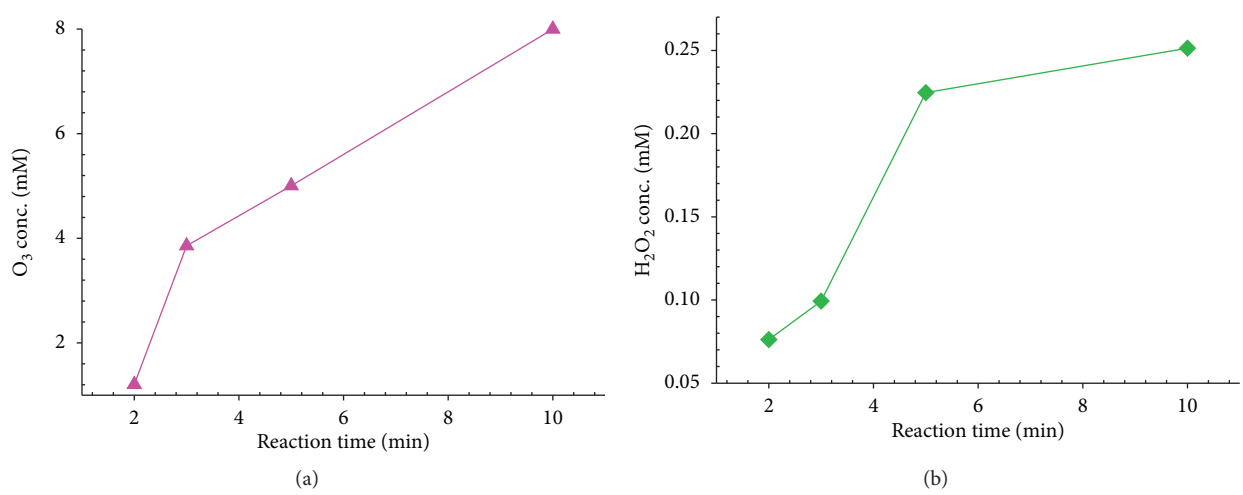

Figure 7: Continued.

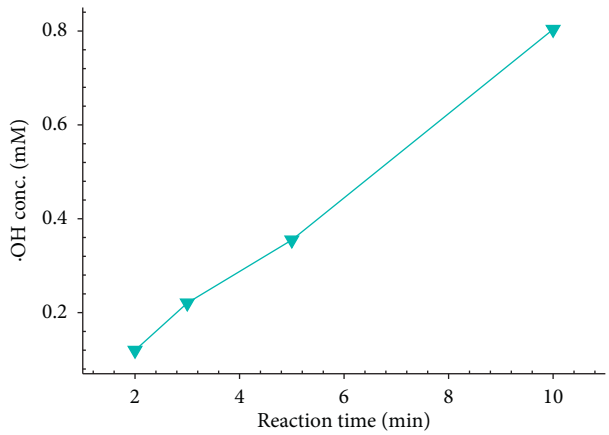

(c)

Figure 7: Effect of the reaction time on the formation of (a) O_3, (b) H_2O_2, and (c) ·OH.

Table 1: Reaction kinetics models for the decomposition of four antibiotics.

Antibiotics	Initial conc. (mg/L)	Reaction order	Regression equation	R^2	Rate constant	$t_{1/2}$ (min)
Ofloxacin	41.23	1	$y = 0.0333x + 0.0993$	0.9214	0.0333 (1/min)	20.82
		2	$y = 0.0014x + 0.0258$	0.9737	0.0014 (L/mg.min)	17.32
		3	$\boldsymbol{y = 0.0001x + 0.0005}$	**0.9896**	$\mathbf{5 \times 10^{-5}}$ (L^2/mg^2.min)	**1.76**
Ciprofloxacin	1.052	**1**	$\boldsymbol{y = 0.2332x - 0.082}$	**0.9790**	**0.2332** (1/min)	**2.97**
		2	$y = 0.6232x + 0.2062$	0.8349	0.6232 (L/mg.min)	1.53
		3	$y = 4.2432x - 6.4031$	0.6643	2.122 (L^2/mg^2.min)	0.64
Cefuroxime	0.273	**1**	$\boldsymbol{y = 0.2421x - 0.0918}$	**0.9626**	**0.2421** (1/min)	**2.86**
		2	$y = 2.6828x + 0.234$	0.7739	2.683 (L/mg.min)	1.37
		3	$y = 79.501x - 131.03$	0.5925	39.75 (L^2/mg^2.min)	0.51
Amoxicillin	23.58	1	$y = 0.0319x + 0.195$	0.9107	0.0319 (1/min)	21.73
		2	$y = 0.0026x + 0.0498$	0.9711	0.0026 (L/mg.min)	16.31
		3	$\boldsymbol{y = 0.0004x + 0.002}$	**0.9826**	$\mathbf{2 \times 10^{-4}}$ (L^2/mg^2.min)	**13.49**

reaction time up to 10 min, the H_2O_2 concentration only reached 0.25 mM, indicating that when the reaction time is doubled, the concentration increase of H_2O_2 is only about 0.02 mM. Compared to H_2O_2 or O_3, the ·OH concentration increased almost linearly with the reaction time and reached the highest concentration of 0.8 mM at 10 min (Figure 7(c)). These results are apparently in agreement with those reported previously on the use of plasma to eliminate pollutants from aqueous solutions [17, 21–23].

3.6. Reaction Kinetic Models for the Decomposition of Antibiotics. To obtain further insights into the reaction kinetics for the decomposition of the antibiotics by cold plasma treatment, the change in the concentration of substances over the reaction time under optimum conditions was carefully investigated. The investigated reaction kinetics models included first-order kinetics, second-order kinetics, and third-order kinetics as reported in our previous studies [15, 16]. Table 1 and Figure S2 show the results obtained, i. e., rate constants, reaction orders, and squared correlation coefficients. The first-order reaction kinetics model revealed the highest squared correlation coefficient for the decomposition of ciprofloxacin and cefuroxime (0.9790 and 0.9626, respectively). Meanwhile, these squared correlation coefficients were the highest for the third-order kinetics reaction of the decomposition of ofloxacin and amoxicillin(0.9896 and 0.9826, respectively).

Table 2 below summarizes the removal efficiencies for antibiotics using cold plasma reported in recent studies. In addition to the Corona plasma systems similar to those used herein, other plasma systems such as DBD were utilized. Specifically, only this study discussed real wastewater containing a high concentration, as well as mixed contaminants, of antibiotics compared to a single antibiotic in an aqueous solution or synthetic wastewater in the references. In a shorter time, this study reaches a suitable result as compared with other reference studies. The removal efficiencies of all antibiotics were extremely high (>99% for cefuroxime and ciprofloxacin and >72% for amoxicillin and ofloxacin). These values are greater than the treatment efficiencies of tetracycline (61.9%) and β-oestradiol (70%) reported in studies by He et al. [23] and Panorel et al. [24], respectively. The lower removal results for mixed compounds compared to individual compounds using AOPs can be found in some previous studies [42, 43].

Table 2: Some recent findings of cold plasma treatment for the elimination of antibiotic compounds in water or wastewater.

Antibiotics	Matrix	Plasma conditions	Efficiency (%)	References
Ofloxacin ciprofloxacin	Synthetic meat effluent (10 mg/L antibiotics)	DBD reactor (25 mL), applied voltage of 80 kV, degradation kinetics: first-order, during a reaction time of 25 min	Ofloxacin 92% Ciprofloxacin 89%	[21]
Carbamazepine clofibric acid iopromide	Aqueous solution and synthetic landfill leachate carbamazepine (23.6 mg/L), clofibric acid (21.5 mg/L), iopromide (79.1 mg/L)	DBD-rotating drum reactor (1000 mL), discharge power of 500 W during, reaction time of 60 min	Carbamazepine 94% Clofibric acid 100% Iopromide 98%	[22]
Tetracycline	Aqueous solution (50 mg/L)	Corona with gas bubbling (250 mL), discharge power of 36 W during a reaction time of 24 min	61.9%	[23]
Paracetamol β-oestradiol	Aqueous solution of paracetamol (100 mg/L) β-oestradiol (3 mg/L)	Corona with liquid shower (40 L), discharge power of 250 W during a reaction time of 30 min	Paracetamol 80% β-Oestradiol 70%	[24]
Lincomycin, ciprofloxacin, enrofloxacin, chlortetracycline, oxytetracycline, sulfathiazole, sulfamethoxazole, sulfamethazine trimethoprim	Aqueous solution (5 mg/L antibiotics)	Cylindrical DBD reactor (1000 mL), supplied O_2, discharge power of 6.8 W corresponding energy requirements: 0.39–2.06 kJ/mg antibiotic during a reaction time of 30 min	Over 90%	[27]
Amoxicillin cefuroxime ofloxacin ciprofloxacin	Real HWW amoxicillin (23.58 mg/L), cefuroxime (0.273 mg/L), ofloxacin (41.23 mg/L), ciprofloxacin (1.052 mg/L)	Corona with a liquid discharge system (600 mL), applied voltage of 30 kV, initial pH of 10, and an interelectrode distance of 10 mm during a reaction time of 15 min	Amoxicillin 75.80% Cefuroxime 99.20% Ofloxacin 72.13%, ciprofloxacin 99.60%	This study

4. Conclusions

In this study, the cold plasma technique was demonstrated to be a simple, efficient method for eliminating antibiotic contaminants from real hospital wastewater in Ho Chi Minh City, Vietnam. The degradation efficiency of these antibiotic compounds was considerably dependent on the initial pH and reaction time as it possibly affected the formation of oxidants (such as O_3, H_2O_2, and ·OH) during the plasma process. The obtained results also indicated that the applied voltage and electrode distance affect the treatment process. Under the optimum conditions (initial pH of 10, electrode distance of 10 mm, reaction time of 15 min, and applied voltage of 30 kV), the removal efficiencies of all antibiotics were high (>72% for ciprofloxacin and cefuroxime and >99% for amoxicillin and ofloxacin), in addition to the complete removal of COD and ammonia. The significant formation of ·OH and rapid decomposition of O_3 and H_2O_2 under alkaline conditions might prove to play a key role in the production of OH during this plasma treatment for such contaminants. In this study, contamination by the four antibiotics also was detected in the effluent of seven hospitals in Ho Chi Minh City, directly leading to the environment. Such environmental pollution could be alarming due to the antibiotic pollutants from the hospital wastewater in Vietnam.

Data Availability

The data used are included in the manuscript.

Conflicts of Interest

The authors declare that they have no conflicts of interest.

Acknowledgments

The authors thank the Ho Chi Minh Department of Science and Technology, Vietnam, for the support through the project code: 77/2019/HĐ-QPTKHCN.

Supplementary Materials

Supplemental Table. Table S1: Evaluated factors and their established ranges for the plasma tests. Table S2: Characterization of wastewater from the seven hospitals. Supplemental Figure. Figure S1: The study area and regional map (a). Ho Chi Minh City area (b), and Hospital sampling site in Ho Chi Minh City (c). Figure S2: Third-order reaction kinetics models of (a) ofloxacin and (b) amoxicillin, and first-order reaction kinetics models of (c) ciprofloxacin and (d) cefuroxime. (*Supplementary Materials*)

References

[1] J. B. Carbajo, A. L. Petre, R. Rosal et al., "Continuous ozonation treatment of ofloxacin: transformation products, water matrix effect and aquatic toxicity," *Journal of Hazardous Materials*, vol. 292, pp. 34–43, 2015.

[2] N. Hassoun-Kheir, Y. Stabholz, J.-U. Kreft et al., "Comparison of antibiotic-resistant bacteria and antibiotic resistance genes

abundance in hospital and community wastewater: a systematic review," *Science of The Total Environment*, vol. 743, pp. 1–11, 2020.

[3] S. Bergeron, R. Boopathy, R. Nathaniel, A. Corbin, and G. LaFleur, "Presence of antibiotic resistant bacteria and antibiotic resistance genes in raw source water and treated drinking water," *International Biodeterioration & Biodegradation*, vol. 102, pp. 370–374, 2015.

[4] H. Q. Anh, T. P. Q. Le, N. Da Le et al., "Antibiotics in surface water of East and Southeast Asian countries: a focused review on contamination status, pollution sources, potential risks, and future perspectives," *Science of The Total Environment*, vol. 764, p. 142865, 2021.

[5] N. A. Khan, S. Ahmed, I. H. Farooqi et al., "Occurrence, sources and conventional treatment techniques for various antibiotics present in hospital wastewaters: a critical review," *TrAC Trends in Analytical Chemistry*, vol. 129, Article ID 115921, 2020.

[6] S. Yousefzadeh, E. Ahmadi, M. Gholami et al., "A comparative study of anaerobic fixed film baffled reactor and up-flow anaerobic fixed film fixed bed reactor for biological removal of diethyl phthalate from wastewater: a performance, kinetic, biogas, and metabolic pathway study," *Biotechnology for Biofuels*, vol. 10, p. 139, 2017.

[7] E. Ahmadi, B. Kakavandi, A. Azari et al., "The performance of mesoporous magnetite zeolite nanocomposite in removing dimethyl phthalate from aquatic environments," *Desalination and Water Treatment*, vol. 57, pp. 27768–27782, 2016.

[8] D. J. Naghan, A. Azari, N. Mirzaei et al., "Parameters effecting on photocatalytic degradation of the phenol from aqueous solutions in the presence of ZnO nanocatalyst under irradiation of UV-C light," *Bulgarian Chemical Communications*, vol. 47, pp. 14–18, 2015.

[9] P. Chinnaiyan, S. G. Thampi, M. Kumar, and M. Balachandran, "Photocatalytic degradation of metformin and amoxicillin in synthetic hospital wastewater: effect of classical parameters," *International Journal of Environmental Science and Technology*, vol. 16, no. 10, pp. 5463–5474, 2019.

[10] K. M. S. Hansen, A. Spiliotopoulou, R. K. Chhetri, M. Escolà Casas, K. Bester, and H. R. Andersen, "Ozonation for source treatment of pharmaceuticals in hospital wastewater - ozone lifetime and required ozone dose," *Chemical Engineering Journal*, vol. 290, pp. 507–514, 2016.

[11] Y. Qian, X. Liu, K. Li et al., "Enhanced degradation of cephalosporin antibiotics by matrix components during thermally activated persulfate oxidation process," *Chemical Engineering Journal*, vol. 384, Article ID 123332, 2020.

[12] M. Yegane Badi, S. Fallah Jokandan, A. Esrafili et al., "Optimization of advanced oxidation process based on persulfate ($Uv/Na_2S_2O_8/Fe_2+$) for phthalic acid removal from aqueous solutions with response surface methodology," *Journal of Babol University of Medical Sciences*, vol. 20, pp. 13–21, 2018.

[13] S. Ahmadzadeh and M. Dolatabadi, "Removal of acetaminophen from hospital wastewater using electro-Fenton process," *Environmental Earth Sciences*, vol. 77, pp. 1–11, 2018.

[14] R. Changotra, J. P. Guin, S. A. Khader, L. Varshney, and A. Dhir, "Electron beam induced degradation of ofloxacin in aqueous solution: kinetics, removal mechanism and cytotoxicity assessment," *Chemical Engineering Journal*, vol. 356, pp. 973–984, 2019.

[15] N. N. Duy, T. N. Hieu, T. P. Luu et al., "Removal of leucomalachite green in an aqueous solution by the electron beam process," *Journal of Water Process Engineering*, vol. 40, Article ID 101781, 2020.

[16] D. N. Nguyen, H. T. Nguyen, T.-L. Pham et al., "Degradation of tricyclazole from aqueous solution and real wastewater by electron-beam irradiation," *Environmental Technology & Innovation*, vol. 21, Article ID 101315, 2021.

[17] H. Zeghioud, P. Nguyen-Tri, L. Khezami, A. Amrane, and A. A. Assadi, "Review on discharge Plasma for water treatment: mechanism, reactor geometries, active species and combined processes," *Journal of Water Process Engineering*, vol. 38, Article ID 101664, 2020.

[18] C. Sarangapani, N. N. Misra, V. Milosavljevic, P. Bourke, F. O'Regan, and P. J. Cullen, "Pesticide degradation in water using atmospheric air cold plasma," *Journal of Water Process Engineering*, vol. 9, pp. 225–232, 2016.

[19] H.-J. Kim, C.-H. Won, and H.-W. Kim, "Pathogen deactivation of glow discharge cold plasma while treating organic and inorganic pollutants of slaughterhouse wastewater," *Water, Air, & Soil Pollution*, vol. 229, pp. 1–10, 2018.

[20] L. H. Tecer, A. Gündüz, R. Atav, S. Soysal, and F. Yıldız, "Investigation of the treatment of textile wastewater with cold atmospheric plasma reactor (profoks) and reuse of recycled water in reactive dyeing process of cotton," *Journal of Natural Fibers*, vol. 40, pp. 1–8, 2020.

[21] C. Sarangapani, D. Ziuzina, P. Behan et al., "Degradation kinetics of cold plasma-treated antibiotics and their antimicrobial activity," *Scientific Reports*, vol. 9, pp. 1–15, 2019.

[22] H. Krause, B. Schweiger, E. Prinz, J. Kim, and U. Steinfeld, "Degradation of persistent pharmaceuticals in aqueous solutions by a positive dielectric barrier discharge treatment," *Journal of Electrostatics*, vol. 69, no. 4, pp. 333–338, 2011.

[23] D. He, Y. Sun, L. Xin, and J. Feng, "Aqueous tetracycline degradation by non-thermal plasma combined with nano-TiO2," *Chemical Engineering Journal*, vol. 258, pp. 18–25, 2014.

[24] I. Panorel, S. Preis, I. Kornev, H. Hatakka, and M. Louhi-Kultanen, "Oxidation of aqueous pharmaceuticals by pulsed corona discharge," *Environmental Technology*, vol. 34, no. 7, pp. 923–930, 2013.

[25] P. Lukes and B. R. Locke, "Plasmachemical oxidation processes in a hybrid gas-liquid electrical discharge reactor," *Journal of Physics D: Applied Physics*, vol. 38, no. 22, pp. 4074–4081, 2005.

[26] J. Lou, N. Lu, J. Li, T. Wang, and Y. Wu, "Remediation of chloramphenicol-contaminated soil by atmospheric pressure dielectric barrier discharge," *Chemical Engineering Journal*, vol. 180, pp. 99–105, 2012.

[27] K.-S. Kim, C.-S. Yang, and Y. S. Mok, "Degradation of veterinary antibiotics by dielectric barrier discharge plasma," *Chemical Engineering Journal*, vol. 219, pp. 19–27, 2013.

[28] R. B. Baird, *Standard Methods for the Examination of Water and Wastewater, 23rd, Water Environment Federation*, American Public Health Association, Washington, DC, USA, 2017.

[29] ASTM E222-17, *Standard Test Methods for Hydroxyl Groups Using Acetic Anhydride Acetylation*, ASTM International, West Conshohocken, PA, USA, 2017.

[30] ASTM D6363-98(2013), *Standard Test Method for Determination of Hydrogen Peroxide and Combined Organic Peroxides in Atmospheric Water Samples by Peroxidase Enzyme Fluorescence Method*, ASTM International, West Conshohocken, PA, 2013.

[31] M. Magureanu, N. B. Mandache, and V. I. Parvulescu, "Degradation of pharmaceutical compounds in water by non-thermal plasma treatment," *Water Research*, vol. 81, pp. 124–136, 2015.

[32] X. Liao, D. Liu, S. Chen, X. Ye, and T. Ding, "Degradation of antibiotic resistance contaminants in wastewater by atmospheric cold plasma: kinetics and mechanisms," *Environmental Technology*, vol. 42, no. 1, pp. 58–71, 2021.

[33] B. Nikravesh, A. Shomalnasab, A. Nayyer, N. Aghababaei, R. Zarebi, and F. Ghanbari, "UV/Chlorine process for dye degradation in aqueous solution: mechanism, affecting factors and toxicity evaluation for textile wastewater," *Journal of Environmental Chemical Engineering*, vol. 8, no. 5, Article ID 104244, 2020.

[34] R. Xie, X. Meng, P. Sun et al., "Electrochemical oxidation of ofloxacin using a TiO_2-based SnO_2-Sb/polytetrafluoroethylene resin-PbO_2 electrode: reaction kinetics and mass transfer impact," *Applied Catalysis B: Environmental*, vol. 203, pp. 515–525, 2017.

[35] T. Liu, Q. Xue, J. Jia et al., "New insights into the effect of pH on the mechanism of ofloxacin electrochemical detection in aqueous solution," *Physical Chemistry Chemical Physics*, vol. 21, no. 29, pp. 16282–16287, 2019.

[36] W. Guo, Q.-L. Wu, X.-J. Zhou et al., "Enhanced amoxicillin treatment using the electro-peroxone process: key factors and degradation mechanism," *RSC Advances*, vol. 5, no. 65, pp. 52695–52702, 2015.

[37] U. E. Osonwa, J. I. Ugochukwu, E. E. Ajaegbu, K. I. Chukwu, R. B. Azevedo, and C. O. Esimone, "Enhancement of antibacterial activity of ciprofloxacin hydrochloride by complexation with sodium cholate," *Bulletin of Faculty of Pharmacy, Cairo University*, vol. 55, no. 2, pp. 233–237, 2017.

[38] B. Ghimire, J. Sornsakdanuphap, Y. J. Hong, H. S. Uhm, K.-D. Weltmann, and E. H. Choi, "The effect of the gap distance between an atmospheric-pressure plasma jet nozzle and liquid surface on OH and N2 species concentrations," *Physics of Plasmas*, vol. 24, Article ID 073502, 2017.

[39] Z. B. Wang, G. X. Chen, Z. Wang, N. Ge, H. P. Li, and C. Y. Bao, "Effect of a floating electrode on an atmospheric-pressure non-thermal arc discharge," *Journal of Applied Physics*, vol. 110, pp. 1–5, 2011.

[40] A. Eslami, F. Mehdipour, K.-Y. A. Lin, H. Sharifi Maleksari, F. Mirzaei, and F. Ghanbari, "Sono-photo activation of percarbonate for the degradation of organic dye: the effect of water matrix and identification of by-products," *Journal of Water Process Engineering*, vol. 33, Article ID 100998, 2020.

[41] C.-H. Kuo, L. Zhong, M. E. Zappi, and A. P. Hong, "Kinetics and mechanism of the reaction between ozone and hydrogen peroxide in aqueous solutions," *The Canadian Journal of Chemical Engineering*, vol. 77, no. 3, pp. 473–482, 1999.

[42] D. A. Yaseen and M. Scholz, "Treatment of synthetic textile wastewater containing dye mixtures with microcosms," *Environmental Science and Pollution Research*, vol. 25, no. 2, pp. 1980–1997, 2018.

[43] A. Saha, A. S. Ahammed Shabeer TP, V. T. Gajbhiye, S. Gupta, and R. Kumar, "Removal of mixed pesticides from aqueous solutions using organoclays: evaluation of equilibrium and kinetic model," *Bulletin of Environmental Contamination and Toxicology*, vol. 91, no. 1, pp. 111–116, 2013.